UNIVERSITY OF WITWATERSRAND

MASTERS DISSERTATION

Quantum Walks with Classically Entangled Light

Author:
Bereneice C. SEPHTON

Supervisor:
Prof. Andrew FORBES
Dr. Angela DUDLEY

A dissertation submitted in fulfillment of the requirements for the degree of Masters in Science

in the

The Structured Light Group
Department of Physics

September 11, 2018

Declaration of Authorship

I, Bereneice C. SEPHTON, declare that this thesis titled, “Quantum Walks with Classically Entangled Light” and the work presented in it are my own. I confirm that:

- This work was done wholly or mainly while in candidature for a research degree at this University.
- Where any part of this thesis has previously been submitted for a degree or any other qualification at this University or any other institution, this has been clearly stated.
- Where I have consulted the published work of others, this is always clearly attributed.
- Where I have quoted from the work of others, the source is always given. With the exception of such quotations, this thesis is entirely my own work.
- I have acknowledged all main sources of help.
- Where the thesis is based on work done by myself jointly with others, I have made clear exactly what was done by others and what I have contributed myself.

Signed: ____________________________________

Date: ____________________________________

"*Somewhere, something incredible is waiting to be known"*

Carl Sagan

UNIVERSITY OF WITWATERSRAND

Abstract

Faculty of Science
Department of Physics

Masters in Science

Quantum Walks with Classically Entangled Light

by Bereneice C. SEPHTON

At the quantum level, entities and systems often behave counter-intuitively which we have come to describe with wave-particle duality. Accordingly, a particle that moves definitively from one position to another in our classical experience does something completely different on the quantum scale. The particle is not localized at any one position, but spreads out over all the possibilities as it moves. Here the particle can interfere with itself with wave-like propagation and generate, what is known as a Quantum Walk. This is the quantum mechanical analogue of the already well-known and used Random Walk where the particle takes random steps across the available positions, building up a series of random paths.

The mechanics behind the random walk has already proved largely useful in many fields, from finance to simulation and computation. Analogously, the quantum walk promises even greater potential for development. Here, with many of the algorithms already developed, it would allow computations to outperform current classical methods on an unprecedented level. Additionally, by implementing these mechanics on various levels, it is possible to simulate and understand various quantum mechanical systems and phenomenon. This phenomenon consequently represents a significant advancement in several fields of study.

Although there has been considerable theoretical development of this phenomenon, its potential now lies in implementing these quantum walks physically. Here, a physical system is required such that the quantum walk may be sustainably achieved, easily detected and dynamically altered as needed. Many systems have been subsequently proposed and demonstrated, but the criteria for a useful quantum walk leaves many such avenues lacking with the largest number of steps yet to reach 100 to the best of our knowledge. As a result, we explored a classical take on the quantum walk, utilizing the wave properties of light to achieve analogous mechanics with the advantage of the increased degree of control and robustness. While such an approach is not new, we considered a particular method where the quantum walk could be implemented in the spatial modes of light. By exploiting the non-separability (classical entanglement) of polarization and orbital angular momentum, such a classical quantum walk could be realized with greater intuitive implications and the potential for further study into the quantum mechanical nature of this phenomenon, over and above that of the other schemes, by walking the quantum-classical divide.

The work presented here subsequently centres on experimentally achieving a quantum walk with classically entangled light for further development and useful implementation. Moreover, this work focused on demonstrating the sustainability, control and robustness necessary for this scheme to be beneficial for future development.

In Chapter 1, an intuitive introduction is presented, highlighting the mechanics of this phenomenon that make it different from the Random walk counterpart. We also explore why this phenomenon is of such great importance with an overview of applications that physical implementation can result in. A more in-depth look into the dynamics and mathematical aspects of this walk is found in Chapter 2. Here a detailed look into the mechanisms behind the walk is taken with mathematical analysis. Furthermore, the subsequent differences and implications associated

with utilizing classical light is explored, answering the question of what is quantum about the quantum walk. As the focus of this chapter is largely cemented in establishing a solid theoretical background, we also look into the physics behind classical light and develop the theoretical basis in the direction of structured light, with an emphasis on establishing classically entangled beams.

Chapters 3 and 4 present the experimental work done throughout the course of this dissertation. With Chapter 3 we establish and characterize the elements necessary for obtaining a quantum walk in the spatial modes of light by utilizing waveplates as coins, q-plates as step operators and entanglement generators as well as mode sorters in a detection system. We also look into the characteristics of the modes that will be produced with these elements, allowing the propagation properties of the beam to be experimentally accounted for. In Chapter 4, we examine the experimental considerations of how to achieve a realistic and sustainable quantum walk. Here, we consider and implement the scheme proposed by Goyal et. al. [] where a light pulse follows a looped path, allowing the physical resources to be constant throughout the walk. We also show the experimental limitations of the equipment being utilized and the various steps needed to compensate. Finally, we not only implement a quantum walk with classically entangled light for the first time, but also demonstrate the flexibility of the system. Here, we achieve a maximum of 8 steps and show 5 different types of walks with varying dynamics and symmetry.

The last chapter (Chapter 5) gives a summary of the dissertation in context of the goals and achievements of this work. The outlook and implications of these results are discussed and future steps outlined for extending this scheme into a highly competitive alternative for viable implementation of quantum walks for computing and simulation.

Acknowledgements

I would like to express my sincerest gratitude for everyone that has given me support throughout the undertaking of my MSc. Specifically, I would like to thank the following people who have made this journey that much easier:

My supervisors, Prof. Andrew Forbes and Dr. Angela Dudley, thank you for the invaluable guidance, time, effort and support you have given to me throughout this endeavour. You both have inspired me to do my best and keep trying when it became hard. In particular, I am grateful to Dr. Dudley for always being a soft sounding board when I came across problems in the lab and had trouble understanding concepts, for listening to my nervous (and numerous) attempts at presenting and navigating murky waters. Thank you for the countless hours you put in at (and after) work, making sense of the proposals, papers, posters and, finally, this dissertation. Your advice is always valuable and greatly appreciated.

I am grateful to Prof. Forbes for being an inspiring mentor when looking at science and what we can do with it. Thank you for your advice which helped me overcome many of the challenging aspects (and blonde moments) I faced in the lab. You have taught me how to better think about and communicate science, both on paper and in presentations, for a variety of audiences. Thank you for the opportunities to expand my network, explore science beyond South African boarders and learn at an international level.

Thank you to everyone that has been part of the Structured Light Group throughout my MSc. Everyone has added colour to the days spent doing experiments and just visiting from CSIR. A few individuals stand out for offering endless support on the days needed. Thank you, Hend, for always being there when it became tough and always being a phone call away. You became a great friend throughout this experience and I couldn't imagine it without your friendship. Thank you, BV (the dictator), for your fun take on science and endless patience explaining concepts. It is always interesting listening to your perspectives, ideas and ways of pushing the boundaries of science. Isaac and Nkosi, thank you for all the 'night shifts' and inspiration to push through to the finish. It has been such a legendary experience, starting from that memorable trip to the unknown in Iran. To the Nickelodeon, the office is lots of fun with your pranks keeping everyone on their toes. Thank you for slogging through my attempts to avoid butchering maths. Carmelo and Adam, thank you for your advice and support in the lab.

I am greatly appreciative to the CSIR National Laser Centre for providing me with the opportunity and funding to conduct this research as well as attend national and international conferences. At the CSIR, I would like to thank Gary for taking me through the basics of optics care and for always being there to help when needed. Thank you Ameeth for the countless lab emergencies as I tried to grapple with the electronic side of things. Without your help, this work would not have been possible. Thank you Sat for all the extended-extended deadlines with the camera so I could complete measurements. I would like to thank my office-mate, Mosima, for your serious take on things, being my 'secretary' and helping me keep up to date with everything. It will be strange working without you. Darryl, thank you for being the emergency sounding board when Angela wasn't available, help moving equipment, lab checks and for your calm outlook that puts things into perspective. Chemist, Tebogo and Daniel, thank you for all the lunch time discussions and helping me get used to CSIR. Lucas, thank you for the many 'night shift' discussions and encouragement to keep up the work.

I would like to thank my family for their unending patience and support throughout the frustrating and exciting times that have made up this experience. Thank you for all the catch-up Skypes, countless prayers over the phone, always being available and chocolate overdoses. Thank you for your interest in what I'm doing and the enjoyable discussions on death-rays. Without you, I would not have made it through.

A moment of silence for the 2 mirrors, precision pinhole, ND filter and lens that did not survive the undertaking. May your sacrifice not be in vain.

Last, but not least, may all the glory, honour and praise be to God, for “I can do all things through Christ who strengthens me” ˘ Philippians 4:13

Contents

List of Figures

List of Tables

To my Dad

Chapter 1

Introduction

1.1 Random Walking

1.1.1 Classical Random Walks

Random motion is ubiquitous in nature from the path of tiny dust particles as they float in still air to the motion of molecules in the liquid state. It is an integral part of how the world operates and facilitates many of the fundamental processes that maintain the earth, such as heat transport in materials [1] and the transport of gasses like oxygen [2] which are crucial to survival. Furthermore, it is also present in the foraging of wildlife [3] and may be extended to the financial sector [4] as well.

The most famous discovery of random motion can be dated back to 1827 when botanist, Robert Brown noted the stochastic movements of pollen floating on water [5]. He observed the motion of these particulates as moving in many random stochastic directions, but eventually having no real net displacement. This opened the door to the study of atoms and was eventually explained as the result of the random motion of fast-moving molecules bombarding the pollen grains such that different sides experienced slightly greater forces due to these random bombardments [5]. Subsequently the pollen motion exhibited a random motion of its own. Mathematical formulation of this phenomenon, however, came from the work of Albert Einstein in 1905 [6] and found experimental proof in 1908 through Jean Baptiste Perrin [7], consolidating random motion as a foundation in many scientific studies today.

Understanding and being able to predict such motion lies in the ability to simulate it. However, the basic feature of something that is random is that there is no definable pattern. How does one then do this for something that should not be predictable? The answer lies in the concept of the random walk [8].

Consider for a moment the idea of using the coin flip to make a decision such as deciding which direction to move in: left or right. This concept is illustrated with Bob in Fig. 1.1.

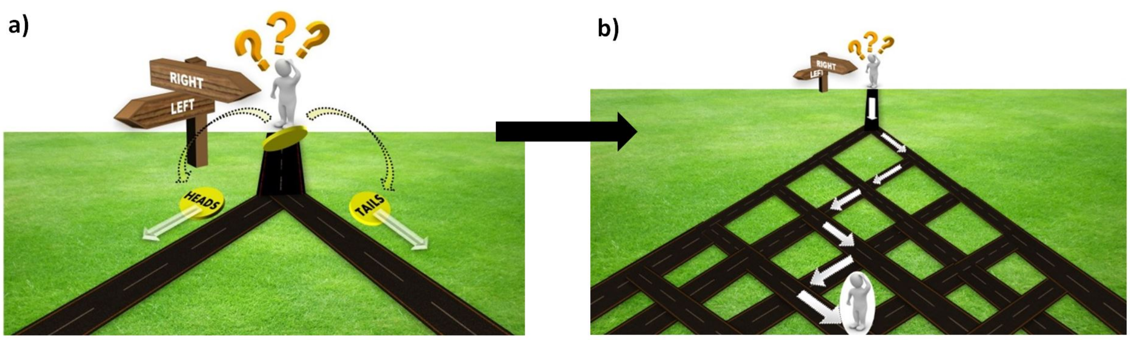

FIGURE 1.1: Illustration of a one-dimensional random walk whereby (a) random movement is generated by a coin flip. A succession of such movements then results in (b) a random path which is known as the random walk.

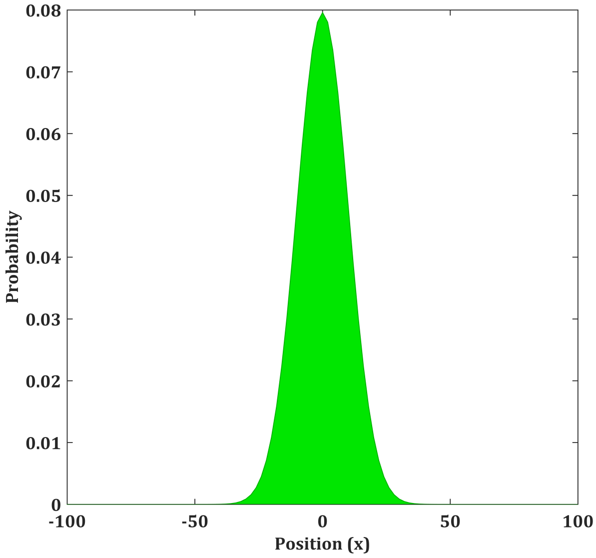

FIGURE 1.2: Graph of the probability distribution for a 1-dimensional random walk after 100 successive random movements or steps whereby the most frequent outcome remains at the same lateral position.

One accordingly assigns a side of the coin to a particular direction; for instance, heads to left and tails to right. By flipping the coin and moving in that direction, a random movement has resulted. Now by flipping the coin again and moving according to the outcome, another random movement is carried out. Doing this repeatedly in fact results in the random motion or, more specifically, a random walk as depicted by Fig. 1.1 (b). It follows that by assigning values to the particular options of a system and then randomly generating those assigned values, the 'randomness' of the system can be simulated by acting upon the randomly generated values [9]. The outcomes of the system can thus be predicted. The output of such a simulation is consequently a probability distribution such as that shown in Fig. 1.2 for 100 such steps.

The random walk probability distribution is that of a Gaussian where the most probable outcome, and thus that which will most frequently occur, would be to remain at the same position [9]. Consequently, it would be expected that no net displacement should occur on average for forces with equal magnitudes acting on the pollen. This is exactly what Robert Brown noted for the randomly moving pollen. The concept of random walks does not only apply to natural phenomena where it is amongst the best known methods to model processes such as Brownian motion [10; 11], deoxyribonucleic acid synapsis [12] and interface mobility in materials [13], but also extends to nearly all scientific fields. For instance, in computing it has great algorithmic utilization which includes determination of differential equation solutions [14], fractal problems [15] and even database basis search algorithms [16].

The rate at which a probability distribution spreads with the number of steps taken (coin flips) is of particular interest when characterizing the operation of such an algorithm and is subsequently a trademark identification for the classical random walk. This is a consequence of the relation to time taken to find or detect a selected sate, known as the hitting time [17]. Accordingly, the variance σ^2 is considered which may be shown to vary linearly with the number of steps (n) taken in the characteristic random walk probability distribution [18; 19]:

$$\sigma^2 \propto n \tag{1.1}$$

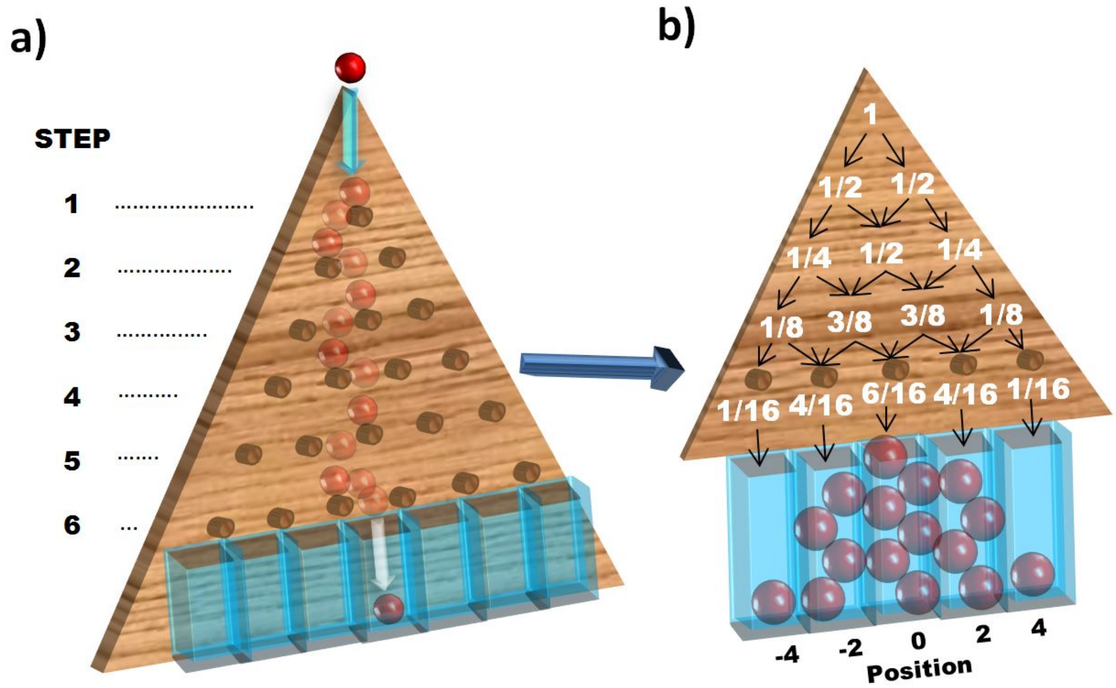

FIGURE 1.3: Illustration of Galton board mechanics for (a) n = 6 steps and (b) the probability propagation for n = 4 steps which yields the Gaussian probability distribution associated with random walks.

Due to the linearity, it is termed a *diffusive* spread.

Subsequent mechanics of a random walk may be generalized into a walker (Bob), a random value generator (coin), a position space (road intersections) where the random values are assigned to particular directions and a propagator which moves the walker in the randomly generated direction (walking). It follows that the previous one-dimensional random walk, and thus the concept of random motion, can be extended to many more dimensions by adding additional directions and extending the set of random values. This has in fact been done (see, among others, [20] for a d-dimensional lattice and [21] where it has been generalized to a d-dimensional hypercube). The scope of this dissertation lies within the one-dimensional realm however and therefore theory for additional dimensions shall not be discussed.

Another conceptual introduction into the random walk involves the mechanics of the Galton board or Galton quincunx [9; 22; 23]. This approach affords a more intuitive glance into the physics behind the random walk. The board consists of a triangular array of pins with the point located at the top as displayed in Fig. 1.3.

When a ball is positioned directly above the top pin and allowed to fall, it will randomly bounce off the pin to either one of the pins in the level below and continue the cascade until reaching the end of the pin array. The ball will then land in one of the bins at the bottom, indicating the eventual position of the ball as dictated by a series of random events. In this case, the random 'event' is each deflection of the ball to either the right or left when hitting the pin, dictating which of the next round of pins will be hit.

Repeatedly sending or dropping balls into this Galton board will result in a collection of these balls in the bins below with the number in each bin indicating the probability of the ball ending up in a particular position as a result of the random motion; in other words, a probability distribution results that is visually illustrated by the 'binning' of the balls sent through. Figure 1.3 (b) depicts this for a succession of 4 rows of pins. Each horizontal row of pins represents a step taken in the random walk as each successive pin that is hit moves the ball's position with respect to the bins. This random walk can then be generalized into the same formulation discussed for that of the coin case. Here the ball plays the role of the walker, the pin the role of the coin (random value generator yielding either right or left), gravity the role of the propagator and the bins represent position space.

Determination of the probability associated with each position or bin can be intuitively obtained by propagating the probabilities after each step. This is indicated explicitly in Fig. 1.3 (b). Due to 50 percent probability of falling to either the right or left of the pin, the probabilities associated with the adjacent successive pins are halved. Probabilities for positions where two pins from the previous row may result in the ball falling on it (i.e. all the inner pins) are calculated by adding the probabilities from each of the pins as they would occur independently from each other (different balls with different paths at different times). As can be suspected by the random walk discussion above, the resulting probability distribution occurring is that of a binomial distribution or a Gaussian in the limit of an infinite number of balls being sent through an endless array of pins.

1.1.2 Quantum Random Walks

As the random walk has been largely successful in the realm of classically described phenomena, the question arises as to the effect of such a method in the world of quantum mechanics i.e. what can be accomplished if the mechanics of the random walk framework was extended to work under the principles of the quantum regime? Here, Aharonov *et. al.* [24] explored such a possibility in 1993, resulting in the introduction of the quantum random walk which has sparked a large amount on interest and research. Over the 20+ years from Aharonov *et. al.*, the mechanics have been further refined to yield the quantum walk being investigated today. Interestingly, principals behind this quantum walk, can be dated back much further where its basis is associated with the Dirac equation. As discussed by Meyer (1996), the use of a 'discrete space-time path integral' to produce a propagator for the one-dimensional Dirac equation in the continuum limit for Feynman's checkerboard employed the principals that Aharonov *et. al.* utilized [9; 25].

Two types of quantum walks have been developed and as such require distinction [17]. The discrete time quantum walk (DTQW) is the focus of this study and as such shall be referred to as a quantum walk (QW) only for brevity. Here, iterative implementation of the coin and propagation is required to evolve the walk, similar to that described for the random walk above [9; 17; 26]. The continuous time quantum walk (CTQW) established by Farhi *et. al.*. in 1998 [27] only requires temporal propagation of the initial state, however. This is due to incorporation of the coin action into the mechanics as an auxiliary parameter where a coupling term in the position space determines the probability of moving to adjacent positions as opposed to the coin operator. As such, it takes place entirely in the position basis or space [9; 17; 26].

Implementation of quantum mechanical principals to the random walk lies in the phenomenon of quantum superposition whereby an entity can exist as a linear superposition of more than one basis state [28]. It follows that the coin in the random walk can no longer be either heads or tails in the quantum equivalent, but is rather a superposition of heads and tails [9]; roughly speaking, it is simultaneously in the state of landing on heads and tails as depicted by the cartoon in Fig. 1.4 (a). This is mathematically described in terms of complex probability amplitudes in Hilbert space whereby how much each state is favoured is weighted by the relative value of the complex probability [9; 23]. Accordingly, it can be noted that the coin may be weighted such that it is more strongly 'present' in the heads state than the tails state or *vice versa* [26; 29]. (The result of weighting the coin would affect the spread of the probability distribution. Associatively, influencing the respective phases contributes towards asymmetrical spreading in the position space direction [26; 29]. This will be discussed in further detail later.) To gain a crude impression for what is occurring, one can think of this as causing the movement of the walker or Bob to both the right and left at the same time such that Bob is now in a superposition of occupying both positions +1 and -1 simultaneously.

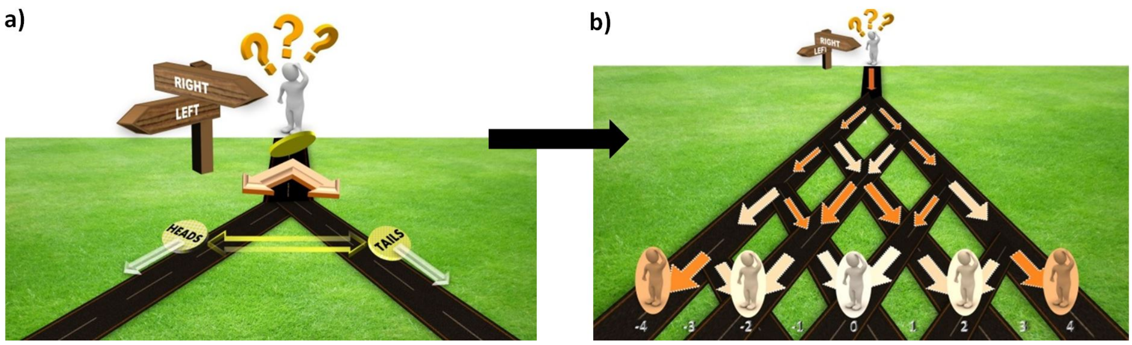

FIGURE 1.4: Illustration of a one-dimensional quantum random walk whereby (a) the coin is in a superposition of all possible states/random values. A succession of such movements then results in (b) the superposition of all possible random paths.

'Flipping' the coin again results in a superposition of heads and tails for Bob at each of the $+1$ and -1 positions, resulting in Bob moving left and right again. An overlap in the states being simultaneously occupied then occurs i.e. Bob at $+1$ moves to $+2$ and 0 while Bob also at -1 moves to -2 and 0 such that there are 'two movements' to 0. It follows that the position at 0 is more strongly favoured than that of ± 2, resulting in constructive interference of the probabilities associated with these states. Bob will thus be more likely to be found at 0 when looking for him (taking a measurement). As these are complex probability amplitudes the interaction is more convoluted than described above and as such these 'overlapping states' may also result in destructive interference [9]. Subsequently, a position may be less strongly favoured in such a case, resulting in a reduced probability of finding Bob there. In some cases, this can entirely annihilate the probability of finding Bob at a certain position. It is this interference that forms a significant difference between the random walk and quantum random walk and is illustrated in Fig. 1.4 (b). Here shades of the arrows pointing to the intersections (positions) indicate constructive (dark orange) and destructive interference (white). For instance, the constructive interference described for position 0 at the second coin flip (step two) is shown through the two bright orange arrows pointing at the corresponding intersection at the second set of horizontal vertices.

The shades of Bob spread out between the positions in the last step in Fig. 1.4 (b) depict a destructive interference occurring at the center which seems counter-intuitive to what was seen in the random walk. In fact, the greatest probability of finding Bob is close to the ends of the distribution as shown by the dark orange shading at positions ± 2. This different distribution characterizes the quantum random walk and is the source of interest for researchers as will be discussed later. Figure 1.5 (a) gives the probability distribution for a one-dimensional quantum random walk of 100 steps.

As can be seen, the probability distribution is distinctly different to that of the Gaussian or binomial occurring in the classical case where the destructive interference plays a large role. Here the probability of finding the walker is closest to the ends of the distribution while minimal probability occurs at the original position (position 0) [26]. In fact, the larger the number of steps taken, the smaller this probability becomes. Several variations on the probability distributions can also be made by changing the input state or the weighting of the coin such that greater favour is given to the probabilities along one direction of the quantum walk [30]. This is illustrated in Fig. 1.5 (b) whereby an asymmetrical input state biased the probability propagation towards the left.

While this distribution characterizes the quantum random walk, it is the hitting time of the process which has resulted in the interest that has spurred its development. Here the spread or variance has been shown as *ballistic* [19; 31].

$$\sigma^2 \propto n^2 \tag{1.2}$$

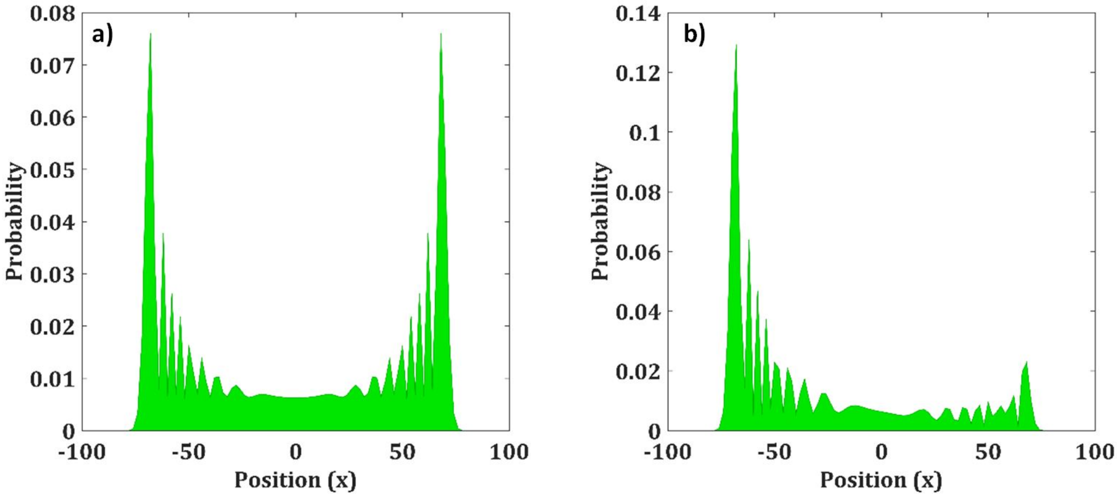

FIGURE 1.5: Graph of the probability distribution for a 1-dimensional quantum walk after 100 successive movements or steps for a (a) symmetrical and (b) asymmetrical input state.

In other words, the probability distribution spreads out quadratically faster than that of the classical case. This has several significant implications that are discussed in Section 1.2.2.

Curiously, despite the random nature of the classical random walk, the quantum random walk is in fact not a random process, but is rather deterministic as was noted by [32]. Equivalent probability amplitudes - given the same initial state and coin weighting - occur regardless of repetition. Now as this is the complete description of the quantum system due to the nature of the quantum superposition phenomenon, there is no randomization in the outcome. Therefore, the quantum random walk shall henceforth be referred to as only a quantum walk despite its initial presentation as the former by Aharonov *et. al.*.

In congruence to the random walk, there is an analogous Galton board that affords another level of intuitive understanding for the QW concept. This hybrid or optical Galton board given in Fig. 1.6 involves beam-splitters taking on the role of the pins while a photon replaces the ball [9; 33; 34]. As this scheme exploits the wave nature of photons, it yields a convincing demonstration of the probability amplitude interference behind the mechanics of the QW. This scheme was first investigated experimentally by Bouwmeester *et. al.* [35] without reference to its QW implications which was later pointed out by Knight *et. al.*. [32].

It follows that a photon incident on a side of the beam-splitter as depicted by the wave packet in Fig. 1.6 has a 50% chance of reflectance and a 50% chance of transmittance [33]. Due to the nature of the particle on this scale, a quantum superposition is formed where it is both reflected and transmitted. The photon then propagates to both beam-splitters (positions) in the level below. Incidence upon these beam-splitters creates two other sets of reflectance and transmittance superpositions [33]. This results in the middle beam-splitter on the third row now receiving two inputs, one from both of the previous beam-splitters. The photon is now interfering with itself! Further propagation through the beam-splitters cause the formation of more superpositions such that all of the following intermediate beam-splitters experience a mixing or interference of the adjacent previous amplitudes. Consequently, various degrees of constructive and destructive interference occur as the photon travels along the levels (steps) of the optical Galton board to yield probability distributions akin to that shown in Fig. 1.5.

To complete the relation of this Galton board to the coined QW, the photon can be identified as the walker and the beam-splitter as the coin in a superposition of states where reflectance could be related to tails and transmittance to heads or vice versa. It follows that incidence of the photon

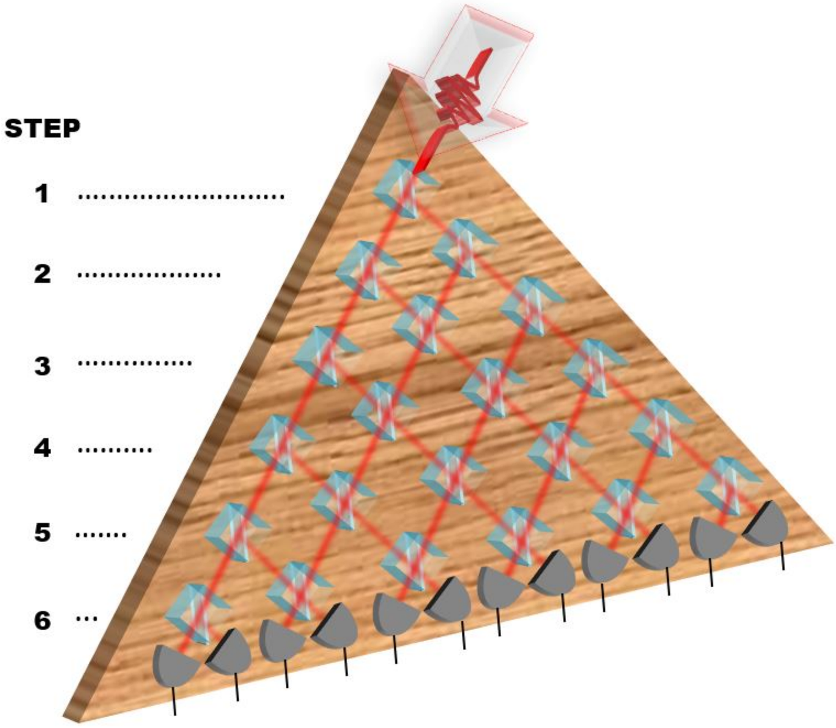

FIGURE 1.6: An optical Galton board can be used to generate QWs.

on each beam splitter in a row (step) is like 'flipping' the quantum coin for each simultaneously occupied position. Velocity plays the role of the propagator and the detectors at the bottom of the board form the bins/position space with a twist: each pair of adjacent detectors for adjacent beam splitters form one bin for a position as indicated in Fig. 1.7 (a)-(c). This is due to the detectors measuring the path of the photon as opposed to position propagated to (the next beam-splitter).

Probabilities associated with different positions in the QW can be intuitively calculated through the use of "Feynman diagrams" as outlined by [34] for one-fold probability. Each diagram indicates a possible path that the photon can take towards a chosen detector. Figure 1.7 (a)-(c) illustrates this for the two detectors that contribute to the probability associated with position 0 after undergoing n = 4 steps. The purple path corresponds to the possibilities resulting from the detector on the left firing while the green path for the detector on the right firing. Here the probability amplitude coefficients for reflectance (R) and transmittance (T) that accumulates upon each interaction with a 50:50 beam-splitter is given by [33; 34]:

$$T = \frac{1}{\sqrt{2}} \tag{1.3}$$

$$R = \frac{i}{\sqrt{2}} \tag{1.4}$$

as a 90 degree phase difference (i) is introduced upon reflection of the photon and such that $|R|^2+|T|^2 = 1$ (the photon must be somewhere). It follows that multiplication of the accumulated coefficients yields the total probability amplitude for a path [34]. Let the paths in the diagrams (a)-(c) be labelled A-C respectively for each detector. Now consider the probability amplitude of the path leading to the detector on the left in Fig. 1.7 (a). For example, the photon is transmitted by the first two beamsplitters before being reflected by the second-to-last one and then transmitted into the detector. The probability amplitude for path A to the left detector is then given by:

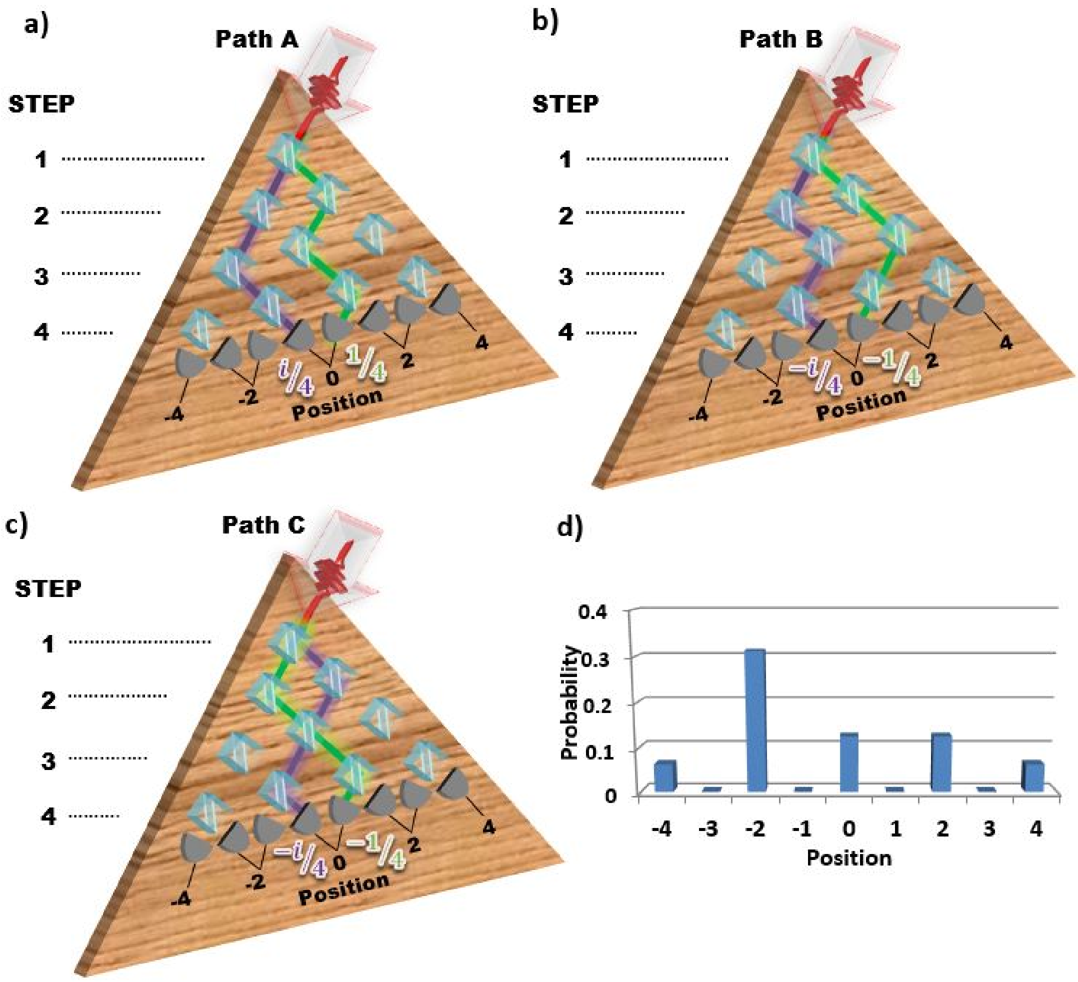

FIGURE 1.7: Feynman diagrams (a)-(c) used to determine probabilities associated with a photon being detected by the left (right) detector. All possible paths for position 0 detectors are highlighted in purple (green) with the associated probability amplitudes indicated next to the detector. The complete associated probability distribution (as determined through the Feynman diagram method) in this 4-step quantum walk is illustrated in (d).

PATH A:

$$T^2RT = (\frac{1}{\sqrt{2}})^2(\frac{i}{\sqrt{2}})(\frac{1}{\sqrt{2}}) = \frac{i}{4} \tag{1.5}$$

It then follows for paths B and C:

PATH B:

$$TR^3 = (\frac{1}{\sqrt{2}})(\frac{i}{\sqrt{2}})^3 = -\frac{i}{4} \tag{1.6}$$

PATH C:

$$R^2TR = (\frac{i}{\sqrt{2}})^2(\frac{1}{\sqrt{2}})(\frac{i}{\sqrt{2}}) = -\frac{i}{4} \tag{1.7}$$

Now as each path is one of three possibilities, they can be considered to take place independently from each other as they follow independant paths. The total probability amplitude is then a summation of all the amplitudes for the left detector [34]: $PathA + PathB + PathC = \frac{i}{4} - \frac{i}{4} - \frac{i}{4} = \frac{i}{4}$. Due to probability being the square of the modulus of the probability amplitude [33], the actual probability associated with the photon ending up on the pathway indicated by the left detector is then

$$|PathA + PathB + PathC|^2 = |\frac{i}{4}|^2 = \frac{1}{16} \tag{1.8}$$

Similarly, for the detector to the right:

$$|PathA + PathB + PathC|^2 = |\frac{1}{4} - \frac{1}{4} - \frac{1}{4}|^2 = \frac{1}{16} \tag{1.9}$$

As the complete probability for position 0 is the probabilities of the two detectors combined it follows that the probability is then $1/16 + 1/16 = 2/16$. This is a vast contrast to that predicted in the classical case as shown in Fig. 1.3 with $6/16$. Figure 1.7 (d) shows the complete probability distribution for each position as calculated by this method.

The distribution clearly differs from that of the classical case, with greatest probability being along the left edge. The asymmetry of this distribution is due to the asymmetrical input state of the photon as it enters through one side of the initial beam-splitter. A symmetrical distribution would be achievable if one took 50% of the photon to enter through the left and the other 50% through the right, yielding a symmetrical input state. The result of this may be intuitively determined. Here the number of reflections and transmissions taken to reach the detectors would be inverted about the central position (0) such that amplitude or weightings detected at position -3 becomes that which is detected at position +3 and vice verse. It follows that adding 50% of this probability distribution to 50% of the initial one would then yield the symmetrical case with maxima occurring at the ± 2 positions as was indicated for the coined QW.

1.2 Applications

As such a walk is indeed possible in the quantum mechanical regime; the question may be raised as to what advantages may come from physically realizing this phenomenon. In other words, why walk in the quantum world?

Studies into its application have shown numerous advantages which have spurred on research in the recent period. Drawing on the analogous nature to the random walk, one such application is in quantum algorithms which offer a large speedup over certain classical computations with up to a quadratic increase in the time taken to achieve the answer [26; 36]. After the first created algorithm was constructed for querying a 'black box' to obtain an abstract answer [37], much of the initial algorithmic development lies in database searching. For instance, imagine searching for a particular item in a catalogue based only on the picture of the item or looking for a certain homepage on the world wide web. Finding either of these classically would require randomly choosing pages in the catalogue or randomly clicking on links. Shenvi *et. al.* [38] showed that with the QW, a quadratic speedup can be achieved which would be the equivalent of checking only $\sqrt{N}$ pages or links as opposed to N needed classically. This is possible as QW principals allow a backwards approach whereby one starts with a superposition of all the database answers that converges to the correct entry while a QW is propagated [39]. Further development by Potocek *et. al.* [40] later improved the algorithm and other researchers have suggested ways of going the other way (a forwards approach) as well with spatial searches [41]. Several other problems also have ready algorithms such as element distinctness [18] whereby it may be determined if an entry has multiple places in a database, claw-finding [42] which allows one to determine if a particular function is equivalent for multiple distinct inputs and graph isomorphism [43] that determines if several graphs may be mapped to one another.

Furthermore, by generalizing the QW operation, it is actually possible to achieve a universal set of gates. Here Lovett *et. al.* [44] proved its viability as a universal gate set, extending the power of this phenomenon to beyond implementation of only a few special tasks. It follows that any quantum algorithm can then be implemented with a QW system, opening an alternate avenue for the sought-after development of a feasible and sustainable quantum computer.

Recently, application of the walk into quantum cryptography with protocols designed to encrypt images [45] and implement quantum key distribution [46] have also been developed, allowing the phenomenon to also be used to protect information being passed between different communicating parties.

The usefulness may be further extended into the modeling and understanding of certain natural processes. For example, QWs have been proposed to study energy transport in photosynthetic systems whereby excitons carry energy to the reaction centers with a previously confounding 99% efficiency in certain systems [47]. This is converse to a high energy loss which is expected classically if it were to randomly choose any path to the reaction center. Mohseni *et. al.* [48], however, theoretically found that when propagation of the excitons are modeled as QWs interacting with the environment, the large increase in efficiency occurs, in agreement with what is observed. Quantum walk analysis has also been extended to successfully simulate and study the transport of particles and energy in disordered, or, generally complex, media [49]. Here the respective wave-packet is found to localize as opposed to spreading across the medium. Termed Anderson localization, it is a surprising feature in many systems including Bose-Einstein condensates [50], light traversing semi-conductor powders [51] and three-dimensional elastic systems wherein ultrasound waves are propagating [52]. Additionally, it has been shown that discrete-time QWs can be used to create and study topological phases [53] which occur in many physical systems from high-energy physics to condensed-matter and atomic physics. The dynamics of these phases characterizes the properties of the subsequent materials or systems. This lead to the first direct confirmation of how conduction occurs in conjugated organic polymers such as polyacetylene. It subsequently follows that, among many other uses, QWs also offer an adaptable basis for simulating various complex systems. It's implementation excites avid study into realizing viable physical implementations of this phenomenon.

Chapter 2

Theory

2.1 The quantum walk framework

Following the conceptual introduction in sections 1.1 and 1.2, complete treatment of the quantum walk now involves examination of the mathematical framework providing a description of this phenomenon. Several different frameworks exist based on the different representations available. These include graphs, matrices and Dirac notation. This work will follow the approach first taken by Aharonov *et. al.* [24] and Kempe [26], amongst others, which focuses mainly on Dirac notation with a matrix basis as it provides a clear and simple understanding in terms of ubiquitous quantum physics notation. For completeness, a brief review on the relevant notation and principles shall first be covered before presenting the QW framework. It can be noted that QW analysis in terms of graphs is widely used when regarding its application in algorithms and computing. A comprehensive review of QWs with this perspective may be found in [17].

2.1.1 The language of quantum walks

The well-known wavefunction, ψ, was introduced in 1926 by Schrödinger [54] ensuing the birth of quantum mechanics. Here Born [55] contributed by interpreting it as the probability amplitude and thus successfully denoting it as a complete description of the state of the system. This wavefunction is said to exist as a vector in a complex Hilbert space $(\mathcal{H})$ that uniquely consists of all possible states of the system whereby the space may be very generally described as a "complete inner product space" [56].

Dirac notation, developed by Dirac in 1930, involves the use of vertical bars and angle brackets to represent these quantum states [57]. More specifically, it involves two distinct notations labeled bra and ket [58]. The wavefunction, for instance, is written in terms of a ket, $|\psi\rangle$ denoting it as a state vector in Hilbert space [56]. It follows that if the wavefunction is thought of as a vector, it may be described in terms of a linear combination of orthogonal basis states, $|j\rangle$, spanning the space. In the case of the QW, the wavefunction would represent the state of a particle (the walker), existing in a position Hilbert space $(\mathcal{H}_x)$ containing all the positions required for complete evolution of the walk [9]. The bra notation in this case may be understood as shown by Eq. 4.1 where the wavefunction is expressed as a column vector in the d-dimensional complex Hilbert space:

$$|\psi\rangle = \sum_{x=1}^{d} C_x |x\rangle = \begin{bmatrix} C_1 \\ \vdots \\ C_d \end{bmatrix} \tag{2.1}$$

Here C_x denotes the complex coefficients comprising the probability amplitude of the wavefunction for each of the respective basis states, $|x\rangle$, spanning the space. The finite number of steps in a QW permits exploitation of a finite-sized Hilbert space for conceptual ease, however nothing prevents utilization of an infinite-dimensional Hilbert space. It may be noted that the description of the wavefunction in the equation above exhibits the superposition principle described in the introduction. Here the state of the particle or walker is expressed as a linear combination of basis states with the complex coefficients indicating the probability associated with each basis state, or rather, how ‘strongly favoured’ each position is.

Conversely, bra is denoted by $\langle\psi|$ in the case of the wavefunction above and represents the adjoint of the state [59]. Specifically,

$$\langle\psi| = \sum_{x=1}^{d} C_x^* \langle x| = \begin{bmatrix} C_1^* & \dots & C_d^* \end{bmatrix} = |\psi\rangle^\dagger \tag{2.2}$$

where C_x^* is the complex conjugate of the respective coefficients described for Eq. 4.1 and $\dagger$ denotes conjugate transpose of the superscripted state. The bra has certain importance when paired to the left of the ket as shown for the case of complex vectors $|u\rangle$, $|v\rangle$:

$$\langle u|v\rangle = \begin{bmatrix} u_1^* & \dots & u_d^* \end{bmatrix} \begin{bmatrix} v_1 \\ \vdots \\ v_d \end{bmatrix} = u_1^* v_1 + \cdots + u_d^* v_d \tag{2.3}$$

which forms an inner product between the two vectors [56]. This may subsequently be translated as the equivalent of taking a position measurement of $|x\rangle$, with result, x, for instance, on the state of a particle $|\psi\rangle$. Collapse of the wavefunction to a value ensues, from which the probability of such an occurrence may then be derived as indicated in Eq. 2.4.

$$P_x = |\langle x|\psi\rangle|^2 = |\sum_{x'=1}^{d} C_x \langle x|x'\rangle|^2 = |C_x \langle x|x\rangle|^2 = |C_x|^2 \tag{2.4}$$

Due to the orthonormality of the position basis, i.e. $\langle x|x'\rangle = \delta_{(x,x')}$ where δ is the Kronecker delta, the complex amplitude coefficient associated with the chosen value is isolated. Consequently, P_x is the probability associated with obtaining the particle described by the wavefunction at position x and is given by the absolute value of the amplitude squared [23]. The normalization condition,

$$\langle\psi|\psi\rangle = \sum_{x'} \sum_{x} C_x^* C_x \langle x|x'\rangle = \sum_{x} |C_x|^2 \tag{2.5}$$

follows accordingly, indicating that the particle must exist somewhere in the space.

It follows that the outer product of two vectors is denoted by interchanging the order used for the inner product and as such transforms between vectors [59]. For instance, the outer product is denoted by $|u\rangle\langle v|$ for vector $|u\rangle$ spanning space U and $|v\rangle$ spanning space V such that when acting on vector $|v'\rangle \in V$,

$$|u\rangle\langle v|(|v\rangle) = |u\rangle\langle v|v'\rangle = \alpha|u\rangle$$

where $\alpha = \langle v|v'\rangle$ is a scalar and the vector is projected into U.

Progression of the QW lies in the application of linear operators. Consequently, the operation is demonstrated here in terms of Dirac notation for a linear operator, $\hat{D}$, associated with some observable of a quantum system with wavefunction, ψ, yielding the eigenvalue, d i.e.

$$\hat{D}\psi = d\psi$$

Therefore, in terms of Dirac notation:

$$\hat{D}|\psi\rangle = d|\psi\rangle$$

Additionally, in the case of acting on an inner product [56]:

$$\hat{D}\langle x|\psi\rangle = \langle x|\hat{D}|\psi\rangle$$

One ubiquitous linear operator of particular note for the purposes of this work is the projection operator ($\hat{P}$) defined in Eq. 2.6 [56].

$$\hat{P} = |i\rangle\langle i| \tag{2.6}$$

As can be seen, it is based on the outer product discussed earlier whereby action on a vector results in its projection onto the one-dimensional subspace spanned by $|i\rangle$. This is demonstrated for the vector $|v\rangle$ such that:

$$\hat{P}\,|v\rangle = |i\rangle\,\langle i|v\rangle = c\,|i\rangle$$

where the scalar value $c = \langle i|v\rangle$ isolates the component of $|v\rangle$ that 'lies along' $|i\rangle$.

When a system state is comprised of two or more independent states such that each composition state subsequently exists in separate spaces, representation of the system as a pure state lies in tensor mathematics. Here, as a 1D example, the tensor for the two vectors $|u\rangle\ spanning\ U$ and $|v\rangle\ spanning\ V$ described above may be illustrated as shown [59]

$$|u\rangle \otimes |v\rangle = \begin{bmatrix} u_1 \\ \vdots \\ u_d \end{bmatrix} \otimes \begin{bmatrix} v_1 \\ \vdots \\ v_d \end{bmatrix} = \begin{bmatrix} u_1v_1 \\ \vdots \\ u_1v_d \\ \vdots \\ u_dv_1 \\ \vdots \\ u_dv_d \end{bmatrix} \tag{2.7}$$

such that the vector $|u\rangle \otimes |v\rangle$ now span the space $|U\rangle \otimes |V\rangle$ of the system state.

More specifically, consider for instance the QW where the walker exists and moves in position space $\mathcal{H}_x$, however the 'coin' indicating which direction the walker must move in exists in a different coin space $\mathcal{H}_c$ [26]. Respectively spanned by the position vectors $\{|x\rangle\}_{x=-\infty}^{\infty}$ and $|H\rangle\,, |T\rangle = |c\rangle_{c=H}^{T}$ where H indicates heads and T indicates tails, the state of the QW is comprised of the position states of the walker as well as an internal coin state for each position state [26]. It follows that these states are independent of each other and as such describe the states of the QW in terms of a tensor product vector, $|u\rangle \otimes |v\rangle = |x, c\rangle$, spanning the QW Hilbert space which is subsequently a tensor product of the position and coin spaces: $\mathcal{H}_x \otimes \mathcal{H}_c$.

2.1.2 Coin, steps and walking a line

Development of the QW mathematical framework may be achieved by decomposing it into individual, iterative operations. In particular, the QW may be evolved through periodic applications of a coin and step operation on a chosen initial state, mimicking the repetitive coin flip and movement of the walker. Execution of such operations relies upon the development of a coin, $\hat{C}$ and step, $\hat{S}$ operator reflecting the nature of the desired QW [26]. It follows from the order of operations that the coin state and operator shall first be considered.

Utilizing Dirac notion, the initial coin state may be expressed as [9]

$$|c\rangle = \alpha\,|H\rangle + \beta\,|T\rangle\,, \tag{2.8}$$

where the quantum nature of the coin is evident through the superposition of its basis states. Here α and β are the respective state complex amplitudes where their squares yield the probability of the coin being in each state ($|\alpha|^2 + |\beta|^2 = 1$). 'Flipping' the coin however lies in the application of a coin operator to the internal coin state of each position occupied by the walker [9]. After application, each position then carries an internal superposition of coin states that correlates to the coin type being employed. As previously indicated, the operator may take on many forms corresponding to different types of QWs with the sole restriction requiring the operation be unitary. Accordingly, the operator for a 1D walk on a line may be described by

$$\hat{C} = [\sqrt{\eta}\,|H\rangle + e^{i\Phi}\sqrt{1-\eta}\,|T\rangle]\,\langle H| + [e^{i\varphi}\sqrt{1-\eta}\,|H\rangle - e^{i\varphi+\Phi}\sqrt{\eta}\,|T\rangle]\,\langle T| \tag{2.9}$$

such that the generality is preserved [9]. Here η is the coin bias or weighting and $0 \leq (\Phi, \varphi) \leq 2\pi$ describes the relative phase between the basis states. Consider as an example the application of the coin operator to a coin state $|H\rangle$,

$$\begin{aligned}
\hat{C}\,|H\rangle &= [\sqrt{\eta}\,|H\rangle + e^{i\Phi}\sqrt{1-\eta}\,|T\rangle]\,\langle H|H\rangle + [e^{i\varphi}\sqrt{1-\eta}\,|H\rangle - e^{i\varphi+\Phi}\sqrt{\eta}\,|T\rangle]\,\langle T|H\rangle \\
\hat{C}\,|H\rangle &= [\sqrt{\eta}\,|H\rangle + e^{i\Phi}\sqrt{1-\eta}\,|T\rangle]\,\langle H|H\rangle + 0 \\
\hat{C}\,|H\rangle &= \sqrt{\eta}\,|H\rangle + e^{i\Phi}\sqrt{1-\eta}\,|T\rangle
\end{aligned} \tag{2.10}$$

where the coin is clearly ‘flipped’ to yield a new superposition of the basis states. In the event of a balanced coin as described for the RW case in Section 1.1, an equivalent superposition of the basis states is expected. Setting the bias $\eta = 1/2$ and $\varphi, \Phi = 0$, Eq. 2.10 becomes

$$\hat{C}\,|H\rangle = \frac{1}{\sqrt{2}}\,|H\rangle + [\frac{1}{\sqrt{2}}\,|T\rangle \tag{2.11}$$

which is in compliance with expectations. A similar outcome ensues from operation on the other basis state. The coin resulting from these parameters is known as a Hadamard coin [26].

Converting to matrix representation, the coin basis states may be expressed as [23]

$$|H\rangle = \begin{bmatrix}1\\0\end{bmatrix} \tag{2.12a}$$

$$|T\rangle = \begin{bmatrix}0\\1\end{bmatrix} \tag{2.12b}$$

with the general 1D coin operator taking on the form

$$\hat{C} = \begin{bmatrix}\cos\chi & e^{i\varphi}\sin\chi \\ e^{i\phi}\sin\chi & -e^{i\varphi+\Phi}\cos\chi\end{bmatrix} \tag{2.13}$$

where $\cos\chi$ and $\sin\chi$ respectively take on the roles of $\sqrt{\eta}$ and $\sqrt{1-\eta}$ for reasons soon to be apparent.

Perspective on this general operator may be gained through consideration of a Bloch or Poincaré sphere. Briefly, the Bloch sphere is a visual representation of all possible states between two orthogonal basis states (e.g. $|H\rangle$, $|T\rangle$) positioned on opposite poles as indicated in Fig. 2.1 (a) [60]. A point on the surface of the sphere then represents a particular state for a unique combination of the orthogonal basis states. Specification of angles χ and Φ locate the state where χ determines the latitude and Φ the longitude. Consequently, $\alpha = \cos\frac{\chi}{2}$ and $\beta = \exp\{i\Phi\}\sin\frac{\chi}{2}$ in Eq. 2.8 as it yields the weighting for each basis state in spherical coordinates with $0 \leq \Phi \leq 2\pi$ and $0 \leq \chi \leq \pi$ such that [60]

$$|c\rangle = \cos\frac{\chi}{2}\,|H\rangle + e^{i\Phi}\sin\frac{\chi}{2}\,|T\rangle = \begin{bmatrix}\cos\frac{\chi}{2}\\ e^{i\phi}\sin\frac{\chi}{2}\end{bmatrix} \tag{2.14}$$

An arbitrary state corresponding to this expression is illustrated in Fig. 2.1 where it may be seen to isolate a particular point on the surface of the sphere. Alteration of the coin states occur through a class of unitary operations which in this instance are the coin operators [9]. Upon application of these operators, the weightings are changed through a modification of the angles specifying the coin state according to the type of coin chosen. As an elementary example, consider Eq. 2.13 with

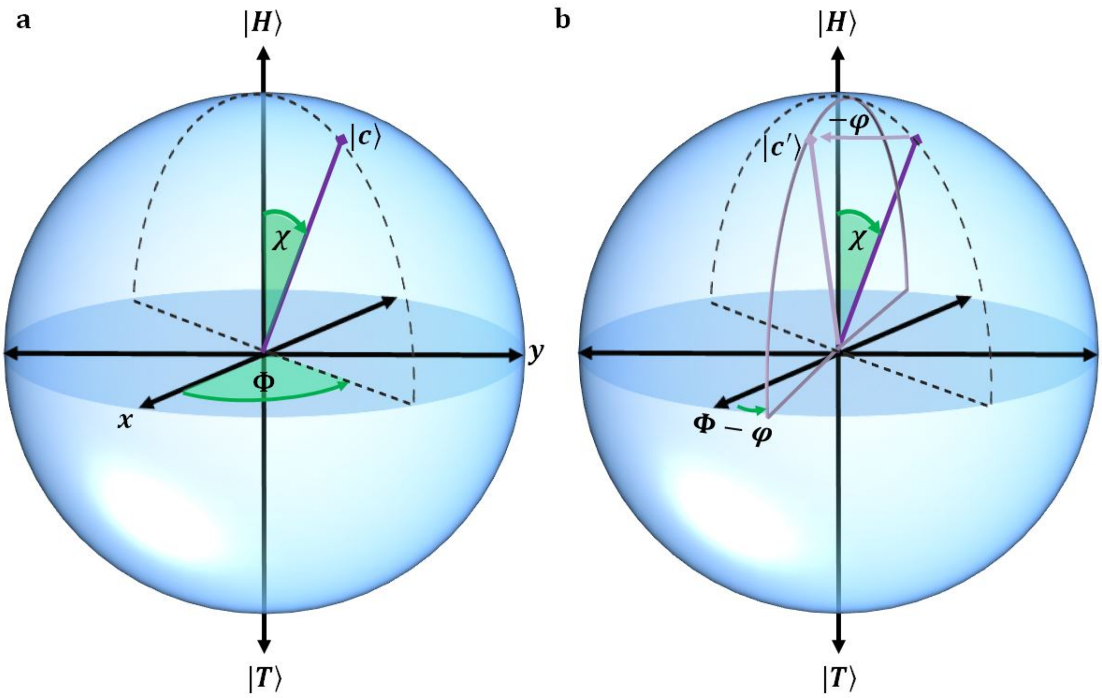

FIGURE 2.1: Illustrations of (a) coin states represented on a Bloch sphere and (b) a simplified 'rotation' of states about the z-axis in response to application of the coin operator with $\chi = 0$ and $\Phi = 0$.

$\chi = 0$, $\Phi = 0$ and $\varphi = -\varphi$, resulting in the operator:

$$\hat{C} = \begin{bmatrix} 1 & 0 \\ 0 & e^{-i\varphi} \end{bmatrix}$$

By applying this operator to the state represented in Fig. 2.1 (a) (Eq. 2.14), the state is altered to that depicted in Fig. 2.1 (b) as seen by

$$\left|c'\right\rangle = \hat{C}\left|c\right\rangle = \begin{bmatrix} 1 & 0 \\ 0 & e^{-i\varphi} \end{bmatrix} \begin{bmatrix} \cos\frac{\chi}{2} \\ e^{i\Phi}\sin\frac{\chi}{2} \end{bmatrix}$$

$$\Rightarrow \left|c'\right\rangle = \cos\frac{\chi}{2}\begin{bmatrix} 1 \\ 0 \end{bmatrix} + e^{i\Phi-\varphi}\sin\frac{\chi}{2}\begin{bmatrix} 1 \\ 0 \end{bmatrix}$$

$$\Rightarrow \left|c'\right\rangle = \cos\frac{\chi}{2}\left|H\right\rangle + e^{i\Phi-\varphi}\sin\frac{\chi}{2}\left|T\right\rangle$$

where the angle specifying the longitudinal position is altered by $-\varphi$ specified by the operator. In Fig. 2.1 (b), it appears as if the state vector is rotated about the z-axis to yield the new coin state. As a result, application of these operators is often referred to as 'rotating' the states where the vector is rotated about some arbitrary axis specified by the coin type (and thus coin operator) [60].

The operator discussed (Eq. 2.9), however, is only effective for localized action on a chosen position. The coin operator must act on every occupied position (i.e. 'flipping' the coin at each position occupied by the walker) in order to propagate the quantum effects of the walk. Bearing in mind the position space of the QW,

$$\sum_x |x\rangle = \begin{bmatrix} 1 \\ \vdots \\ 1 \end{bmatrix}_d , \tag{2.15}$$

this is achieved by specifying a matrix spanning the space such that the operator acts on the associated coin states at each position individually as given in Eq. 2.16,

$$\hat{C}' = \begin{bmatrix} \ddots & 0 & 0 & 0 & 0 \\ 0 & \hat{C}'_{-1} & 0 & 0 & 0 \\ 0 & 0 & \hat{C}'_0 & 0 & 0 \\ 0 & 0 & 0 & \hat{C}'_1 & 0 \\ 0 & 0 & 0 & 0 & \ddots \end{bmatrix}_{d\times d} = \begin{bmatrix} \ddots & 0 & 0 & 0 & 0 \\ 0 & 1 & 0 & 0 & 0 \\ 0 & 0 & 1 & 0 & 0 \\ 0 & 0 & 0 & 1 & 0 \\ 0 & 0 & 0 & 0 & \ddots \end{bmatrix} \otimes \hat{C}, \tag{2.16}$$

where the $\hat{C}'_{-1} = \hat{C}'_0 = \hat{C}'_1 = \hat{C}$ and the subscript denotes the position upon which the coin is acting [9]. As the coin operator for each position is identical, it may be factored out, yielding the $d = (2n + 1)$-dimensional identity matrix ($\mathbb{I}$). Here n refers to the number of steps taken by the walker. Based on Eq. 2.7, the coin 'flip' for each step in the walk may then be represented by the tensor product, $\hat{C}' = \mathbb{I} \otimes \hat{C}$.

Commencement of a QW involves specification of the initial state of the walker $|\psi\rangle_0$, stipulating the initial position of the walker with an internal coin state [26]. This is exemplified in Eq. 2.17,

$$|\psi\rangle_0 = |0\rangle \otimes |H\rangle , \tag{2.17}$$

for a walker at position 0 with a coin state of $|H\rangle$ such that the probability of finding the walker at the origin is 100% with a positive directional influence indicated by $|H\rangle$. The initial state of the walker has a significant effect on the type of probability distribution obtained for the QW [26]. As will be portrayed further on, the symmetry of this state with respect to the coin operator is a substantial factor influencing the symmetry of the QW.

After application of the coin operator, the step operator, $\hat{S}$ is required in order to move the walker in the directions indicated by the internal coin states such that interference of the probabilities occur resulting in the desired speed up in the spread of the probability distribution. Following the coin operator introduction, the step operator may be defined utilizing similar principles from the Dirac notation, producing the expression in Eq. 2.18 [26].

$$\hat{S} = \sum_x [|x+1\rangle \langle x| \otimes |H\rangle \langle H|] + [|x-1\rangle \langle x| \otimes |T\rangle \langle T|] \tag{2.18}$$

The tensor product of position and coin outer products ensures occupied positions with $|H\rangle$ advance in position space while those with $|T\rangle$ regress such that the indicated directional movement takes place. For instance, consider application of the step operator directly to the initial state in Eq. 2.17.

$$|\psi\rangle_R = \hat{S}\,|\psi\rangle_0 = \sum_x [|x+1\rangle \langle x| \otimes |H\rangle \langle H|]\, |0\rangle \otimes |H\rangle + [|x-1\rangle \langle x| \otimes |T\rangle \langle T|]\, |0\rangle \otimes |H\rangle$$

Only the $x = 0$ terms survive as a result of the orthogonality of the basis vectors, thus

$$\begin{aligned}
|\psi\rangle_R &= [|0+1\rangle\langle 0| \otimes |H\rangle\langle H|]\,|0\rangle \otimes |H\rangle + [|0-1\rangle\langle 0| \otimes |T\rangle\langle T|]\,|0\rangle \otimes |H\rangle \\
&= [|0+1\rangle\langle 0|0\rangle \otimes |H\rangle\langle H|H\rangle] + [|0-1\rangle\langle 0|0\rangle \otimes |T\rangle\langle T|H\rangle] \\
&= |1\rangle \otimes |H\rangle
\end{aligned}$$

Here it is clear from the resultant state of the walker, $|\psi\rangle_R$ that the step operator has moved the walker to the right (position 1) in accordance with the directional indication of the coin state. The complete description of the QW operations is then given by pairing the step and coin operations to form an expression as shown in Eq. 2.19 for a Hadamard coin.

$$\hat{S}\hat{C} = \sum_x [|x+1\rangle\langle x| \otimes \frac{1}{\sqrt{2}}(|H\rangle + |T\rangle]\,\langle H| + \sum_x [|x-1\rangle\langle x| \otimes \frac{1}{\sqrt{2}}(|H\rangle - |T\rangle]\,\langle T| \tag{2.19}$$

The matrix representation involves the definition of several operators, namely the coin projection operators,

$$C^H = |H\rangle\langle H| = \begin{bmatrix} 1 & 0 \\ 0 & 0 \end{bmatrix} \tag{2.20a}$$

$$C^T = |T\rangle\langle T| = \begin{bmatrix} 0 & 0 \\ 0 & 1 \end{bmatrix}, \tag{2.20b}$$

and shift operators (over all x),

$$S^+ = \sum_{x=-n}^{n+1} |x+1\rangle\langle x| = \begin{bmatrix} 0 & 0 & 0 & 1 \\ 1 & 0 & 0 & 0 \\ 0 & 1 & 0 & 0 \\ 0 & 0 & 1 & \ddots \end{bmatrix}_{d\times d} \tag{2.21a}$$

$$S^- = \sum_{x=-n}^{n+1} |x-1\rangle\langle x| = \begin{bmatrix} 0 & 1 & 0 & 0 \\ 0 & 0 & 1 & 0 \\ 0 & 0 & 0 & 1 \\ 1 & 0 & 0 & \ddots \end{bmatrix}_{d\times d} = (S^+)^\dagger, \tag{2.21b}$$

where $|n+1\rangle = |-n\rangle$ and shifts the input vector up one position (Eq. 2.21 (a)) and down one position (Eq. 2.21 (b)) [9]. Substituting these into the Eq. 2.18 then gives the relation,

$$\hat{S} = [S^+ \otimes C^H] + [S^- \otimes C^T]$$

such that

$$\hat{S} = \begin{bmatrix} 0 & C^T & 0 & C^H \\ C^H & 0 & C^T & 0 \\ 0 & C^H & 0 & C^T \\ C^T & 0 & C^H & \ddots \end{bmatrix}_{2d\times 2d} \tag{2.22}$$

preforms that same conditional translation operation as indicated by the Dirac notion [9].

As indicated previously, a step in the QW involves 'tossing' the coin followed by the conditional movement of the walker. It follows that a single step of the walker is then achieved through the concatenation of the coin and step operators [26]. Several steps thus lead to repetitive application which may then be simplified by raising the initial concatenation of these matrices to the nth

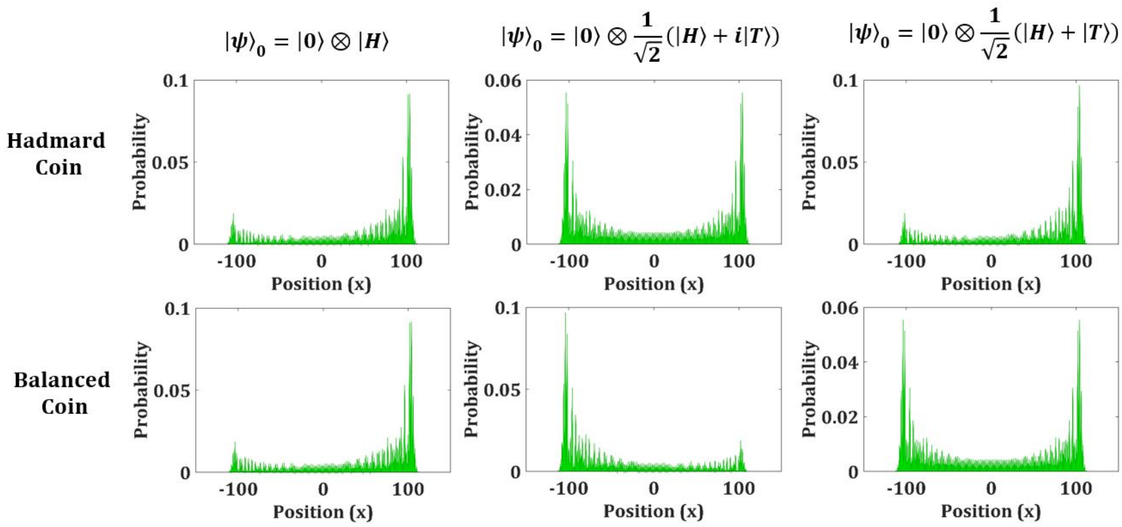

FIGURE 2.2: Different QW distributions resulting from differences in symmetry with regards to the initial walker state and coins used. Distributions (a,b) result from an asymmetrical initialization of the walker while (c-f) result from a symmetrical initialization of the walker.

power where n refers to the number of steps taken [23]

$$|\psi\rangle_n = [\hat{S}\hat{C}']^n |\psi\rangle_0 . \tag{2.23}$$

Here $|\psi\rangle_n$ refers to the state of the walker after n steps and $|\psi\rangle_0$ the initial state of the walker such as that given in Eq. 2.17. It is possible to examine effects of symmetry on the type of distributions utilizing Eq. 2.24 and 2.25 with regards the coin and initial state of the walker. Figure 2.2 illustrates this for asymmetrical and symmetrical initial states with two common coins, namely the Hadamard coin

$$\hat{C}_H = \frac{1}{\sqrt{2}} \begin{bmatrix} 1 & 1 \\ 1 & -1 \end{bmatrix} \tag{2.24}$$

and balanced coin [26]

$$\hat{C}_B = \frac{1}{\sqrt{2}} \begin{bmatrix} 1 & i \\ i & 1 \end{bmatrix} . \tag{2.25}$$

The first column exhibits the effects of an asymmetrical initial state while the last two exhibits the effects of symmetrical initial states. It is clear that the initial state symmetry has a significant effect on the distribution of the walker where an asymmetrical initial state as given for Fig. 2.2 (a,b) results in the distribution containing a 'drift' in the probability as it propagates. This generates a larger peak in the direction of the asymmetry (to the right in the case of H). Replacement of H with T in (a) and (b) would subsequently cause a 'drift' towards the left (a mirror distribution about the y-axis). Figures 2.2 (c-d) developed from a symmetrical initialization of the walker, yielding symmetrical probability distributions in (c) and (f) for the Hadamard and balanced coins respectively.

The asymmetric distributions in (e) and (d) are attributed to coin parameters. Insight into the effect of coin parameters lies in how the probability amplitudes propagate upon their application. More specifically, the symmetrical distribution, characterized by identical peaks away from the initial walker position, requires the directional drift of H and T from the initial state to occur independently such that no interference between the superpositions occur [26]. It is this interference that leads to the asymmetrical distribution as additional constructive (destructive) interference occurs in the direction of (away from) the bias. The introduction of i to one of the initial basis states (i.e. T in Fig 2.2 (c)) gives rise to propagation of one initial coin state in imaginary space while the other occurs in real space, causing them to evolve independently.

As the Hadamard coin (Eq. 2.24) does not insert any imaginary components, independence of the amplitude evolution is maintained and as such yields the symmetrical distribution. The lack of this separation by an imaginary component in Fig. 2.2 (e) then causes the two basis state evolutions to interfere additionally to provide a drift in the distribution [26]. Additionally, one may consider the imbalanced treatment of the initial states by the coin where application of the coin to the T state results in the accumulation of a $e^{i\pi} = -1$ relative phase between the basis states of the 'flipped' component that does not occur for application to the T state:

$$\begin{aligned} \hat{C}_H |H\rangle &\rightarrow \frac{1}{\sqrt{2}}(|H\rangle + |T\rangle) \\ \hat{C}_H |T\rangle &\rightarrow \frac{1}{\sqrt{2}}(|H\rangle - |T\rangle) \end{aligned} \tag{2.26}$$

It follows that an asymmetric result may also then be intuitively expected where these initial states are not separated from each other.

Conversely, the balanced coin does contain imaginary components and as such the application of this operator to the initial state of Fig. 2.2 (d) will result in additional interference during evolution of the initial basis state amplitudes. Likewise, multiplication of the imaginary terms in the application of the coin to the $i|T\rangle$ state results in an additional respective phase of -1 between the $|H\rangle$ 'flipped' states that does not occur for the $|T\rangle$ state. Subsequently, an imbalance in how the coin treats each state occurs, causing asymmetry. Application of the balanced coin to the initial state in Fig. 2.2 (f) then results in the separation of the initial basis states' evolution as no imbalance occurs in its application to either of the coin basis states (i.e. there is no difference between the 'flipped' states for application of the coin to either of the basis states):

$$\hat{C}_B(|H\rangle + |T\rangle) \rightarrow (1+i)|H\rangle + (1+i)|T\rangle)$$

It follows that symmetry of the distribution may be generalized to be a result of the relative phase incurred between the 'flipped' states of the coin basis states (i.e. $|H\rangle$ and $|T\rangle$) such that when there is a difference in the 'flipped' states, asymmetry occurs. Considering the coin operator in Eq. 2.9, it is clear that the phase parameters, Φ and φ, are responsible for the QW bias once the relative phase in the initialized state is accounted for. Illustration of this effect is given in Fig. 2.3 where the phase parameter, φ is changed from -60 to 60 degrees with $|\psi\rangle_0 = |0\rangle \otimes \frac{1}{\sqrt{2}}(|H\rangle + i|T\rangle)$, $\theta = 45^o$ and $\Phi = 0$. A clear transition occurs from a symmetrical state when $\varphi = 0$ to asymmetrical states when $\varphi \neq 0$ where the extent of asymmetry varies. The asymmetry is a consequence of the amount of bias between the generated 'flipped' states of the coin basis states. As a result, φ modulates the degree of asymmetry where the amount of destructive interference to the left (right) and constructive to the right (left) increases with the positive (negative) angle until 180 (-180) degrees. The effect of Φ on the asymmetry is insignificant, however, as its term globally modulates both coin states. It may be noted that symmetrical variance in the probability distribution does not influence the spread or width of the positions occupied in the distribution.

Conversely, the weighting parameter (χ) has significant influence on how widespread the distribution is [29]. This is illustrated for both the symmetrical (Fig. 2.4 (a,b)) and asymmetrical case Fig. 2.4 (c,d)) where the phase parameters are set to 0.

In particular, weighting the coin through alteration of χ, from the balanced ($\frac{1}{\sqrt{2}}$) output obtained with $\chi = 45^o$, results in noticeable effects regarding the distribution variance. The subsequent states vary from an extreme 50% probability split between outermost values at $\chi = 0^o$,

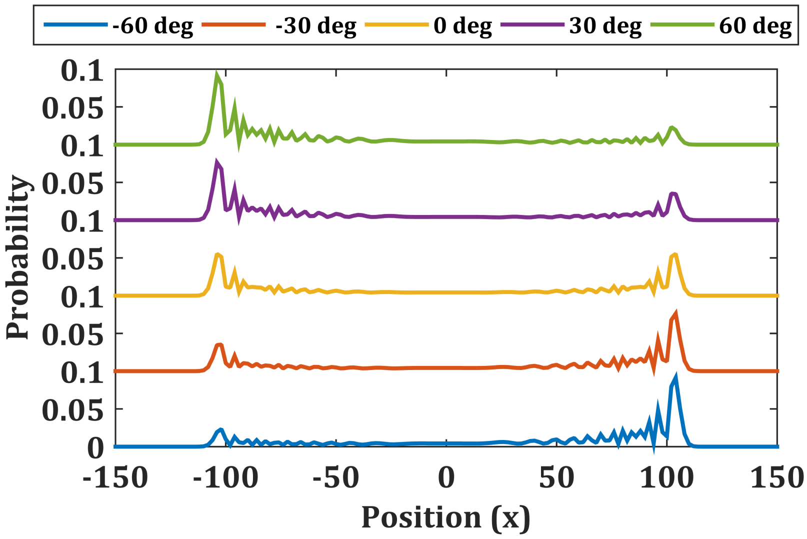

FIGURE 2.3: Biasing effect illustration for the introduction of relative phase between the 'flipped' states generated upon application of the coin operator to the coin basis states as dominated by the phase parameter, φ. For clarity, only the occupied (odd) positions where plotted.

to maintaining 100% probability occupying the initial position when $\chi = 90^o$ before spreading out again. Accordingly, the QW variance alters periodically with every $n\pi$ where n is an integer. This is showcased in Fig. 2.4 (b) through the light blue 'diagonals' indicating inward movement of the QW peaks and thus a decrease in the spread until 90^o where the peaks spread out again indicating an increase in the QW distribution spread. The same trend is seen in Fig. 2.4 (d), however there is only one light blue 'diagonal as the asymmetry results in only one large peak near the end of the distribution. It follows that the peak asymmetry switches after the 90^o mark. The superimposed transverse profiles with selected weighting distributions are given as Fig. 2.4 (a) for the symmetrical distribution and Fig. 2.4 (c) for the asymmetrical distribution. Figure 2.4 (a,c) highlight the two extremes of outermost positions and initial position occupation as well as the switch in asymmetry for a weighting angle greater than 90^o. These two extreme cases emphasize the limits possible in the distribution spread. Consequently, they are products of the extreme instances of probability amplitude interaction where at 0^o the states are propagated away from the other without any diffusion or interference while at 90^o the states traverse across the other such that they remain centered near the initial position [29]. Accordingly, intermediary χ-values yield intermediate degrees of interference and thus distribution spread.

Calculation of the n^{th} step quantum walk variance may be determined through application of the population variance equation [61]:

$$\sigma^2(n) = \sum_{x=-N}^{N+1} P(x,n)(x - x_0)^2 \tag{2.27}$$

where $P(x,n)$ is the probability associated with occupying position x and x_0 refers to the initial position of the walk. Plots of the variance against the QW progression for choice parameters can be found in Figure 2.5. Here the effects of χ on the spread or variance of the walk are clearly demonstrated with $\chi = 0^o, 45^o$ and 90^o. Asymmetry in the QW was introduced through variance of both the coin phase parameter as well as input state symmetry where all conditions yielded the same variance as indicated by the cross points in Fig 2.5. Subsequently, indifference of the

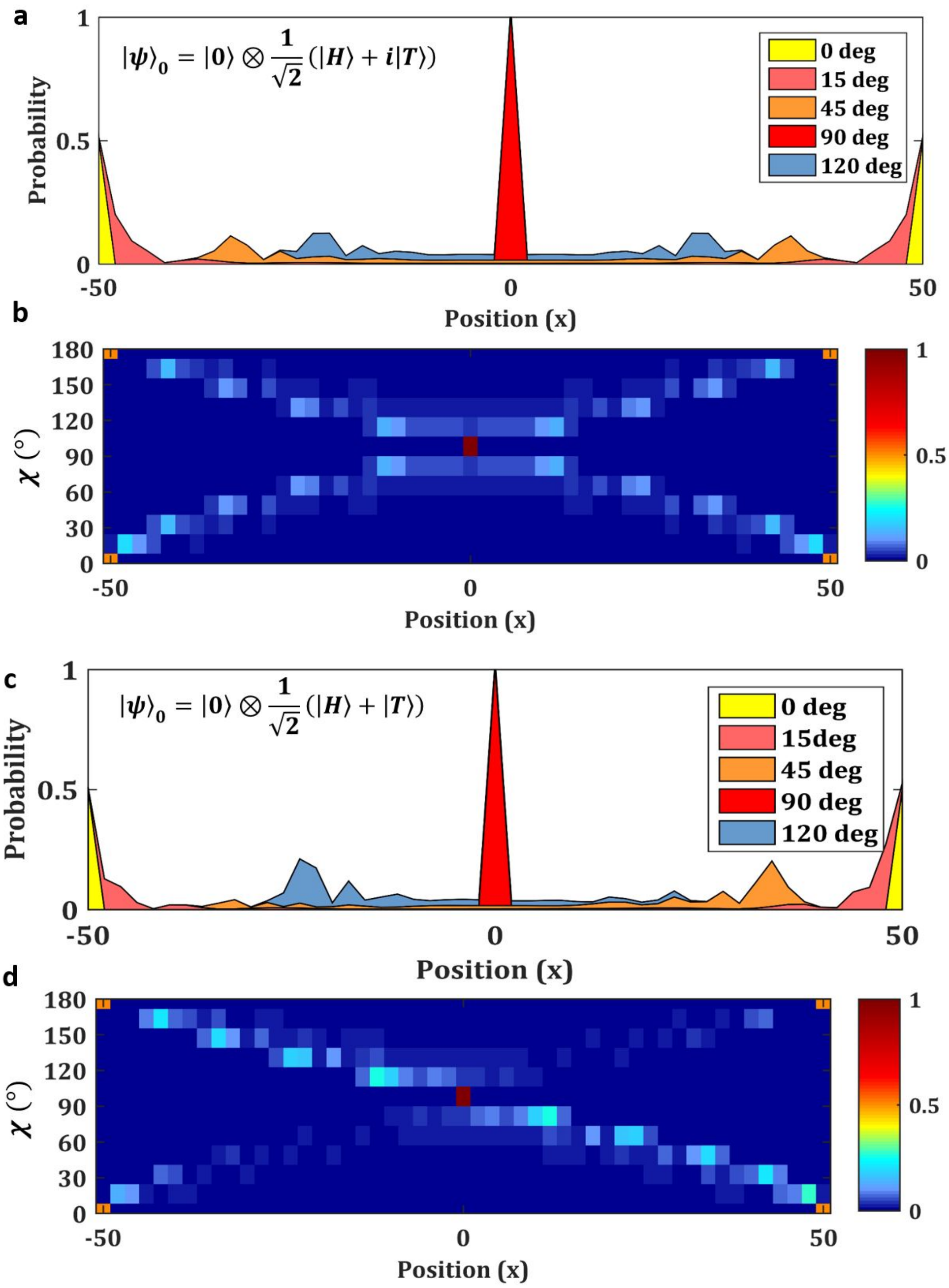

FIGURE 2.4: Coin weighting parameter effect on symmetrical distributions of 50 steps as shown by selected parameter values in a (a) 2D plot and more comprehensively in a density plot (b); similarly, in the asymmetrical case with a (c) 2D and (d) density plot.

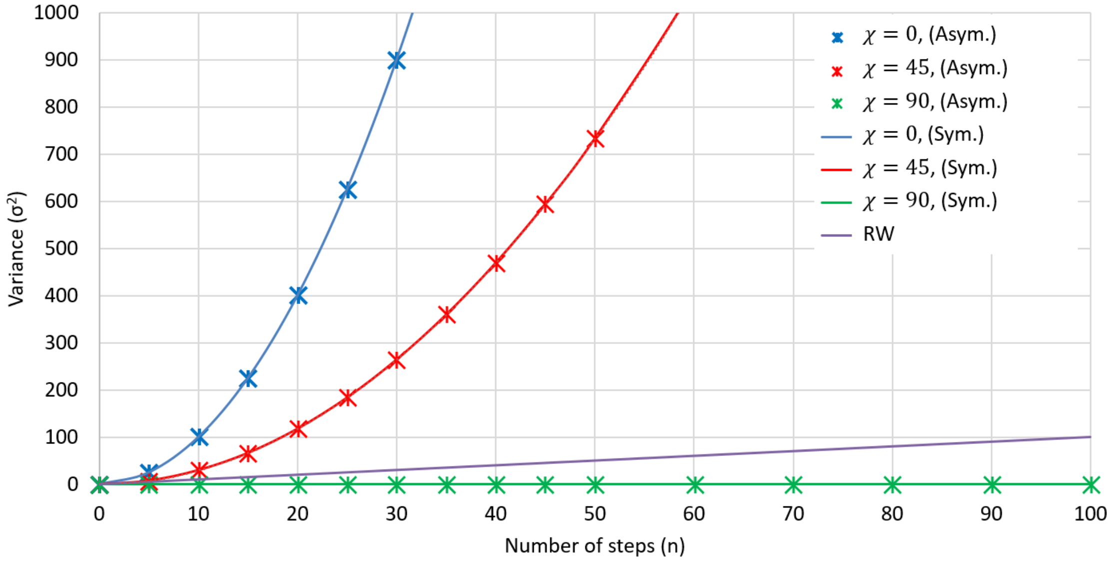

FIGURE 2.5: Graphs illustrating the change in variance with number of steps taken (as determined from Eq. 2.27) for the classical random walk as well as symmetric (Sym.) and asymmetric (Asym.) quantum walks, generated with the indicated coin weighting parameter as well as the input state and coin phase parameter.

walk symmetry to the variance as shown by overlap between walks with identical weightings, but different symmetry can be seen. A clear comparison between the variance expected for a random walk and QW is also provided, where the remarkable quadratic speedup is seen in contrast to the linear trend characteristic of the classical case.

It follows that the QW distribution and variance is significantly influenced through a combination of the initialization state and coin as respectively dictated by the relative phase and weighting. It consequently yields a diverse array of distributions contingent upon modification of the quantum interference that forms the foundation of this phenomenon.

2.1.3 Spreading into momentum space

Another approach that has been taken in the analysis of QWs is propagating them in momentum space [62; 63]. This affords a different perspective as it enables the allowed energies of the walker to be determined and subsequently the velocities by simply evaluating the dispersion relations associated with the type of walk. It also affords extraction of additional information on the walk dynamics such as the degree of entanglement generated between the coin and position states as was explored in [64; 65]. Transformation of the walk dynamics from position space $(\mathcal{H}_x)$ to momentum space $(\mathcal{H}_k)$ may be achieved through Fourier transformation of the relevant operators and states. More specifically, transformation is only required for the step operator and initial state as the coin operator and states are position independent, implying that the action remains unchanged in both spaces [23].

Conversion to the Fourier basis is achieved through the following relation [63]:

$$|k\rangle = \sum_{x=-\infty}^{\infty} e^{-ikx} |x\rangle \tag{2.28}$$

where $|k\rangle$ is a basis vector in momentum space and $|k\rangle \in [-\pi, \pi]$. Consequently, transformation of the position basis states, $|x\rangle$, is a case of taking the inverse transform of Eq. 2.28.

$$|x\rangle = \frac{1}{2\pi}\int_{k=-\pi}^{\pi} e^{ikx}\,|k\rangle\,dk \tag{2.29}$$

It follows that a symmetric initial state in position space such as $|\psi\rangle_{0,x} = |0\rangle \otimes \frac{1}{\sqrt{2}}(|H\rangle + |T\rangle)$ becomes

$$\begin{aligned}|\psi\rangle_{0,x} &= \frac{1}{2\pi}\int_{k=-\pi}^{\pi} e^{ik(0)}\,|k\rangle\,dk \otimes \frac{1}{\sqrt{2}}(|H\rangle + |T\rangle)\\ &= \frac{1}{2\pi\sqrt{2}}\int_{k=-\pi}^{\pi} |k\rangle\,dk \otimes (|H\rangle + |T\rangle)\end{aligned} \tag{2.30}$$

where the walker equivalently occupies all momentum space states, $|k\rangle \in [-\pi, \pi]$, resulting in an undefined initial momentum for the walker. This is in agreement with the uncertainty principle: $\Delta k \Delta x \geq \frac{\hbar}{2}$ as the initial position of the walker is fully defined to be 0. Considering the step operator (Eq. 2.18),

$$\hat{S} = \sum_x \overbrace{[|x+1\rangle\langle x| \otimes |H\rangle\langle H|]}^{\text{Part 1}} + \overbrace{[|x-1\rangle\langle x| \otimes |T\rangle\langle T|]}^{\text{Part 2}},$$

the transformation process may be divided into two as indicated by the square brackets. Due to the state invariance to the transformation, the coin states will be excluded in the process and reintroduced at the end.

Considering part 1:

$$\begin{aligned}\hat{S}_x^H &= \sum_{x=-\infty}^{\infty} [|x+1\rangle\langle x| \otimes |H\rangle\langle H|]\\ \Rightarrow \hat{S}_k^H &= \sum_{x=-\infty}^{\infty} \frac{1}{2\pi}\int_{k=-\pi}^{\pi} e^{-ik(x+1)}\,|k\rangle\,dk \times \frac{1}{2\pi}\int_{k'=-\pi}^{\pi} e^{-ik'x}\,|k'\rangle\,dk'\\ &= \frac{1}{4\pi^2}\int_{k=-\pi}^{\pi} e^{ik}\int_{k'=-\pi}^{\pi}\sum_{x=-\infty}^{\infty} e^{-ix(k-k')}\,|k\rangle\langle k'|\,dk'dk\end{aligned}$$

However, $\delta(k-k') = \frac{1}{2\pi}\sum_{x=-\infty}^{\infty} e^{-ix(k-k')}$ where $\delta(k-k')$ is the Dirac-delta function [66], thus

$$\Rightarrow \hat{S}_x^H = \frac{1}{2\pi}\int_{k=-\pi}^{\pi} e^{ik}\int_{k'=-\pi}^{\pi} \delta(k-k')\,|k\rangle\langle k'|\,dk'dk$$

where integration over the delta function isolates $k-k'$ momentum states, yielding

$$\Rightarrow \hat{S}_x^H = \frac{1}{2\pi}\int_{k=-\pi}^{\pi} e^{ik}\,|k\rangle\langle k|\,dk \tag{2.31}$$

Similarly, for part 2:

$$\begin{aligned}
\hat{S}_x^T &= \sum_{x=-\infty}^{\infty} [|x-1\rangle \langle x| \otimes |T\rangle \langle T|] \\
\Rightarrow \hat{S}_k^T &= \sum_{x=-\infty}^{\infty} \frac{1}{2\pi} \int_{k=-\pi}^{\pi} e^{-ik(x-1)} |k\rangle \, dk \times \frac{1}{2\pi} \int_{k'=-\pi}^{\pi} e^{-ik'x} |k'\rangle \, dk' \\
&= \frac{1}{4\pi^2} \int_{k=-\pi}^{\pi} e^{-ik} \int_{k'=-\pi}^{\pi} \sum_{x=-\infty}^{\infty} e^{-ix(k-k')} |k\rangle \langle k'| \, dk' dk \\
&= \frac{1}{2\pi} \int_{k=-\pi}^{\pi} e^{-ik} \int_{k'=-\pi}^{\pi} \delta(k-k') |k\rangle \langle k'| \, dk' dk \\
&= \frac{1}{2\pi} \int_{k=-\pi}^{\pi} e^{-ik} |k\rangle \langle k| \, dk
\end{aligned} \tag{2.32}$$

It follows from Eq. 2.31 and 2.32 that the step operator in momentum space is given by

$$\hat{S}_k = \frac{1}{2\pi} \int_{k=-\pi}^{\pi} e^{ik} |k\rangle \langle k| \, dk \otimes |H\rangle \langle H| + \frac{1}{2\pi} \int_{k=-\pi}^{\pi} e^{-ik} |k\rangle \langle k| \, dk \otimes |T\rangle \langle T| \tag{2.33}$$

where e^{ik} is the eigenvalue of $\hat{S}_x^H$ and e^{-ik} the eigenvalue of $\hat{S}_x^T$. From Eq. 2.28, it can be seen that propagation of the QW in the coin basis occurs through a phase shift of $e^{\pm ik}$ for a walker with momentum k moving to the right or left in position space, respectively [23]. This may be exemplified through the application of the step operator onto the initial state in Eq. 2.30 where the coin states are already in superposition.

$$\hat{S}_k |\psi\rangle_{0,k} = \frac{1}{2\pi\sqrt{2}} [\int_{k=-\pi}^{\pi} e^{ik\times 1} |k\rangle \, dk \otimes |H\rangle + \int_{k=-\pi}^{\pi} e^{ik\times -1} |k\rangle \, dk \otimes |T\rangle]$$

Here the multiplicative factors in the exponential terms indicate that the position of the walker has moved to ± 1 for the heads and tails states respectively, which may be clearly seen as the first step when converted back into position space with Eq. 2.29.

$$\hat{S}_k |\psi\rangle_{0,k} = \frac{1}{\sqrt{2}} [|1\rangle \otimes |H\rangle + |-1\rangle \otimes |T\rangle]$$

Subsequent representation of the step operator in matrix format is given in Eq. 2.34:

$$\hat{S}_k = \begin{bmatrix} \hat{S}_H^k & 0 \\ 0 & \hat{S}_T^k \end{bmatrix} = \begin{bmatrix} e^{ik} & 0 \\ 0 & e^{-ik} \end{bmatrix} \tag{2.34}$$

in the coin basis where the previous $|H\rangle = \begin{bmatrix} 1 \\ 0 \end{bmatrix}$ and $|T\rangle = \begin{bmatrix} 0 \\ 1 \end{bmatrix}$ definitions stand. It follows that the evolution of the walker in momentum space is generated by the concatenation of the coin operator (Eq. 2.13) with the new step operator, yielding

$$\begin{aligned}
\hat{U}_k = \hat{S}_k \hat{C} &= \begin{bmatrix} e^{ik} & 0 \\ 0 & e^{-ik} \end{bmatrix} = \begin{bmatrix} \cos\chi & e^{i\varphi} \sin\chi \\ e^{i\phi} \sin\chi & -e^{i\varphi+\Phi} \cos\chi \end{bmatrix} \\
&= \begin{bmatrix} [\cos\chi] e^{ik} & [e^{i\varphi} \sin\chi] e^{ik} \\ [e^{i\phi} \sin\chi] e^{-ik} & -[e^{i\varphi+\Phi} \cos\chi] e^{-ik} \end{bmatrix}
\end{aligned} \tag{2.35}$$

As in Eq. 2.23, n steps of the quantum walk are simply obtained through application of Eq. 2.35, raised to the n^{th} power, to the initialized walker state.

$$|\psi\rangle_n = [\hat{S}_k \hat{C}']^n \, |\psi\rangle_{0,k} \, . \tag{2.36}$$

It follows that the QW spatial distribution may be obtained by directly employing the evolution operator, $\hat{U}_k$, in the coin basis, giving the distribution as a summation of exponential k-terms. The multiplicative factor in each exponential then indicates the spatial positions occupied and the subsequent exponential term coefficients indicate the walker's probability amplitude for each position in each of the respective coin bases. This is illustrated for a Hadamard coin and the state initialized in the heads basis ($|\psi\rangle_{0,k} = \frac{1}{2\pi}\int_{k=-\pi}^{\pi} |k\rangle \, dk \otimes |H\rangle$ where $n = 2$:

$$\begin{aligned}
|\psi\rangle_2 &= [\hat{S}_k \hat{C}']^2 \, |\psi\rangle_{0,k} \\
&= (\frac{1}{\sqrt{2}} \begin{bmatrix} e^{ik} & e^{ik} \\ e^{-ik} & e^{-ik} \end{bmatrix})^2 \begin{bmatrix} 1 \\ 0 \end{bmatrix} \\
&= \frac{1}{2} \begin{bmatrix} e^{2\times ik} + e^{0\times ik} & e^{2\times ik} - e^{0\times ik} \\ e^{0\times ik} - e^{-2\times ik} & e^{0\times ik} + e^{-2\times ik} \end{bmatrix} \begin{bmatrix} 1 \\ 0 \end{bmatrix} \\
&= \frac{1}{2} \begin{bmatrix} e^{2\times ik} + e^{0\times ik} \\ e^{0\times ik} - e^{-2\times ik} \end{bmatrix}
\end{aligned}$$

where,

$$P(x) = P^H(x) + P^T(x) = | \, \langle x|\psi\rangle \, |^2 \, \langle H| + | \, \langle x|\psi\rangle \, |^2 \, \langle T| \, ,$$

resulting in the expected probability distribution shown below

$$\Rightarrow \text{Probability} : |\frac{1}{-2}|^2 \, |{-2}\rangle + (|\frac{1}{2}|^2 + |\frac{1}{2}|^2) \, |0\rangle + |\frac{1}{-2}|^2 \, |2\rangle \;\; \Rightarrow \text{Probability} : \frac{1}{4} \, |{-2}\rangle + \frac{1}{2} \, |0\rangle + \frac{1}{4} \, |2\rangle \, .$$

There is a distinct advantage with this method over the evolution in position space. Here n applications of the evolution operator, $\hat{U}_k$ does not change the 2×2 dimension of the resultant matrix whereas the matrix dimension scales as $(2n+1) \times (2n+1)$ in position space [23]. Furthermore, propagation of the states in this space allows additional dynamics to be easily extracted such as the allowed energies and velocities of the walker through its dispersion relation, as mentioned earlier. Here the analysis will be restricted to the case where only the weighted coin is considered, i.e. $\varphi = \Phi = 0$ in Eq. 2.14, for convenience although it may be further extended to include these factors. For this, however, the full set of eigenvectors must be considered. It is possible to obtain these eigenvalues by diagonalizing the evolution matrix derived in Eq. 2.13, such that [23],

$$\hat{U}_k = \lambda_+ \, |\rho_+(k)\rangle \, \langle \rho_+(k)| + \lambda_- \, |\rho_-(k)\rangle \, \langle \rho_-(k)| \, , \tag{2.37}$$

where $|\rho_\pm(k)\rangle$ are the evolution eigenvectors with the associated eigenvalues, $\lambda_\pm$. It follows that to obtain the respective eigenvectors and eigenvalues, the determinant is taken where

$$\det(\hat{U}_k - \mathbb{I}\lambda) = \det \begin{bmatrix} \cos\chi e^{ik} - \lambda & \sin\chi e^{ik} \\ \sin\chi e^{-ik} & -\cos\chi e^{-ik} - \lambda \end{bmatrix} = 0.$$

Letting $\Pi = \frac{\lambda}{\cos\chi}$,

$$\begin{aligned}
&\Rightarrow -\cos^2\chi(e^{ik}-\Pi)(e^{-ik}+\Pi) - \sin\chi^2 e^{ik}e^{-ik} = 0\\
&\Rightarrow -\cos^2\chi(e^{ik}-\Pi)(e^{-ik}+\Pi) - 1 - \cos^2\chi = 0\\
&\Rightarrow (e^{ik}-\Pi)(e^{-ik}+\Pi) = \frac{1}{\cos^2\chi} - 1\\
&\Rightarrow -1 + \Pi(e^{-ik}-e^{ik}) + \Pi^2 = \frac{1}{\cos^2\chi} - 1\\
&\Rightarrow \Pi^2 + \Pi(e^{-ik}-e^{ik}) - \frac{1}{\cos^2\chi} = 0\\
&\Rightarrow \Pi_\pm = -\frac{1}{2}(e^{-ik}-e^{ik}) \pm \frac{1}{2}\sqrt{(e^{-ik}-e^{ik}) - 4(1)(-\frac{1}{\cos^2\chi}}\\
&\Rightarrow \Pi_\pm = \frac{1}{2}(e^{ik}-e^{-ik}) \pm \frac{1}{2}\sqrt{(e^{2ik}+e^{-2ik}-2) + \frac{4}{\cos^2\chi}}.
\end{aligned}$$

Now since $2\cos 2k = e^{2ik} + e^{-2ik}$,

$$\Pi_\pm = i\sin k \pm \sqrt{\frac{1}{2}(\cos 2k - 1) + \frac{1}{\cos^2\chi}}.$$

and since $2\sin^2 k = 1 - \cos 2k$,

$$\Pi_\pm = i\sin k \pm \sqrt{\frac{1}{\cos^2\chi} - \sin^2 k}.$$

Letting $a = \sqrt{\frac{1}{\cos^2\chi}} = \frac{1}{\cos^2\chi}$ and $x = \frac{\sin k}{a}$, the eigenvalues can be structured in the form

$$\begin{aligned}
&\Pi_\pm = a\lambda_\pm = a(ix \pm \sqrt{1-x^2})\\
&\Rightarrow \lambda_\pm = ix \pm \sqrt{1-x^2}.
\end{aligned}$$

Utilizing the trigonometric identities, $\cos\sin^{-1}(x) = \sqrt{1-x^2}$ and $\sin\sin^{-1}(x) = x$, the eigenvalues may thus be written as

$$\begin{aligned}
&\lambda_\pm = i\sin\sin^{-1}(x) \pm \cos\sin^{-1}(x)\\
&\Rightarrow \lambda_\pm = \pm e^{\pm i\sin^{-1}(x)} = \pm e^{\pm i\sin^{-1}(\cos\chi\sin k)}
\end{aligned}$$

Taking the ansatz, $\lambda_\pm = e^{i\omega_\pm(k)}$ [23] subsequently results in the following spectrum

$$\omega_+(k) = \sin^{-1}(\cos\chi\sin k) \tag{2.38a}$$
$$\omega_-(k) = \pi - \sin^{-1}(\cos\chi\sin k) \tag{2.38b}$$

with Eq. 2.38 (b) ensuing from the relations: $\cos(\pi - X) = \cos(X)$ and $\sin(\pi - X) = -\sin(X)$. Determination of the eigenvectors are then obtained from $(\hat{U}_k - \mathbb{I}\lambda)\rho_+ = 0$ where

$$
\begin{aligned}
&(\begin{bmatrix}\cos\chi e^{ik} & \sin\chi e^{ik}\\ \sin\chi e^{-ik} & -\cos\chi e^{-ik}\end{bmatrix} - \begin{bmatrix}\lambda & 0\\ 0 & \lambda\end{bmatrix})\begin{bmatrix}\rho_{+1}\\ \rho_{+2}\end{bmatrix} = \begin{bmatrix}0\\0\end{bmatrix}\\
&\begin{bmatrix}\cos\chi(e^{ik} - \frac{\lambda}{\cos\chi}) & \sin\chi e^{ik}\\ \sin\chi e^{-ik} & -\cos\chi(e^{-ik} + \frac{\lambda}{\cos\chi})\end{bmatrix}\begin{bmatrix}\rho_{+1}\\ \rho_{+2}\end{bmatrix} = \begin{bmatrix}0\\0\end{bmatrix}\\
&\Rightarrow \sin\chi e^{-ik}\rho_{+1} - \cos\chi(e^{-ik} + \frac{\lambda}{\cos\chi})\rho_{+2} = 0\\
&\Rightarrow \sin\chi e^{-ik}\rho_{+1} = (\cos\chi + \frac{\lambda}{\cos\chi})\rho_{+2}\\
&\Rightarrow \sin\chi e^{-ik}\rho_{+1} = (\cos\chi\cos k - i\cos\chi\sin k + i\cos\chi\sin k + \cos\omega_+(k))\rho_{+2}\\
&\Rightarrow \sin\chi e^{-ik}\rho_{+1} = (\cos\chi\cos k + \cos\omega_+(k))\rho_{+2}
\end{aligned}
$$

Similarly, for $(\hat{U}_k - \mathbb{I}\lambda)\rho_- = 0$,

$$\sin\chi e^{-ik}\rho_{-1} = (\cos\chi\cos k + \cos\omega_-(k))\rho_{-2}$$

such that [67]

$$|\rho_\pm(k)\rangle = \frac{1}{\mathcal{N}_\pm}\begin{bmatrix}\cos\chi\cos k + \cos\omega_\pm(k)\\ \sin\chi e^{-ik}\end{bmatrix} \tag{2.39}$$

Here $\mathcal{N}_\pm$ are the respective normalization factors where $\mathcal{N}_\pm = \sqrt{\rho_{\pm 1}\rho^*_{\pm 1} + \rho_{\pm 2}\rho^*_{\pm 2}}$, so that

$$
\begin{aligned}
\mathcal{N}_+^2 &= [\cos\chi\cos k + \cos\omega_+][\cos\chi\cos k + \cos\omega_+] + [\sin\chi e^{-ik}][\sin\chi e^{ik}]\\
\Rightarrow &= [\cos^2\chi\cos^2 k + 2\cos\chi\cos k\cos\omega_+] + \sin^2\chi
\end{aligned}
$$

Now as $\cos\omega_+ = \sqrt{1 - \cos^2\chi\sin^2 k}$,

$$\mathcal{N}_+^2 = 2(\cos^2\chi\cos^2 k + \sin^2\chi + \cos\chi\cos k\sqrt{1 - \cos^2\chi\sin^2 k}) \tag{2.40a}$$

Likewise,

$$\mathcal{N}_-^2 = 2(\cos^2\chi\cos^2 k + \sin^2\chi - \cos\chi\cos k\sqrt{1 - \cos^2\chi\sin^2 k}) \tag{2.40b}$$

This spectrum (Eq. 2.37) may also be used to determine the evolution of the QW in momentum space [23], however, in a more complicated manner to that shown in the example for Eq. 2.33. Here the walk is evolved in the basis of the eigenvectors determined for the evolution operator. Subsequently, for the same initialized state as in the previous example with a Hadmard coin ($\chi = 45, \varphi = \Phi = 0$), the basis may be changed to obtain:

$$
\begin{aligned}
|\psi\rangle_{0,k} &= \frac{1}{2\pi}\int_{k=-\pi}^{\pi} |k\rangle\, dk \otimes |H\rangle\\
|\psi\rangle_{0,k} &= \frac{1}{2\pi}\int_{k=-\pi}^{\pi} |k\rangle \otimes |\rho_+(k)\rangle\langle\rho_+(k)|H\rangle + |\rho_-(k)\rangle\langle\rho_-(k)|H\rangle\, dk\\
|\psi\rangle_{0,k} &= \frac{1}{2\pi\sqrt{2}}\int_{k=-\pi}^{\pi} |k\rangle \otimes (\frac{(1+\sqrt{2})}{\mathcal{N}_+}|\rho_-(k)\rangle + \frac{(1+\sqrt{2})}{\mathcal{N}_+}|\rho_-(k)\rangle)dk
\end{aligned}
$$

Any following step in the walk is thus a case of applying the evolution operator in the same basis as described in Eq. 2.37.

$$\begin{aligned}|\psi\rangle_{n,k} &= [\hat{U}_k]^n\,|\psi\rangle_{0,k}\\ &= \frac{1}{2\pi\sqrt{2}}\int_{k=-\pi}^{\pi}|k\rangle\otimes(\frac{(1+\sqrt{2})\lambda_+^n}{\mathcal{N}_+}\,|\rho_+(k)\rangle+\frac{(1+\sqrt{2})\lambda_-^n}{\mathcal{N}_-}\,|\rho_-(k)\rangle)dk\end{aligned}$$

This, however, is superfluous to the content already covered where the pertinent information remains in examination of the pseudo-energies associated with the walker as given in Eq. 2.38 with the above example illustrating the validity of the transformation method in achieving the QW. By looking at how the energy of the walker is spread over momentum space, the dispersion relation of the walker may be determined as is shown in Fig. 2.6 (a) and (c) for a selection of weighting parameters for the range $\chi = [0, 90]$ in (a) and $\chi = [90, 180]$ in (c). Here these relations indicate the bands of allowed pseudo-energies allowed for the walker. Taking the derivative of these energy bands with respect to the momentum then yields the transverse group velocity of the walker [67], giving

$$v_\pm = \frac{\partial\omega_\pm(k,\chi)}{\partial k} = \pm\frac{\cos\chi\cos k}{\sqrt{1-\cos^2\chi\sin^2 k}} \tag{2.41}$$

This gives the velocity of the QW distribution for the positive and negative directions in a 1D line. The velocities associated with the dispersion relations in (a) and (c) are plotted alongside them in Fig. 2.6 (b) and (d) respectively. These distributions allow for easy determination and predictions of the QW dynamics. Here the inflection points in the dispersion relations reveal the maximum velocities possible for the walker group packet for each of the positive (negative) directions as indicated by the red (blue) curves. As $\omega_\pm'' = 0$ at $k = 0, \pm\, pi, ...$, it may easily be shown that the walker achieves maximum velocity of $v_{\text{max}\pm} = \pm\cos\chi$, at these points. From this one may determine the QW maximum distance achieved after n steps where n may be viewed as discrete time steps in the dynamics

$$d_{\text{max}\pm} = v_{\text{max}\pm}(\chi)\times[\text{time steps}] = \pm n\cos\chi \tag{2.42}$$

where $d_{\text{max}\pm}$ refers to the maximum distance in either direction. It follows that the greater the velocity of the walker, the further out the distribution can spread, resulting in a larger variance. This is illustrated in Fig 2.6 (b) and (d) where a larger percentage of the walker propagates in the high velocity regime that is shaded in grey. Here it is clear that the QW variance is much larger for the walks with more of the group velocity lying within this region as seen with the variance relations in Fig. 2.5.

Further examination and comparison between the energies and velocities of Fig. 2.6 yields greater insight into how the weighting parameter affects the QW. Looking at Fig. 2.6 (a), it may be seen that as the parameter increases between $[0, 90]$, the range of allowed energies decreases along with the curvature of the bands. This corresponds to a decrease in both the maximum velocity of the walker and the range of allowed velocities as seen in Fig. 2.6 (b). Consequently, one may expect a reduction in the variance of the distribution. Here the maximum velocities and allowed energy range occurs for $\chi = 0$ in both directions as was indicated in the analysis with Fig. 2.4 (a) and (b) where the states were propagated away from each other without interference. This may be seen as a reflection of the linear nature of the energy curve where there is no energy associated with interaction of the states. $\chi = 90$ shows the other extreme where the curvature has been reduced to such a level that it appears as a straight line and reflects the case whereby the walker has no velocity and the states simple traverse across each other causing the distribution to remain at the starting position. It follows that the QWs between these two extremes follow intermediary dynamics as illustrated with $\chi = 45$ for the common Hadamard walk.

The dynamics from $\chi = [90, 180]$ in Fig. 2.6 (c) and (d) shown a reversal where the curvature

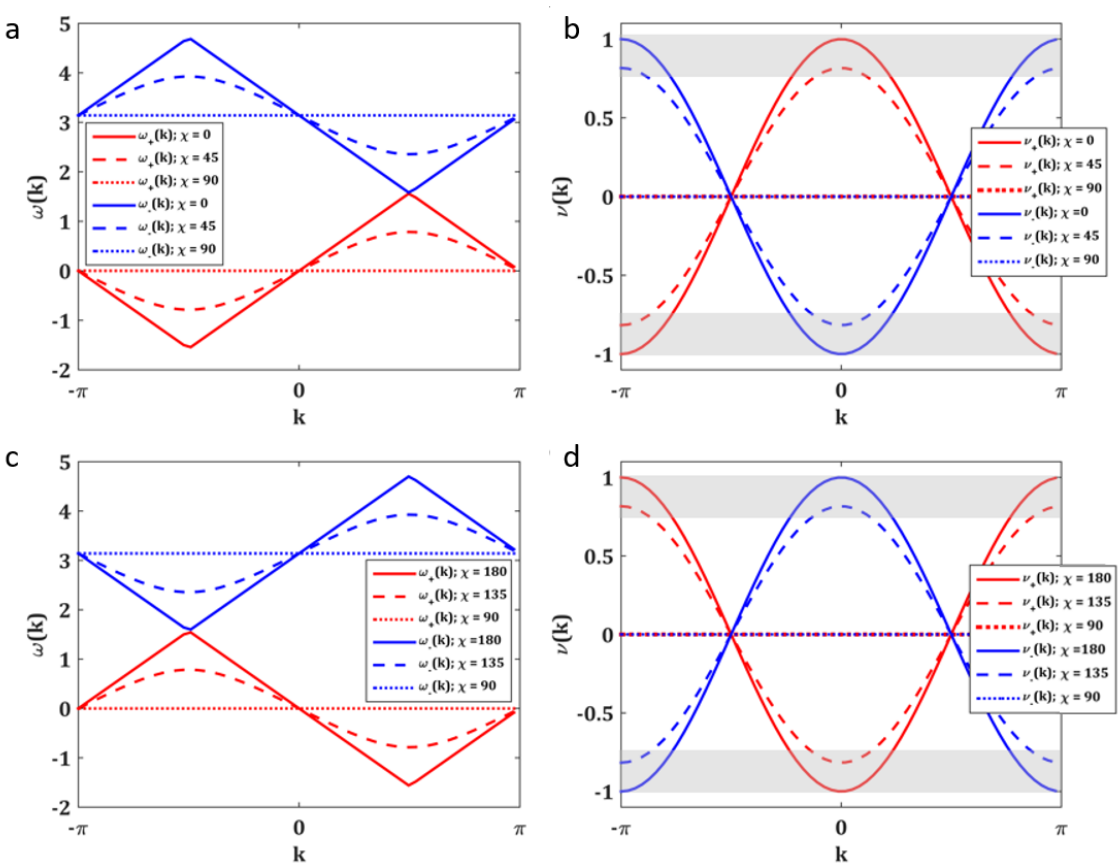

FIGURE 2.6: Plots of dispersion relations show the bands of allowed pseudo-energies for the walker and how this varies for a change in weighting parameters from (a) $\chi = [0, 90]$ and (c) $\chi = [90, 180]$. The associated transverse velocities are illustrated in (b) and (d) respectively. Here the red (blue) curves represent the walker dynamics for an initial positive (negative) direction.

in the energy bands flip and increase along with the range of allowed energies as the parameter increases again. Here this is subsequently accompanied by an increase in range of velocities taken on by the walker and the maximum velocity for the walker, however, in the opposite direction. Here the positive velocities take on the signs of what the negative velocities had for the initial weighting parameter range. This reversal in the direction at which the walker moves is seen clearly by the asymmetrical distributions plotted in Fig. (c) and (d) where the largest spike in the QW probabilities is seen to occur on the other side of the position space in the same range for the weighting parameter.

2.2 The 'quantum' in quantum walking

It is well known that classical systems are described in terms of either a wave or a particle. With a set of dynamics one can associate with each description such as waves diffracting around boundaries in comparison to particles being inhibited by the boundary. For instance, one may hear a person on the other side of a wall, but a ball thrown towards a person, with a wall in between, will not reach the person on the other side. On the quantum mechanical scale, however, the same entity exhibits both of these properties such that a complete description of the system now requires consideration of wave-particle duality [56]. This is a well-known result of several observed phenomena such as in the Davisson-Germer experiment where electrons impacting nickel gave rise to diffraction patterns described by Bragg's law, indicating a wave nature [68]. However, it was already established through J.J. Thomson's experiment (and others) that electrons acted as particles where deflection of electrons accelerated towards a phosphorescent screen in an evacuated cathode-ray tube resulted in ejection of photons in correspondence with particle behavior [69]. Similar conclusions hold for the observation of rainbows (waves) and the photoelectric effect (particles) respectively when considering the nature of light.

In 1926 Erwin Schrödinger unified these conflicting descriptions with the famous Schrödinger equation such that the dynamics of a quantum mechanical system is described in terms of a differential wave equation, solidifying the theory of quantum mechanics [54]. Here the role of this equation is comparable to that of Newton's second law where any dynamical value of interest (i.e. energy, velocity etc.) may be determined once the evolution of the particle's position is known [56]. Application of the second law then allows the path of the classical particle to be predicted deterministically [70]. Similarly, the dynamics of a quantum system may be determined with the Schrödinger equation, however, instead of a positional evolution, the entity (particle) is described by a solution to Schrödinger's equation, given a set of initial conditions; in other words, the entity is described by a wavefunction as introduced in Section 2.2.1 [56].

Accordingly, the wavefunction describes all the possibilities available to the entity in terms of probability amplitudes such that it interferes with itself and other entities roughly according to what we classically see as wave mechanics in some cases [71]. Here the probability amplitude also evolves deterministically according to the equation [70]. For particles, it is not unusual to be able to classically describe a system in terms of the probabilities of the possible outcomes – in fact, this is generic statistics - however, in quantum mechanics the system is actually occupying all the outcomes at exactly the same time as determined by the associated dynamical interactions, only assuming one of them when a measurement is taken [71]. The particle nature is then revealed when taking a measurement, or rather, collapsing the wavefunction to reveal a single outcome such that the entity localizes (exhibits particle nature) in one of the possible states [56]. Successive measurements on identical systems reveal that the frequency at which an allowed state is assumed concurs with the square of the probability amplitude i.e. the Born-interpreted probability. It is this localization of the quantum particle that yields the 'randomness' associated with quantum mechanics in contrast to the probability amplitude evolution [70]. A good experimental observation of this is in Young's double slit experiment with electrons [72]. Accelerating a single electron towards two slits reveals an interference pattern after integrating over many measurements for identical repetitions, showing that the electron probability amplitude interferes with itself (wave). However, for each measurement, only a single localized position is detected for the electron as is expected for a particle.

Based on the wavefunction description of a quantum mechanical entity, such as the walker in the QW, it follows that its interactions and characteristics may be somewhat associated with classical waves and the measured outcome is an associated selection of the quantized possibilities (corresponding to basis states) in the measurement basis. Consequently, the principal of superposition covered in Section 1.1 comes into play where the particle may, in some interpretations, be thought of as simultaneously occupy basis states which seem intuitively incompatible such as two different spatial positions (more than one position on the QW position space) or, as in the common example of Schrödinger's cat, be alive and dead at the same time. Measurement or observation of the superposition then collapses the superposition [56]. Interestingly, observation of the QW after every step actually reverts the QW back to the classical RW as the walker is then forced to assume a particular position after every step such that the choices for the next step is again limited to right or left from a specific position, just as in the RW [26]. Accordingly, observation of QW forces the quantum mechanical dynamics to revert to classical dynamics as commonly seen in convergence between quantum and classical mechanics. Additionally, interference as wave phenomenon in quantum dynamical evolution also applies such that certain possibilities are reduced or increased (e.g. the decrease in the probability at the center of the QW and increase in probability at the ends of the QW distribution) compared to the expected classical outcomes for a particle.

Classical waves can also evolve with similar dynamics, for a few special cases, if there are analogues that can exert the same type of influences experienced by the quantum particle. The classical outcome, however, would then be an integration of many measurements of identical systems for the quantum mechanical case. For instance, classical waves can also occupy basis states simultaneously. Consider the intersections and positions described for the QW. A classical wave can fill the space to occupy any number of positions or intersections at the same time, according to the boundary conditions supplied by the environment. However, measurement of the wave does not eliminate any of the occupied states. Additionally, analogous interference of classical waves would reveal the same distribution, yet, again, with a very distinct difference. Measurement of the wave intensity (square of the amplitude) would yield the entire distribution whereas measurement of the quantum mechanical system would yield a single basis state outcome with a probability related to the relative intensity of the classical wave. Subsequently, many repeated quantum mechanical measurements would be required to replicate the same distribution.

As these interference and superposition principals determining the QW are present in classical wave analogues, the question follows: what if we did the QW with classical waves? How would a classical implementation of this innately quantum mechanical developed phenomenon fair? Also, how much more advantageous is such a classical experiment which is inherently more robust than quantum mechanical ones? It should be stressed here that some evolution characteristics may be shared in this quantum-classical pairing where the line may be blurred, but fundamentally, classical and quantum mechanics operate under distinctly different principals such that many phenomena exist for which classical waves cannot be used as a representative analogue.

An additional characteristic that has not yet been covered, but plays a large role in terms of the QW evolution and associated dynamics, is entanglement. This refers to the occurrence of correlations between subsystems, whereby a measurement revealing a particular state for one subsystem results in a prediction about the state of another subsystem [71]. Here the states also form a non-separable relation when considering the mathematical formalism shown further on. Schrödinger described entanglement as not being able to describe two previously known systems, once temporarily interacted, as before the interaction where each had their own individual representation

[73]. Herein lies the ‘spookiness’, as Einstein termed it, of quantum mechanical interactions between systems. A common example of entanglement is a two spin-$1/2$ singlet state [74],

$$|\psi\rangle = |\psi_1\rangle \otimes |\psi_2\rangle = \frac{1}{\sqrt{2}}(|\uparrow\rangle_1 |\downarrow\rangle_2 + |\uparrow\rangle_2 |\downarrow\rangle_1) \tag{2.43}$$

for a composite system of two particles: particle 1 ($|\psi_1\rangle$) and particle 2 ($|\psi_2\rangle$), with basis states of spin up and down, as indicated by the arrows in the equation. If a measurement on the spin of subsystem 1 (particle 1) reveals a spin up ($|\uparrow\rangle_1$) state, the state of subsystem 2 (particle 2) is definitely known to be spin down ($|\downarrow\rangle_2$) and vice versa, regardless of the distance between the subsystems. Observation of the entangled states above shows that the subsystem basis states cannot be factorized into a product state of the individual subsystems. Mathematically, entanglement is described as the non-separability of the composite states of a system [74–76]. Moreover, entanglement is not just the non-separable pairing of different particles or entities, but also extends to any set of states that form individual spaces or systems themselves [74]. Specifically, entanglement also refers to a non-separable relation between different properties of a single entity, such as in the first step of the Hadamard QW,

$$|\psi\rangle_1 = \frac{1}{\sqrt{2}}(|1\rangle |H\rangle + |-1\rangle |T\rangle), \tag{2.44}$$

where the tensor products have been omitted for convenience. Here non-separability of the internal coin and position states exhibit entanglement between the walker’s subspaces for these properties of the QW system. This type of non-separability is not actually confined to quantum mechanical systems, but based on the mathematical definition. It also extends into the classical realm where internal properties of a single classical system may also be ‘classically entangled’ [74–76] such as between polarization and orbital angular momentum of classical light [76; 77] as will be discussed in Section 2.3.4.

The classical analogue may only be extended so far, though. ‘Classical entanglement’ or non-separability may only occur between the internal degrees of freedom of a single entity, implying that non-locality is not possible between classically entangled subsystems [74]. Additionally, the outcomes cannot be mutually exclusive as no collapse occurs from particle indivisibility when taking a measurement. In fact, Luis [76] showed classical and quantum entanglement exhibits no definite relation. Additionally, the term ‘classical entanglement’ has sparked some controversy in the scientific community. Some contest the term, advocating that it should rather be termed ‘classical non-separability’, leaving entanglement for the quantum mechanical cases only [78]. For the purpose of this thesis, however, classical non-separability will be referred to as classical entanglement due to the intuitive implications in a classical QW.

Is it not then possible to implement a QW classically within the properties of a light wave such that the internal degrees of freedom are used to entangle and interfere the wave along superpositions of its internal states for two different properties? Here, by taking a fixed amount of a classical light wave, such as a pulse, can we not analogously play with the particle (pulse) and wave (classical wave dynamics) characteristics to formulate a QW? How far can these quantum-classical boundaries be exploited?

2.3 Delving into the classical realm

Based on the questions raised in Section 2.2, it is necessary to look further into the characteristics of light in the classical sense beginning with electromagnetism (EM). Due to the extensive nature of EM theory, it will only be covered briefly for completeness. Here we look into how light may be structured to from fundamental eigenmodes of free-space that serve as spatial basis states. Additionally, it can be seen that certain modes carry orbital angular momentum, allowing for a convenient space in which to play for a QW. When considering polarization as another state space in which to pair the spatial modes, the implications in terms of classical entanglement enables another way to look at generating a QW in classical terms.

2.3.1 Electromagnetic wave theory

Before the formation of quantum mechanics where wave-particle duality lay at the crux, light was periodically and controversially argued to be either a wave or a particle. The eventual consensus aligned with the wave theory proposed by Christiaan Huygens in his 1690 treatise "*Traité de la Lumière*" [79] as opposed to particle theory, first implied by Sir Isaac Newton's in 1671 [80] and further explored in his book "*Opticks: A treatise of the reflections, refractions, inflexions and colours of light*" [81]. This classical description was later consolidated by the formulation of Maxwell's equations. Famous for unifying the theories of electricity and magnetism, these equations have been developed to form a comprehensive description of classical phenomena and interactions in these fields when paired with Lorentz's force law and Newton's second law of motion [82]. Accordingly, this applies in the case of light in the classical sense due to its oscillating electric and magnetic field composition. The task associated with these equations lies in 'unpacking' them due to their compact nature correlating with the extent of classical electromagnetic theory. These renowned equations [83] are listed in their differential form as Eq. 2.45 for reasons that will soon become clear.

$$\nabla \times \mathbf{E} = -\frac{\partial}{\partial t}\mathbf{B} \tag{2.45a}$$

$$\nabla \times \mathbf{H} = -\frac{\partial}{\partial t}\mathbf{D} + \mathbf{J} \tag{2.45b}$$

$$\nabla \cdot \mathbf{D} = \rho \tag{2.45c}$$

$$\nabla \cdot \mathbf{B} = 0 \tag{2.45d}$$

Here bold formatting is used to denote vectors and $\nabla = \frac{\partial}{\partial x}\hat{\mathbf{x}} + \frac{\partial}{\partial y}\hat{\mathbf{y}} + \frac{\partial}{\partial z}\hat{\mathbf{z}}$ denotes the del operator for 3-dimensional Cartesian space spanned by the orthogonal unit vectors $[\hat{\mathbf{x}}, \hat{\mathbf{y}}, \hat{\mathbf{z}}]$. These equations define the relationships between electric field strength $\mathbf{E}$, magnetic flux density $\mathbf{B}$, electric flux density $\mathbf{D}$, magnetic field strength $\mathbf{H}$, current density $\mathbf{J}$ and volume charge density ρ. Additional relations between field strength and flux density exist for the electric and magnetic cases when in a vacuum. These are given in Eq. 2.46 respectively

$$\mathbf{D} = \epsilon_0 \mathbf{E} \tag{2.46a}$$

$$\mathbf{H} = \frac{1}{\mu_0}\mathbf{B} \tag{2.46b}$$

where $\epsilon_0 = 8.854 \times 10^{-12}$ F/m (Farad per meter) and $\mu_0 = 4\pi \times 10^{-7}$ H/m (Henry per meter) are physical constants known as the permittivity and permeability of free space [82]. Permittivity is the resistance associated with the formation of an electric field [83]. Analogously, permeability is the resistance associated with the formation of a magnetic field [83]. It follows that these constants take on different values and properties when the electric and magnetic fields are present in media. The above equations are in fact a specialized case for the more general relations [84]:

$$\mathbf{D} = \epsilon_0 \mathbf{E} + \mathbf{P} \tag{2.47a}$$

$$\mathbf{H} = \frac{1}{\mu_0}\mathbf{B} - \mathbf{M} \tag{2.47b}$$

which are applicable to any medium. Here $\mathbf{P}$ is the polarization density which along with $\mathbf{D}$ describes the dielectric properties of the medium. $\mathbf{M}$ is the magnetization density which along with $\mathbf{H}$ similarly describes the magnetic properties of the medium.

Properties of the medium affect the subsequent values of **P** and **M**, correlating to the description of said medium. In certain cases this results in the permittivity and permeability coefficients taking on values related to the medium. One such medium of particular interest with regards to the propagation of electromagnetic waves is known as a dielectric medium which exhibits linearity, homogeneity, isotropy, is nondispersive, source-free and non-magnetic [84; 85]. More specifically, nondispersive refers to spatially and temporally localized reaction by the medium to field strength, homogenous refers to the medium properties being spatially constant (i.e. permittivity and permeability constants do not change throughout the medium), isotropy implies the medium properties are directionally invariant for the propagation of the field vectors **E**, **H** and source-free indicates no net current density and volume charge density ($\mathbf{J} = 0; \rho = 0$) [85]. Furthermore, linearity describes the effect of the medium as the same on a linear combination input fields as the corresponding linear combination of output fields [85]. This results in the polarization density, **P** being linearly related to the electric field, **E** [84]. Combination of these properties results in the polarization density of the medium being described by [83]

$$\mathbf{P} = \epsilon_0 \chi \mathbf{E} \tag{2.48}$$

where χ, in this case, is the electric susceptibility such that

$$\mathbf{D} = \epsilon_0 (1 + \chi) \mathbf{E} \tag{2.49}$$

This yields the permittivity constant of the medium, $\epsilon = \epsilon_0(1 + \chi)$. Similar results also generate a permeability constant of the medium μ, however in the case of no magnetism: $\mu = \mu_0$ and the refractive index, $n = \sqrt{1 + \chi}$ [83]. Mathematically, this results in a difference of replacing the permittivity constant with that of the medium as given by the refractive index of the medium: $\epsilon_0 \to \epsilon_0 n^2$ [83].

Materials exhibiting properties that vary from those given for the above defined dielectric medium results in other interesting results such as non-linear optical effects, photonic crystals and the magneto-optic effect [85]. Analysis of these different media is a substantial endeavor and not directly related to this work. As such, it exceeds the theoretical scope of the dissertation and shall only be noted here.

A fundamental finding for electromagnetic theory was the discovery that Maxwell's equations in the absence of sources and currents result in a wave equation with regards to both magnetic and electric fields. The electric field derivation thereof follows for a vacuum [83]:

Consider the curl of Faraday's law of induction (Eq. 2.45 (a)),

$$\nabla \times (\nabla \times \mathbf{E}) = \nabla \times (-\frac{\partial}{\partial t}\mathbf{B})$$

This allows for the implementation of the identity $\nabla \times (\nabla \times \mathbf{E}) = \nabla(\nabla \cdot E) - \nabla^2 E$, such that

$$\nabla \times (\nabla \times \mathbf{E}) = \nabla(\nabla \cdot \mathbf{E}) - \nabla^2 \mathbf{E} = \nabla \times (-\frac{\partial}{\partial t}\mathbf{B}) \tag{2.50}$$

However in a vacuum Eq. 2.45 (c) changes to

$$\nabla \cdot \mathbf{D} = 0 \Rightarrow \nabla \cdot \mathbf{E} = 0$$

as there is no charge density ($\rho = 0$). It follows that Eq. 2.50 becomes

$$-\nabla^2 \mathbf{E} = \frac{\partial}{\partial t}(\nabla \times \mathbf{B}) \tag{2.51}$$

Elimination of the magnetic field is achieved through exploitation of Eq. 2.45 (b) with the relations in Eq. 2.46 and $\mathbf{J} = 0$ (vacuum):

$$\nabla \times \mathbf{H} = \frac{1}{\mu_0}\nabla \times \mathbf{B} = -\frac{\partial}{\partial t}\mathbf{D} + 0 = -\epsilon_0\frac{\partial}{\partial t}\mathbf{E}$$
$$\nabla \times \mathbf{B} = -\mu_0\epsilon_0\frac{\partial}{\partial t}\mathbf{E} \tag{2.52}$$

Substituting 2.52 into 2.51 then yields:

$$\nabla^2\mathbf{E} = \mu_0\epsilon_0\frac{\partial^2}{\partial t^2}\mathbf{E} \tag{2.53}$$

which is in fact the wave equation, relating the spatial change of a wave to its speed (v), when compared to the well-known generic 1D case ubiquitous in undergraduate texts

$$\frac{\partial^2 y}{\partial x^2} = \frac{1}{v^2}\frac{\partial^2 y}{\partial t^2} \tag{2.54}$$

for the propagation of a sinusoidal wave, y along the x-direction.

Comparison of the generic case (Eq. 2.54) to that derived from Maxwell's equations (Eq. 2.53) indicates that the velocity of the electric wave is given by the relation

$$\frac{1}{v^2} = \mu_0\epsilon_0$$

Rearrangement results in the derivation of the speed of light (c) as is expected for light propagating in a vacuum.

$$v = c = \frac{1}{\sqrt{\mu_0\epsilon_0}} = 2.998 \times 10^8 \text{m per s}$$

In the case of the dielectric medium described previously, the speed is related to the refractive index as shown below

$$v = \frac{1}{\sqrt{n^2\mu_0\epsilon_0}} = \frac{1}{n\sqrt{\mu_0\epsilon_0}} = \frac{c}{n} \tag{2.55}$$

Wave structure in the spatial domain has application in many classical fields regarding structured light with the different structures being termed modes [85]. Such modes are acquired by obtaining solutions to wave equations. It follows that determination of these spatial solutions requires elimination of the temporal component. This time-independent wave equation is termed the Helmholtz equation and is obtained through application of the separation of variables technique which assumes a function may be separated into separate functions of the variables comprising it [86; 87]. Equation 2.55 demonstrates this technique for a wave function in the spatial and temporal domains for an electric field, $E(x, y, z, t)$.

$$E(x, y, z, t) = U(x, y, z)T(t) \tag{2.56}$$

Majority of the solutions widely used, including those applicable to this work, are associated with the scalar Helmholtz wave equation. As such the derivation of the Helmholtz equation [86; 87] shall be limited to this case. Subsequently, substitution of Eq. 2.56 into Eq. 2.53 yields

$$
\begin{aligned}
\nabla^2 U(x,y,z)T(t) &= \frac{1}{c^2}\frac{\partial^2}{\partial t^2}U(x,y,z)T(t) \\
\Rightarrow T(t)\nabla^2 U(x,y,z) &= \frac{1}{c^2}U(x,y,z)\frac{\partial^2}{\partial t^2}T(t) \\
\Rightarrow \frac{1}{U(x,y,z)}\nabla^2 U(x,y,z) &= \frac{1}{c^2 T(t)}\frac{\partial^2}{\partial t^2}T(t)
\end{aligned} \tag{2.57}
$$

such that the spatial and temporal functions are separated from each other. As both sets of variables are independent of the other, changing the one side will not affect the other. Consequently, both sides of the equation must equate to a constant to render Eq. 2.57 true. For reasons that will soon become clear in the subsequent solution, let the chosen constant be $-k^2$:

$$
\Rightarrow \frac{1}{U(x,y,z)}\nabla^2 U(x,y,z) = \frac{1}{c^2 T(t)}\frac{\partial^2}{\partial t^2}T(t) = -k^2
$$

Replacing the right side of the equation in Eq. 2.57 with the constant then eliminates the temporal dependence. Rearrangement then produces the Helmholtz equation as given in Eq. 2.58 (b)

$$
\frac{1}{U(x,y,z)}\nabla^2 U(x,y,z) = -k^2
$$

$$
\Rightarrow \nabla^2 U(x,y,z) = -k^2 U(x,y,z) \tag{2.58a}
$$

$$
\Rightarrow (\nabla^2 + k^2)U(x,y,z) = 0 \tag{2.58b}
$$

where k is the wave-number due to the spatial derivative of a wave function yielding a product of the wavenumber with the wave function as seen for Eq. 2.58 (a). k is consequently defined as $k = \frac{\omega}{c} = \frac{2\pi}{\lambda}$ where ω is angular frequency and λ wavelength.

2.3.2 Solutions to the Helmholtz equation

As mentioned earlier, solutions to the Helmholtz equations constitute modes which are essential to many applications regarding the structuring of light. In particular, when observing the equation closely, it can be seen that these solutions are in fact eigenmodes of the wave equation for a certain system – free space for example [88]. This indicates that the solution satisfies the requirements for existence in that system and thus its structure is preserved as it propagates. Furthermore, the solutions form a set related to the respective scenario solved for. Elements of the derived set differ through variation of internal parameters associated with the scenario. These different elements are termed the modes of that set which have an additional property of orthogonality resulting in the set forming a complete orthogonal basis for the system [85]. Consequently, any arbitrary field existing in the system may be completely described through a linear combination of these basis modes [85].

The plane wave

The most fundamental of such cases is derived [83] through the application of the separation of variables technique, utilized earlier, in the Cartesian coordinate system. Subsequently, let the electric field $U(x,y,z)$ satisfying the wave equation be expressed in terms of functions for each coordinate $F(x)$, $G(y)$ and $H(z)$ as illustrated in Eq. 2.59.

$$
U(x,y,z) = F(x)G(y)H(z) \tag{2.59}
$$

Substituting Eq 2.59 into the Helmholtz equation (Eq. 2.58) results in

$$(\nabla^2 + k^2)F(x)G(y)H(z) = 0$$
$$\Rightarrow G(y)H(z)\frac{\partial^2 F(x)}{\partial x^2} + F(x)H(z)\frac{\partial^2 G(y)}{\partial y^2} + F(x)G(y)\frac{\partial^2 H(z)}{\partial z^2} = -k^2 F(x)G(y)H(z)$$

Dividing both sides by $U(x, y, z)$ then yields

$$\Rightarrow \frac{1}{F(x)}\frac{\partial^2 F(x)}{\partial x^2} + \frac{1}{G(y)}\frac{\partial^2 G(y)}{\partial y^2} + \frac{1}{H(z)}\frac{\partial^2 H(z)}{\partial z^2} = -k^2, \tag{2.60}$$

such that the variables are separated between the terms. Similar logic to the other case regarding independent variables leads to the requirement that each term must be equal to a constant for which the sum equates to $-k^2$ on the right hand side of Eq. 2.60. The constants are chosen to be $-k_x^2, -k_y^2 and - k_z^2$, for each term as indicated in Eq. 2.61.

$$\frac{1}{F(x)}\frac{\partial^2 F(x)}{\partial x^2} = -k_x^2 \Rightarrow \frac{\partial^2 F(x)}{\partial x^2} = -k_x^2 F(x) \tag{2.61a}$$
$$\frac{1}{G(y)}\frac{\partial^2 G(y)}{\partial y^2} = -k_y^2 \Rightarrow \frac{\partial^2 G(y)}{\partial y^2} = -k_y^2 F(y) \tag{2.61b}$$
$$\frac{1}{H(z)}\frac{\partial^2 H(z)}{\partial y^2} = -k_z^2 \Rightarrow \frac{\partial^2 H(z)}{\partial z^2} = -k_z^2 H(z) \tag{2.61c}$$

Again, the choice of constant is due to convenience regarding the final solution such that

$$k_x^2 + k_y^2 + k_z^2 = k^2 \tag{2.62}$$

when substituted into Eq. 2.60. Equation 2.62 indicates that each of the constants are the x-,y-and z-components of the wave vector. It follows that choice of a negative value for any of these constant would result in the component being imaginary which leads to the phenomenon of evanescent waves. The simplest, however, is to keep all constants positive which is the route taken. Each of the Equations 2.61 (a-c) may be solved separately to form a composite solution for this scenario. It follows that the differential equation solutions in complex form are

$$F(x) = e^{-ik_x x}, G(y) = e^{-ik_y y} \text{ and } H(z) = e^{-ik_z z}.$$

The negative exponent was chosen to indicate a positive direction of propagation with regards to the wave vector. Substituting the separate solutions into Eq. 2.59 then yields the final result,

$$U(x, y, z) = e^{-ik_x x}e^{-ik_y y}e^{-ik_z z} = e^{-i\mathbf{k}\cdot\mathbf{r}}, \tag{2.63}$$

where $\mathbf{k} = k_x\hat{\mathbf{x}} + k_y\hat{\mathbf{y}} + k_z\hat{\mathbf{z}}$ and $\mathbf{r} = x\hat{\mathbf{x}} + y\hat{\mathbf{y}} + z\hat{\mathbf{z}}$. To recover the time-dependence of the field, the equation may be multiplied by the factor $e^{i\omega t}$ such that the full expression becomes

$$U(x, y, z) = e^{i(\omega t - \mathbf{k}\cdot\mathbf{r})}, \tag{2.64}$$

which is in fact a plane wave propagating to the right in the direction determined by the wave vector.

The paraxial limit of the Helmholtz equation

Another well-known example of a solution to the wave equation are Bessel beams which are generated by considering the Helmholtz equation in cylindrical coordinates [85]. This, however is not used here and is only noted as evidence of the other solutions present for the wave equation determined due to altering system conditions. The solutions of relevance, conversely, result from an approximation made with the Helmholtz equation known as the paraxial approximation. Derivation of the equation in the paraxial regime follows.

The paraxial approximation results from considering waves in the paraxial regime where the direction of propagation for the waves constituting a beam remains close to the beam axis [85]. Another way to conceptualize the approximation would be to think of the wave front normals as approximately parallel [84]. In agreement with this approximation, the complex form of the scalar electric field forming the beam takes on the form given in Eq. 2.65 [84].

$$U(x, y, z) = a(x, y, z)e^{-ikz}, \tag{2.65}$$

Here $a(x, y, z)$ the complex amplitude of the wave that varies with position and e^{-ikz} represents a plane wane travelling in the z-direction (as indicated by Eq. 2.63). It follows that Eq. 2.65 represents a complex-amplitude modulated wave propagating along the z-axis. Additionally, for the parallel approximation to be valid, variation of the complex amplitude, or rather the modulation should be minor in comparison to the wavelength [84].

Substituting Eq. 2.65 into the Helmholtz equation (Eq. 2.58) permits derivation of the paraxial form of this time-independent wave equation.

$$\begin{aligned}
&(\nabla^2 + k^2)a(x, y, z)e^{-ikz} = 0\\
&\Rightarrow (\frac{\partial^2}{\partial x^2} + \frac{\partial^2}{\partial y^2} + \frac{\partial^2}{\partial z^2})a(x, y, z)e^{-ikz} + k^2 a(x, y, z)e^{-ikz} = 0\\
&\Rightarrow (\frac{\partial^2}{\partial x^2} + \frac{\partial^2}{\partial y^2})a(x, y, z)e^{-ikz} + \frac{\partial^2}{\partial z^2}a(x, y, z)e^{-ikz} + k^2 a(x, y, z)e^{-ikz} = 0\\
&\Rightarrow (\frac{\partial^2}{\partial x^2} + \frac{\partial^2}{\partial y^2})a(x, y, z)e^{-ikz} + [X] + k^2 a(x, y, z)e^{-ikz} = 0
\end{aligned} \tag{2.66}$$

where

$$\begin{aligned}
X &= e^{-ikz}\frac{\partial^2}{\partial z^2}a(x, y, z) + 2\frac{\partial}{\partial z}a(x, y, z)\frac{\partial}{\partial z}e^{-ikz} + a(x, y, z)\frac{\partial^2}{\partial z^2}e^{-ikz}\\
&= e^{-ikz}\frac{\partial^2}{\partial z^2}a(x, y, z) + 2ike^{-ikz}\frac{\partial}{\partial z}a(x, y, z) - k^2 e^{-ikz}a(x, y, z)\\
&= e^{-ikz}(\frac{\partial^2}{\partial z^2} + 2ik\frac{\partial}{\partial z} - k^2)a(x, y, z)
\end{aligned} \tag{2.67}$$

Substituting 2.67 into 2.66 and dividing by e^{-ikz}:

$$\begin{aligned}
&(\frac{\partial^2}{\partial x^2} + \frac{\partial^2}{\partial y^2})a(x, y, z) + [(\frac{\partial^2}{\partial z^2} + 2ik\frac{\partial}{\partial z} - k^2)a(x, y, z)] + k^2 a(x, y, z) = 0\\
&\Rightarrow (\frac{\partial^2}{\partial x^2} + \frac{\partial^2}{\partial y^2})a(x, y, z) + [(\frac{\partial^2}{\partial z^2}a(x, y, z)] + 2ik\frac{\partial}{\partial z}a(x, y, z) = 0
\end{aligned}$$

Considering this equation, the condition for paraxial approximation given earlier regarding the complex amplitude translates to the mathematical statement [89; 90]:

$$|\frac{\partial^2}{\partial z^2}a(x, y, z)| << |\frac{\partial}{\partial z}a(x, y, z)| \tag{2.68}$$

as $k = \frac{2\pi}{\lambda}$. Equation 2.68 accordingly states that the amplitude variation along the direction of propagation is slight in contrast to the wavelength of the beam. Hence, the bracketed central term may be neglected, yielding the paraxial Helmholtz wave equation (Eq. 2.69) [85].

$$\Rightarrow \left(\frac{\partial^2}{\partial x^2} + \frac{\partial^2}{\partial y^2}\right)a(x, y, z) + 2ik\frac{\partial}{\partial z}a(x, y, z) = 0 \quad (2.69)$$

Gaussian beams

Following the derivation of the paraxial equation, consideration may now be given to the solutions relevant to this work. The Gaussian mode is the most fundamental solution and generic in real-world applications as it usually forms the basis mode for manipulation of light due its simplicity and uncomplicated generation. It is also the initial mode utilized in the laboratory for the experiments preformed. Moreover, it provides a good platform on which to introduce the different characteristics associated higher-order Gaussian modes such as Hermite-Gaussian or Laguerre-Gaussian beams. The complex-amplitude expression resulting in a Gaussian beam is given by [84]

$$a(r, z) = \frac{w_0}{w} e^{\frac{r^2}{w^2}} e^{\frac{-ikr^2}{2R}} e^{-i\vartheta} \quad (2.70)$$

in polar coordinates where $r = \sqrt{x^2 + y^2}$ is the transverse radial coordinate. Properties characterizing the structure of the beam as well as how it evolves upon propagation may be related to several of the variables expressed above. A depiction of the evolution of this beam as it propagates the z-axis is illustrated in Fig 2.7 with a longitudinal cross-section through the center. The vertical curves inside the beam are depicting the wavefronts of the compositional waves.

One characterizing quality of the beam is the beam width, denoted by w. This may be thought of as the radius of the beam [88]. As may be initially seen in Fig. 2.7, the beam converges (before $z = 0$) before diverging (after $z = 0$) as it propagates. Subsequently, the beam possesses a minimal beam width known as the beam waist, w_0, which is located at $z = 0$ in the diagram [84]. Considering how the beam width must then change with propagation, a ratio relating the degree of change in beam width with the distance traveled may be defined. This ratio is labeled as the Raleigh range (z_R) [88] and is the distance at which the beam width becomes a factor of $\sqrt{2}$ larger than the beam waist. Analytically, the Raleigh range is defined by the function given in Equation 2.71,

$$z_R = \frac{\pi w_0^2}{\lambda} \quad (2.71)$$

where it is directly proportional to the smallest transverse cross-sectional area and inversely proportional to the wavelength. This value consequently serves as a measure of the rate of beam divergence with respect to distance whereby a small value indicates fast divergence while a large value indicates slow divergence. Following the Raleigh range definition, it is then possible to

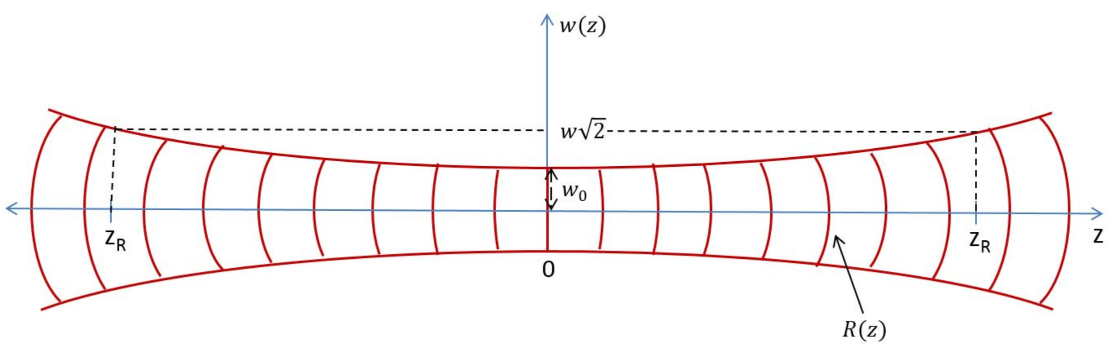

FIGURE 2.7: Longitudinal cross-section through the center of a Gaussian beam indicating its characteristics and evolution upon propagation.

quantify how the beam width changes in terms of the beam waist [89].

$$w = w_0\sqrt{1+\frac{z}{z_R}} \tag{2.72}$$

As the beam diverges (or converges), the wavefront associated with the beam must additionally change as the individual rays change direction. More specifically, the divergence or convergence results from the 'bending' of the wavefront. The change in wavefront is subsequently characterized through its radius of curvature, R as given by Eq. 2.73 [89].

$$R = z[1+(\frac{z_R}{z})^2] \tag{2.73}$$

Furthermore, there is also a phase shift that occurs with propagation of the beam along the z-axis. This shift is termed the Gouy Phase or the Gouy effect. It is defined as [84]

$$\vartheta = \tan^{-1}(\frac{z}{z_R}) \tag{2.74}$$

for the ϑ in Eq. 2.70 and thus ranges asymptotically between $-\frac{\pi}{2}$ for $z=-\infty$ and $\frac{\pi}{2}$ for $z=\infty$. The effect of this term can be seen when combining the complex phase amplitude with the z-propagating plane wave as in Eq. 2.65 and looking at the propagation axis ($r=0$). The total phase of the beam is then given by

$$\delta = kz - \vartheta \tag{2.75}$$

which indicates a retardation in the wavefront in comparison to that of the plane wave (kz) [84]. Accordingly, a collective retardation of π is incurred over a propagation distance spanning from negative to positive infinity.

The optical intensity distribution, $I(r,z)$ for the solution may also be obtained from the complex amplitude (Eq. 2.65) through the standard relation, $I(r,z) = |a(r,z)|^2$ [91] where the intensity is subsequently functions of the propagation position (z) as well as the transverse radial coordinate (r). Application of the relation to the Gaussian beam yields the intensity distribution in Eq. 2.76 [91].

$$\begin{aligned} I(r,z) &= |\frac{w_0}{w}e^{\frac{-r^2}{w^2}}e^{\frac{-ikr^2}{2R}}e^{-i\vartheta}|^2 \\ &= (\frac{w_0}{w}e^{\frac{-r^2}{w^2}})^2(e^{\frac{-ikr^2}{2R}}e^{-i\vartheta})(e^{\frac{ikr^2}{2R}}e^{i\vartheta}) \\ &= (\frac{w_0}{w})^2 e^{\frac{-2r^2}{w^2}} \end{aligned} \tag{2.76}$$

Figure 2.8 depicts the Gaussian beam intensity as determined by Eq. 2.76. It can be seen that the intensity distribution has a distinctly Gaussian profile which may be attributed to the exponential term in the equation. As such, a Gaussian profile will always result for any axial distance, elucidating the given appellation as Gaussian. It follows that peak intensity occurs at the center of the beam $I(0,0)$ before decreasing monotonically with outwards radial direction $(r\rightarrow\infty)$. This is clearly depicted in Fig. 2.8 (a) with the 3D plot and indicated in the transverse density plot (Fig. 2.8 (b)) through the variation in color from light (at the center) to dark (radially outward). Figure 2.8 (b) is a customary plot used to illustrate intensity distributions of structured light and as such is included for comparison and familiarity.

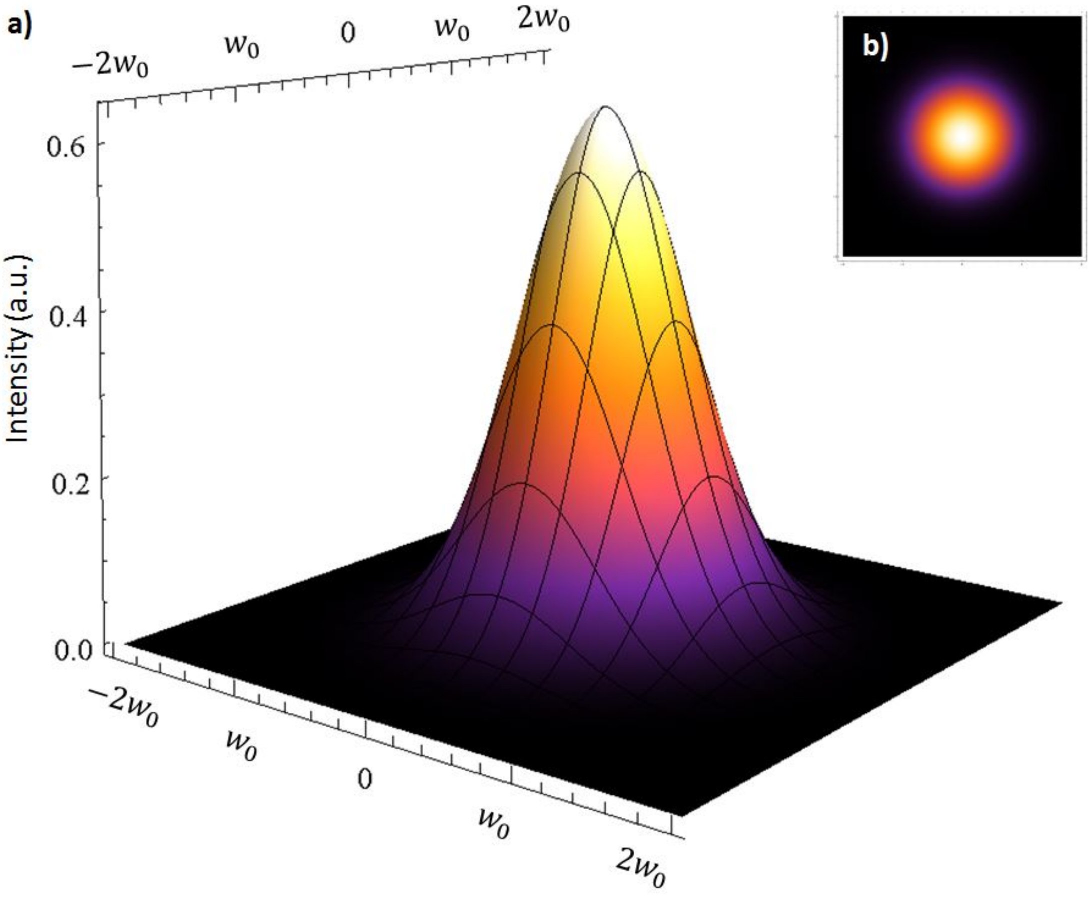

FIGURE 2.8: A (a) 3D plot and (b) transverse density profile of a Gaussian beam intensity distribution at the beam waist $(z = 0)$.

Laguerre-Gaussian beams

When converting and solving for the paraxial Helmholtz equation in cylindrical coordinates (r, ϕ, z) through the separation of variables, another set of solutions are obtained, denoted Laguerre-Gaussian (LG) beams [92]. These beams form a significant part of experimentation carried out in this work and as such require exploration. The resulting complex amplitude is [92]

$$a(r,\phi,z) = \sqrt{\frac{2p!}{w^2\pi(p+|l|)!}}\left(\frac{r\sqrt{2}}{w}\right)^{|l|} L_p^{|l|}\left(\frac{2r^2}{w^2}\right) e^{\frac{-r^2}{w^2}} e^{-il\phi} e^{\frac{-ikr^2}{2R}} e^{-i\vartheta_{p,l}} \tag{2.77}$$

where r retains the previous definition, ϕ is the azimuthal angle and $L_p^{|l|}(x) = (x^{-|l|}\frac{e^x}{p!})(\frac{d}{dx})^p(x^{|l|+p}e^{-x})$ is the generalized Laguerre polynomial of orders $p \geq 0 \in \mathbb{Z}, l \in \mathbb{Z}$. Comparison with the Gaussian solution (Eq. 2.70) reveals common terms such as the beam width, w and radius of curvature, R which retain their definitions (Eq. 2.71 to 2.73). A modification to the Gouy phase $\vartheta_{p,l}$ occurs, however, for LG solutions where an additional dependence arises on the indices l, p as given by [92]

$$\vartheta = (2p + l + 1)\tan^{-1}\left(\frac{z}{z_R}\right) \tag{2.78}$$

Motivation for the previous description as higher order Gaussian modes may be found for the primary order $(p = 0 = l)$ where the Laguerre polynomial equates to one and the expression simplifies to the Gaussian mode (Eq. 2.70). The subsequent appellation Laguerre-Gaussian derives from the combination of Gaussian terms and the Laguerre polynomial.

Optical intensities related to these modes were obtained through the same method outlined for the Gaussian case and is

$$I(r,z) = \frac{2p!}{w^2\pi(p+|l|)!}\left(\frac{r\sqrt{2}}{w}\right)^{2|l|}\left[L_p^{|l|}\left(\frac{2r^2}{w^2}\right)\right]^2 e^{\frac{-2r^2}{w^2}} \tag{2.79}$$

Analysis of the different intensity distributions associated with the indices l, p allows selected interpretation in terms of their effects. Consequently, a series of 3D profiles with transverse density plot insets are illustrated in Fig 2.9. Based on the coordinate space and cylindrical variable dependency, these beams possess circular symmetry as may be observed in the series of plots in Fig. 2.9. The p-index defines the number of radial nulls in intensity, resulting in $p + 1$ concentric rings occurring in the distribution [93]. For example, in the case of $[l, p] = [0, 2]$ (top right), two dark rings are present inside the intensity distribution, indicating intensity nulls; hence, three intensity rings result corresponding to the $p + 1 = 3$. As a result this is often referred to as the radial index. When $[l, p] = [0, 0]$, it is clearly evident from the uppermost plot that the distribution reduces to the Gaussian case as previously noted. This indicates that the l, p indices are responsible for modulating a Gaussian intensity distribution and as such LG beams are defined in terms of these indices. Considering the l-index, a non-zero value can be observed to result in a central null $(r = 0)$ in intensity. This null may be linked to the $(\frac{r\sqrt{2}}{w})^{2|l|}$ term in Equation 2.79 where the l-value is modulating the Gaussian intensity distribution (Laguerre polynomial is one when $p = 0$).

Further observation of the size of these modes upon modulation by these indices, indicates a clear deviation from that of the Gaussian case where introduction of non-zero l and p values cause the beam size to increase with an increase in either of these values. Analysis of this effect was carried out by R. Phillips and L. Andrews in their 1983 [94] paper, resulting in the derivation of an equation allowing the beam size to be related to that of the Gaussian case and thus calculated from it. This relation was given as

$$w_{LG} = [\sqrt{2p + l + 1}]w \tag{2.80}$$

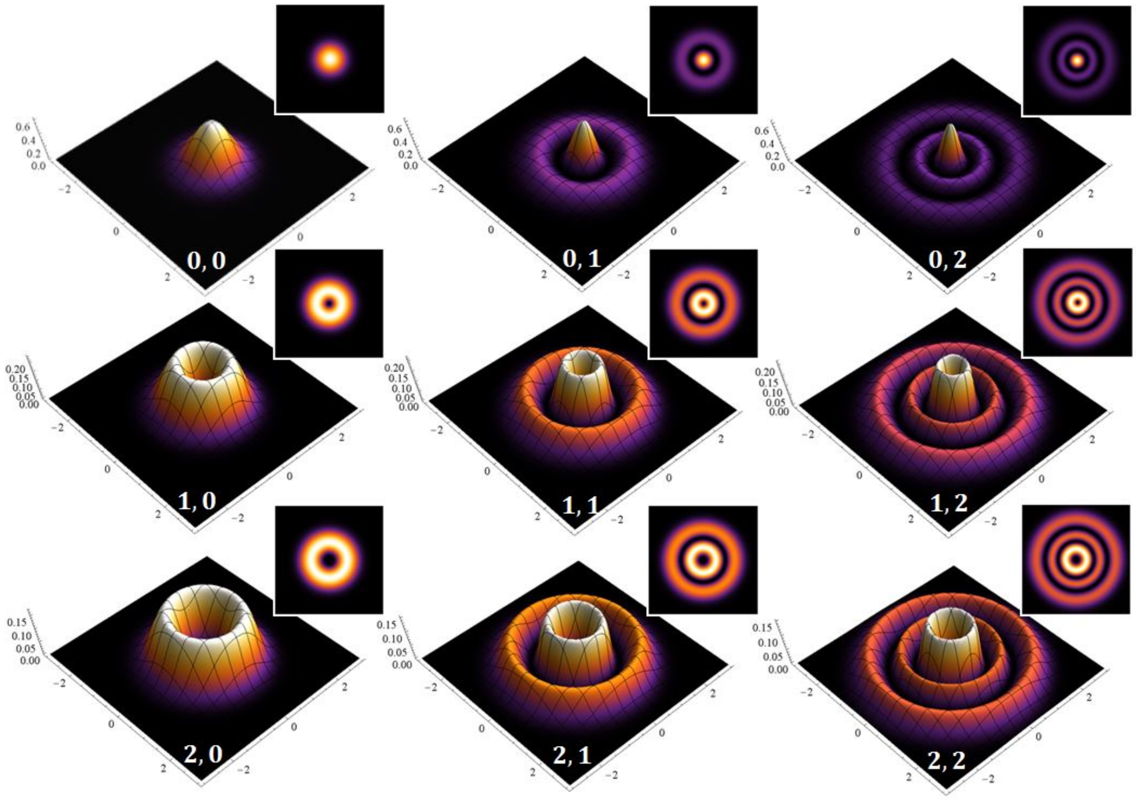

FIGURE 2.9: 3D intensity distributions of selected $LG_{l,p}$ beams for $l = [0, 2]$ and $p = [0, 2]$ (indicated in bold white) at the beam waist $(z = 0)$. Transverse density plot insets to the upper right corner are included for comparison.

where w refers to the Gaussian beam width in Eq. 2.72.

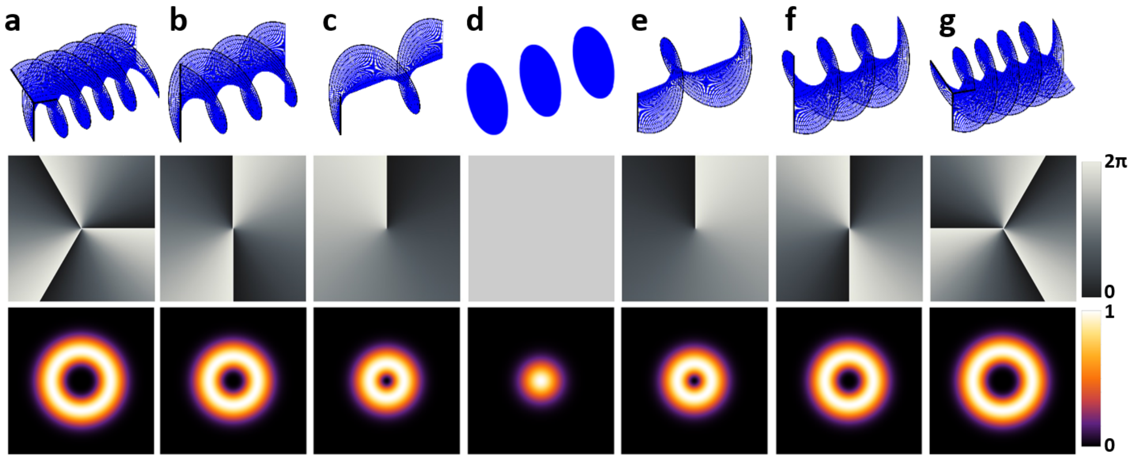

FIGURE 2.10: Illustration of the 3D wavefront (top row), transverse phase variation (middle row) and intensity distribution (bottom row) for $l = [-3, 3]$ from (a)-(g).

Returning to the LG complex amplitude, an additional term, $e^{il\phi}$ has not been reviewed which carries significant influence in the beam physics. This term introduces an azimuthal dependence to the phase as it propagates which is influenced by l. It results in an azimuthal rotation of the wavefront where the number of rotations per wavelength or wavefront spirals is related to the absolute value of the index [93]. This is often referred to as a helical twisting along the direction of propagation, resembling that of a corkscrew. The index sign impacts the handedness where a positive l is associated with clockwise rotation and negative l with anti-clockwise. Figure 2.10 illustrates the phase variation across the wavefront (middle) along with a 3D rendering along the propagation axis (top) and the associated transverse intensity profile (bottom).

This spiral form of the wavefront is linked to well-defined orbital angular momentum (OAM) carried by the beam in the paraxial regime such that it contains an OAM of $l\hbar$ per photon [95]. Discussion of this interpretation as OAM is deferred to the next section (2.3.3), however. It may additionally be seen from the images that the azimuthal phase variation results in a phase singularity at the central axis $(r = 0)$ which is then expressed as null intensity.

2.3.3 Orbital Angular Momentum

Following the discovery that light was composed of oscillating electromagnetic fields, came the deduction that it must indeed transport energy, which is of little surprise when considering the effects of standing in the sun too long. Analytical evidence of this was derived by Poynting in the form of the Poynting vector [83],

$$\mathbf{S} = \frac{1}{\mu_0}(\mathbf{E} \times \mathbf{B}). \tag{2.81}$$

Here $\mathbf{S}$ may be also considered the energy flux density and yields the energy per unit time per area [82]. The important aspect of this vector is that it indicates the direction of energy flow. It follows that light exerts pressure and thus carries a linear momentum whereby the linear momentum density $(\mathbf{L})$ is related to the Poynting vector through [83]

$$\mathbf{L} = \epsilon_0 \mu_0 \mathbf{S}. \tag{2.82}$$

Interpretation of the momentum of light with a helical wavefront as described by the azimuthal phase term ($e^{il\phi}$) referred to in the previous section lies in the determination of the angular momentum along the propagation axis (z). This quantity is established by the relation for angular momentum density [83; 85],

$$\mathbf{j_z} = (\mathbf{r} \times \mathbf{L}_\phi) = \epsilon_0 \mathbf{r} \times (\mathbf{E} \times \mathbf{B})_\phi \tag{2.83}$$

where the cross product is taken between the radial vector and the azimuthal component of linear momentum (Eq. 2.82).

Mathematical evaluation of this in terms of paraxial beams may be simplified through application of the Lorentz Gauge as indicated in the original derivation by Allen et. al. [95] and followed by others [85; 87; 96] where

$$\nabla \cdot \mathbf{A} = \epsilon_0 \mu_0 \frac{\partial}{\partial t} V \tag{2.84a}$$

$$\Rightarrow \nabla^2 \mathbf{A} = \epsilon_0 \mu_0 \frac{\partial^2}{\partial t^2} \mathbf{A} \tag{2.84b}$$

in free space with V being the electric potential [83]. Similarly, elimination of the spin angular momentum component (linear polarization) affords further simplicity such that the associated vector potential may be represented as [87]

$$\mathbf{A} = u(x, y, z) e^{i(kz - \omega t)} \hat{\mathbf{x}} \tag{2.85}$$

such that $u(x, y, z) = u$ is the complex amplitude satisfying the paraxial wave equation for a field linearly polarized in the x-direction. Utilizing the relation, $\mathbf{B} = \nabla \times \mathbf{A}$, and applying the paraxial condition $\frac{\partial u}{\partial z} \rightarrow 0$ as $\frac{\partial u}{\partial z} << ku$ results in the magnetic field

$$\mathbf{B} = ik[u\hat{\mathbf{y}} - \frac{1}{ik}\frac{\partial u}{\partial y}\hat{\mathbf{z}}]e^{i(kz-\omega t)} \tag{2.86}$$

Further manipulation of the relation in Eq. 2.52 as detailed below allows a relation between the electric and magnetic field to be established

$$\begin{aligned}
&\nabla \times \mathbf{B} = \frac{1}{c^2}\frac{\partial \mathbf{E}}{\partial t} \\
&\Rightarrow \nabla \times \int \mathbf{B} \partial t = \frac{1}{c^2} \int d\mathbf{E} \\
&\Rightarrow \mathbf{E} = c^2 ik \nabla \times [u\hat{\mathbf{y}} - \frac{1}{ik}\frac{\partial u}{\partial y}\hat{\mathbf{z}}]e^{ikz} \int e^{-i\omega t} dt \\
&= c^2 ik \frac{i}{\omega} \nabla \times [u\hat{\mathbf{y}} - \frac{1}{ik}\frac{\partial u}{\partial y}\hat{\mathbf{z}}]e^{i(kz-\omega t)} \\
&= \frac{ic^2}{\omega} \nabla \times \mathbf{B}
\end{aligned} \tag{2.87}$$

Substitution of Eq. 2.86 into 2.87 and application of the paraxial condition whereby second derivatives, first product derivatives as well as $\frac{\partial u}{\partial z}$ are taken to be zero [95], then yields the electric field expression,

$$\mathbf{E} = i\omega[u\hat{\mathbf{x}} - \frac{1}{ik}\frac{\partial u}{\partial x}\hat{\mathbf{z}}]e^{i(kz-\omega t)} \tag{2.88}$$

Due to the fast oscillation of EM waves, interest lies in the real time-averaged aspect of the Poynting vector, $\langle \mathbf{S} \rangle_\mathcal{R}$ where the associated electric and magnetic fields may be expressed as $\langle \mathbf{E} \rangle_\mathcal{R} = \frac{1}{2}(\mathbf{E} + \mathbf{E}^*)$ and $\langle \mathbf{B} \rangle_\mathcal{R} = \frac{1}{2}(\mathbf{B} + \mathbf{B}^*)$ respectively [87] where $*$ denotes the complex conjugate such that

$$\langle \mathbf{S} \rangle_{\mathcal{R}} = \frac{1}{2\mu_0}[(\mathbf{E}\times\mathbf{B}^*) + (\mathbf{E}^*\times\mathbf{B})] \tag{2.89}$$

Substitution of Eq. 2.86 and 2.88 into 2.89, then yields

$$\begin{aligned}\langle \mathbf{S} \rangle_{\mathcal{R}} &= \frac{1}{2\mu_0}[(-\frac{i}{k}u^*\frac{\partial u}{\partial x}\hat{\mathbf{x}} + \frac{i}{k}u\frac{\partial u^*}{\partial y}\hat{\mathbf{y}} + u^*u\hat{\mathbf{z}})\omega k + (\frac{i}{k}u\frac{\partial u^*}{\partial x}\hat{\mathbf{x}} - \frac{i}{k}u^*\frac{\partial u}{\partial y}\hat{\mathbf{y}} + u^*u\hat{\mathbf{z}})\omega k] \\ &= \frac{\omega}{2\mu_0}[iu(\frac{\partial u^*}{\partial x}\hat{\mathbf{x}} + \frac{\partial u^*}{\partial y}\hat{\mathbf{y}}) - iu^*(\frac{\partial u}{\partial x}\hat{\mathbf{x}} + \frac{\partial u}{\partial y}\hat{\mathbf{y}}) + 2k|u|^2\hat{\mathbf{z}} \\ &= \frac{\omega}{2\mu_0}[iu\nabla u^* - iu^*\nabla u + 2k|u|^2\hat{\mathbf{z}}] \end{aligned} \tag{2.90}$$

where the dell operator is confined to two-dimensions i.e. $\nabla = \frac{\partial}{\partial x}\hat{\mathbf{x}} + \frac{\partial}{\partial y}\hat{\mathbf{y}}$.It follows that the general expression for the subsequent linear momentum density is given by

$$\mathbf{L} = \epsilon_0\mu_0\langle \mathbf{S} \rangle_{\mathcal{R}} = \frac{\epsilon_0\omega}{2}[iu\nabla u^* - iu^*\nabla u + 2k|u|^2\hat{\mathbf{z}}] \tag{2.91}$$

from which the angular momentum may be calculated for a chosen linearly polarized field conforming to the paraxial approximation. Subsequently, in the case of beams with azimuthal phase variations such as the Laguerre-Gaussian beams, one may assume a general field of the form

$$u(r,\phi,z) = u_0(r,z)e^{il\phi} \tag{2.92}$$

for a complex amplitude obeying the paraxial approximation. One may then convert Eq. 2.91 to cylindrical coordinates ($\nabla = \frac{\partial}{\partial r}\hat{\mathbf{r}} + \frac{1}{r}\frac{\partial}{\partial \phi}\hat{\phi}$) for convenience. The resultant linear momentum density components by substituting Eq. 2.92 into 2.91 may easily be shown as

$$\mathbf{L}_r = 0\hat{\mathbf{r}} \tag{2.93a}$$

$$\mathbf{L}_z = \epsilon_0\omega k|u_0(r,z)|^2\hat{\mathbf{z}} \tag{2.93b}$$

$$\mathbf{L}_\phi = \frac{\epsilon_0\omega l}{r}|u_0(r,z)|^2\hat{\phi} \tag{2.93c}$$

It may be noted that the radial term (Eq. 2.93 (a) indicates the beam divergence during propagation and is zero here as a result of the analysis in terms of a non-diffracting beam. A diffracting beam however, elicits a non-zero value which may be found in several references including [95; 96] for interest. The z-term yields the linear momentum in the direction of propagation which leaves the azimuthal term for determination of the angular momentum.

Considering angular momentum density in Eq. 2.83 for the beam axis, Eq. 2.93 (c) must be substituted in to yield

$$\mathbf{j_z} = (r\hat{\mathbf{r}}\times\hat{\phi})\frac{\epsilon_0\omega l}{r}|u_0(r,z)|^2 = \epsilon_0\omega l|u_0(r,z)|^2\hat{\mathbf{z}} \tag{2.94}$$

along the propagation axis. Due to the linear polarization condition, no spin angular momentum is present, implying Eq. 2.94 reflects the orbital angular momentum (OAM) density. The derivation may be extended to where spin angular momentum is included as in reference [97]. This simply results in an additional term appearing for this component, accounting for the additional angular momentum.

Continuing with OAM, interpretation of l lies in taking the ratio of the beam energy density ($\varepsilon = cxL_z = \epsilon_0\omega^2|u_0(r,z)|^2$) to that of the OAM density (Eq. 2.94) and integrating over all space, resulting in the relation [85]

$$\frac{j_z}{\varepsilon} = \frac{\iint \epsilon_0 \omega l |u_0(r,z)|^2 r dr d\phi}{\iint \epsilon_0 \omega^2 |u_0(r,z)|^2 r dr d\phi} = \frac{\epsilon_0 \omega l \iint |u_0(r,z)|^2 r dr d\phi}{\epsilon_0 \omega^2 \iint |u_0(r,z)|^2 r dr d\phi} = \frac{l}{\omega} \tag{2.95}$$

Equation 2.95 represents the angular momentum to energy ration per unit length. Now taking the ratio of angular to linear momentum yields

$$\frac{angular}{linear} = \frac{\omega l}{\omega k} = \frac{l\lambda}{2\pi} \tag{2.96}$$

This indicates possession of OAM proportional to l per photon for the beam, which upon full evaluation yields a total OAM of $l\hbar$ per photon [85]. Therefore, the integer l describes a well-defined OAM carried by the paraxial beam which is proportional to its value and features the azimuthal phase dependence as the source of the OAM contained by the beam.

2.3.4 Polarization and vector beams

Polarization has been established and thoroughly researched for many decades, but has regained popularity in view of its angular momentum interpretation along with the discovery that light with helical wavefronts carry OAM. More specifically, Poynting [98] predicted that the polarization of light can be associated with spin angular momentum (SAM). This was secured experimentally in 1936 by Beth [99] where circularly polarized light transferred SAM to a quarter-wave plate. It has subsequently been well known that paraxial beams with circular polarization carry spin angular momentum of $\pm\hbar$ (as alluded to in the previous section) where the handedness of the circular polarization determines the sign.

The new interest regarding polarization lies in the establishment of vector beams whereby the OAM and SAM are paired and combined in a non-separable manner. Due to certain aspects of these beams, like smaller beam sizes when focused, they offer applications in particle manipulation [100], particle acceleration [101], microscopy [102] and quantum information [103], amongst others, which offers promising advances in many research avenues.

Polarization

Polarization refers to the directionality of the electric field oscillation as light propagates [84]. Consequently, in the paraxial regime, it is mathematically described by the transverse electric field vectors of a wave in some orthogonal basis such as Cartesian coordinates [84; 93]. Extension of the wave expression introduced in Eq. 2.65 yields a complex form of the electric field vectors that results in the light beams being utilized. This is given in Eq. 2.97 for a plane wave propagating in the z-direction.

$$E(x,y,z,t) = (\alpha E(x,y,z)_x e^{i\varphi_x}\hat{\mathbf{x}} + \beta E(x,y,z)_y e^{i\varphi_y}\hat{\mathbf{y}})e^{i(\omega t - kz)} \tag{2.97}$$

Here $E(x,y,z)_x$ is the complex amplitude associated with the electric field oscillating in the x-direction with weighting α and $E(x,y,z)_y$ the complex amplitude associated with the electric field oscillating in the y-direction with weighting $\beta = 1-\alpha$. The respective phases, φ_x and φ_y, of each component affect the oscillation direction of the net electric field vector and as such determine the polarization state of the beam along with the amplitudes. It follows that it is the relative phase which determines the net electric field vector and as such the equation may be modified to the following form

$$E(x,y,z,t) = (\alpha E(x,y,z)_x \hat{\mathbf{x}} + \beta E(x,y,z)_y e^{i\varphi}\hat{\mathbf{y}})e^{i(\omega t - kz)} \tag{2.98}$$

TABLE 2.1: Principal polarization states with associated parameters illustrating different types of polarization states.

Polarization	Amplitude	Phase (φ)	Polarization
Horizontal	$E_y = 0$	0	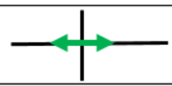
Vertical	$E_x = 0$	0	
Diagonal	$E_x = E_y$	0	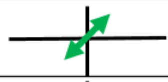
Antidiagonal	$E_x = E_y$	π	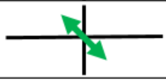
Right Ellipse	$E_x = E_y$	$\frac{\pi}{4}$	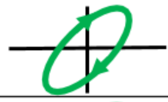
Left Ellipse	$E_x = E_y$	$-\frac{\pi}{4}$	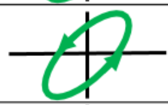
Right Circular	$E_x = E_y$	$\frac{\pi}{2}$	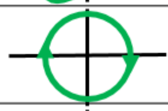
Left Circular	$E_x = E_y$	$-\frac{\pi}{2}$	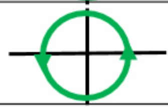

where $\varphi = \varphi_y - \varphi_x$ and $e^{i\varphi_x}$ is taken out as an unimportant global phase. Polarization states may be classified into to the categories of linear, elliptical and circular polarizations [84]. Linear polarization occurs when the oscillation of the electric field is confined to a specific plane along the axis of propagation where the angle of the plane from the x-axis denotes the polarization [84]. Elliptical and circular polarization refers to a rotation of the electric field oscillation about the propagation axis. In the case of elliptical polarization, the rotation follows an elliptical pattern determined by amplitude ratio and phase, while a circular pattern is followed for circular polarizations [84]. Illustration of principal polarization states with the associated parameters are given in Table. 2.1 where $\beta = \alpha$. Further consideration of the states will be confined to the case of $\beta = \alpha$ for clarity until noted otherwise in the next section.

As may be seen, linear polarization is achieved when the relative phases are the same (i.e. the orthogonal components are in phase) or directly out of phase (a phase difference of π). Circular polarization, however, requires a phase difference of $\pi/2$ for right circular and $-\pi/2$ for left circular polarization. Elliptical polarization results from any other variation across the range in which right-handed ellipticity applies to a positive phase difference and left-handed ellipticity to a negative phase difference [93].

Jones matrices and the Poincaré sphere

Equation 2.97 can be awkward to work with when considering polarization transformations through modification of the parameters by elements such as waveplates. In 1941, R.C. Jones simplified this issue with the development of a new formalism, known as Jones Matrices or Jones Calculus [104]. As suggested by the name, Jones utilized matrices to express the orthogonal components of the

TABLE 2.2: Jones matrices for the polarization states discussed in Table 2.1.

Polarization	Jones Matrix	Normalized Matrix	Polarization
Horizontal	$\begin{bmatrix} E_x \\ 0 \end{bmatrix}$	$\begin{bmatrix} 1 \\ 0 \end{bmatrix}$	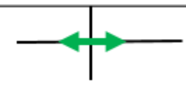
Vertical	$\begin{bmatrix} 0 \\ E_y \end{bmatrix}$	$\begin{bmatrix} 0 \\ 1 \end{bmatrix}$	
Diagonal (45°)	$\begin{bmatrix} E_x \\ E_x \end{bmatrix}$	$\frac{1}{\sqrt{2}}\begin{bmatrix} 1 \\ 1 \end{bmatrix}$	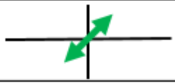
Antidiagonal (-45°)	$\begin{bmatrix} E_x \\ E_x e^{i\pi} \end{bmatrix}$	$\frac{1}{\sqrt{2}}\begin{bmatrix} 1 \\ -1 \end{bmatrix}$	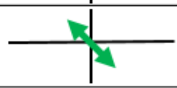
Right Ellipse	$\begin{bmatrix} E_x \\ E_x e^{i\pi/4} \end{bmatrix}$	$\frac{1}{\sqrt{2}}\begin{bmatrix} 1 \\ e^{i\pi/4} \end{bmatrix}$	
Left Ellipse	$\begin{bmatrix} E_x \\ E_x e^{-i\pi/4} \end{bmatrix}$	$\frac{1}{\sqrt{2}}\begin{bmatrix} 1 \\ e^{-i\pi/4} \end{bmatrix}$	
Right Circular	$\begin{bmatrix} E_x \\ E_x e^{i\pi/2} \end{bmatrix}$	$\frac{1}{\sqrt{2}}\begin{bmatrix} 1 \\ i \end{bmatrix}$	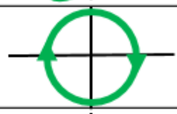
Left Circular	$\begin{bmatrix} E_x \\ E_x e^{-i\pi/2} \end{bmatrix}$	$\frac{1}{\sqrt{2}}\begin{bmatrix} 1 \\ -i \end{bmatrix}$	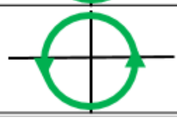

electric field in a format that is easy to manipulate. This is shown in Eq. 2.99 for Eq. 2.98,

$$E(x, y, z) = \begin{bmatrix} E(x, y, z)_x \\ E(x, y, z)_y e^{i\varphi} \end{bmatrix}, \tag{2.99}$$

such that a vector matrix yields the polarization state of the beam. Jones matrices are commonly normalized for simplicity which result in the well-known matrices given in Table 2.2 for the polarization states listed in Table 2.1.

Operation of elements that alter the polarization state of the beam is then easily achieved through a matrix multiplication of the element Jones matrix with the Jones polarization state vector [84]. The output then reveals the new state vector. The Jones matrices of these optical elements subsequently constitute a 4x4 matrix describing the action of the element on all possible input polarization states. Investigation into such matrices and the physics of operation shall be deferred to Chapter 3 however, where it may be explored in greater detail.

Revisiting the various polarization states, it is possible to utilize the Bloch sphere introduced in Section 2.1 to visually represent every possible polarization state. This polarization sphere is known as a Poincaré sphere in honour of Poincaré's suggestion to do so in 1892 [105]. Equivalently, each point on the sphere surface represents a unique polarization state and all the points collectively form all possible coherent polarization states. Furthermore, it is possible to use the sphere to represent partially polarized states by considering points inside [106], but this shall not form part of the reviewed theory here. Specification of each state additionally occurs from the use of the familiar polar, χ and azimuthal, Φ angles as illustrated in Figure 2.11 (a). Here the sphere has been rotated to favor the circular polarization states for reasons that will become clear further on. The amplitude weightings consequently play a large role here where the weightings may be determined by the functions $\alpha = \cos\chi$ and $\beta = \sin\chi$. It follows that the Jones state vector

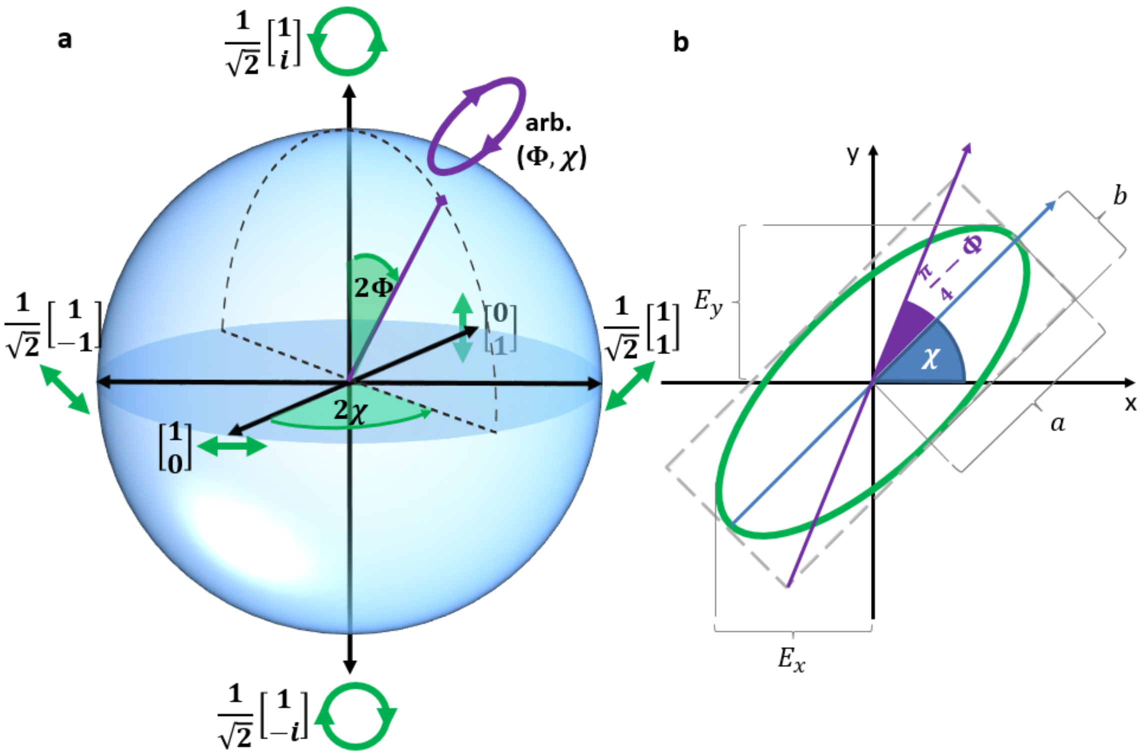

FIGURE 2.11: Illustration of (a) the Poincaré sphere and (b) the associated elliptical parameters that specify the polarization states on the sphere.

described by the angles is

$$Polarization = \begin{bmatrix} \cos\chi \\ e^{i(\pi/2-2\Phi)}\sin\chi \end{bmatrix}, \tag{2.100}$$

as was determined by the relation specified in Eq. 2.15, with the bases rotated, where $-\pi/2 \leq 2\Phi \leq 3\pi/2$ and $0 \leq 2\chi \leq \pi$. The Poincaré sphere in Fig. 2.11 (a) depicts the six cardinal states used to demonstrate the different forms of polarization with the associated Jones vectors. Here circular polarization is situated on the north and south poles with linear polarizations occurring along the equator. It follows that varying degrees of elliptical polarization are represented by the surfaces between the poles and equator. Clarification on how polarization transitions across the sphere may be achieved through consideration of the elliptical parameters associated with polarization, as depicted in Fig. 2.11 (b), along with how the associated angles correlate to Eq. 2.100. Angle χ represents the orientation of the ellipse semi-major axis (as illustrated by the blue line); $\pi/4 - \Phi$ then represents the ellipticity (purple line) which is the ratio of the semi-major (a) and -minor (b) axes as indicated in Eq. 2.101 [93].

$$Ellipticity = \frac{b}{a} = \tan(\pi/4 - \Phi) \tag{2.101}$$

It may subsequently be shown that the amplitude and phase difference between the x- and y-components of the electric field relate to the Poincaré sphere representation through Eqs. 2.102 and 2.103 [84].

$$\tan(2\chi) = \frac{2r}{1-r^2}\cos(\varphi) \tag{2.102}$$

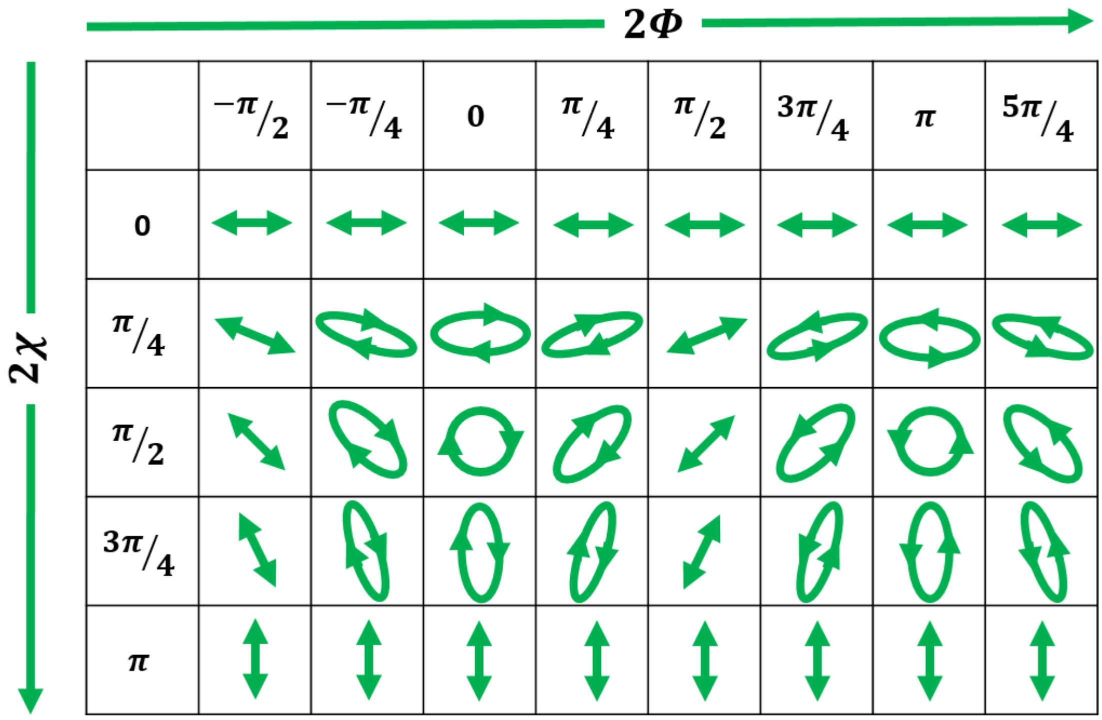

FIGURE 2.12: Evolution of polarization states across the Poincaré sphere surface.

$$\sin\left(\pi/2 - 2\Phi\right) = \frac{2r}{1+r^2}\sin\left(\varphi\right) \tag{2.103}$$

with $r = \frac{E_y}{E_x}$. Substituting in the range of angles describing points in the Poincaré sphere into the associated Jones matrix (Eq. 2.100), yields the evolution of these states across the surface. This is presented in Fig. 2.12.

Accordingly, it can be seen that all the antipodal states on the sphere are orthogonally orientated which may be confirmed through inspection of any two states π-apart in Fig. 2.12. The major states outlined in Fig. 2.11 (a) form the axes of the sphere and as such enlighten the analysis of this polarization state representation by considering the evolution across respective hemispheres for these orthogonal axial pairs. For example, the diagonal and anti-diagonal polarizations form an orthogonal axial pair with their respective hemispheres being centered on the state. The circle outlined by all the other axial states then form the hemispherical boundary where the effects of the hemispherical opposing states are equally weighted. Additionally, the rows in Fig. 2.12 indicate longitudinal trends across the sphere due to χ remaining constant while the columns reveal latitudinal trends as a result of Φ being constant.

It follows that the ellipsoid semi-major axis (or linear polarization orientation) changes directionality as you traverse the longitudinal lines across the sphere with a horizontal to vertical evolution as indicated by the axial polarizations and along the columns in Fig 2.12. A ± 45-degree orientation then results for all states along the line bounding the respective hemispheres with exception to the two polar states. The slope of the semi-major axis is determined by the position with respect to the diagonal and anti-diagonal hemispheres where a positive slope occurs in the diagonal hemisphere and a negative slope in the anti-diagonal hemisphere. The boundary states then naturally maintain either a horizontal or vertical extreme based on which respective hemisphere the states occur. The trend across the circular polarization hemispheres are related to the ellipticity of the state. Here the ellipticity decreases from the poles to the equator. As such, the ellipticity changes from 1 at both the left and right circular poles ($b = a$) before decreasing to 0

($b = 0$) along the bounding equator where the effects of the two states equate resulting in linear polarizations.

Due to orthogonality of the antipodal states, it is possible to express polarization in terms of other bases such as circular polarization where the following mapping relation applies [92]:

$$|H\rangle = \frac{1}{\sqrt{2}}[|L\rangle + |R\rangle] \tag{2.104}$$

$$|V\rangle = \frac{i}{\sqrt{2}}[|L\rangle - |R\rangle] \tag{2.105}$$

where $|H\rangle$, $|V\rangle$ respectively represent horizontal and vertical polarization in Dirac notation. Likewise, $|R\rangle$, $|L\rangle$ respectively describe the right and left circular polarizations. Consequently, with minor modifications to the Poincaré sphere configuration angles, a new general Jones state vector may be derived with the change in basis [93]. For the above Poincaré sphere configuration, it is simply the case of changing the angle definitions where Φ now becomes the polar angle and χ the azimuthal angle such that $0 \leq 2\Phi \geq \pi$ and $0 \leq 2\chi \geq 2\pi$. Subsequently, the Jones state vector for the Poincaré sphere in terms of left and right circular polarization is given by Eq. 2.106. Here the top index refers to right circular polarization basis and the bottom to left circular polarization basis.

$$Polarization = \begin{bmatrix} \cos\Phi \\ e^{i2\chi}\sin\Phi \end{bmatrix}, \tag{2.106}$$

Vector beams

The beams described and categorized on the Poincaré sphere in the previous section are known as scalar beams where the complex amplitudes, $E(x, y, z)_x$ and $E(x, y, z)_y$ were either equivalent or one was null. As the spatial distribution of the beams are determined by the complex amplitudes in the expression (Eq. 2.79), it follows that the spatial and polarization distributions are independent of the other and thus result in beams with a polarization distribution that is homogeneous across the associated spatial distribution [92; 107]. Mathematically, this is correlated to being able to factor the complex amplitude out. For example, consider the Laguerre-Gaussian beams (Eq. 2.77) introduced in Section 2.3.2, denoted $LG_{p,l}$ here, as the complex amplitude in the equation (with the time dependence removed) where $E_x = E_y$:

$$\begin{aligned} \mathbf{E}(x,y,z) &= \frac{1}{\sqrt{2}}(LG_{0,1}\hat{\mathbf{R}} + e^{i\varphi}LG_{0,1}\hat{\mathbf{L}}) \\ \Rightarrow \mathbf{E}(x,y,z) &= LG_{0,1}\frac{1}{\sqrt{2}}(\hat{\mathbf{R}} + e^{i\varphi}\hat{\mathbf{L}}) \end{aligned} \tag{2.107}$$

Here the basis has been changed, however, from transverse to circular (with right, $\hat{\mathbf{R}}$ and left, $\hat{\mathbf{L}}$ circular polarization) for convenience due to the circular symmetry associated with LG beams. It can thus be seen from Eq. 2.107' that the amplitude and polarization are separable, resulting in the above equation falling under the solutions of the scalar Helmholtz equation and ensuing the appellation scalar beams [85].

Conversely, considering the vector Helmholtz equation [107],

$$\nabla \times \nabla \times \mathbf{E} - k^2\mathbf{E} = 0$$

where the symbols have the usual meanings, it is possible to derive more intricate solutions. Certain solutions belong to the extended category of beams that has generated much interest recently, known as vector beams. They are characterized by a spatially inhomogeneous polarization distribution across the beam cross-section [85; 93]. One such example are Bessel-Gauss beams, derived with the paraxial approximation under the condition of azimuthal polarization symmetry [85]:

$$BG(r,z) = AJ_1(\frac{\beta r}{1+iz/z_R})e^{\frac{-i\beta^2 x}{2k(1+iz/z_R)}}a(r,z) \tag{2.108}$$

with the electric field orientated in the azimuthal direction i.e. $E(r,z,t) = BG(r,z)e^{i(\omega t - kz)}\hat{\phi}$. A is a normalization term, $a(r,z)$ the Gaussian amplitude (Eq. 2.70), J_1 is the 1st order Bessel function, β a constant scale factor and the other symbols have the usual meanings. Considering the beam waist where β is minute, the Bessel-Gauss beam becomes approximately [85]: approximation under the condition of azimuthal polarization symmetry [85]:

$$E = Are^{\frac{-r^2}{w^2}}\hat{\phi} \tag{2.109}$$

which can be viewed as a combination of the $LG_{0,1}$ and $LG_{0,-1}$ at the waist whereby the azimuthal phase term (or OAM) is negated [108].

It follows that the solution illustrated above can then be related to the notation of Eq. 2.107 whereby the complex amplitudes are unrelated (i.e. not equivalent or multiples of the other) and neither is null. This is exemplified below for the same case described in Eq. 2.107, but an additional LG mode being associated with the other polarization basis state.

$$\mathbf{E}(x,y,z) = \frac{1}{\sqrt{2}}(LG_{0,1}\hat{\mathbf{R}} - LG_{0,-1}\hat{\mathbf{L}}) \tag{2.110}$$

Here it is clear that the amplitude can no longer be factored out, thus making the spatial and polarization components inseparable. It follows that the orientation of each electric field oscillation across the beam depends on the location of observation (i.e. the point along the beam wavefront) [108]. Based on the discussion of entanglement in Section 2.2, a parallel may be drawn for vector beams due to their non-separability and as such these beams possess the same implications of entanglement. More specifically, they fall under the category of 'classical entanglement' with the associated properties applying [77].

Illustrations of these spatial and polarization relations are depicted in Fig. 2.7.

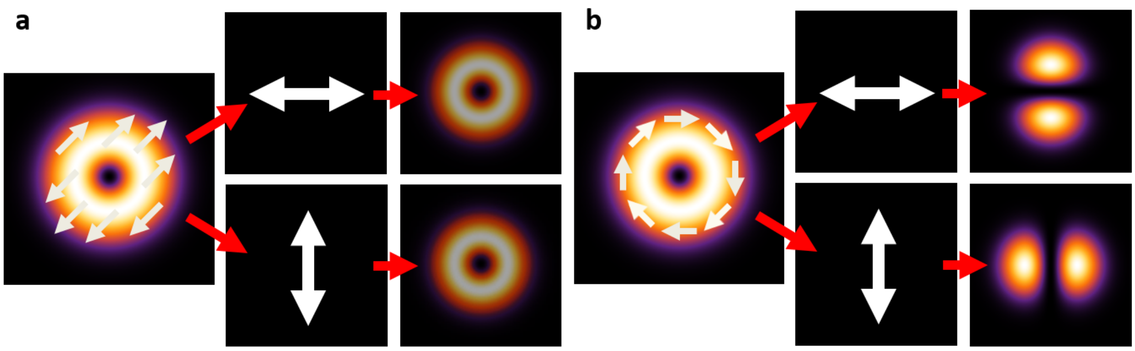

FIGURE 2.13: Examples of a (a) scalar (Eq. 2.107) and (b) azimuthal vector (Eq. 2.110) beam with uniform and non-uniform polarizations respectively. The black boxes with white arrows indicate vertical and horizontal linear polarizers which project the beam into the respective polarization bases, yielding the intensity distributions to the right of them (far right of each beam).

Here Fig. 2.13 (a) depicts the scalar $LG_{0,1}(\hat{\mathbf{R}}+i\hat{\mathbf{L}})$ beam given in Eq. 2.107 with φ taken to be $\pi/2$ (i.e. diagonal polarization). The arrows indicate the direction of the electric field oscillations across the beam profile. It follows that by placing a linear polarizer in front of the beam, it can be projected into the horizontal and vertical bases by assuming the associated orientations. The black squares with arrows to the immediate right of the scalar beam represent the polarizer orientations being imposed upon the beam, resulting in the spatial distributions displayed to the right of them. As may be seen, the spatial distribution remains unchanged from that of the original beam (excepting a variation in the overall intensity in the projected bases), indicating both the separability of the properties as well as implied uniformity of the polarization distribution. It may be noted that the instantaneous opposing directions are a result of inhomogeneous phase along the beam cross-section [85].

Conversely, Fig. 2.13 (b) displays the vector beam, $\frac{1}{\sqrt{2}}(LG_{0,1}\hat{\mathbf{R}} - e^{i\varphi}LG_{0,-1}\hat{\mathbf{L}})$, given in Eq. 2.110 (with $\varphi = \pi$). It can already be seen that the polarization arrows indicate a clear variation in polarization as the spatial distribution is traversed. This is made clearer through the projections into the horizontal and vertical bases resulting in a different spatial distribution than that of the original beam in addition to variation of the spatial distributions of each basis.

It may be noted that although polarization is confined to two orthogonal polarization basis states (2 dimensional), the spatial mode orthogonal basis extends over an infinite range. Accordingly, vector beams may be classified into different orders based on the spatial distribution mode order [92]. Here the number of spatial bases increases with the mode order. However, as the spatial modes are paired with the polarization states, the state of any vector beam is confined to a 2D combination in its simplest form [92].

Furthermore, the type of vector beams created depends on the spatial-to-polarization basis combination where clarification may be obtained by considering implications on the orbital (l) and spin (circular polarization) angular momentum carried by the subsequent beams. First order beams refer to the vector beams occurring from the combination of spatial modes up to $l = \pm 1$, e.g. $LG_{0,1}$ and $LG_{0,-1}$ exemplified earlier, and $LG_{0,0}$. It follows that this vector beam order is the simplest as there are only three spatial basis states to consider, however, for convenience only $l = \pm 1$ will be used to further demonstrate types of vector beams. Figure 2.14 illustrates the types of vector beams possible in view of different OAM-to-SAM combinations.

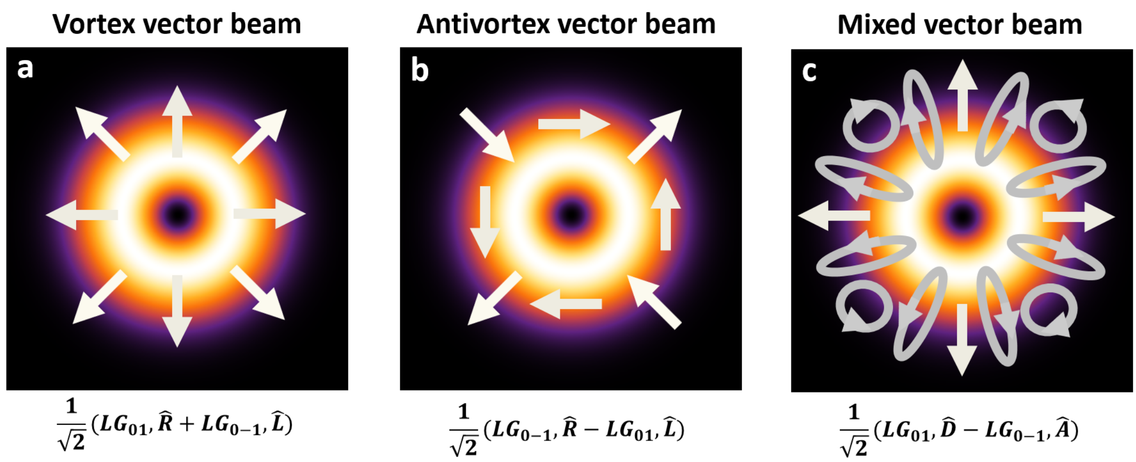

FIGURE 2.14: Illustration of a (a) vortex vector beam, (b) antivortex vector beam and (c) mixed vector beam created due to various OAM-to-SAM combinations as indicated by the equations listed below the beam cross-section. Arrows indicate the polarization type and direction.

When the OAM and SAM handedness match i.e. right-handed (left-handed) OAM with right-handed (left-handed) SAM, vortex vector beams are created whereby the polarization distribution follows a spiral trend along with the azimuthal angle as indicated in Fig 2.14 (a) [92]. Conversely, when the paired OAM and SAM handedness is reversed (left with right and right with left), antivortex beams are created as seen in Fig. 2.14 (b) [92; 109]. Here the polarization rotates counter to that of the spiral trend along the azimuthal angle [92].

Vortex and antivortex vector beams are the result of pure angular momentum state combinations. Combinations are also possible, however, where a pure OAM state may be paired with a mixed SAM state or vice versa, depending on the basis set used to express the state [92]. In the expression below Fig 2.14 (c), diagonal, $\hat{\mathbf{D}}$ and antidiagonal, $\hat{\mathbf{A}}$ polarization bases are used as they represent mixed SAM states (linear combinations of RCP and LCP) since they consist of linear combinations of right ($+\hbar$ SAM) and left ($-\hbar$ SAM) circular polarizations. Note that if the beam were expressed in terms of the circular polarization basis, the paired OAM would be expressed as $\pm$OAM mixed states. These hybrid or mixed vector beams have the property of a variation in the polarization ellipticity along with the oscillation direction along the beam cross-section [92]. This is illustrated in Fig. 2.14 (c) where the polarization changes from linear to circular and back as the azimuthal angle increases through to 90^o. A corresponding change in handedness additionally occurs each 90^o-cycle.

The higher order Poincaré sphere

As the vector beam state is confined to a dimensionality of 2 (polarization has only two orthogonal basis states), it follows that a Poincaré sphere may thus be used to describe all the possible vector beams within a particular spatial mode to polarization basis combination. This extension of the Poincaré sphere concept was established by Milione *et. al.* [110], allowing greater insight into vector beams in a similar fashion to that of the polarization states discussed previously. These visual representations of vector beams were termed higher-order Poincaré spheres (HOPSs). The Poincaré sphere illustrated in Fig. 2.15 is an example of such a HOPS for a $\pm l$ vortex vector beam pairing. The states are expressed in Dirac notation with OAM used to indicate the LG spatial mode so as to emphasize the changes and conservation of angular momentum as the sphere is traversed.

Here Eq. 2.106 applies to the description of AM change (and thus change in the vector beam) across the sphere with the top index referring to the paired basis state $|1, R\rangle$ and the bottom to the paired basis state $|-1, L\rangle$.

Accordingly, Φ indicates the relative weighting of the OAM while χ indicates the relative phase between the beams. As the opposing OAM states are of the same order (just opposite handedness), the total spatial distribution remains constant for all the possible modes. It may be noted that in cases where the modulus OAM is not the same (or there are unequal radial modes), the overall spatial distribution will exhibit changes related to the weighting of the contributing spatial bases due to the effects indicated by Eq. 2.99 [92].

The beams or modes at the poles contain only one basis pair and as such represent the contributing scalar beams that form the vector beams. This is illustrated by the uniform circular polarization distributions along the beam cross-sections at the poles of the sphere. Every other state along the sphere is non-factorizable and as such are vector beams. These two states accordingly have maximal OAM and SAM as there are no negating influences from the opposing state.

It follows from the equal weighting of opposite circular polarizations that the polarization distribution state across the beams located at the equator are linear. Direction of the instantaneous polarization across the beam varies azimuthally with a spiral trend as indicated for vortex vector beams. Here, χ specifies the angle of the linear polarization orientation from the normal of the circumference of a circle with a center corresponding to that of the beam center. This is illustrated in the inset (b). The vector beams along the equator are well-known as a subset labeled cylindrical vector (CV) beams due to their axial symmetry in both phase and amplitude [108]. These beams in Fig. 2.15 (a) subsequently carry no net AM as the equal weighing of opposite respective AMs result in a net AM of null for each type.

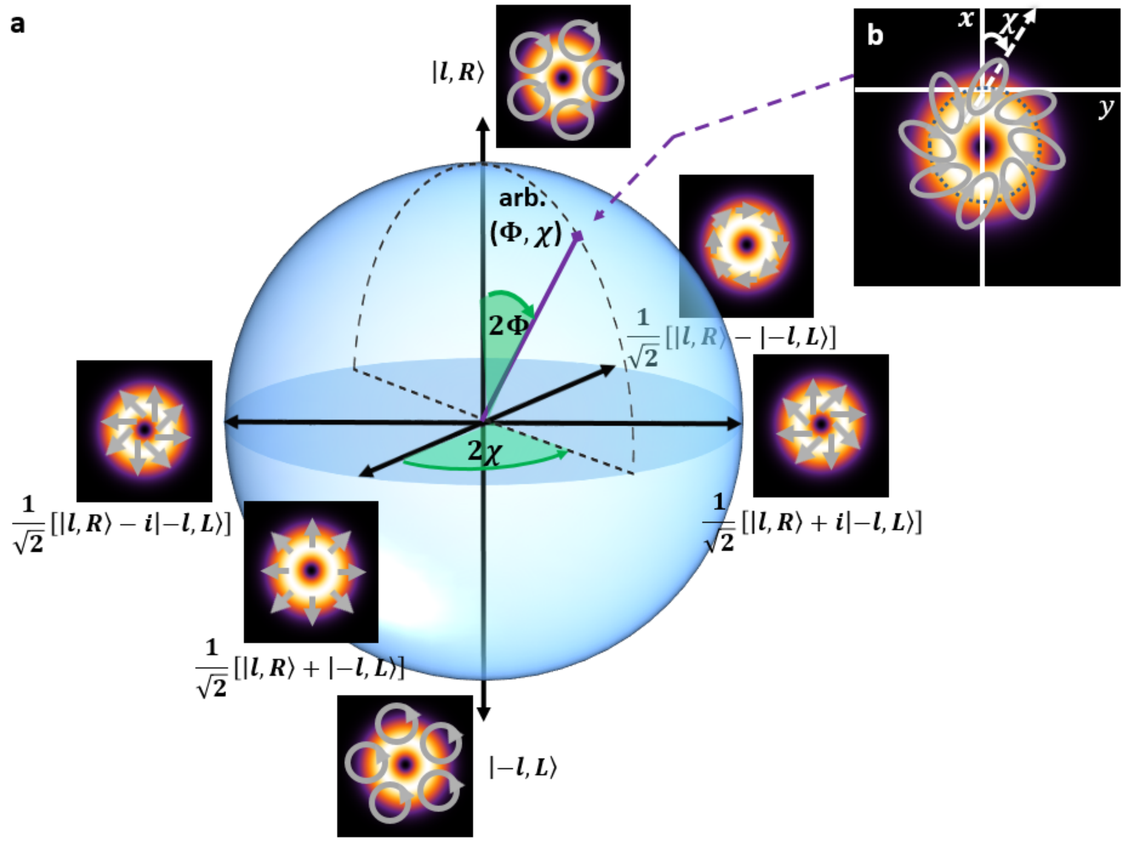

FIGURE 2.15: Diagram of a (a) higher order Poincaré sphere for $\pm l$, including an illustration of a (b) generalized first-order vector beam.

Moving longitudinally, variation in Φ results in a variation in the circular polarization causing polarization states of varying ellipticity. The handedness and ellipticity and directionality then follows the same logic as that of the Poincaré sphere in Fig. 2.11 with an azimuthally dependent axis as depicted for Fig. 2.15 (b). Latitudinally, χ then rotates the polarization semi-major axis direction from the azimuthal normal. The generalized case for these vector beams is then exemplified by Fig. 2.15 (b).

It should be noted that the respective weightings of either of the OAM and SAM coupling extremes at the poles indicate the degree of classical entanglement between the 'basis/pole' modes or, otherwise stated, the degree of separation varies [77]. It follows that maximum entanglement occurs at the equator where equal amounts of each state are present. McLaren *et. al.* [77] and Ndagano *et. al.* [111] developed a corresponding measure for the separability of beams by leaning on existing quantum mechanical tools for quantizing entanglement. When revisiting the original mathematical definition of vector beams given previously, it follows that this entanglement approach in fact measures the beam vector property. Consequently, this was denoted the beam 'vectorness', allowing one to determine the quality of the vector nature of the beam quantitatively. As a result, modes along the equator or CV beams with maximum non-separability have a vectorness of 1 that decreases on either side of the equator until a 0 value is reached at the respective poles, indicating no separability and thus a scalar beam [111].

Chapter 3

A Toolbox for a QW in the spatial modes of light

3.1 Quantum walking

Due to the extensive possibilities attached to realising the QW, many avenues and systems have been explored for achieving its physical implementation, each with its own advantages and disadvantages. This consequently solicits the question: what is required to physically realize a QW? Choosing a system to engineer a QW may be broken down into several properties or criteria. Here the walker must contain or be contained in a sufficiently extensive orthogonal space which may serve as the position space for the walker. The walker must then be able to form a superposition over any and all of these position states. Additionally, the walker must have a property with dimensions correlated to that of the position space which can form a coin subspace. For instance, in a 1D QW, a 2D coin subspace is needed. As the coin is a property of the walker, it is evident that it can exist as a subspace to each position state. There must then exist a mechanism whereby the coin states may be rotated into various superpositions and whereby the coin subspace may be used as a consistent control for movement of the walker in the position space. Using the action of these mechanisms to manipulate the intrinsic properties of the walker in its position space, one may then build a physical QW.

Numerous subsequent proposals and implementations of physically achieving this QW have since been developed where walks have been demonstrated. Here different QWs are briefly mentioned for context, illustrating the extensive variety and importance of this subject. A good review of schemes, both implemented and proposed, may be found in a book written by Wang and Manouchehri [9]. Some of the many systems include the use of NMR [112], electrons [113], atoms [114], ions [115; 116], photons [117; 118], Bose-Einstein condensate [119], optical fiber time loops [120; 121], and photonic waveguide arrays [122; 123] in the quantum regime. Here the steps achievable was limited to below 63 [121] to the best of the authors knowledge at this time. A major contributing factor to this limit, and thus the practicality, involves the fragility of quantum systems to environmental factors in addition to the difficulty of maintaining precise control of the walker as required for carrying out a QW.

An alternative implementation involves exploitation of the interference and superposition nature of this phenomenon. Here light is an advantageous tool due to the wave nature causing interference, thus allowing one to play with the amplitude which leads to quantum simulation. Knight *et. al.* [32] noted the viability of implementing QWs with classical light due to the analogous dynamical principals. This spurred additional schemes and implementations utilizing optical cavities [35], photonic crystal chips [124], and optical fiber time loops [125], increasing the number of achievable steps. These schemes, however, have not, to the author's knowledge, reached steps greater than 75 [125] (where a compensating amplifier was employed). It follows that by utilizing the classical QW approach, not only is control of the walker easier, but a more robust response to environmental influence may be expected. This limit in the number of steps also suggests that additional schemes, implementations and improvements are required to further the usefulness and practicality of this phenomenon.

One interesting approach with classical light involves the exploitation of the OAM and polarization degrees of freedom [126] that were covered in Chapter 2. As will be discussed near the end of this chapter, these properties fulfill the requirements listed earlier. Here, an additional analogous relation may be considered in the application of QWs with classical light. More specifically, classical entanglement occurs between OAM and polarization. As entanglement is a quintessential property associated with QWs whereby the coin and position degrees-of-freedom (DoF) exhibit non-separable correlations after several steps are taken [65], it follows then that these dynamics may be additionally exploited in a way that has been largely unconsidered in the other classical implementations. More specifically, QWs act as entanglement generators [127] which may be easily seen in the OAM and polarization DoF of classical light with classical non-separability.

In fact, analogous implementation of quantum mechanical phenomenon utilizing this special case of shared dynamical properties have already been shown for quantum communication links [128], superdense coding [129], teleportation [130], game strategies [131], polarization metrology [132] and Fourier transforms [133]. Furthermore, the strength of this analogue can be seen where where the OAM and polarization scheme has been demonstrated in both the quantum and classical regime by generating photon pairs as well as attenuating bright light, respectively. This quantum implementation was carried out by Cardano *et. al.* in 2015 [117] and 2016 [118] as well as recently in the attenuated light regime [134] with the same fundamentals of the scheme published by Ref. [126] and generalized in [135].

In this work we explore this classical realization of a QW in the spatial modes of light. Here OAM and polarization of the light are exploited according to the scheme in Ref. [126] in order to demonstrate a practical system that may be utilized for furthering the exploitation of QWs, however with additional advantages over that undertaken by Ref. [134].

To physically actualize such a walk, the tools required for manipulating light in both the spatial and polarization degrees of freedom requires some exploration. Here we characterize the operation of various optical elements, beginning with polarization control from waveplates and extending the toolbox to include q-plates for OAM generation as well as efficient detection of these OAM modes with mode sorters. The types of OAM modes generated by q-plates are also considered with the corresponding implications for higher-order modes. Utilizing this toolbox, it can then be seen how one may exploit polarization as a control for OAM and thus actualize a physical QW with classical light in the polarization and spatial degrees of freedom.

3.2 Waveplates

As the polarization of light is determined by the orientation of the electric field oscillation, it is possible to alter the polarization of a wave by introducing phase shifts between the orthogonal components of the transverse electric field vector [84; 136]. This consequently causes a new orientation in which the electric field will be confined to oscillate within (a different polarization state). Common elements used to achieve this are known as waveplates for which the physics behind this will be briefly covered. The Jones matrix formalism introduced in Chapter 2 are used as the mathematical basis to describe the operation of these elements.

3.2.1 Working principles

Waveplates are made from birefringent materials such as quartz and mica which possess different indices of refraction for the orthogonal orientations and thus orthogonal polarization states [136]. More specifically, when light traverses the waveplate, one polarization component 'sees' one index of refraction known as the ordinary refractive index (n_o) along the ordinary (slow) axis of the material while the orthogonal component 'sees' a different index of refraction known as the

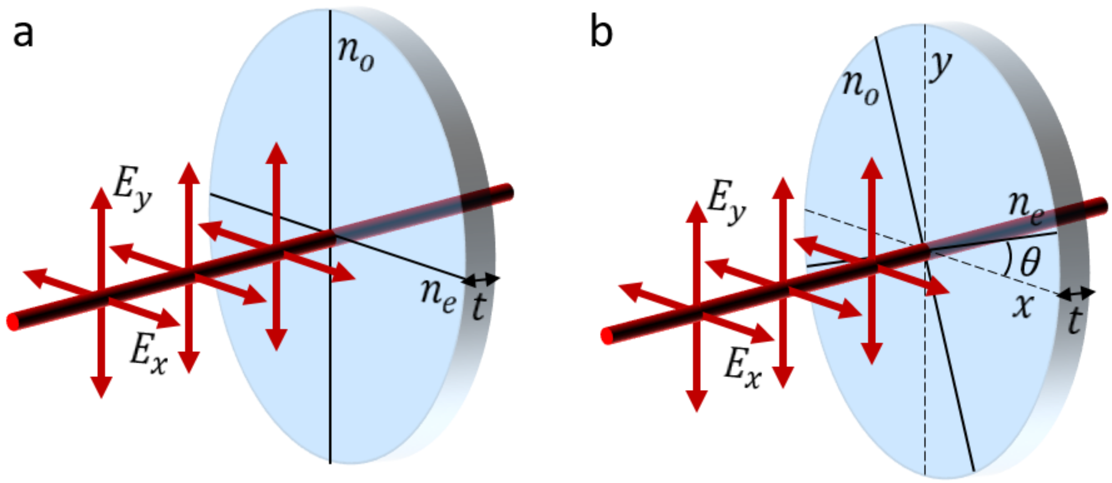

FIGURE 3.1: : Illustration of an electric field incident on a waveplate of thickness, t with the fast axis (a) aligned with the global x-axis and (b) rotated some angle, θ, from the x-axis.

extraordinary refractive index (n_e) along the principal (fast) axis of the crystal [136]. Now from Eq. 2.55 of Chapter 2,

$$v = \frac{c}{n},$$

it is clear that the refractive index dictates the speed at which the electric field traverses the material. By altering the speed of a wave, the overall phase of the wave is thus shifted according to the total retardance experienced. This is illustrated in Fig. 3.1 (a) where the horizontally polarized electric field (E_x) coincides with the fast axis while the vertical component experiences the ordinary index of refraction.

Traversal of the waveplate then gives rise to dynamical phase, which is described by Eq. 3.1 [136],

$$\phi_d = \frac{2\pi n t}{\lambda}, \tag{3.1}$$

where t is the thickness of the medium possessing the refractive index, n for light of the wavelength, λ. Accordingly, if the orthogonal components of the electric field experience different refractive indices, they will incur different phase shifts according to the axis traversed and as such a relative phase difference may be created between the components as described by [136]

$$\delta\phi_d = \phi_{de} - \phi_{do} = \frac{2\pi(n_e - n_o)t}{\lambda}. \tag{3.2}$$

In a simplified case where the vertical and horizontal polarization states are orientated along the ordinary and principal axes respectively, such as in Fig. 3.1 (a), the relative phase incurred is then,

$$\delta\varphi = \varphi_y - \varphi_x = \frac{2\pi(n_e - n_o)t}{\lambda}. \tag{3.3}$$

based on Eq. 2.99. The output state then becomes the generalized Jones matrix expression where $\delta\varphi = \varphi$

$$E = \begin{bmatrix} E_x \\ E_y e^{i\varphi} \end{bmatrix}$$

as was covered in Chapter 2. Here it may thus be seen that alteration of the polarization can be achieved with the correct thickness, t. For example, choosing t such that $\varphi = \pi/2$ when $E_x = E_y$ results in diagonal polarization converting into right circular polarization according to Table 2.2. Similarly, $\varphi = \pi$ generates anti-diagonal polarization and $\varphi = \pi/4$ an ellipse.

In terms of Jones matrix notation, the operation of an optical element assumes a 2x2 matrix such that multiplication of an input state vector results in the appropriate output vector. Here this relation is given by [84]

$$\begin{bmatrix} E_{out,x} \\ E_{out,y} \end{bmatrix} = \begin{bmatrix} W_{11} & W_{12} \\ W_{21} & W_{22} \end{bmatrix} \begin{bmatrix} E_{in,x} \\ E_{in,y} \end{bmatrix} \tag{3.4}$$

where E_{in} refers to the input state of the wave, E_{out} refers to the resultant state and W_{ij} are the elements of the optical element matrix acting on the input state when the wave traverses it. In the case where the horizontal and vertical components are aligned with the relative axes, as for Eq. 3.4, the following matrix describes the action of the waveplate based on the wave notation, $e^{i(\omega t - kz)}$ [136],

$$WP = \begin{bmatrix} e^{-i\frac{2\pi t}{\lambda}n_e} & 0 \\ 0 & e^{-i\frac{2\pi t}{\lambda}n_o} \end{bmatrix} = e^{-i\frac{2\pi t}{\lambda}n_e} \begin{bmatrix} 1 & 0 \\ 0 & e^{-i\frac{2\pi t}{\lambda}(n_o - n_e} \end{bmatrix} \tag{3.5}$$

Here it may clearly be seen that the horizontal component, $H = \begin{bmatrix} 1 \\ 0 \end{bmatrix}$, experiences the phase retardance $e^{-i\frac{2\pi t}{\lambda}n_e}$ as determined by the fast axis while the vertical component, $H = \begin{bmatrix} 0 \\ 1 \end{bmatrix}$, experiences the retardance $e^{-i\frac{2\pi t}{\lambda}n_o}$ as determined by the slow axis. The expression may then be simplified to

$$WP = \begin{bmatrix} 1 & 0 \\ 0 & e^{-i\varphi} \end{bmatrix} \tag{3.6}$$

by extracting the extraordinary component as a global phase.

Equation 3.6, however, is a simplified case with the waveplate axes placed at a specific position. This may be generalized to consider the action of a waveplate when the axes are rotated at an angle $theta$ from the x-axis [85], which is illustrated in Fig 3.1 (b). By applying the rotation matrix [84],

$$R(\theta) = \begin{bmatrix} \cos(\theta) & \sin(\theta) \\ -\sin(\theta) & \cos(\theta) \end{bmatrix} \tag{3.7}$$

to the waveplate as [84]

$$WP(\theta) = R(-\theta)[WP]R(\theta) \tag{3.8}$$

the rotation of the waveplate optical axis may be described. Action of these rotation matrices may be thought of as rotating the input wave from the laboratory frame of reference to the waveplate axis by $R(\theta)$ and then returning it to the laboratory frame of reference by $R(-\theta)$. The change of polarization exacted by the waveplate axes orientated at the angle θ is then determined. Multiplying out Equation 3.8 yields the general matrix for a waveplate with the fast axis rotated at the angle θ from the x-axis of the laboratory frame of reference:

$$WP_{HV}(\theta) = \begin{bmatrix} \cos^2(\theta) + e^{-i\varphi}\sin^2(\theta) & (1 - e^{-i\varphi})\sin(\theta)\cos(\theta) \\ (1 - e^{-i\varphi})\sin(\theta)\cos(\theta) & e^{-i\varphi}\cos^2(\theta) + \sin^2(\theta) \end{bmatrix} \tag{3.9}$$

Here Eq. 3.9 describes the action of the waveplate in the corresponding horizontal and vertical (HV) basis. A similar expression may be obtained in the circular polarization (CP) basis with the appropriate conversion matrix Equation 3.10 gives the corresponding analytical expression in this basis as was described in Chapter 2 [137].

$$WP_{CP}(\theta) = \begin{bmatrix} \cos\left(\frac{\varphi}{2}\right) & ie^{-i2\theta}\sin\left(\frac{\varphi}{2}\right) \\ ie^{i2\theta}\sin\left(\frac{\varphi}{2}\right) & \cos\left(\frac{\varphi}{2}\right) \end{bmatrix} \tag{3.10}$$

where all the symbols retain their meaning.

A common type of waveplate imperative to achieving polarization control for the quantum walk is the quarter-waveplate (QWP) with a phase retardance of $\varphi = \pi/2$. The corresponding expressions are then [84; 136]

$$QWP_{HV}(\theta) = \begin{bmatrix} \cos^2(\theta) + i\sin^2(\theta) & (1+i)\sin(\theta)\cos(\theta) \\ (1+i)\sin(\theta)\cos(\theta) & -i\cos^2(\theta) + \sin^2(\theta) \end{bmatrix} \tag{3.11}$$

and [137]

$$QWP_{CP}(\theta) = \frac{1}{\sqrt{2}} \begin{bmatrix} 1 & ie^{-i2\theta} \\ ie^{i2\theta} & 1 \end{bmatrix} \tag{3.12}$$

in the HV and CP bases respectively.

Denoted due on its retardance of a quarter wave between orthogonal polarization components, this waveplate allows conversion between linear and circular polarization states as will be seen in the following section.

Similarly ubiquitous, the half-waveplate (HWP) also bears importance in the toolbox of polarization state manipulation. Here the phase retardance is equal to a half a wavelength with $\varphi = \pi$, resulting in the corresponding matrices [84; 136],

$$HWP_{HV}(\theta) = \begin{bmatrix} \cos(2\theta) & \sin(2\theta) \\ \sin(2\theta) & -\cos(2\theta) \end{bmatrix} \tag{3.13}$$

and [137]

$$HWP_{CP}(\theta) = \frac{1}{\sqrt{2}} \begin{bmatrix} 0 & ie^{-i2\theta} \\ ie^{i2\theta} & 0 \end{bmatrix} \tag{3.14}$$

after substitution into Eq. 3.9 and Eq. 3.10 with further simplification.

3.2.2 Demonstration and experimental considerations

As the HWP and QWP are fundamental to flexible manipulation of the polarization degree of freedom, these common waveplate operations were experimentally tested with the setups shown in Fig. 3.2 for projection into the CP polarization basis with Fig 3.2 (a) and the HV basis with Fig 3.2 (b).

A 633 nm HeNe laser, producing horizontally polarized light, was directed through a WP in a rotational mount when looking at the WP action on linear polarization. An additional QWP at 45^o (QWP_i) was placed before the WP, resulting in generation of RCP, when looking at the WP action on CP. For testing the CP output of the waveplates, the modified beam was passed through a polarization grating (PG) which spatially separates the CP polarization components into 1st and 2nd diffraction orders. The output polarization could thus be projected into the CP basis allowing LCP and RCP state weightings and spatial components to then be detected through observation of the modes on a Spiricon SPU620 camera as illustrated in Fig. 3.2(a). Testing the waveplate output in the linear polarization basis was achieved by replacing the polarization grating with a polarizing beam splitter (PBS) and a mirror. This allowed the camera to simultaneously detect the vertically polarized component to the left and horizontally polarized component to the right, as illustrated in the Fig 3.2(b).

Starting with the QWP, the setup in Fig. 3.2(a) was used with WP as a QWP and without QWP_i. Here the linear input state was chosen to be horizontal based on convenience, although

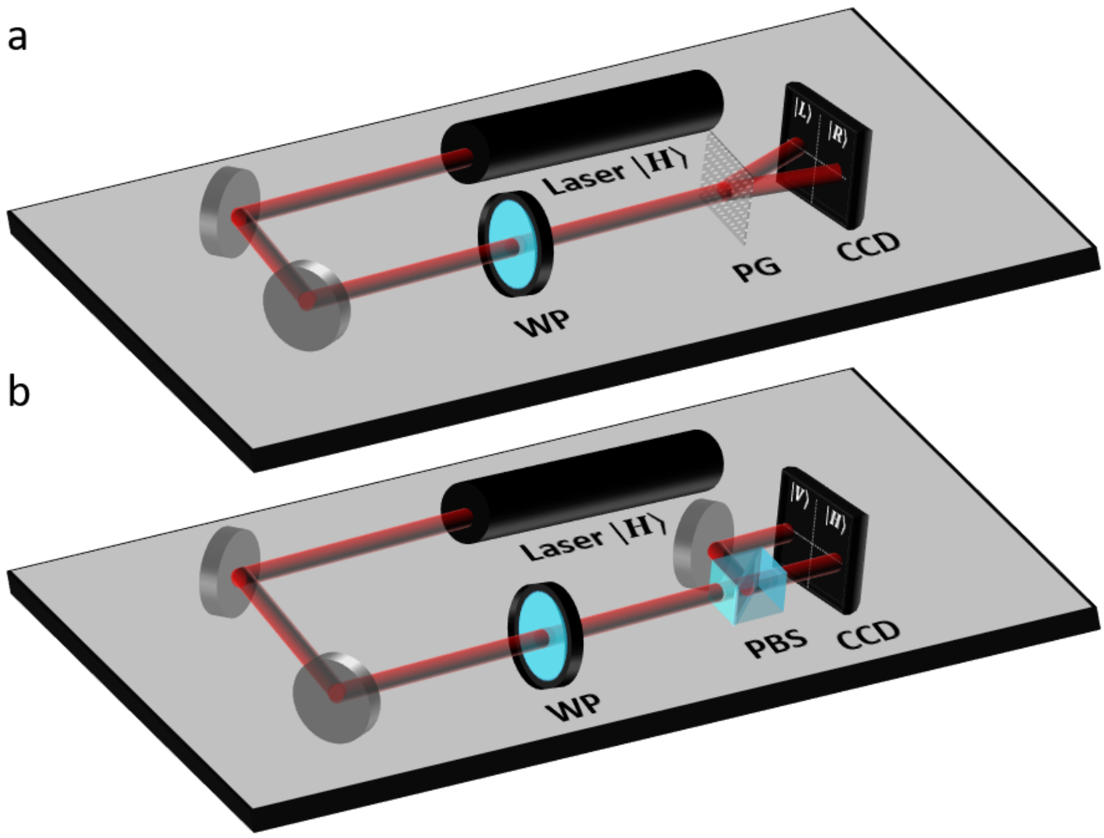

FIGURE 3.2: Experimental setups used to demonstrate waveplate (WP) operations in (a) the circular and (b) and linear (horizontal and vertical) polarization bases. A QWP at 45^o (QWP_i) was included when demonstrating the operations on CP.

any arbitrary linear state may have been used. Effect of the QWP on the horizontally polarized beam ($|H\rangle$) in the HV and CP bases may be determined by taking the product of the matrix for horizontally polarized light (Table 2.1) and the respective QWP matrices. The QWP action as a function of the fast axis rotation then yields the following polarization outputs:

$$QWP_{CP}(\theta)\,|H\rangle = \frac{1}{\sqrt{2}}\begin{bmatrix} 1 & ie^{-i2\theta} \\ ie^{i2\theta} & 1 \end{bmatrix}\frac{1}{\sqrt{2}}\begin{bmatrix} 1 \\ 1 \end{bmatrix} = \begin{bmatrix} 1+ie^{-i2\theta} \\ 1+ie^{i2\theta} \end{bmatrix} \tag{3.15}$$

and

$$\begin{aligned} QWP_{HV}(\theta)\,|H\rangle &= \begin{bmatrix} \cos^2(\theta)+i\sin^2(\theta) & (1+i)\sin(\theta)\cos(\theta) \\ (1+i)\sin(\theta)\cos(\theta) & -i\cos^2(\theta)+\sin^2(\theta) \end{bmatrix}\begin{bmatrix} 1 \\ 0 \end{bmatrix} \\ &= \begin{bmatrix} \cos^2(\theta)+i\sin^2(\theta) \\ (1+i)\sin(\theta)\cos(\theta) \end{bmatrix} \end{aligned} \tag{3.16}$$

Analysis of the WP action by projecting into the HV and CP basis as described in the experimental setup, was achieved by observing the intensities of the output mode in the corresponding states. Analytic determination of the respective outputs corresponds to taking the square of the modulus of each term in the rows for each output vector. For instance, the RCP output would be taken from the top row of Eq. 3.15 while LCP would be that of the bottom row:

$$\begin{bmatrix} I_R \\ I_L \end{bmatrix} = \frac{1}{4}\begin{bmatrix} |1+ie^{-i2\theta}|^2 \\ |1+ie^{i2\theta}|^2 \end{bmatrix} = \frac{1}{4}\begin{bmatrix} 1+\sin(2\theta) \\ 1-\sin(2\theta) \end{bmatrix} \tag{3.17}$$

Plotting these values as a function of θ resulted in the expected operation of the QWP in the CP basis described in Fig. 3.3 (a) and (b). Here the red (blue) lines indicate the right (left) CP output with the crosses yielding the experimental projection measurements. Insets above each plot show the polarization projections for choice angles as observed on the CCD with a false colour map. Operation of the QWP on this linear polarization shows the intensities of the RCP and LCP light fall between the periodic extremes as described by the sinusoidal functions in Eq. 3.17. Similarly, for the projection into the HV basis, the following relation is found:

$$QWP_{HV}(\theta)\,|H\rangle = \begin{bmatrix} I_H \\ I_V \end{bmatrix} = \frac{1}{4}\begin{bmatrix} |\cos^2(\theta)-i\cos^2(\theta)|^2 \\ |(1+i)\cos(\theta)\sin(\theta)|^2 \end{bmatrix} = \frac{1}{4}\begin{bmatrix} 3+\cos(4\theta) \\ 1-\cos(4\theta) \end{bmatrix} \tag{3.18}$$

where the periodicity remains between [0.5,1] for horizontal polarization and between [0,0.5] for vertical polarization. Here analogous representation stands in Fig 3.3(c) and (d) with horizontal (vertical) calculated and measured values are given in red (blue).

In greater detail, 0^o results in no change in the input polarization with equal intensities between the CP states as indicated in the mapping from Chapter 2:

$$|H\rangle = \frac{1}{\sqrt{2}}[|L\rangle + |R\rangle]$$

$$|V\rangle = \frac{i}{\sqrt{2}}[|L\rangle - |R\rangle]$$

This is further observed with the projection in the HV basis where approximately no intensity is detected in the vertical polarization bin.

Further increase in the fast axis angle results in an increase (decrease) in the weighting for RCP (LCP) until an extreme of 1 (0) for RCP (LCP) is reached as 45^o. This corresponds to a decrease (increase) in the horizontal (vertical) polarization state until reaching an equal superposition at 45^o

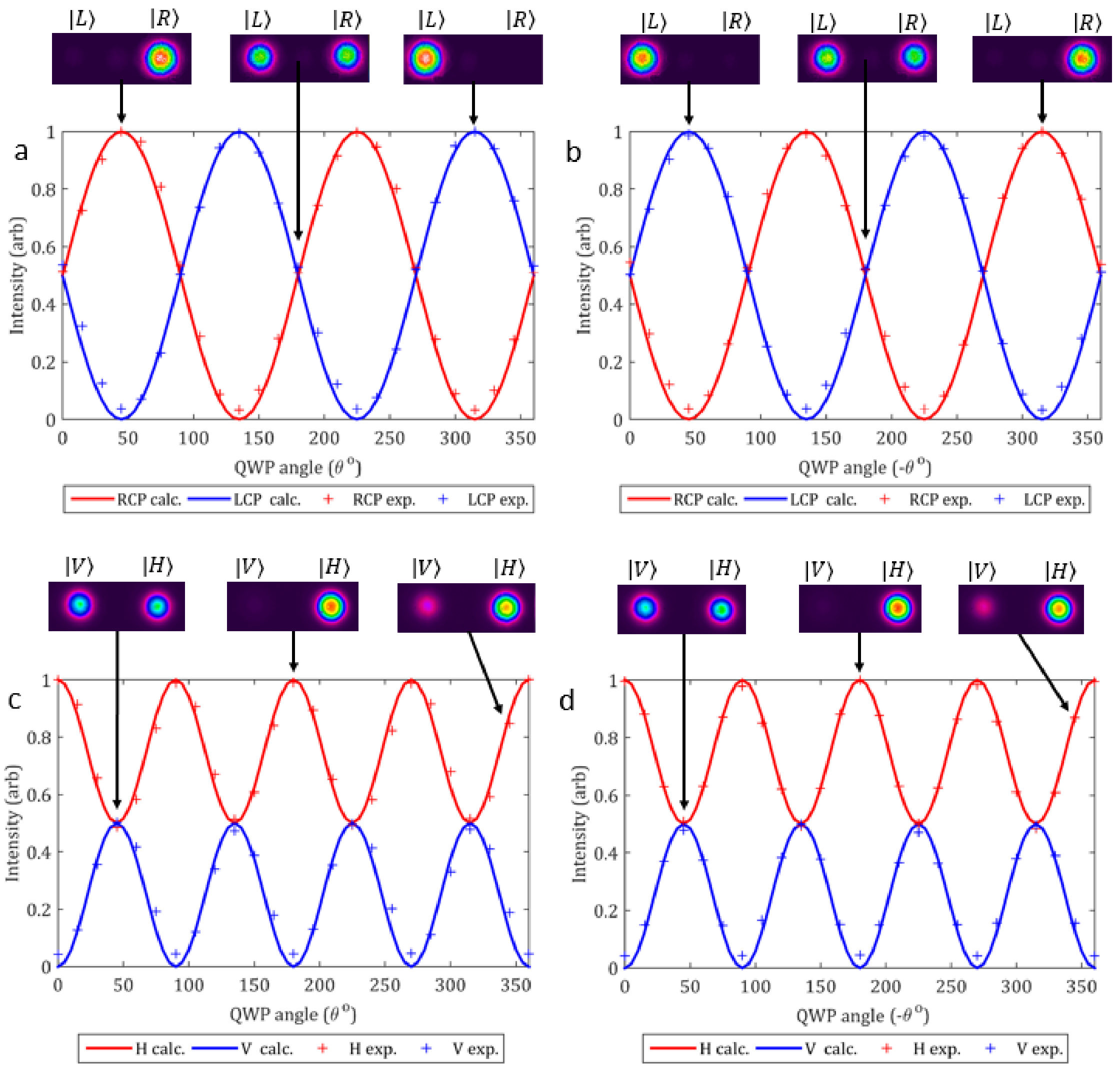

FIGURE 3.3: Experimental test of the QWP with a linear (horizontal) input state in the (a,b) circular and (c,d) linear polarization bases for incidence upon the (a,c) front and (b,d) back of the optical element.Insets above the graphs show the LCP and RCP modes detected on the CCD for the extreme cases of an equal superposition as well as only LCP and RCP states.

as may be expected from a reverse mapping of the basis states:

$$|R\rangle = \frac{1}{\sqrt{2}}[|H\rangle + i\,|V\rangle] \tag{3.19}$$

Afterwards, the RCP (LCP) begins to decrease (increase) until another equal superposition is reached whereby the output returns to H-polarization at 90^o. Increasing the rotation angle continues the decrease (increase) in RCP (LCP) until 130^o whereby only LCP results, corresponding to another equal superposition of H and V polarization:

$$|L\rangle = \frac{i}{\sqrt{2}}[|H\rangle - i\,|V\rangle] \tag{3.20}$$

with a phase difference between the linear bases of $e^{-i\pi/2}$. Continued rotation to 180^o returns the CP to an equal superposition equal to the linear polarization of the initial state. The trend is then repeated in the full 360^o rotation.

In summary, it may be observed that alteration in the linear polarization projected has a 90^o periodicity, while CP alteration carries a 180^o periodicity with the QWP. Intuitively, as the QWP induces a quarter-wave shift in between the orthogonal linear polarizations, when only one component is incident at 90^o angles from the x-axis, the wave only sees a global phase and as such the linear states remains the same. When the fast axis is rotated, the effective magnitude of orthogonal polarization components seen by the waveplate is altered, causing an associated quarter wave change between these components and resulting in rotation of the polarization. However, as the magnitudes in each component are altered, so is the rotational path. This generates elliptical polarization states which are related to the relative magnitudes seen by the fast axes. Consequently, when equal magnitude is seen at 45^o with the horizontal polarization (relative diagonal orientation), right circular rotation of the electric field occurs. Incidence with the same equal magnitude, but with the components reversed about the x-axis, as at 135^o (anti-diagonal relative orientation), CP again results from the retardation. Conversely, the resulting rotation occurs in the opposite (left) direction. It follows that with the fast axis moving between these extremes in Fig 3.3 (a), the relative CP weighting ratios vary between 0.5, 0 and 1 with the corresponding HV magnitudes as seen by the waveplate fast axis. It may be additionally noted that the elliptical states obtainable remain within the A-H-V hemisphere of the Poincare sphere as the input mode is horizontally polarized, which is reflected in the intensity ranges for the HV components. Reversal of this relationship and elliptical state space will thus occur if the incident polarization was changed to vertical.

The waveplate operation was also tested to determine directional sensitivity. More specifically, it was assumed that a wave travelling back through a WP would encounter the fast axis as if it were in the opposite orientation. This corresponds to making the WP angle negative and which results in Fig. 3.2(b). A reserve action on the LCP (blue) and RCP (red) transformation results, such that the curves are switched between the two WP orientations (Fig 3.1(a) and (b)) in the CP basis. For the linear basis, however, the orientation appears to an insensitivity in the magnitude of the projected states, however, this does not hold for phase as is shown in the switch with the CP projection. Experimentally, the results are in excellent agreement, showing that the QWP is directionally sensitive and care should be taken.

Analysis of QWP action on the CP is shown in Fig. 3.4 where QWPi was inserted with the fast axis at 45^o. As the incoming polarization already possesses a quarter-wave difference in phase, it is expected that the effect of the QWP would be to increment that further such that the difference is that of a half wave. As a result CP should be returned to a linear state. This is confirmed where the RCP and LCP magnitudes remain constant with an equal ratio in Fig 3.4 (a) while the linear state magnitudes undergo changes as the fast axis is rotated. It follows that the relative phases between the CP states are altered with theta corresponding to the HV bases states experiencing alteration.

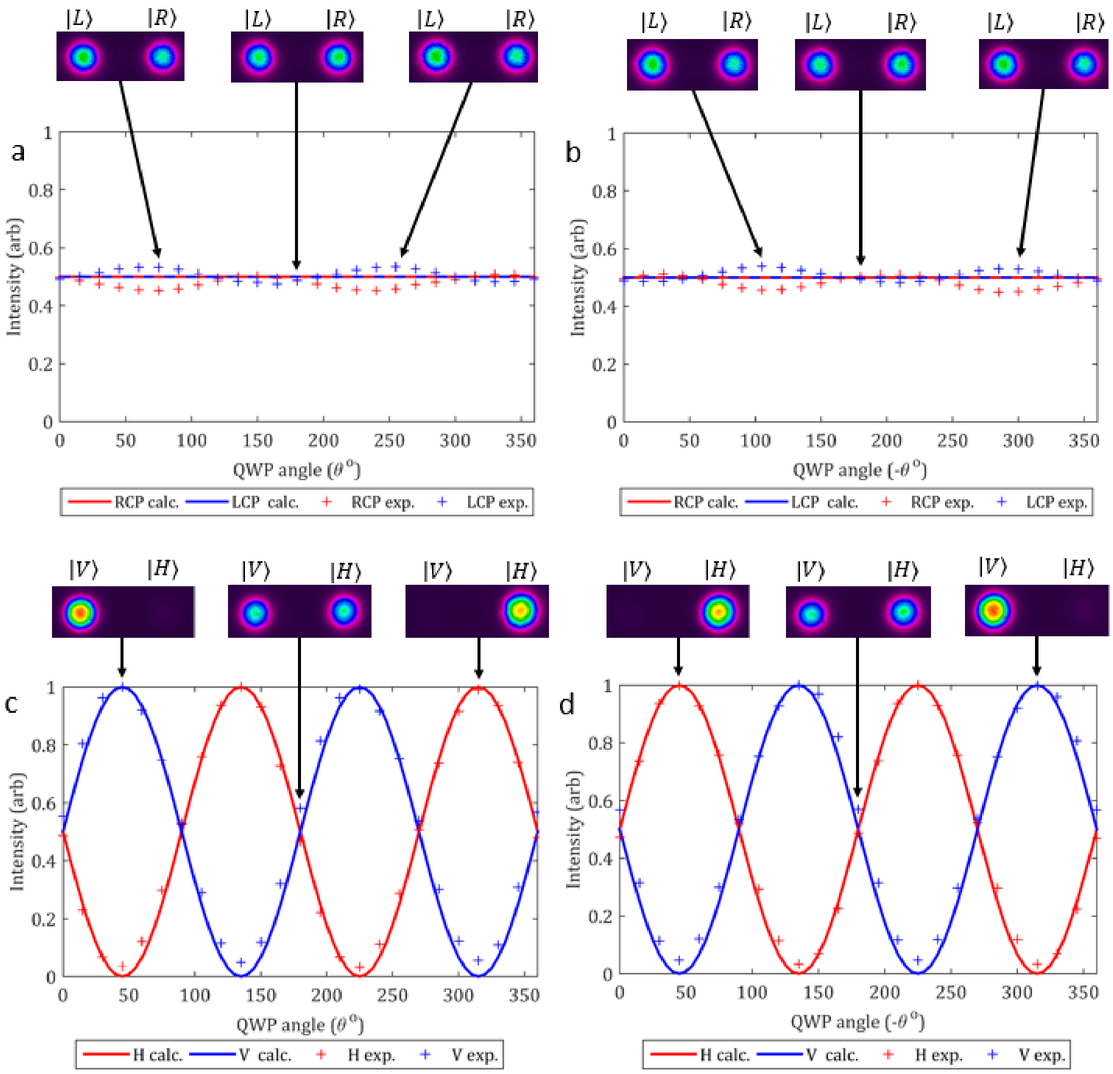

FIGURE 3.4: Experimental test of the QWP with a circular (RCP) input state in the (a,b) circular and (c,d) linear polarization bases for incidence upon the (a,c) front and (b,d) back of the optical element. Insets above the graphs show the LCP and RCP modes detected on the CCD for choice cases indicating variations in the projected states.

A similar trend may be observed in the linear basis as was seen for the CP basis discussed for the previous case. At 0^o an equal superposition (diagonal) may be seen:

$$|D\rangle = \frac{(1-i)}{2\sqrt{2}}[|R\rangle + i\,|L\rangle] \tag{3.21}$$

with a relative phase difference of $e^{i\pi/2} = i$ between the CP states. After which, the vertical polarization increases to 1 at 45^o before beginning to decrease to form another equal superposition (anti-diagonal) at 90^o:

$$|D\rangle = \frac{(i+1)}{2\sqrt{2}}[|R\rangle - i\,|L\rangle] \tag{3.22}$$

where a phase difference of $e^{-i\pi/2} = -i$ is incurred between the CP states.

Further increase in the fast axis angle causes additional decrease in the vertical polarization component until the output state is purely horizontally polarized at 135^o. The vertical polarization component then increases again to from another (diagonal) superposition at 180^o. Repetition of the relation then occurs for the next 180^o. Again, the QWP displays sensitivity to orientation with a trend reversal for Fig. 3.4(d). It follows that for CP input, the QWP action may be visualized as traversing the equator of the poincare sphere where the fast axis angle, $\theta = 2\chi$ on the sphere. Excellent agreement may be seen in Fig 3.4 (c) and (d) between the calculated and measured values. A larger deviation is evident for Fig 3.4 (a) and (b) however, where a small oscillation between [0.45,0.55] is observed about the expected 0.5 position. The correlation, however, is large enough for the WP action to be concluded to follow the calculated trend. Here the deviation may be attributed to a combination of systematic errors from slight inefficiencies in the waveplate conversions.

The same setups as shown in Fig 3.2 were used for testing the HWP with WP = HWP. Analysis of the HWP for incident linear polarization, as shown in Fig. 3.5, was similarly done with horizontal polarization where QWPi was not present. Accordingly, Fig 3.4(a) and (b) display the calculated and measured data for in the CP and HV polarization bases respectively. Calculation of the intensities in either basis follows on from the QWP example as shown:

$$HWP_{CP}(\theta)\,|H\rangle = \begin{bmatrix} 0 & ie^{-i2\theta} \\ ie^{i2\theta} & 0 \end{bmatrix} \frac{1}{\sqrt{2}} \begin{bmatrix} 1 \\ 1 \end{bmatrix} = \frac{i}{\sqrt{2}} \begin{bmatrix} e^{-i2\theta} \\ ie^{i2\theta} \end{bmatrix} \tag{3.23}$$

and

$$HWP_{HV}(\theta)\,|H\rangle = \begin{bmatrix} \cos(2\theta) & \sin(2\theta) \\ \sin(2\theta) & -\cos(2\theta) \end{bmatrix} \frac{1}{\sqrt{2}} \begin{bmatrix} 1 \\ 0 \end{bmatrix} = \frac{i}{\sqrt{2}} \begin{bmatrix} \cos(2\theta) \\ \sin(2\theta) \end{bmatrix} \tag{3.24}$$

where

$$\begin{bmatrix} I_R \\ I_L \end{bmatrix} = \frac{1}{2} \begin{bmatrix} |ie^{-i2\theta}|^2 \\ |ie^{i2\theta}|^2 \end{bmatrix} = \frac{1}{2} \begin{bmatrix} 1 \\ 1 \end{bmatrix} \tag{3.25}$$

and

$$\begin{bmatrix} I_H \\ I_V \end{bmatrix} = \frac{1}{2} \begin{bmatrix} |\cos(2\theta)|^2 \\ |\sin(2\theta)|^2 \end{bmatrix} = \frac{1}{2} \begin{bmatrix} \cos^2(2\theta) \\ \sin^2(2\theta) \end{bmatrix} \tag{3.26}$$

As the HWP imparts half a wave phase difference between the two orthogonal components, it follows that a linear input polarization should remain so, resulting in a variation of the orthogonal component magnitudes. Additionally, a constant equal superposition in the CP bases may also be expected as was described for the QWP case when incident with CP. Both the calculated and measured values show similar trends to that seen in Fig 3.4 (a) and (c), indicating intuitive agreement. Here the LCP and RCP remain constant with 0.5 intensity weightings which may also be seen directly from Eq. 3.26. Furthermore, Fig. 3.5 (c) shows complimentary oscillations between [0,1] for the H and V-polarization basis.

There are two distinct differences, however. Rotation of the HWP fast axis corresponds to double the rotation resulting from the terms in the matrix, as seen in Eq. 3.24. As a result, the fast axis rotation also corresponds to double of that seen for the QWP. The periodic repetition for the linear states in Fig. 3.5 (c) subsequently occurs every 90^o as opposed to the 180^o seen in the QWP. It follows that for a linear input polarization, action of the HWP may be visualized as traversing the equator of the Poincare sphere, however for the HWP, $\theta = 4\chi$.

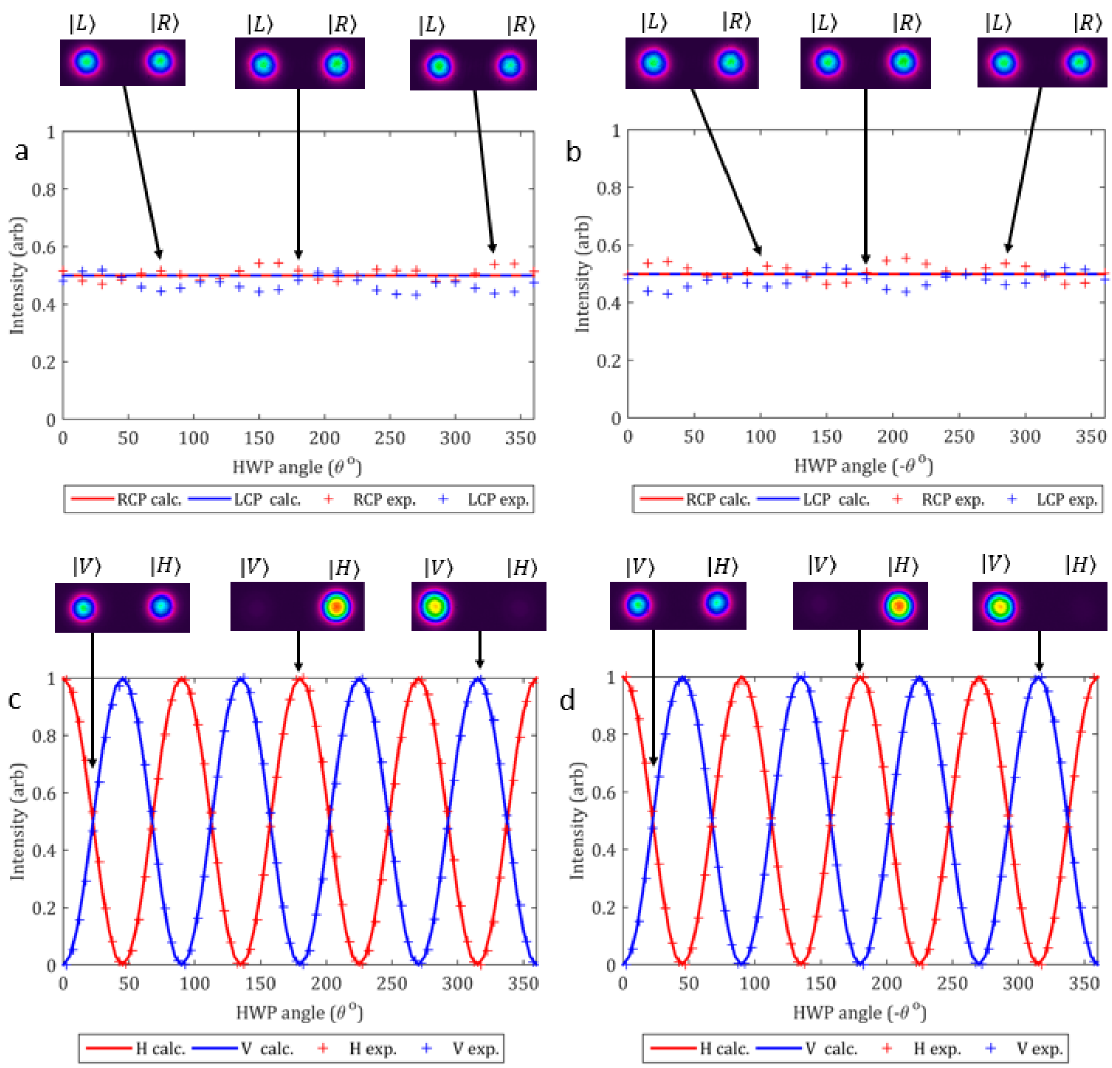

FIGURE 3.5: Experimental test of the HWP with a linear (horizontal) input state in the (a,b) circular and (c,d) linear polarization bases for incidence upon the (a,c) front and (b,d) back of the optical element. Insets above the graphs show the LCP and RCP modes detected on the CCD for choice cases, indicating variations in the projected states.

The second variation from the QWP case is that of the initial state at 0^o. Here, similar logic is applied to that of linear polarization incident on the QWP. The linear state remains the same with some global phase factor when incident along either of the ordinary or extraordinary axes (i.e. integer multiples of 90^o). Placement of the fast axis at 45^o (or integer multiples of 90^o added to it) flips the polarization to the orthogonal component, such that H-polarization is converted to V-polarization. Equal superpositions occur at 45^o intervals from 22.5^o with diagonal polarization at 22.5^o and antidiagonal polarization at 67.5^o. In both projection cases, the HWP appears to be invariant to the incident direction, however, it should be noted that closer observation the diagonal and anti-diagonal bases will show a flipping such that at 22.5^o in Fig. 3.5(d) the polarization is antidiagonal while 67.5^o it is diagonal. As such, directional care should also be taken for the HWP with linear polarization inputs.

Excellent agreement between the measured and calculated values are again seen in the HV polarization basis with Fig. 3.5 (c) and (d). Similarly, systematic errors are also evident with small oscillations between [0.42,0.57] in the CP basis in Fig. 3.5 (a) and (b), however, correlation is still apparent between the calculated and measured cases.

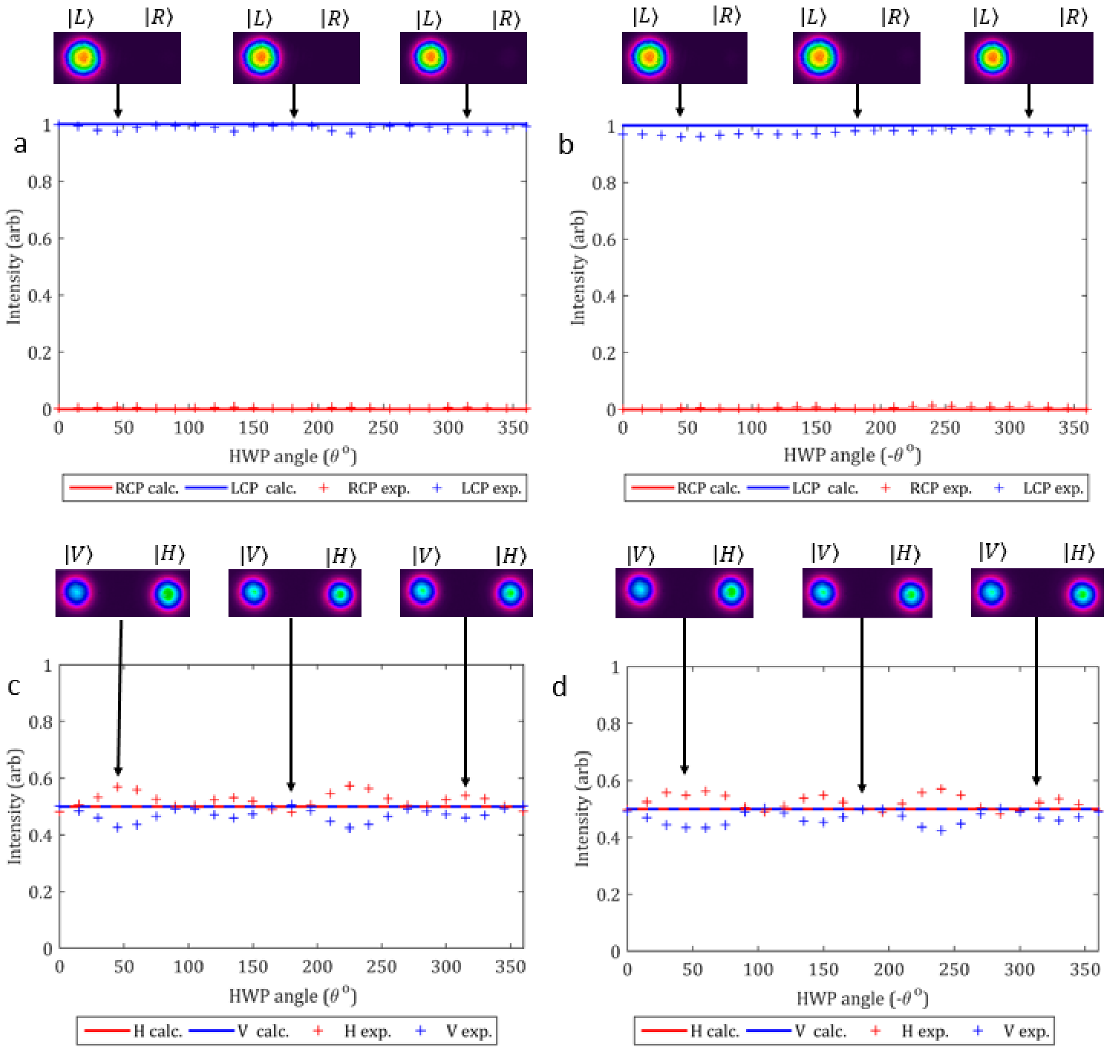

FIGURE 3.6: Experimental test of the HWP with a circular (RCP) input state in the (a,b) circular and (c,d) linear polarization bases for incidence upon the (a,c) front and (b,d) back of the optical element. Insets above the graphs show the LCP and RCP modes detected on the CCD for the extreme cases of an equal superposition as well as only LCP or RCP states.

Placing the QWP_i with the fast axis at 45^o in the experimental setups of Fig 3.2 generated RCP, allowing the WP = HWP to be analyzed when incident with CP. Due to the π-phase retardance, incidence with CP results in a particularly different result from the previous cases as may be seen in Fig. 3.6 (a-d). Here, as shown by Fig. 3.6(a), RCP is flipped to the orthogonal state, LCP, which then remains invariant to rotation of the fast axis. This invariance is also seen in Fig 3.6(c) with the HV polarization basis where polarization maintains a constant equal superposition between the basis states with fast axis rotation, in keeping with Eq. 3.17. Furthermore, the state remains invariant to directional incidence of the CP as indicated in Fig 3.6 (b) and (d). It follows that this is a special case whereby directionality CP incident on the HWP is not an issue. The result of changing the fast axis angle will be discussed in further detail in Section 3.2.2 with regards to operation of the QP.

Experimental values follow the calculated outcome closely in Fig. 3.6(a) and (b), indicating good agreement and repeatability with the HWP. Figures 3.6 (c) and (d) exhibit the periodic fluctuations about the calculated value, as seen in the other cases where a 0.5 constant superposition between the bases was expected. Here the fluctuation is slightly higher, falling within the interval [0.4,0.6], which may be explained through compounded systematic errors due inefficiencies in two WPs along with the PBS. Nevertheless, Fig. 3.6 (c) and (d) show an acceptable degree of correspondence, indicating a fairly constant outcome. It may also be seen that the deviation is higher in both linear and CP input cases of the HWP in comparison to the QWP, indicating slightly better efficiency from the QWP than the HWP.

It follows that the QWP is useful for manipulating CP states as was seen with conversion of linear states to CP and back in addition to being able to generate various elliptical states. Consequently, the QWP may be used to engineer various states with varying weightings of SAM. Additionally, when incident with CP, the QWP may be used to traverse all the possible linear polarization states as represented by the equator of the Poincaré sphere. The HWP may also traverse the linear polarization states through alteration of the relative phases between the LCP and RCP bases, however this is achievable when incident with linear polarization. Here no alteration of the incident beam SAM is possible. Additionally, a unique invariance occurs when operating on CP. The HWP flips the CP, and as such the SAM of the incoming beam, but maintains a constant output state with rotation of the fast axis. Subsequently, sufficient control of polarization of the SAM states of a beam is achievable through engineered combinations of these waveplates.

3.3 The q-plate

Since development of the q-plate (QP) in 2006 [138], it has become a common element employed to generate beams containing OAM. The working principles behind OAM generation with the q-plate has offered several applications with simplistic generation of vector beams such as radial or azimuthal vector vortex beams used for optical trapping [139; 140] and surface microstructure processing [141], among others. Based on the method by which the q-plate generates OAM, it additionally opens the possibility of physically realizing a QW in OAM space [126]. Design of the QP dictates the OAM value generated and the polarization of the incoming beam controls the handedness of the OAM generated. It follows that polarization may thus be used as a control for the laddering of OAM to higher or lower values in either handedness (positive or negative OAM). Here we consider the physical principles behind how the QP achieves this transformation and experimentally characterize its operation in view of using the operation rules as a means to physically implement such a QW.

3.3.1 Working principles

In Section 3.2.1, dynamic phase could be utilized as a property to retard directional electric fields, allowing the polarization of a wave to be changed. Dynamic phase, however, is not the only mechanism by which phase changes in light may be brought about. Another type of phase introduced by altering parameters adiabatically in a closed loop fashion is geometric phase [142]. This additional phase is acquired by a state or property of a system (such as the phase of a light wave) when the parameters (polarization), on which the state/property depends, undergoes alterations that bring the parameters back to the initial values [142]. Essentially, these alterations may be viewed as a mapping out a closed loop path in the parameter space as illustrated in Fig. 3.2(b). Berry [143] and Pancharatnum [144; 145] showed that the acquired phase is equivalent to half the solid area bounded by the transformations in the parameters space, denoted Ω is the figure. This effect is known generally as anholonomy in physics whereby a parameter-dependent property does not return to the same value when the parameters return to the original value after undergoing a closed path adiabatic evolution [142]. Anholonomy is also not confined to physics, but is also known as parallelism or, contradictorily, 'holonomy' in mathematics [142].

This specific case of geometric phase concerning light waves was described by Pancharatnum in 1996 [144] where he observed that an evolution of polarization that returned to the initial state resulted in an additional phase being gained by the light. Berry later studied the effect in quantum mechanics where a non-relativistic quantum system adiabatically traversing a circuit in parameter space incurred an additional circuit-dependent 'geometrical' phase [143], generalizing the phenomenon.

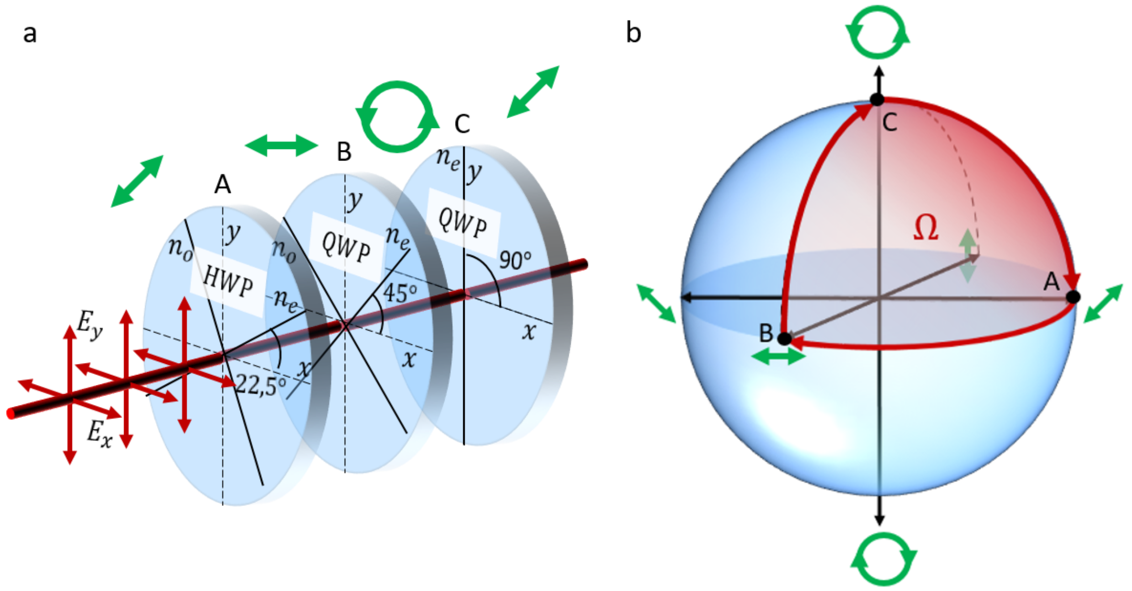

FIGURE 3.7: (a) Illustration of a diagonally polarized light beam traversing a series of waveplates that take the states through a closed loop transformation which is (b) depicted in the polarization parameter space with a Poincaré sphere.

For the purpose of this dissertation, however, it is the polarization related geometric phase, often called the Parachatnum-Berry phase that requires exploration. This effect may easily be seen by considering the evolution of polarization by the action of a series of waveplates. Consider Figure 3.7(a). Here diagonal polarization is passed through a HWP with the fast axis orientated at 22.5^o, converting it to horizontally polarized light. On the Poincare sphere (Fig. 3.2(b)), this is seen by the change in position from A to B. Passing the light through a QWP at 45^o then alters the state to right circular polarization (RCP) or C in Fig 3.7(b). By including the action of another QWP at 90^o, the RCP is changed back to diagonal polarization and a closed loop has been formed on the Poincare sphere. The light at this stage is not just diagonally polarized, however, but also has a supplementary phase of $e^{i\Omega/2}$ where Ω is the area enclosed by the evolution.

This effect is exploited with the q-plate operating mechanism in a slightly more conceptually complicated regime: the spatial domain [138]. Where in the previous example the change in polarization occurred sequentially and thus evolved in the time domain, Bomzon et al. [146] showed that if a change in polarization occurs at points across the transverse spatial plane of the incoming beam, an associated spatially-varying geometric phase is also generated.

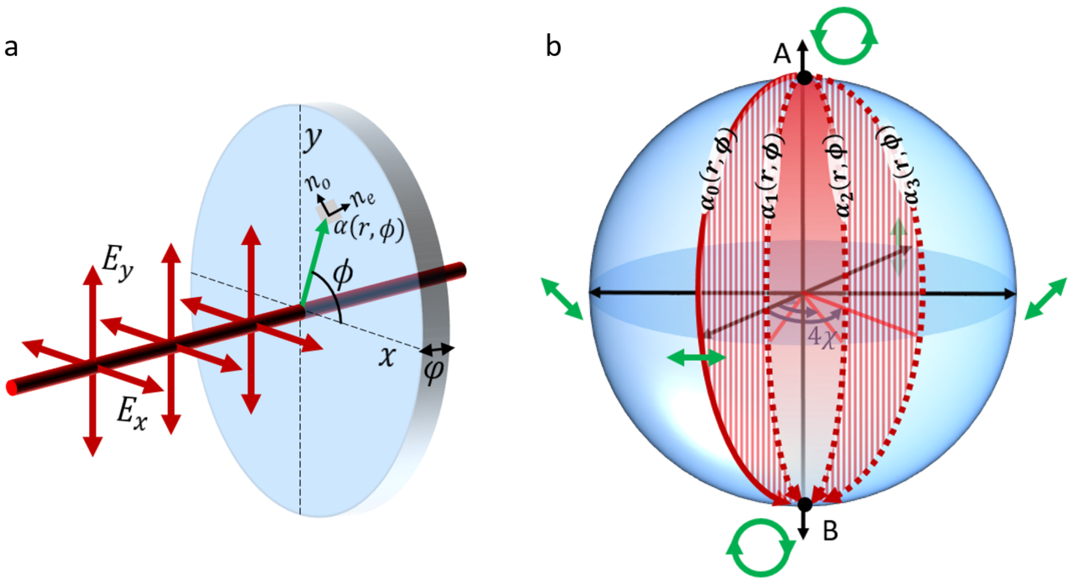

FIGURE 3.8: Depiction of an element with spatially varying optical indices of refraction which may be considered as a series of HWPs with varying optical axes. (b) Illustration of associated paths taken by different rays of a light beam traversing an element with four arbitrary HWPs with varying fast axis rotational angles.

To achieve this spatial variance of polarization of along the incoming beam cross-section, the element requires spatially varying optical indices of refraction [138; 147]. This may be thought of as small waveplates patterned across the element with the each of the optical axes varying in orientation. Figure 3.8 (a) illustrates this in polar coordinates. Here, for a specific coordinate on the element, (r, ϕ), the optical axis (n_o and n_e) has a specified direction different to the surrounding points so the polarization change in the wave incident at this point is different from that of the surrounding waves. Traditionally the QP achieves this spatially dependent polarization alteration with liquid crystals (LCs) as they have anisotropic inhomogeneous properties when interacting with light [138]. Consequently, the LC contains extraordinary and ordinary indices of refraction which alter the polarization of the interacting light wave [84; 136]. By fashioning the LCs in specific spatially varying orientations the polarization may likewise be manipulated. Lately, this has also been exploited with metamaterials [148].

Figure 3.8 (b) shows how geometric phase may be mapped between the waves incident for four different points on the element, arbitrarily denoted $\alpha_0(r, \phi)$ to $\alpha_3(r, \phi)$. Here the incident beam is RCP and the 'waveplates' are taken to induce a π phase shift between the electric field vectors (i.e. a HWP) for reasons soon to become clear. Each arrow indicates a HWP action on the wave at that point where the optical axis of said waveplate is orientated at the angle θ. Based the discussion in Section 3.2.1, each angle of the HWP, θ, corresponds to a 4χ rotation around the linear axis on Poincaré sphere.

With the polarization change occurring spatially, the 'closed path' is formed by the difference in path between the other elements, resulting in the geometric phase being both relative and spatially varying [146; 149]. For example, the path between $\alpha_0(r, \phi)$ and $\alpha_1(r, \phi)$ results in $\alpha_1(r, \phi)$ acquiring the geometric phase, relative to $\alpha_0(r, \phi)$, that is equal to half the striped area to the left ($e^{i2\theta_1}$). Similarly, $\alpha_2(r, \phi)$ picks up the geometric phase indicated by the clear area in the middle relative to element $\alpha_1(r, \phi)$ ($e^{i2(\theta_2-\theta_1)}$). The geometric phase acquired by $\alpha_2(r, \phi)$ relative to $\alpha_0(r, \phi)$, however, is the sum of the clear and striped parts ($e^{i2\theta_2}$). One may therefore engineer the relative optical axis orientations (θ) to generate any number of variable geometric phase acquisitions that may be used to manipulate the spatial mode of the overall beam.

The QP exploits this by patterning the optical axis orientation, such that the relative phase changes azimuthally and thus creates an azimuthal phase across the entire beam [138]. The waves subsequently twist alongside each other in a helical fashion, resulting in OAM generation. This patterning of the optical axis is described by Eq. 3.27 [138].

$$\alpha(r, \phi) = q\phi + \alpha_o \tag{3.27}$$

Here the QP is taken to be in the xy-plane, α_o is the angle formed by the optical axis from the x-axis, q is a constant defining the number of times the optical axis rotates in a path as it traverses once around the plate center and α_o is the permanent offset of the optical axis from the element's x-axis. A discontinuity occurring at $r = 0$ is evident with the special occurrence of the discontinuity not forming a line in the plate when q is a semi-integer or integer.

Easy description of the subsequent QP action can be done in terms of a Jones matrix [147]:

$$QP = \cos\left(\frac{\varphi}{2}\right) = \begin{bmatrix} 1 & 0 \\ 0 & 1 \end{bmatrix} + i\sin\left(\frac{\varphi}{2}\right)\begin{bmatrix} \cos\left(2\alpha(r,\phi)\right) & \sin\left(2\alpha(r,\phi)\right) \\ \sin\left(2\alpha(r,\phi)\right) & -\cos\left(2\alpha(r,\phi)\right) \end{bmatrix} \tag{3.28}$$

Here ϕ refers the efficiency of QP which is tied into the retardance of the slow and fast axes in element. The cosine term alongside the identity matrix indicates that this portion of the incident beam remains unaffected where no polarization or phase changes occur. The second matrix term refers to the action of the QP whereby an azimuthally-varying geometric phase is imparted as described by Eq. 3.27. It may thus be seen that when $\phi = \pi$ (HWP retardance), the QP is 100% efficient, with the fist matrix term falling away [147; 150]. Q-plates meeting this condition are referred to as 'tuned'. The subsequent matrix of a tuned QP with α_o set to 0 is thus given as

$$QP = \begin{bmatrix} \cos(2q\phi) & \sin(2q\phi) \\ \sin(2q\phi) & -\cos(2q\phi) \end{bmatrix} \tag{3.29}$$

in the linear basis. When converting to the CP basis (Eq. 3.26) [150], additional intuitive understanding of the action is afforded.

$$QP = \begin{bmatrix} 0 & ie^{-i2q\phi} \\ ie^{i2q\phi} & 0 \end{bmatrix} \tag{3.30}$$

Incident RCP, $|R\rangle = \begin{bmatrix} 1 \\ 0 \end{bmatrix}$, then gains the phase, $e^{i2q\phi}$, resulting in an OAM of $l = 2q\hbar$ per photon and the polarization is flipped to LCP. Similarly, LCP, $|L\rangle = \begin{bmatrix} 0 \\ 1 \end{bmatrix}$, acquires the phase $e^{-i2q\phi}$, resulting in negative OAM of $l = -2q\hbar$. The i-value multiplying the phase terms is global and thus may be ignored. It follows that the QP operation may be condensed into the following selection rules:

$$\hat{QP}\,|l, R\rangle = |l + 2q, L\rangle \tag{3.31a}$$
$$\hat{QP}\,|l, L\rangle = |l - 2q, R\rangle \tag{3.31b}$$

Using Fig. 3.9, it is possible to intuitively follow how the QP achieves the azimuthal phase change with $q = 0.5$ as an example. Figure 3.9 (a) is a diagram, often used to describe the patterning of the QP optical axis [151]. The black lines correspondingly refer to the optical axis orientations, spatially distributed across the element. A red semi-transparent circle with an arbitrary distance, r, has been superimposed on the diagram so as to help follow the azimuthal variation of the optical axes around the central point of the element.

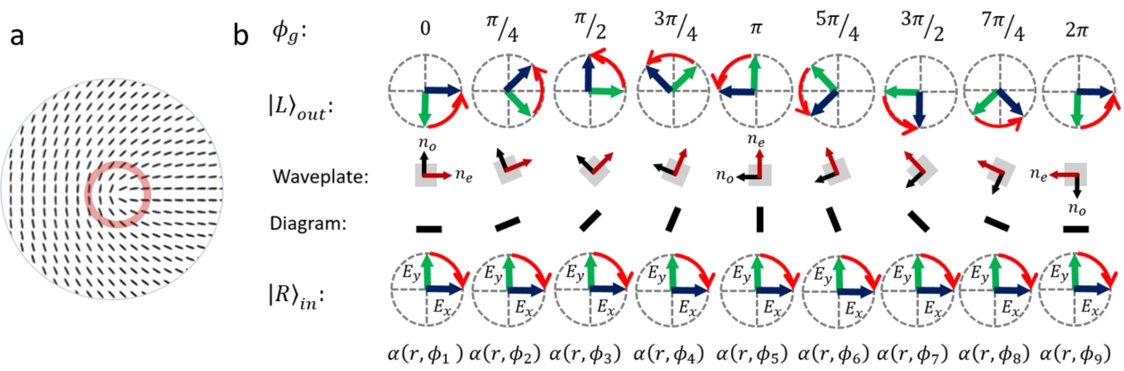

FIGURE 3.9: (a) Diagram of a $q = 0.5$ QP where the optical axis spatial variance is depicted. An arbitrary region about the center is highlighted in red. (b) Conceptual depiction of the optical axis variation (adapted from ref [152]) within the highlighted region of the QP diagram, showing the geometric phase incurred from the optical axis orientations shown.

Starting from the x-axis, variation of the optical axis orientations on the circle are mapped out in Fig 3.9 (b) as it is traversed in a counter-clockwise direction. From the HWP action of the QP, incident RCP light is converted into LCP with E_y being retarded by π as shown by the flipping of the green arrow about the fast axis. This in turn reverses the handedness of the CP and, correspondingly, the red arrow. The second and third rows (from the bottom) show the orientation of the markers in Fig. 3.9 (a) alongside the associated waveplate orientations with the fast axis (n_e) colored in red and the slow axis (n_o) in black. As the angle of optical axis increases, the phase shift can be seen diagrammatically in the 4th row and numerically in the top row where $\phi_(g) = 2\theta$. Here the geometric phase picked up by the wave is shown relative to the first case where the fast axis (blue arrow) is also orientated in the x-direction. Following the azimuth of the circle in Fig 3.9 (a), the optical axis spatially rotates by $0.5x2\pi$ (half the circle), which corresponds to the charge (q) describing the QP. A total phase change of $2qx2\pi = 2\pi$ is then experienced, causing the waves to twist and generating the $2q$ OAM value.

This effective twisting of the light beam produced by geometric phase has additional implications in the physical interpretation whereby the CP polarization may also be seen in terms of SAM. Here when RCP is incident on the QP, OAM of $2q\hbar$ per photon is generated, and the flip in CP corresponds to a flip in SAM from $1\hbar$ per photon to $-1\hbar$. It is well known that transference of SAM and OAM can occur between light and certain matter [150]. Here, SAM interaction occurs in optically anisotropic media such as birefringent material and OAM in transparent inhomogeneous, isotropic media [138]. The combination of a thin birefringent (liquid crystal) plate with an inhomogeneous optical axis in the QP subsequently results in the element coupling these two forms of angular momentum such that flipping in the SAM may be seen to generate OAM, making the QP a spin-to-orbital angular momentum converter (STOC) where the symmetry of the optical axis patterning effects the conversion values [150].

3.3.2 Spin angular momentum conversion

Experimental analysis was undertaken on a $q = 0.5$ QP to analyse the performance as an STOC as well as any possible experimental considerations required in view of implementing it as a propagation operator in a physical realization of the QW. Figure 3.10 illustrates the experimental setup used to achieve this. A horizontally polarized HeNe laser (633 nm) was shone through a QWP before being incident on the QP. A polarization grating (PG) was placed before a Spiricon SPU620 camera which acted to spatially separate the left and right CP of the QP generated beam.

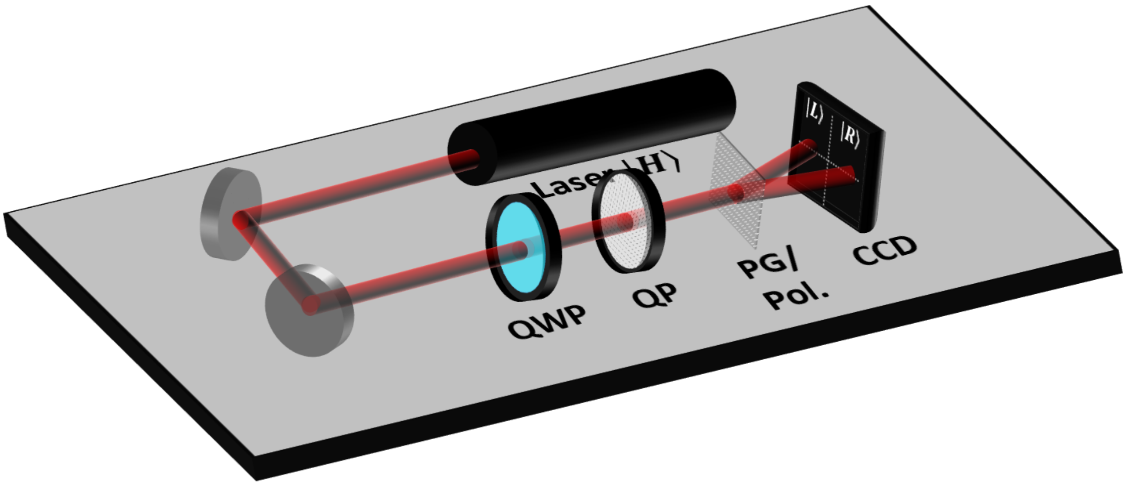

FIGURE 3.10: (a) Schematic of the experimental setup used to examine the SAM conversion and mode generation of a $q = 0.5$ QP.

Variation of the incoming SAM or CP onto the QP was obtained by rotating the QWP fast axis as was demonstrated in the previous section with Fig. 3.3 (a). It follows that superpositions of SAM with various weightings were incident onto the QP based on the QWP angle. These input weightings are shown in Fig 3.11 (a) through projection into RCP and LCP states as taken from Fig 3.3 (a). The expected action of the QP is then to inverse the circular polarization (CP) states and add OAM of $2q = 1$ to the RCP beam while adding OAM of $2q = -1$ to the LCP beam, as evident from the selection rules in Eq. 3.31 It follows that the action of the QP on light propagating through it in both forward and reverse directions is anticipated to be:

$$\hat{QP}\,|0, R\rangle = |+1, L\rangle \tag{3.32a}$$

$$\hat{QP}\,|0, L\rangle = |-1, R\rangle \tag{3.32b}$$

The calculated and measured outcome of passing these SAM or CP superpositions (as indicated in Fig 3.11 (a)) through the QP is given in Fig. 3.11 (b) where the output was also projected into the CP basis. Comparison of these two figures show that the LCP and RCP input weightings are inverted after passing through the QP. For instance, at 45^o, RCP generated by the QWP is detected as LCP after passing through the QP. Similarly, at 135^o, the generated LCP is converted to RCP after the QP. At 105^o, the CP state with majority weighting is changed from LCP after the QWP to RCP after the QP. It follows that the QP acts to invert the SAM of the incident beam.

Further observation of the spatial modes of the beams can be seen from the insets. Here the Gaussian profile of the input beam is evident in Fig. 3.11 (a) with the false colour map. The spatial profile of the beam after the QP shows the doughnut distribution with a central intensity null, characteristic of OAM carrying beams as was seen in Chapter 2. These modes consequently, indicate OAM is generated by the QP for both incoming LCP and RCP as well as superpositions thereof. Further analysis of the OAM beam charge as well as the handedness requires another technique which will be covered further on.

As the QP works through acting on CP with a HWP retardance, it is expected that the same directional invariance seen in Fig. 3.6 is maintained with the QP operation. As such, the order of OAM assignment with regards to the state of polarization when the direction of propagation is reversed is presumed to remain the same. The experimental outcome is given in Fig. 3.11 (c) where the QP side of incidence was reversed in the setup, causing the incoming beam to traverse through the back of the element. Comparison of Fig. 3.11 (b) and (c) shows the experimentally

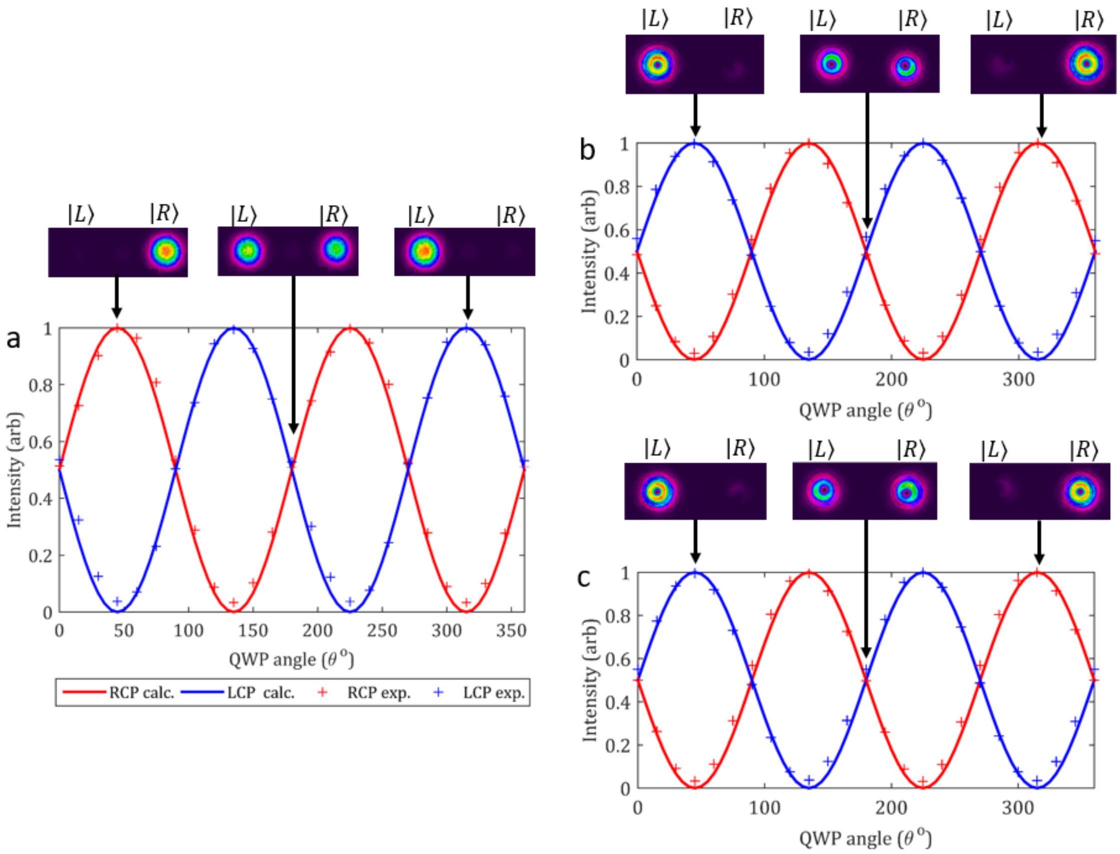

FIGURE 3.11: Spin angular momentum transformations by the QP for varying incident superpositions as shown in (a) with left and right CPs. Here (b) are the corresponding output modes when incident upon the front side of the QP as well as (c) the back side of the QP.

measured projections are identical with the QP reversed, enacting the same SAM inversion on the incoming beam. Therefore, it may be concluded that the QP operation follows the directional invariance that was seen for the HWP. Analysis as to whether the OAM imparted to the respective CPs retain the handedness with reversal of the input direction of the QP will be additionally tested in the following section along with the OAM values mentioned previously. Slight off-sets in the intensity nulls of the vortex beams may be seen between the LCP and RCP insets at 180^o. This may be due to a small variation in the QP singularity with respect to the polarization as a result of aberrations in the device as well as a slight inefficiency in the polarization grating polarization separation. The general vortex form, however, may be notably identified.

3.3.3 OAM characterization and modal decomposition

An important technique, essential for analysing the generated beams in terms of established modes, is modal decomposition. This technique is often used for characterizing beams, whereby any optical field may be expressed as a linear combination of basis modes [153–155]:

$$U(r) = \sum_j c_j \phi_j(r) \tag{3.33}$$

Here $r = (x, y)$ is the spatial coordinate in the transverse plane and $\phi_j(r)$ represents the basis mode. The complex correlation coefficient, $c_j = \rho_j e^{i\delta\varphi_j}$ weights the contribution of each of the basis modes where ρ_j is the corresponding mode amplitude and $\delta\varphi_j$ the intermodal phase difference between the jth mode and a selected reference mode. It thus follows that the beam generated by the QP may easily be expressed in terms of the LG modes ($LG_{p,l}(r)$) described in Chapter 2:

$$U^l(r, \phi) = \sum_p c_p LG_{p,l}(r). \tag{3.34}$$

Accordingly, any arbitrary input field, U(r), may be described by a weighted superposition of these modes. Orthonormality of the LG elements can be exploited to ascertain the weighting coefficients ($c_{p,l}$) by taking an inner product between the input field and desired LG mode [154; 155]:

$$c_{p,l} = \langle U(r) | LG_{p,l(r)} \rangle = \iint_{\mathcal{R}^2} U(r) LG^*_{p,l}(r) d^2r \tag{3.35}$$

where integration is over all space and $LG^*_{p,l}$ is the complex conjugate of Eq. 2.77. The complex conjugate of a basis mode is often referred to as a match filter [156; 157]. Determination of the coefficient in terms of the field product ($U(r)LG^*_{p,l}$) is possible by taking the Fourier transform of Eq. 3.35 to yield:

$$U_{p,l}(k_x, k_y) = \iint U(x, y) LG^*_{p,l}(x, y) e^{-i(k_x x + k_y y)} dxdy \tag{3.36}$$

where k_x, k_y are wave vectors. The on-axis point $(k_x, k_y) = (0, 0)$, produces an expression equivalent to Eq. 3.35:

$$U_{p,l}(0, 0) = \iint_{\mathcal{R}^2} U(r) LG^*_{p,l}(r) d^2r = c_{p,l} \tag{3.37}$$

It follows that the intensity at the field center, $I(0, 0)$, will then yield the power weighting (i.e. square of the weighting coefficient)

$$I^\rho_j(0, 0) = |U_{p,l}(0, 0)|^2 = |c_{p,l}|^2 \tag{3.38}$$

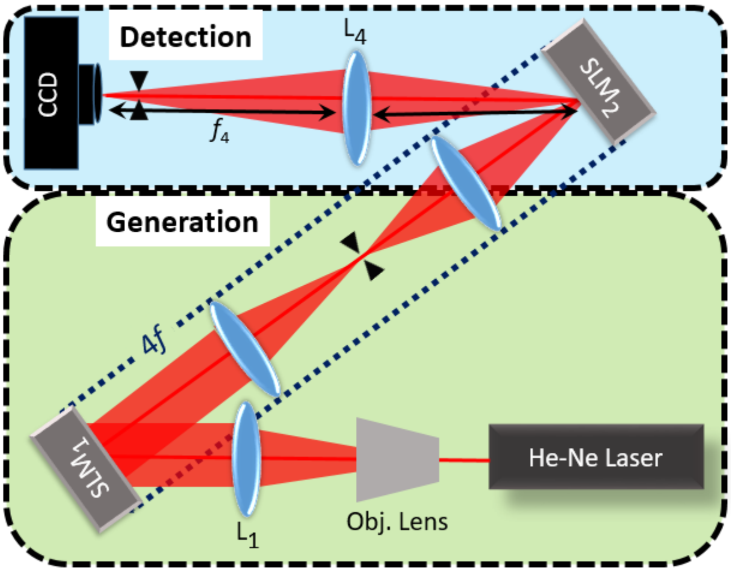

FIGURE 3.12: Simplified schematic of the experimental setup utilized to generate and decompose a beam so as to experimentally verify the accuracy of the system before decomposition of the QP was attempted.

It is additionally possible to extend this technique to determine the intermodal phase between the basis modes by interfering with a reference mode. Characterization of this QP generated beam, however, only extends to intensity correlations and not intermodal phase decomposition. Therefore, for the scope of this dissertation, decomposition was restricted to determining only the amplitude terms as described above.

Experimentally, this characterization technique may be implemented with the use of a spatial light modulator (SLM). Here the SLM works by applying specified voltages over a transverse array of LC molecules to change their orientation [158]. This results in a change in the refractive index according to the voltage applied [85]. As was seen with Eq. 3.1 for the waveplates, a dynamical phase may thus be imparted to the wave interacting with each orientated molecule due to the refractive index change. By applying different voltages to each molecule, the phase across an impinging beam may be changed as desired to manipulate the phase profile across the beam cross-section.

Manipulation of the voltage applied to each molecule may be achieved through the patterning of what is known as a hologram. A hologram in this case refers to a gray-scale image with dimensions corresponding to the SLM LC array, or liquid crystal display [159]. Here the gray-scale has color levels which are made to correspond to the intensity of the voltage being applied to the LCs [159]. By choosing the grey-scale values across the image and displaying it on the LC display, one is essentially choosing the voltage and thus the phase imparted to the beam interacting with the LCD at each point. These images may be digitally generated as was shown by Ref. [158]. Additionally, one may fashion the hologram to manipulate the amplitude as well as the phase of the interacting beam [159]. There are several methods for encoding these holograms to achieve the correct outcome from an impinging beam. This is summarized in a good review article by Ref. [160].

It follows that by patterning the SLM, OAM beams may be generated through modulating the phase. By including amplitude modulation, LG basis modes may be generated as well. Taking the product of an arbitrary beam, such as that generated by the QP, and the LG basis mode ($U(r)LG^*_{p,l}(r)$ in Eq. 3.35) is then a case of interacting the generated beam with the SLM displaying the match filter of the basis mode being considered. Taking the Fourier transform may also be

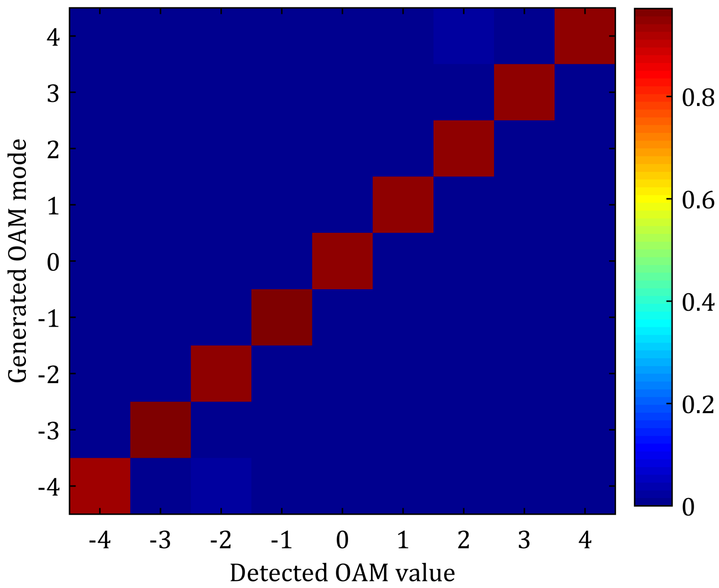

FIGURE 3.13: Modal decomposition for a series of $LG_{p,l}$ modes for OAM(l) ranging between $[-4, 4]$.

achieved optically by placing a lens focal length away from the desired plane and then looking in the focal plane of that lens.

Experimental demonstration of this technique was accomplished with the setup shown in Fig. 3.12. Here the modes were both generated and decomposed using amplitude and phase modulation on SLMs (SLM_1 and SLM_2 respectively).

To generate these LG beams, a horizontally polarized HeNe laser of wavelength 633 nm was expanded through a 10X objective lens and collimated by L_1 $(f1 = 400mm)$, before being directed onto a reflective PLUTO-VIS HoloEye spatial light modulator (8 μm, 1920 x 1080 pixels, calibrated at a 2π phase shift for 633 nm) marked as SLM_1. SLM_1 was programmed with the desired LG mode phase and amplitude profile, resulting in the 1st diffraction order possessing the required structure. Consequently, experimental amplitude decomposition was obtained through an optical inner product measurement (Eq. 3.35) between the experimental field, $U(r)$, generated by SLM_1 and the match filter, LGp,l(r)* on SLM_2 with a thin lens performing the Fourier transformation. First, isolation and imaging of the 1st diffraction order onto the match filter (SLM_2) was achieved through a $4f$ imaging system (lenses L_2 ($f2$ = 300 mm) and L_3 ($f3$ = 300 mm)) with an aperture placed in the Fourier plane. The Fourier transform of the resultant field after SLM_2 $(U(r)LG^*_{p,l}(r))$ was achieved with lens L_4 ($f4$ = 200 mm). The on-axis intensity at the Fourier plane (i.e. at the CCD plane) provided a physical measurement of the inner-product given in Eq. 3.37. An aperture placed before the camera (PointGrey Flea3) isolated the 1st diffraction order, allowing the optical inner-product to be recorded where an on-axis signal accordingly dictated a correlation between the generated mode and match-filter, while an on-axis null indicated a mismatch.

This demonstration served as a system test, indicating the expected accuracy for any results obtained from the system before characterizing the OAM generated by the QP. Figure 3.13 shows the results obtained for this system test. Here, a series of LG modes with $l = [-4, 4]$ were generated on SLM_1 along with a corresponding match filter series for the same modal range on SLM_2. The decomposition was subsequently completed for LG modes where the radial value was kept at zero $(p = 0)$ with the same beam waist used in the match filter as the generated beam.

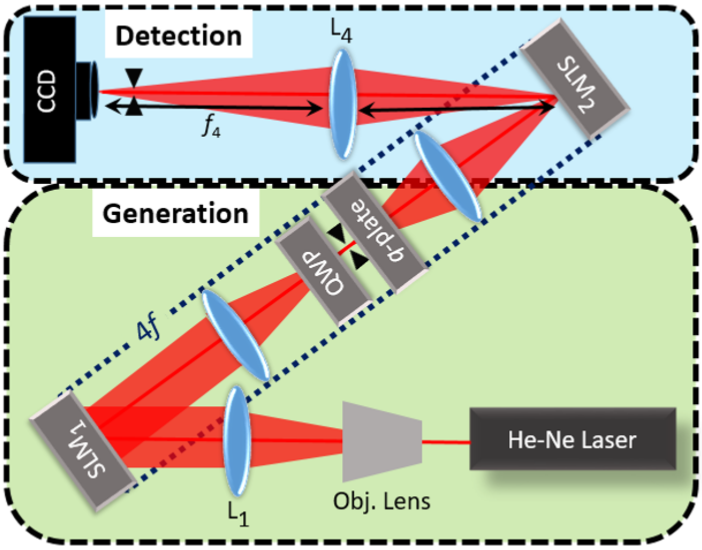

FIGURE 3.14: Simplified schematic of the experimental setup utilized to generate polarization dependant modes from a $q = 0.5$ QP and subsequently decompose them into the LG OAM mode basis.

The clear red diagonal in the density plot indicates detection of OAM modes that correspond to that which was generated on SLM_1. Negligible cross-talk from system aberrations may be seen a few negligibly lighter shaded blue bins off the red diagonal, which is within acceptable bounds (<5%). Subsequently, it may be concluded that the modal decompositions for OAM modes in the system will yield acceptably accurate results.

Modal decomposition of the QP OAM modes for an input Gaussian beam was attained through modification of the setup in Fig. 3.12. Figure 3.14 illustrates this modified setup where a QWP and the $q = 0.5$ QP was inserted before and in the Fourier plane respectively. SLM_1 was encoded with a Gaussian beam and the corresponding horizontal polarization was converted to LCP and RCP states by rotating the QWP optical axis to $\pm 45^o$ respectively. Afterwards the modified beam was made to traverse the QP before being directed onto the match filters displayed on SLM_2. Modal decomposition of the QP of the OAM values imparted by the QP was then completed as was described for Fig. 3.12 in the LG $(p = 0)$ basis.

This decomposition was repeated for the QP positioned in the reverse orientation, corresponding to the 'front' and 'back' labels given in Fig. 3.15. From the QP selection rules, it follows that the RCP input beam is theoretically expected have a OAM of $+1$ and the LCP input is expected to have an OAM of -1. Additionally, as was discussed with the polarization results, the same outcome is anticipated for a reversal of the QP orientation. Slight variations of the QP detected OAM weightings may be explained due to the experimental cross-talk detected in the decomposition. Figure 3.15 contains the modal decomposition results in (b) along with the simulated plot in (a) for comparison.

Good correlation between expectations (Eq. **??** and Fig. 3.15 (a)) and the experimental results (Fig. 3.15 (b)) may be seen whereby a 0 OAM RCP beam traversing the QP, resulted in a detection of $+1$ OAM in accordance to the simulated outcome. Similarly, a LCP input beam of 0 OAM incurred -1 OAM. Furthermore, the same trend is observed for the reversal of QP orientation (as denoted by Side 1 and Side 2 in the figure). This is clear in the density plot with the high intensity values of relevant beam l-values (red blocks) and minimal intensities for the surrounding OAM states. Minimal cross-talk is observed in Fig. 3.15 (b) (lighter blue) with below 5% weighting spread out over the other OAM coefficients. This corresponds to the error found for the

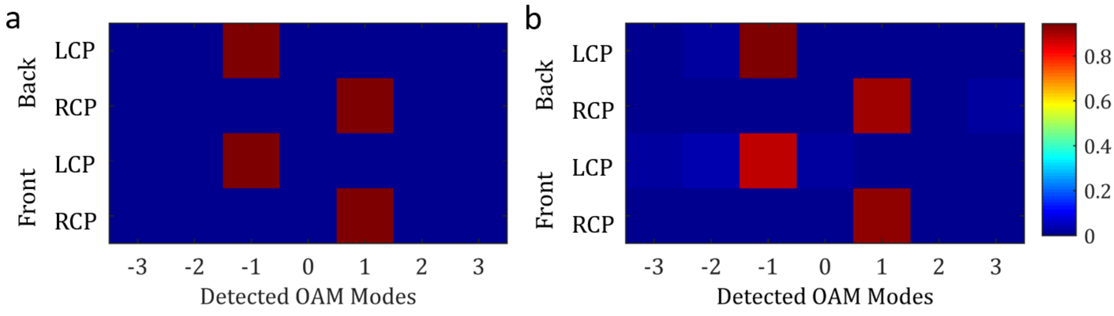

FIGURE 3.15: (a) Theoretical and (b) experimental modal decomposition results for QP generated modes from CP inputs onto the front and back of the QP in the LG ($p = 0$) basis.

demonstrated modal decomposition in Fig. 3.13. Subsequently, it can be concluded with sufficient accuracy that the QP generates OAM with a handedness related to the incident CP in accordance to the analytical expression (Eq. 3.29). Additionally, the operation retains the assumed directional invariance with regards to the SAM and OAM handedness pairing.

3.3.4 A classical entanglement generator

Now that the operation of the QP has been characterized, the type of modes generated may be considered in its entirety. In other words, if the polarization and OAM DoFs are paired with STOC and exist in superposition, what kind of beams are generated and how may the QP be viewed in terms of this? This may be explored by considering a specific case. If incident on the QP with a superposition of CP states, such as with vertically polarized light,

$$|V\rangle = \frac{i}{\sqrt{2}}[|L\rangle - |R\rangle],$$

the STOC action affords another feature of the element whereby it becomes a classical entanglement generator. This may be intuitively seen with this QP by applying selection rules (Eq. **??**) to the CP superposition (Eq. 3.19):

$$\hat{QP}\,|0,H\rangle = \frac{i}{\sqrt{2}}\hat{QP}[|0,L\rangle - |0,R\rangle] = \frac{i}{\sqrt{2}}[|-1,R\rangle - |1,L\rangle] \tag{3.39}$$

From the expected states formed, the spatial mode described by OAM = -1 is paired to RCP while OAM = 1 is paired to LCP. As a result, these OAM and polarization degrees of freedom in the beam form a non-separable relation such that neither can be factored out as was seen in Section 2.3.4. Experimentally, the generated mode is shown as the rightmost upper beam in Fig. 3.16 with a doughnut spatial distribution. Separation of this mode into the CP basis yielded the modes to the left of the image where the respective CPs are superimposed on the images. Retention of the doughnut spatial distribution in these bases demonstrates the OAM pairing determined in the modal decomposition and as was discussed for Fig. 3.11.

Further analysis of the mode is shown in the bottom row of the figure. This constituted further projective polarization measurements into the linear polarization basis. It was achieved by replacing the PG shown in the experimental setup of Fig 3.10 with a linear polarizer in a rotational mount. Here, the non-separability of the spatial mode can be seen more intuitively whereby lobes may be seen with orientations that rotate with the polarizer. Specifically, from the leftmost projected distribution, vertical orientation of the lobes coincides with the vertical orientation of the polarizer. Rotating the polarizer though to anti-diagonal, horizontal and diagonal orientations as

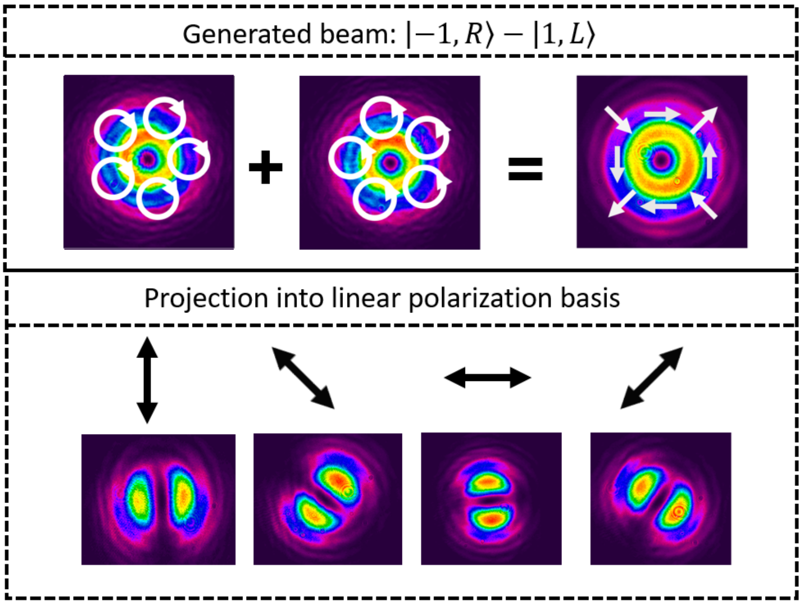

FIGURE 3.16: Example of the QP classically entangling polarization and spatial degrees of freedom with the generation of an azimuthally polarized anti-vortex vector beam from a vertically polarized Gaussian input (scalar beam).

depicted by the arrows above these images shows the lobes assuming the same directionality. It follows that the projective measurements yield the polarization distribution overlaid on the image of the generated beam. The opposite pairing of the OAM and SAM modes results in an azimuthal anti-vortex vector beam being generated. Comparison of both the mathematics and spatial distributions in Fig 3.16 and Fig 2.14, emphasise the QP as a useful element which may be used as an entanglement generator such that orthogonal modes may be both paired and laddered with this element.

3.3.5 Revealing the radial modes in vortex beams

An interesting physical consequence presents when generating OAM beams with QPs. As will be seen, this generation method directly affects the spatial distribution of these types of beams. Here the QP generates a well-defined azimuthal profile across the beam, but neglects the spatial profile associated with the incoming beam. Due to this type of modulation, the energy of the beam begins spreading outwards with the excitation of additional radial modes as the OAM being carried by the beam increases. Based on the popular use of QPs, being aware and compensating for this effect is important and is of particular relevance to this work in light of propagating of a QW in OAM space based on the generation of these modes. Here this effect is explored in detail, demonstrated experimentally. Alternative solutions are also presented on how to overcome this problem by including complex amplitude modulation.

Theory

A vortex beam may be written as an azimuthal phase variation with a Gaussian envelope in the generation (waist) plane:

$$\psi^l(r,\phi) = G(r)e^{-il\phi} \tag{3.40}$$

where $G(r)e^{r/w_0}$ is the Gaussian envelope (Eq. 2.70, section 2.3.2), r is the radial coordinate, w_0 the Gaussian beam waist, $e^{-il\phi}$ the azimuthal phase variation with associated OAM of $l\hbar$ per photon, where l is a non-zero integer. It has been noted that vortex beams may also be expressed as a special case of Hypergeometric-Gaussian modes [78].

This vortex field, however is not a solution to the free-space wave equation and as such vortex beams are not eigenmodes of free-space, resulting in the excitation of supplementary fields [85] and spatial polarization variance with propagation [161].

OAM-carrying beam structures fulfilling the conditions of the free-space paraxial wave equation include Bessel [162; 163] and Laguerre-Gaussian (LG) modes [85; 95; 164] with which these general vortex beams may subsequently be compared. Analysis could be generalized to either of the mode types, but this paper will focus on the LG modes whereby the amplitude at the beam waist (Eq. 2.77, Section 2.3.2) is given by [84]:

$$a(r,\phi,z) = \sqrt{\frac{2p!}{w^2\pi(p+|l|)!}}\,\underbrace{(\frac{r\sqrt{2}}{w})^{|l|} L_p^{|l|}(\frac{2r^2}{w^2})}_{\text{amplitude term}}\, e^{\frac{-r^2}{w^2}}\, e^{-il\phi} \tag{3.41}$$

Accordingly, $L_p^{|l|}$ is the Laguerre polynomial of orders p, l where the radial index, indicating the number radial nodes, is $p \leq 0$.

It can be seen that for pure LG vortex modes (p = 0), there is an additional amplitude term, $(\frac{r\sqrt{2}}{w})^{|l|}$, that ensures the invariance associated with the eigenmodes as they propagate. Similar terms with the same effect are also present in Bessel-Gaussian and other beams that are eigenmodes of free- space. It is often unappreciated that it is this radial amplitude term, which is dependent on the azimuthal index ($|l|$), and not the azimuthal phase term itself ($|l|\phi$), which is responsible for the characteristic beam core intensity null associated with vortex beams. The observation of a null in vortex beams without this amplitude term is instead due to high spatial frequencies induced by the helicity of the phase together with their attenuation due to the finite apertures in the optical system [165].

It is well-known that an optical field may be expressed as a linear combination of basis modes, as was shown with Eq. 3.33 in Section 3.3.3:

$$U(r) = \sum_j c_j\phi_j(r)$$

where the symbols retain the same meanings ($r = (x, y)$, $\psi_j(r)$ represented the basis mode,$c_j = \rho_j e^{i\delta\phi_j}$, ρ_j is the corresponding mode amplitude and $\delta\phi_j$ is the intermodal phase difference). It additionally follows that the vortex beam (of a particular azimuthal index, l) may easily be expressed in terms of LG modes of the same azimuthal index,

Here $|c_p|^2$ yields the power weighting of the vortex beam among the LG modes and can be expressed as [166]:

$$c_p = \sqrt{\frac{(p+|l|)!}{p!}}\frac{\Gamma(p+\frac{|l|}{2})\Gamma(\frac{|l|}{2}+1)}{\Gamma(\frac{|l|}{2})\Gamma(p+|l|+1)} \tag{3.42}$$

where $\Gamma(x)$ is the gamma function. It is clear that the vortex beam is the sum of many radial modes in the LG basis, i.e., the same azimuthal index as the vortex beam but with several radial indices. The implication is that the power in the desired $p = 0$ mode can be very small, approaching zero as the azimuthal index increases.

Ensuing evaluation of the modes indicate a significant spread of the power distribution to the outer spatial distributions, increasing concomitantly with the input OAM content. In other words, rings around the central beam appear due to additional radial indices when analyzed in terms of LG modes. This is illustrated in Fig. 3.17 where the power content of each mode, radial and azimuthal, in the LG basis is shown for a given input azimuthal mode. For example, an input vortex mode of l = 1 has only 78% of its energy in the $LG_{0,1}$ mode, with the rest spread across higher radial modes.

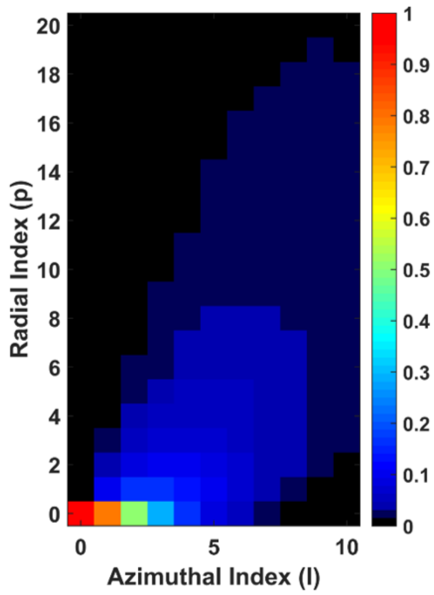

FIGURE 3.17: Theoretical density plot, determined from Eq. 3.42, illustrating the spread of power into radial modes for vortex beams generated through phase-only transformations and thus lacking the amplitude term highlighted in Eq. 3.41.

It can be seen from Fig. 3.17 that there is a clear increase in the modal spreading as the input OAM of the vortex beam is increased: an input vortex mode of l = 10 has only 0.4% of its energy in the $LG_{0,10}$ mode. Consequently, a direct result of the missing amplitude term is an increase in the power distribution as the OAM content of the vortex beam increases. This is seen by the increased spread of blue over the p-values at higher OAM values. Observation of the low intensity also indicates a low power content in any one of the radial modes with higher OAM. Furthermore, there is a movement of power concentration to higher radial modes with OAM as evidenced by the lower intensity (black) for $p = [0, 2]$ of $l = [7, 10]$. In fact, beyond l = 4 the power content of the zeroth radial mode, the desired mode, is close to zero.

Characterization

Characterization of these phase-only modulated modes was carried out with the experimental setup discussed for the QP modal decomposition in Fig. 3.13. Seeing as detection of radial modes were of importance, further test of the system into the radial degree of freedom was also done by generating a range of LG modes where $p = [0, 7]$ and decomposing into the radial basis. Figure 3.18 shows the outcome of this test.

A strong main diagonal concurs with the accuracy seen in the OAM degree of freedom. Cross-talk along the main diagonal here, however, is slightly stronger as the decomposition is more sensitive to the size of the modes and alignment of the optics. This error (<10%) , though, is within acceptable bounds and thus implies the decomposition achieved by the system would be accurate.

Utilizing the same system, SLM_1 was then programmed with an azimuthally varying phase profile (no amplitude modulation). Accordingly, the vortex beams of interest were generated in the 1st diffraction order, allowing them to be studied.

An l = 1 vortex structure (without the amplitude term) was generated by encoding SLM1 as described. Decomposition of the beam was performed for radial modes, $p = [0, 7]$ which yielded values for the power coefficients described by Eq. 3.42. Figure 3.19 displays these experimental

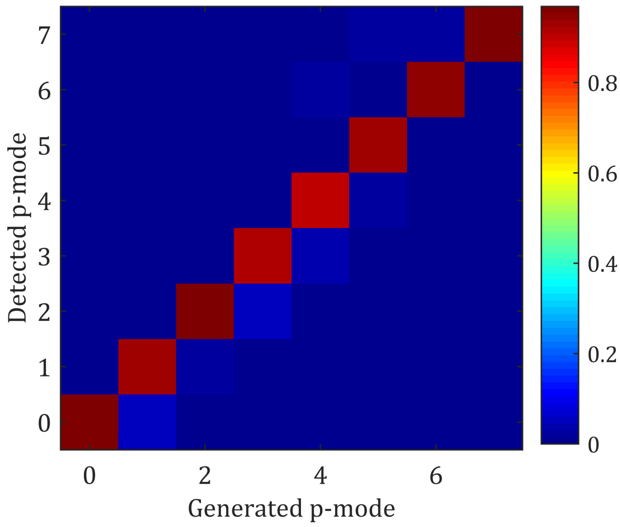

FIGURE 3.18: Modal decomposition for a series of $LG_{p,0}$ modes for p ranging between $[0, 7]$.

values in terms of percentages together with the theoretical values (blue curve) calculated from Eq. 3.42 for comparison.

Majority of the power (78.5%) is still retained within the fundamental radial order, with maximal distribution of the remaining power between immediate adjacent radial modes. Summation over the theoretical power coefficients indicates that 95% of the total power falls within the $p \leq 4$ radial range. The experimental values are in excellent agreement with the expected theoretical values as seen by close positioning of the respective data points and the maximum deviation of 2% occurring within the system error at $p = 0$.

Similarly, encoding SLM_1 with a vortex structure of $l = 10$ (Eq. 3.40) generated a vortex mode of high OAM for radial decomposition and analysis. Decomposition of the field was performed for LG radial modes, $p = [0, 18]$. A plot of results similar to that of Fig. 3.19 is presented in Fig. 3.20 with theoretical (blue curve) and experimental comparison (red data points).

A significant shift and redistribution of power can be seen across the radial modes in comparison to $l = 1$ (Fig. 3.19) as a result of the higher OAM content. The power maximum being centered at $p = [7, 8]$ and a drop of 78.1% power in the fundamental mode (as only 0.4% remains in this mode for Fig. 3.20) clearly illustrates this. Additionally, the maximum power carried in a single radial mode decreased by 76.3% as seen in the power difference between p = 0 (Fig. 3.19) and $p = 7$ (Fig. 3.20), indicating that 76.3% more of the power is distributed amongst other modes than for a mode with OAM of an order of magnitude less. Furthermore, summation over the first 50 theoretical power coefficients only yields 64% of the total beam power and 95% can be seen to be spread over the first 500 radial modes.

Further experimentation including the addition of a QWP and QP as depicted in Fig. 3.14, allowed for a special case of vector vortex modes to be tested. Such q-plates are now routinely used in laboratories to create scalar and vector vortex beams by imparting an azimuthal–only phase to the input beam, as was done with the SLM, but by geometric phase control [138] rather than dynamic phase control. Identical results for the q-plate as reported here for the SLM was found. This is illustrated in Fig. 3.21 where the detected radial modes were removed for an $l = 1$ beam generated by the QP by passing a beam with the amplitude term pre-encoded such that the azimuthal term supplied by the QP creates an eigenmode of free space. It follows that 100% power is expected in the fundamental mode.

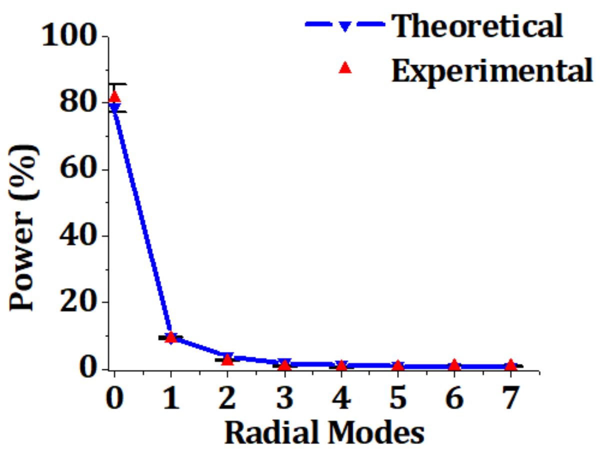

FIGURE 3.19: Experimental and theoretical comparison of power weighting across radial modes $p = [0, 7]$ for a vortex mode of $l = 1$. The blue line (theoretical) is included to guide the eye. Error bars for $p > 0$ are too small to be observed.

It can be seen that maximal intensity exists in the fundamental radial mode, confirming that it is the phase variation itself (the vortex) and not the manner in which it is implemented that matters. Aberrations present in the QP are detected as an additional radial mode $(p = 2)$, causing the slight mismatch. It may thus be concluded that minimal aberrations were present in the QP and as such, poor beam quality would be due to the unmodulated azimuthal induced phase and not the quality of the QP itself.

Clear dissipation of vortex beam power over an increasing number of radial modes can subsequently be seen with beams of higher OAM content which should inspire caution in their utilization and generation for high OAM experiments.

Images of the beams with (LG) and without (azimuthal-only vortex) the amplitude term of different OAM values $(l = 5, 10)$ were taken in the far field for visual illustration of the amplitude term effect. This is presented in Fig. 3.21. The values shown on the bottom-right corners give the corresponding theoretical and experimental percentage power contained in the desired $p = 0$ mode.

Figure 3.22 (a) and (b) display $LG_{0,5}$ and $LG_{0,10}$ beams in the far-field where the power is seen to be confined to the fundamental radial mode as expected. Comparison with the respective beams with missing amplitude terms (c) and (d) clearly show further radial power distribution by the supplementary rings. An increase in the shift of power to farther rings with an increase in OAM is also evident. Additionally, modes (c) and (d) are larger than that of the modes containing the amplitude term, demonstrating the distribution of maximal power to further radial modes as the diameter of the radial mode with the peak power is then larger than the fundamental mode.

This is supported by the power values given in the bottom corners, where a very high percentage of the beam power is seen to be contained in the fundamental radial mode for beams (a) and (b) that contain the amplitude term and much poorer percentages for beams (c) and (d) without the term. Furthermore, the percentage power in the $p = 0$ mode may be appraised as beam purity where the amplitude-containing beams can be seen to have a high beam purity as opposed to the deteriorating purity apparent in the beams without this vital term.

Reconsidering the LG equation (Eq. 3.41) it follows that one could expect the Laguerre term to be solely responsible for the radial power distribution as it controls the radial degree of freedom

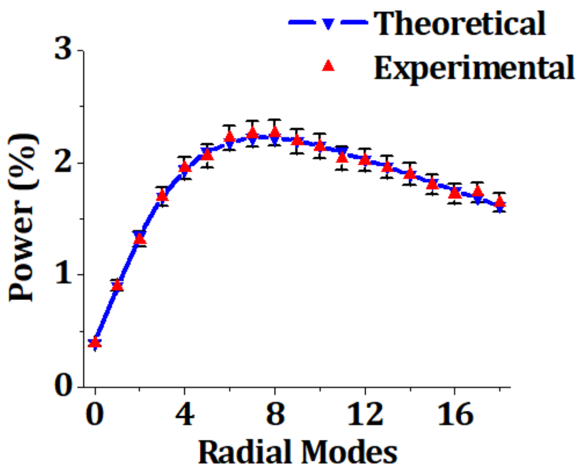

FIGURE 3.20: Experimental and theoretical comparison of power weighting across radial modes = [0, 18] for a vortex mode of l = 10. The blue line (theoretical) is included to guide the eye.

(p). In the case where $p = 0$, however, this polynomial term reduces to 1 and subsequently has no effect on the radial distribution. Examining the OAM modulated amplitude term, it could also be naively expected that it does not contribute to radial distribution, but on comparison of Eq. 3.40 and 3.41, it is clear that for $p = 0$, this is the only non-constant term missing and thus is responsible for the difference observed between these azimuthal-only vortex beams and the LG beams which are eigenmodes of free-space. It follows that exclusion of this term removes the OAM dependent amplitude modulation and forces nature to correct for it by introducing radial distributed fields that may be interpreted as additional radial modes in the LG basis. Outspreading of the beam power is subsequently a direct consequence of forcing nature to exact OAM modulation of the amplitude whereby this unintended effect is rapidly enhanced with increased OAM content in the vortex beam.

Implications of this phenomenon can be deleterious for experimental work where beam power and mode purity is a concern, particularly when beams of higher OAM are required. Generation of these missing-amplitude beams in such experiments could result in many issues such as detection thresholds, increased measurement uncertainties as well as the number of optical components it will be possible to use in the experimental design. Due to this drastic power loss with OAM, utilization of these beams could additionally cause beam power to become an issue in experiments where it would ordinarily not be a consideration.

In establishing amplitude modulation to prevent this, however, there will be initial overall transmissive and/or diffractive power losses induced by the methods currently available including spatial light modulators where there is perceptible loss in beam power. Subsequently, consideration of experimental parameters is an important factor. Beams that are not of small OAM result in radial power distributions to such a degree that the nature-inspired power loss far outweighs the loss induced by the technique required for introducing OAM amplitude modulation.

It follows that results demonstrated a rapid increase in radial power divergence with OAM content along with a shift in the power maximum to farther radial positions. Corresponding deterioration of mode purity was subsequently inferred. Further inspection between the modes led to the deduction that this phenomenon was the natural response to the absence of amplitude modulation by OAM. Subsequently, presence of this amplitude term correlates to a counter-intuitive control of radial power distribution. Awareness of this dissipation of beam power from the zeroth order is important for many experiments that require high levels of beam power in these radial

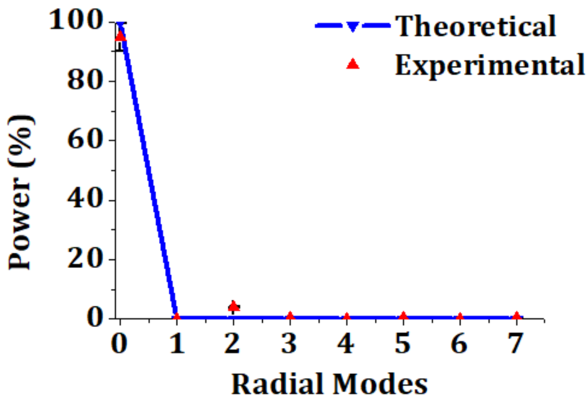

FIGURE 3.21: Experimental and theoretical comparison of power weighting across radial modes $p = [0, 7]$ for a QP-generated vortex mode of $l = 1$ with the radial modes removed. The blue line (theoretical) is included to guide the eye. Error bars for $p > 0$ are too small to be observed.

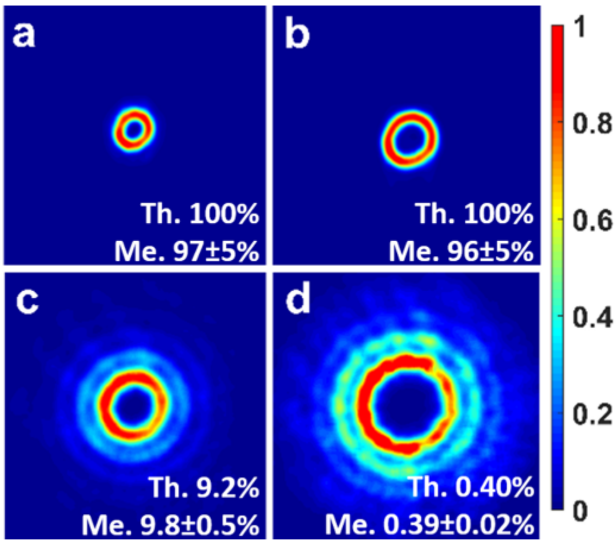

FIGURE 3.22: Experimental far-field images of vortex beams (a) l = 5, (b) l = 10 containing the amplitude term and (c) $l = 5$, (b) $l = 10$ without the amplitude term, illustrating its effect on the retention of beam power within the lower order radial modes as well as encoded beam structure. Measured (Me.) and theoretical (Th.) values for the percentage power occurring in the $p = 0$ mode of the beam are displayed in the bottom-right corner. Intensities are normalized to the highest value for the individual images and thus are not indications of relative power differences between the beams.

modes as well as the solution to this problem by amplitude modulation.

More specifically, when carrying out a QW in OAM space, the OAM charge carried by the beams increase with the number of steps. This large spread in power subsequently results in a greater divergence in the overall beam being worked with than was suggested in Eq. 2.80. As utilizing the QP is essential for OAM laddering by polarization control, the alternative OAM generation methods cannot be utilized. Working with the spread in power is consequently unavoidable and as such this effect may be mitigated by incorporated larger elements and smaller beam sizes into the setup designed for the implementation. Imaging the beam waist plane along the propagation path may also be considered so as to confine the increase in beam size to these factors by eliminating the opportunity for the beam to diverge in the desired planes.

3.4 Detection: unravelling the twist

Using the QP to ladder OAM modes in correspondence to QW propagation rules offers a promising avenue for implementing such a walk, however, tracking or detecting the walk requires determination of both what OAM is present (i.e. "what position the walker occupies") as well as how much of that mode is present in the beam (i.e. "how much of the walker is occupying each position"). There are several options for detecting the OAM modes and weighting of a generated beam. One such option is the modal decomposition technique discussed earlier. This, however, has deterring consequences, namely, large loss of power in diffraction orders as well as restrictions on how many modes may be analyzed, based on the number of match filters that may be multiplexed. Mode sorting offers a promising alternative method that is energy efficient and convenient for detecting these parameters. How this technique works as well as the experimental limitations and accuracy are explored here.

3.4.1 Working principles

Application of geometric transformation concepts such as coordinate transformations to light through the use of optical systems can exact a desired transformation to light [167]. OAM mode sorting relies on the application of such a coordinate transformation. More specifically, the technique takes advantage of the circular geometry associated with OAM so that a geometrical mapping translates circular to rectangular geometry [168] as illustrated in Fig. 3.23 (a). The resultant phase distribution 'unwrapping' causes OAM to be transformed into transverse momentum with a linear phase gradient [169] as demonstrated by in the (u, v) coordinate space of the figure.

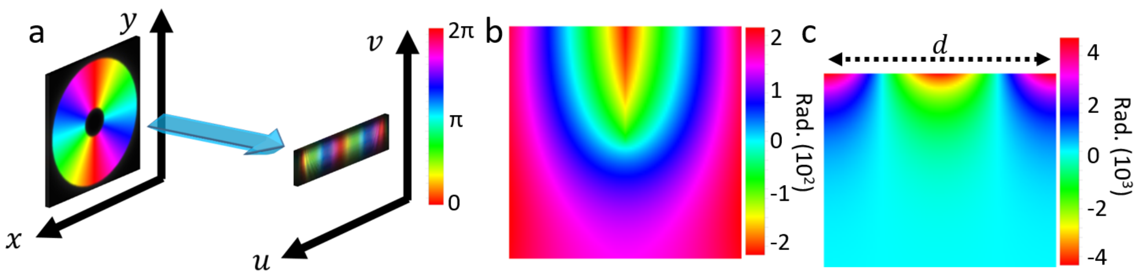

FIGURE 3.23: The (a) illustration of a conformal mapping which 'unwraps' an OAM = 2 mode to a transverse phase gradient and the phase distributions preforming the (a) mapping transformation and (b) correction due path length differences.

Physically, this $(x, y) \rightarrow (u, v)$ transformation is achievable through application of a phase distribution, described in Eq. 3.43.

$$\varphi_1(x, y) = \frac{d}{\lambda f}[y \tan^{-1}(\frac{y}{x}) - x \ln\left(\frac{\sqrt{x^2 + y^2}}{b}\right) + x] \tag{3.43}$$

Visualization of this distribution is generated in Fig. 3.23 (b). Here d is the fixed unwrapped beam length, b affects the location in the (u, v) plane, λ is the wavelength and f the transforming lens focal length. Associated phase distortions in the 'unwrapped' beam from optical path length variation requires correction by a second phase distribution, described in Eq. 3.44 [168; 170] and Fig 3.23 (c).

$$\varphi_2(u, v) = \frac{db}{\lambda f} e^{\frac{-2\pi u}{d}} \cos\left(\frac{2\pi v}{d}\right) \tag{3.44}$$

The resultant phase distribution 'unwrapping' causes an OAM to transverse momentum with a transverse phase gradient of $e^{il \tan^{-1}(\frac{y}{x})} = e^{il\frac{2\pi v}{d}}$ across the beam length [61–63]. The unwrapped beam in the Fourier plane (FP) of a lens forms a diffraction-limited elongated spot [169]. As the 'unwrapped' mode contains a phase gradient limited to the length, d, all OAM modes result in a transverse phase gradient that are integer-multiples of each other (shown in Fig. 3.24 (a)).

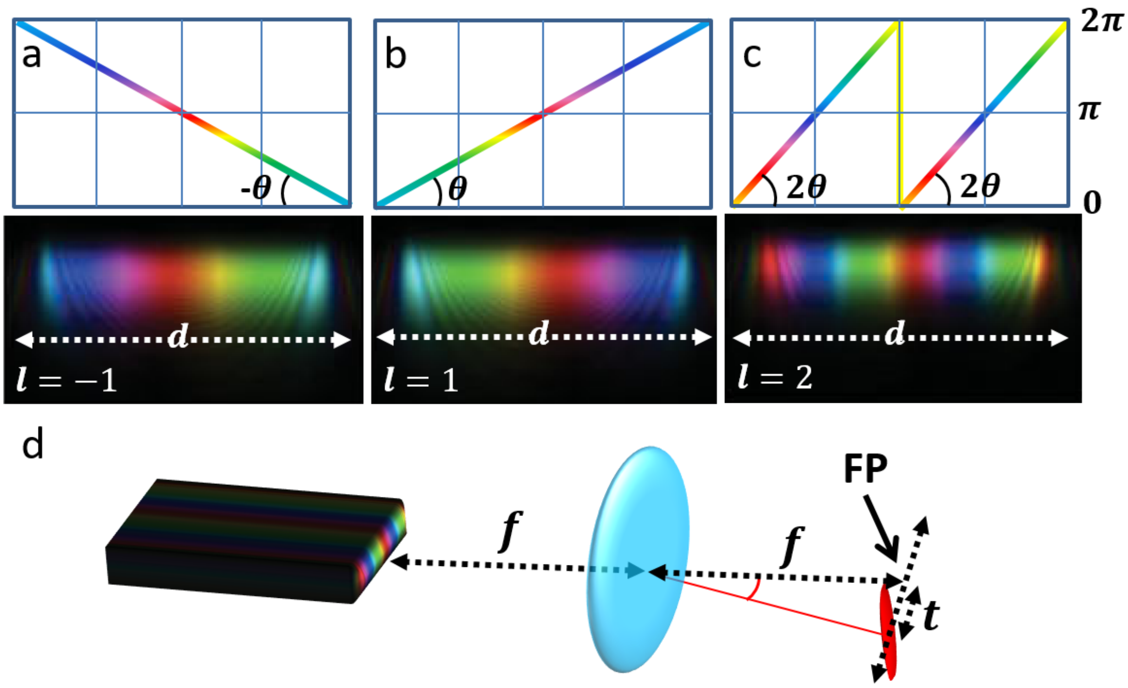

FIGURE 3.24: Colour map illustration of the phase gradient resulting from the OAM geometric transformation for (a) l = -1, (b) l = 1 and (c) l = 2. (d) Depiction of the sorting action performed by a Fourier transforming lens after the phase correction element.

The lens then forms the spot at a phase gradient related position at the focal plane due to its Fourier transforming action. It follows that the spot position (t) is then OAM-dependent (Eq. 3.41) [168].

$$t = \frac{\lambda f l}{d} \tag{3.45}$$

Moreover, intensity of the spot indicates the 'amount' of any OAM-mode present. The mode sorter technique employed with refractive elements allows for efficient detection of a large range of OAM modes and the associated weightings, enabling detection of low intensity sources and in comparison to other techniques such as the SLM modal decomposition mentioned earlier.

A distinct disadvantage occurs with this technique, however, when considering cross-talk between adjacent modes. Due to the finite unwrapped beam size, the width of the spot created in the FP is diffraction-limited, resulting in a constant overlap between modes [168; 169]. It was subsequently demonstrated that a maximum of 80% may be achieved in the required position with good alignment, while the other 20% spreads into the adjacent mode positions [170]. Increasing the unwrapped beam size may appear to remedy the situation as it would increase the separation distance between the spots. This, however, also decreases the phase gradient, resulting in the spot width to spacing ratio remaining similar [169]. Consequently, the overlap between modes is an intrinsic property of the system. A solution was suggested by Berkhout et al. [168], though, whereby the unwrapped beam length may be increased through simply copying the unwrapped modes and placing them next to each other.

As the linear gradient ranges in periods of 0 to 2π for every OAM value, placing copies alongside the the initial unwrapped beam does not disrupt the configuration, allowing this technique to decrease the spot width without altering the spacing [169; 171]. The copied beams then add an extra N_c rotations to this 0 to 2π periodic gradient.

Further investigation and subsequent implementation was then carried out by including two additional phase transformations on SLMs after the mode sorter optics [169; 171]. Here the first transformation copied the phase-correction unwrapped beam according to the phase term:

$$\varphi_{FOE}(x) = \tan^{-1}\left[\frac{\sum_{m=-N}^{N} \gamma_m \sin\left(\left(\frac{2\pi\omega}{\lambda}\right)mx + \alpha_m\right)}{\sum_{m=-N}^{N} \gamma_m \cos\left(\left(\frac{2\pi\omega}{\lambda}\right)mx + \alpha_m\right)}\right] \tag{3.46}$$

which resulted in $N_c = 2N + 1$ copies placed alongside each other based on the angular separation, ω, in the x-direction, causing the element to be labeled a fan-out element (FOE) [169]. γ_m and α_m serve as phase and intensity parameters, respectively, for the different orders (m). The second transformation subsequently served as a correction for this fan-out operation.

Ruffato et al. [172] recently combined the log-polar coordinate and fan-out functions as well as the respective phase corrections to condense the operations into two diffractive elements. There the copying element was combined with the unwrapper so that the beam could be simultaneously copied N_c times and unwrapped alongside each other before encountering the second element. Subsequently, the correction terms for the path length difference from the unwrapper is combined with the corrections for joining the copied beams such that a dual and once-off correction is carried out on the beam. It follows that more accuracy should be expected with this method in addition to the convenience of utilizing a more compact system, where the alignment for the system is restricted to half the elements given in the scheme implemented by Mirhosseini et al. [169].

These mode sorters offer a convenient method in which to extensively detect the OAM modes and weightings present in a spatial mode. The degree to which this method is advantageous, in addition to its accuracy, is consequently of interest for its use as a detection mechanism for the QW. As a result, both the refractive and diffractive elements were examined in the following section.

3.4.2 Experimental test configuration

Testing the performance, limitations and accuracy of these elements was determined using the experimental configuration shown in 3.25.

Here a 633 nm HeNe laser was expanded with a 10x objective lens and collimated onto an PlutoVis SLM, encoded with holograms, patterning the amplitude and phase profile of the incident beam. Light reflected off the SLM was then directed through a $4-f$ system with an aperture in

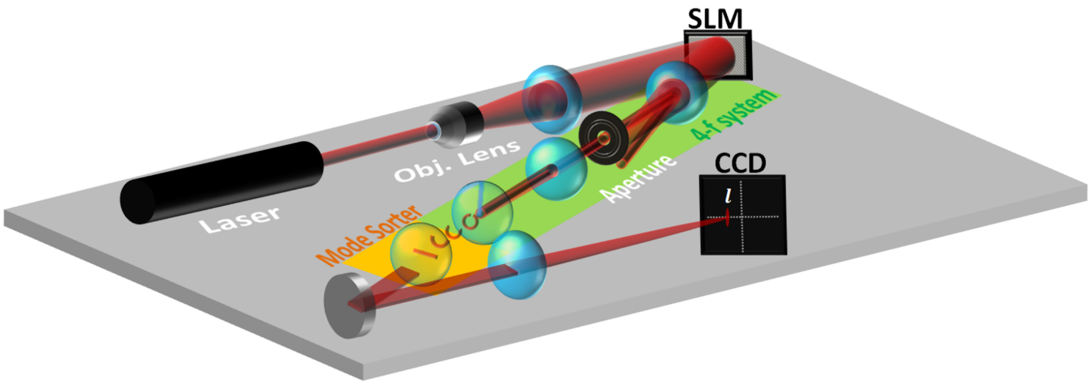

FIGURE 3.25: Schematic of the experimental configuration used to characterize the mode sorter.

TABLE 3.1: Comparison of design parameters for the refractive and diffractive sorters

Design Parameters	**Refractive Sorter**	**Diffractive Sorter**
Element diameter	12.7mm	0.800 mm
Recommended incident beam radius on MS	2-10mm	0.500-0.800 mm
Design wavelength	633 nm	632.8 nm
Recommended wavelength range (λ)	400-1000 nm	532-732 nm
Separation distance between elements	300.5 mm	8.500 mm
Unwrapped beam length (d)	10.5 mm	1.12 mm (1copy) 0.500 mm (3copy)

the FP, spatially filtering and imaging the 1st order with the encoded structure onto the mode sorter system. The 1st element preformed the required geometrical transformation, unravelling the azimuthal phase, with the 2nd element carrying out the required phase corrections. A lens placed in an $f-f$ configuration after the 2nd element served to sort the encoded modes onto a Spiricon SP260U CCD placed in the FP as indicated in Fig 3.25.

Both refractive and diffractive sorters were characterized with this configuration where minor adjustments were applied to accommodate the different parameters. These parameters are summarized in Table 3.1.

Consequently, for characterization of the refractive sorter, the $4-f$ system comprised two 300 mm focal length lenses for a 1:1 magnification of the encoded mode. A 500 mm focal length was then used for the sorting lens. In contrast, a 2:1 demagnification was achieved with 400 mm and 200 mm focal length lenses in the $4-f$ system respectively for the diffractive sorter. This was required so as to contain the encoded beam within the sorter dimensions without sacrificing the effectiveness of the SLM due to its resolution. A 100 mm focal length sorting lens was utilized due to a greater divergence of the unravelled beam in the diffractive case.

3.4.3 Mode sorter performance

Along with the refractive sorter, two different diffractive sorters were characterized, both with the same parameters as shown in Table 3.1. These diffractive sorters varied in the number of copies that were created where 1 and 3 copies were generated respectively. As the 1-copy and refractive sorter both generated a single unwrapped beam, the expected difference in performance between the sorters is limited to the range of OAM modes that can be accurately sorted. This is namely due to the refractive sorter being able to receive beams of lager radii, thus compensating for the increased deviation of the angle of incidence for the beam rays directed to the sorter as the OAM increases. This should then result in a higher range of the sorted OAM values being viably accurate [173]. As a result, evaluation of the refractive sorter was restricted to the comparative OAM ranges while the 1- and 3-copy sorters were further characterized, allowing a more accurate comparison due to the parameter similarities.

Experimentally sorting modes

Figure 3.26 experimentally illustrates the transformation performed by the mode sorter on LG modes ranging from -3 to 3 OAM. Here the top row shows the modes generated by the SLM and directed through the sorter with the OAM per photon written above the respective spatial modes. In the row below, the elongated spots formed in the FP of the sorting lens are shown. Cross-hairs in the images mark the position of the 0 OAM mode. Consequently, the OAM dependent sorting power of the elements may be clearly seen where the negative OAM spots are formed to the left of the cross-hairs and the positive OAM spots to the right. Additionally, the position can clearly be seen to move incrementally in the OAM handedness direction, based on the OAM value.

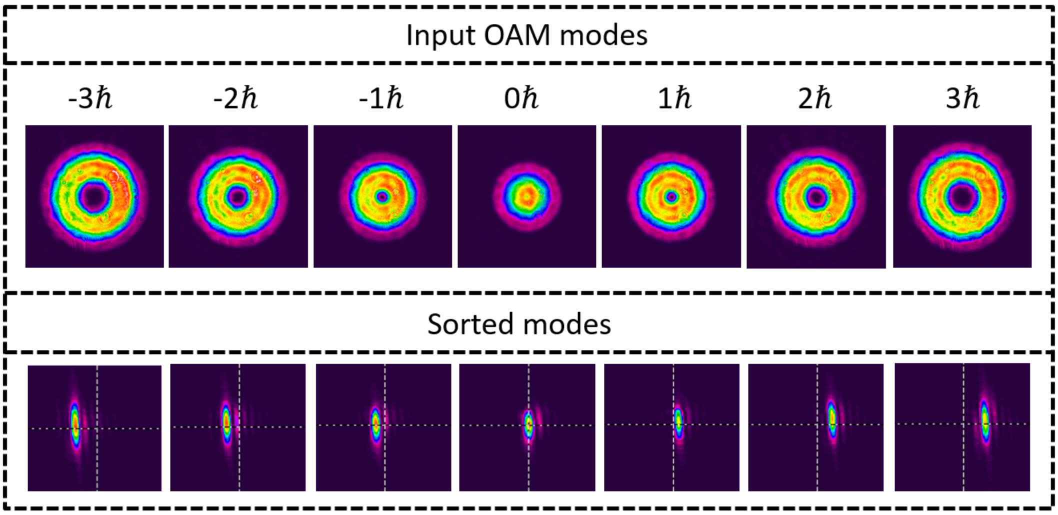

FIGURE 3.26: Illustration of the sorting action of a MS (bottom row) for a range of encoded OAM values (top row) between [-3,3].

Spot positions

As this incremental movement in position is theoretically governed by Eq. 3.45, performance of the mode sorters may be evaluated by experimentally measuring the position of the spots formed for different OAM values. Due to these positions conveying the detection of which OAM modes are present when evaluating an arbitrary beam, comparison of these values allow for the anticipation of both the accuracy and consistency which may be expected for the modes detected by this

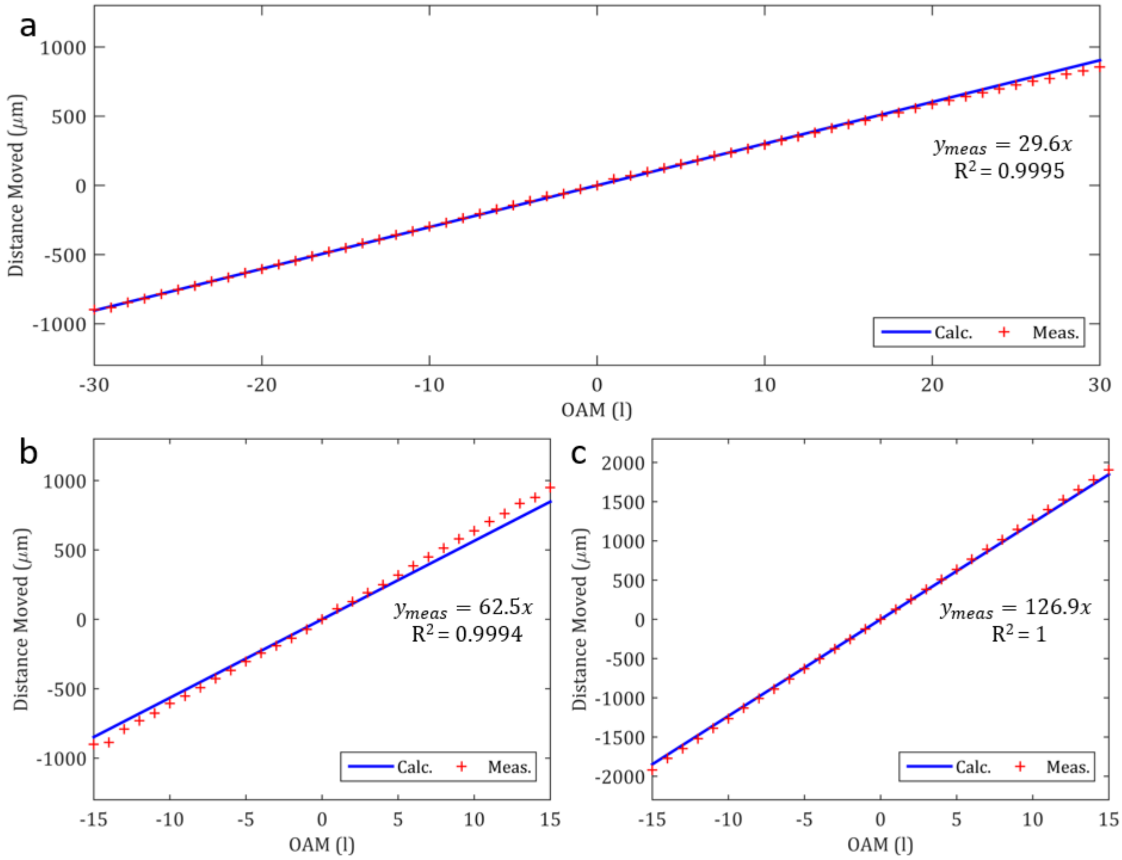

FIGURE 3.27: A comparison of measured (red) sorted spot positions against that which was theoretically expected (blue) based on the designed unraveled beam length, d for the (a) refractive, (b) 1-copy and (c) 3-copy mode sorter.

technique. This was carried out for the refractive and both diffractive sorters. Accordingly, the expected function of the distance between sorted modes relative to the OAM (l) is expected to be

$$t_r = \frac{\lambda f l}{d} = \frac{(633\text{ nm})(500\text{ mm})}{(10.5\text{mm})} l = (30.1l\ \mu\text{m})$$

for the refractive sorter,

$$t_r = \frac{\lambda f l}{d} = \frac{(633\text{ nm})(100\text{ mm})}{(1.12\text{mm})} l = (59.6l\ \mu\text{m})$$

for 1-copy diffractive sorter and

$$t_r = \frac{\lambda f l}{d} = \frac{(633\text{ nm})(100\text{ mm})}{(0.5\text{mm})} l = (126.6l\ \mu\text{m})$$

for the 3-copy diffractive sorter.

The corresponding results are given in Fig. 3.27 where the positions detected for the range of OAM values directed through the sorter are plotted alongside the calculated functions determined above.

Accordingly, these positions were made relative to the $l = 0$ mode. Based on the OAM range logic discussed previously, the OAM range for which the positions were measured was greater for the refractive sorter with OAM = [-30,30], while the diffractive sorter range was evaluated for the range OAM = [-15, 15].

Considering Fig. 3.27 (a), the experimental shift in spacing agrees well with the calculated value obtained from the design parameters with a difference of 30.1μm – 29.6μm = 0.5μm. Additionally, the positions form a straight line as evidenced with the high R^2-value of 0.9995. This indicates a consistent positional shift which should lead to defined boundaries between the experimentally formed OAM spots. As a result, the detected intensities at those positions should be an accurate reflection of the modes and weightings in the beams being sorted.

Based on the spacing calculations, the expected separation distance for the 1-copy mode sorter was 59.6μm compared to the average experimental value of 62.5μm in Fig. 3.27 (b). This deviation is notable with a 62.5μm – 59.6μm = 2.9μm difference as it accumulates with the number of increased modes as evidenced by in Fig 3.27 (b) for the higher OAM modes. A straight line, however, is still formed by the experimental shift in position with OAM. This may be explained by the length of the unwrapped beam where it may have been slightly shorter in the experimental implementation than the parameter quoted. The performance of the 1-copy sorter shall thus be evaluated with the experimental positional shift where adequate performance may be expected with a similarly high R^2-value of 0.9994 compared to the refractive sorter. Accordingly, adequate performance of the sorter may be expected. It may be noted that the refractive sorter has a similar regression coefficient to the 1-copy diffractive sorter as the range is larger, leading to slightly larger deviation from a straight linear fit as a result of the skew angle increasing.

For the 3-copy mode sorter, comparison of the calculated and measured values yield a 126.9μm – 126.6μm = 0.3μm difference, indicating excellent agreement. Additionally, the R^2-value of 1 gives rise to good expectations in terms of detecting the correct OAM values.

Alignment range and cross-talk

It follows that by generating bins along the direction of the spot movement, the intensity may be integrated over to determine both the presence and weighting of the different OAM modes. Here the bin positions were determined by Eq. 3.45 with a slight adjustment in the 1-copy case. Accordingly, determination of the viable range of OAM modes for which the MS may be used was achieved by binning for a range of OAM modes across the captured CCD image for each mode generated. OAM modes from -30 to 30 for the refractive sorter and -15 to 15 for the diffractive sorters were then sent separately through the MS and the detected modes then read out. The results are given in Fig. 3.28 for the different sorters.

Here the presence of cross-talk is indicated by the off-diagonal elements. It may be seen that the minimum cross-talk achievable was 25% for the most aligned spot detected (as shown by the range of the color map) for both the refractive and 1-copy sorters in Fig 3.28 (a) and (b) respectively. It may also be observed that near 0 OAM, the refractive sorter generates a larger amount of cross-talk than in the diffractive mode sorter elements for the best alignments that were achievable. Figure 3.28 (c) yields the characteristic density plot for analysing the 3-copy mode sorter. Here the minimum cross-talk achievable may be seen as substantially reduced with only 10% being detected in the incorrect modes.

Alteration of the strongest detected modes away from the diagonal indicates the OAM mode detected is no longer correct. As a result, the viable sorting range may be established by observing the number of modes where the maximum intensity remains within the diagonal. It follows from the discussion on the effect of the skew angle of the incident beam, that deviation in detected modes is expected to occur as the OAM-value increases. This should occur later in the refractive sorter case, however. The deviation may be observed as a decrease in intensity of the diagonal values in as well as a spreading in the off-diagonal terms as the generated OAM values digress from the central 0 OAM value

In Fig. 3.28 (a), the range of modes for which correct OAM modes are detected may be seen as [-20,20] with the refractive sorter. From Fig. 3.28 (b), with the 1-copy sorter, about 15 modes

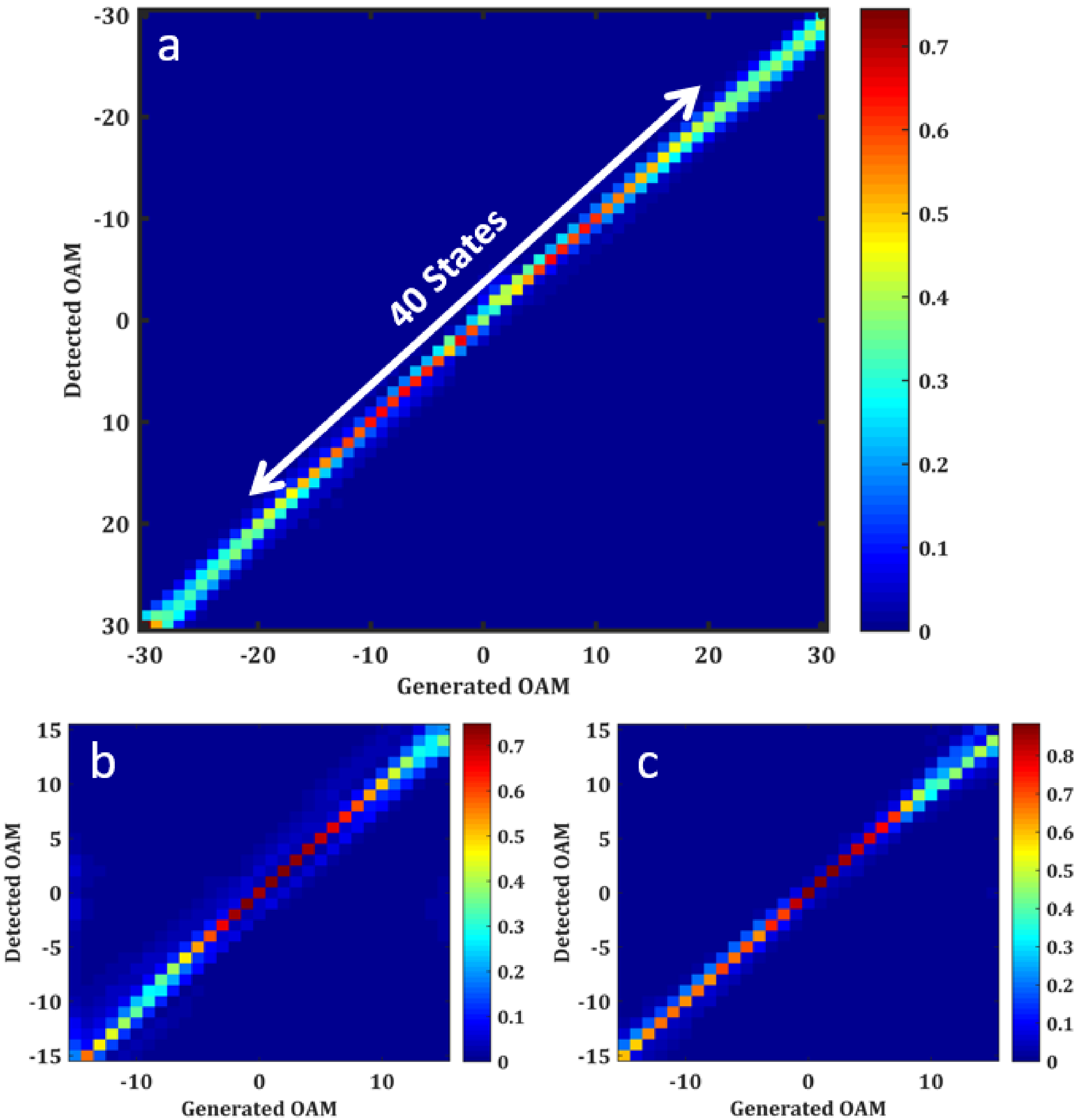

FIGURE 3.28: A density plot showing the sorting power and the associated cross-talk that may be expected with acceptable alignment for the (a) refractive, (b) 1-copy mode sorter and (c) 3-copy mode sorter.

fall within a range of acceptable accuracy where the intensity that is detected in the correct mode remains above 60% (30% results in falsely detected modes). A greater range may be used for the mode sorter, though, provided correction terms are used for the non-existent modes being detected as well as loss of weighting in the correctly detected modes. This, however, is also limited as past 20 modes, the defining spot disintegrates into a fringe array for which the positions are not indicative of the modes present.

The range of viable modes with intensity greater than 60% remaining in the correct element is increased to 23 in the 3-copy case. Additionally, the spread of the cross-talk between mode is reduced as expected due to the additional number of unwrapped beams. A stronger along-side diagonal may be seen, however, in comparison to Figure 3.28 (b). This may be attributed to the greater misalignment between the elements as the sensitivity of the element increased with the number of the beams copied. Subsequently, additional fringes were caused directly adjacent the spot, yielding a stronger presence of erroneous detection of adjacent OAM modes.

It follows that greater accuracy of the detected modes is found with the diffractive sorters, however, the range of OAM modes is diminished by the small radius of the element. As a result, the refractive sorter remained consistent over almost twice the range of the diffractive ones, illustrating this point for a beam size of 6 mm. Increasing the incoming beam size will subsequently also increase the sorting range.

Spot resolution

It is possible to evaluate the resolution of the spots produced when sorting adjacent OAM modes by superimposing sets of alternating OAM spots. This was done for the 1-copy sorter in Fig. 3.29 (a). Here superpositions of even and odd OAM modes in the interval [-7,7] were separately sent through the sorter and imaged. Superimposing these modes allows for clear depiction of how the modes overlap as is evident from the 2D profiles below the spots in the Figure. A clear overlap may consequently be seen which will lead to additional cross-talk for the detection of OAM modes not present.

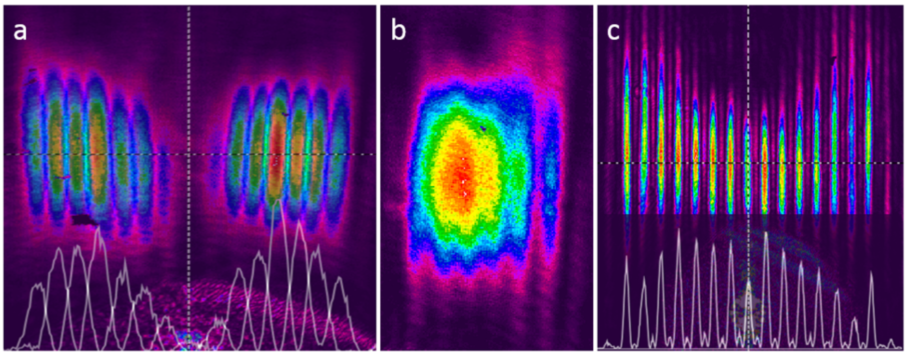

FIGURE 3.29: Images showing resolution for adjacent OAM modes when sorted with (a) a 1-copy mode sorter with the alternating odd and even modes between [-7,7] superimposed along with their 2D profiles, (b) adjacent OAM modes between [-1,-8] sorted by the 1-copy mode sorter and (c) adjacent OAM modes between [-7,7] sorted by the 3-copy mode sorter.

Additionally, a set of OAM (l) = [-1,-8] adjacent modes were sent through the mode sorter to observe the actual effects of the interference between the different spots. This is illustrated in Fig. 3.29 (b). The convolution results in distortion in the intensity spectrum associated with the OAM present as well as eliminating the ability to distinguish a spot's position. The latter may be

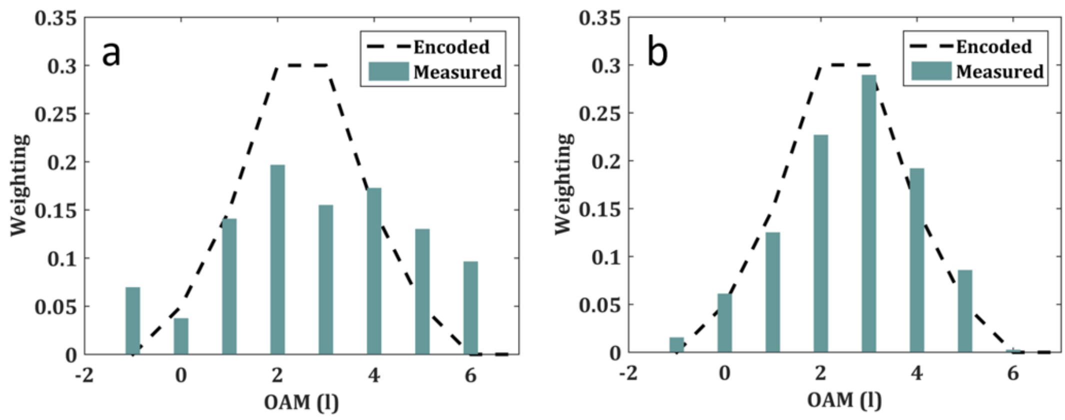

FIGURE 3.30: Relative weightings evaluated for multiplexed OAM modes sent through the mode sorter for the (a) 1-copy and (b) 3-copy mode sorters with respective similarities of S = 0.791 and S= 0.968

evidenced through the appearance of 6 spot 'tails' at the bottom of the convolution when in fact there are 8 OAM modes present.

As expected, the 3-copy mode sorter effectively separates and defines the spots for adjected OAM modes as is illustrated for Fig. 3.29 (c). Here a superposition of adjacent OAM modes [-7,7] was generated the corresponding detected spots shown in the figure. A 2D profile is shown below the spots, clearly illustrating the reduction in overlap and increased spot resolution.

Weighted detection

It follows that detection of the correct weighting for OAM modes being sorted is of importance for the correct characterization of a spatial mode. This was evaluated for the sorters in Fig. 3.30 (a) and (b) for 1- and 3-copy sorters respectively where a distinct superposition of OAM modes were multiplexed by the SLM and sent through the sorters.

The comparative accuracy of the multiplexed and detected OAM modes was determined through its similarity as given by,

$$S = \frac{[\sum_l \sqrt{W_{exp}(l) W_{th}(l)}]^2}{\sum_l W_{exp}(l) \sum_l W_{th}(l)} \tag{3.47}$$

where $W_{th}(l)$ is the theoretical or multiplexed weighting associated with the OAM mode l and $W_{exp}(l)$ is the detected equivalent of the mode. Observation of the Fig. 3.30 (a) and (b) indicate that the multiplexed and detected weightings resemble each other, showing that either of the sorters would be suitable for detection, however, a significant increase in the accuracy of modal detection occurs as the copy numbers increase. More specifically, the similarity of 79.1% for the 1-copy is increased by 22% when adding 2-copies.

It follows that both the refractive and diffractive sorters have advantages and disadvantages associated with their implementation. Specifically, the refractive mode sorter is more robust, allowing a greater range of beam sizes to be easily sorted as well as maintaining a larger range of OAM values when generating larger input beam sizes. The accuracy associated with measuring the weightings associated with a 1-copy sorter, such as the refractive one, however, is adversely affected with a 79.1% accuracy which may be expected if reasonable alignment is achieved. Here, utilizing the 3-copy diffractive sorter becomes an advantage with a large increase of 22% which may be expected with fair alignment. In addition, the cross-talk measured is substantially smaller with a reduction in the power erroneously detected for other OAM values. The trade-off with the implementation of this sorter is then a higher sensitivity to misalignment, resulting in a more sensitive detection system as well as a significant restriction to the size of the beam that can be sorted. Furthermore, the variation of beam sizes that may be sorted is minute with a deviation as small as 0.300 mm possible in comparison to the 8 mm range achievable in the refractive sorter case. Subsequently, for more robust requirements, the refractive sorter is favorable at the expense of the system accuracy; conversely, greater accuracy may be achieved with the 3-copy diffractive sorter at the expense of the range and durability of the system.

Chapter 4

Walking with spatial modes of light

Extending the QW criteria into OAM and polarization properties of light leads to an interesting analogue in the entanglement aspect of the dynamics that has not yet been previously considered in the other classical implementations. Accordingly, this forms an interesting method that allows further intuitive understanding of the QW by walking the quantum-classical divide. Now that the tools required for such a QW have been reviewed and characterized, a formal framework for physically generating such a walk may be covered. Based on the order of the system required, the most optimal experimental configuration may then be determined and discussed in view of, not only creating a physical implementation of the phenomenon, but also looking towards exploitation of the system as a computational and general simulation basis.

4.1 How to do a quantum walk with twisted classical light

As a system considered for implementing a QW requires a large discrete state space for the position space of the walker as well as a subspace of coin states where paired selectable superpositions may be generated, the OAM and polarization properties of light offer a unique case for such a walk using light as the walker. Due to each OAM mode forming non-separable superpositions with polarization, the QP entangles these modes such that the non-separability of these properties results in the possession of many OAM states with directionality that results in this unique interference and spread that is characteristic of a QW. Orthogonality of the modes causes the OAM superpositions to remain despite containing opposite values. Formalizing the actions on the OAM and polarization states of light is simply determined through Jones matrix algebra. As the QW already evolves in momentum space, applying the Jones matrix formalism allows the framework to be developed in the momentum space approach that was covered in Chapter 2 where the evolution took place in the coin space (i.e. in polarization space here).

4.1.1 Polarization flipping and momentum steps

With polarization forming the coin states, it follows that waveplates act as coin operators whereby traversing a WP corresponds to flipping the coin for the walker. This then creates a change in these directional states according to the waveplate parameters (type of coin). For example, consider the QWP characterized in Section 3.2.1. Placing the fast axis at 45^o, or even multiples thereof, resulted in an equal superposition of the bases states which may be equated to a coin flip resulting in an equal weighted superposition of both heads and tails, like the Hadamard or balanced coins discussed in Chapter 2. It is thus possible to use the WPs to implement some common coins, as will be discussed later. Nevertheless, one additional effect must first be considered.

The tuned QP provides a unique opportunity for coupling polarization to OAM in order to cause light to propagate in OAM values. This may be clearly seen in the selection rules determined earlier:

$$\hat{QP}\,|l,R\rangle = |l+2q,L\rangle$$
$$\hat{QP}\,|l,L\rangle = |l-2q,R\rangle \tag{4.1}$$

Accordingly, when sending through LCP (RCP), light moves to the left (right) with a laddering down (up) of OAM by a discrete factor of $2q$. As CP is required by the QP to create this conditional propagation, it follows that the heads and tails states are fabricated from RCP and LCP respectively. Nonetheless, an additional operation is carried out by the QP over that which is required for a propagation operator. This is the flipping of CP or coin states after the OAM translation from the HWP action inherent in the QP coupling process. Due to this action causing the polarization state to be altered, it may then be viewed as an intrinsic coin operation that can be incorporated into the QW design. Pairing the flipping action with any additional waveplate actions to generate the desired QW evolution will achieve this. Mathematically this is accomplished by decoupling the HWP and azimuthal generation processes by rewriting the QP matrix as shown in Eq. 3.45 in the CP basis [126].

$$QP = \begin{bmatrix} 0 & ie^{-i2q\phi} \\ ie^{i2q\phi} & 0 \end{bmatrix} = [HWP_{QP}][\hat{QP'}] = \begin{bmatrix} 0 & i \\ i & 0 \end{bmatrix} \begin{bmatrix} ie^{i2q\phi} & 0 \\ 0 & ie^{-i2q\phi} \end{bmatrix} \tag{4.2}$$

$\hat{QP'}$ then becomes the shift operator

$$\hat{S} = \sum_{l=-\infty}^{\infty} |l+2q\rangle\langle l| \otimes |R\rangle\langle R| + \sum_{l=-\infty}^{\infty} |l-2q\rangle\langle l| \otimes |L\rangle\langle L| \tag{4.3}$$

in Dirac notation, equivalent to the shift operator in Eq. 2.18.

Returning to the QWP example, the coin may be generated by concatenation of the HWP_{QP} and QWP matrices:

$$\hat{C}(\theta)_{QWP} = [QWP][HWP_{QP}] = \begin{bmatrix} 1 & ie^{-i2\theta} \\ ie^{i2\theta} & 1 \end{bmatrix} \begin{bmatrix} 0 & i \\ i & 0 \end{bmatrix} = i \begin{bmatrix} ie^{-i2\theta} & 1 \\ 1 & ie^{i2\theta} \end{bmatrix} \tag{4.4}$$

Placing the QWP axis at 45^o then generates the Hadamard coin [126],

$$\hat{C}(45)_{QWP} = i \begin{bmatrix} 1 & 1 \\ 1 & -1 \end{bmatrix} \tag{4.5}$$

yielding the Hadamard coin operator,

$$\hat{C}(45)_{QWP} = \frac{1}{\sqrt{2}}[(|R\rangle + |L\rangle)\langle R| + (|R\rangle - |L\rangle)\langle L| \tag{4.6}$$

in Dirac notation where i was extracted as a global phase. Subsequently, it is trivial to show that the concatenation of a QP and QWP results in the following operator [126] relating to Eq. 2.19.

$$[\hat{C}(45)_{QWP}][\hat{QP'}] = \sum_{l=\infty}^{-\infty}[|l+2q\rangle\langle l| \otimes \frac{1}{\sqrt{2}}(|R\rangle + |L\rangle]\langle R| + \sum_{l=\infty}^{-\infty}[|l-2q\rangle\langle l| \otimes \frac{1}{\sqrt{2}}(|R\rangle - |L\rangle]\langle L| \tag{4.7}$$

Therefore, it may clearly be seen that concatenating the QWP and QP results in a QW in the polarization and spatial degrees of freedom with classical light as the walker. The type of walk may be altered by changing the input state or the waveplate parameters.

Bringing the concept back to the Feynman diagrams from Chapter 1, one may intuitively observe this with an OAM Galton board (Fig. 3.31).

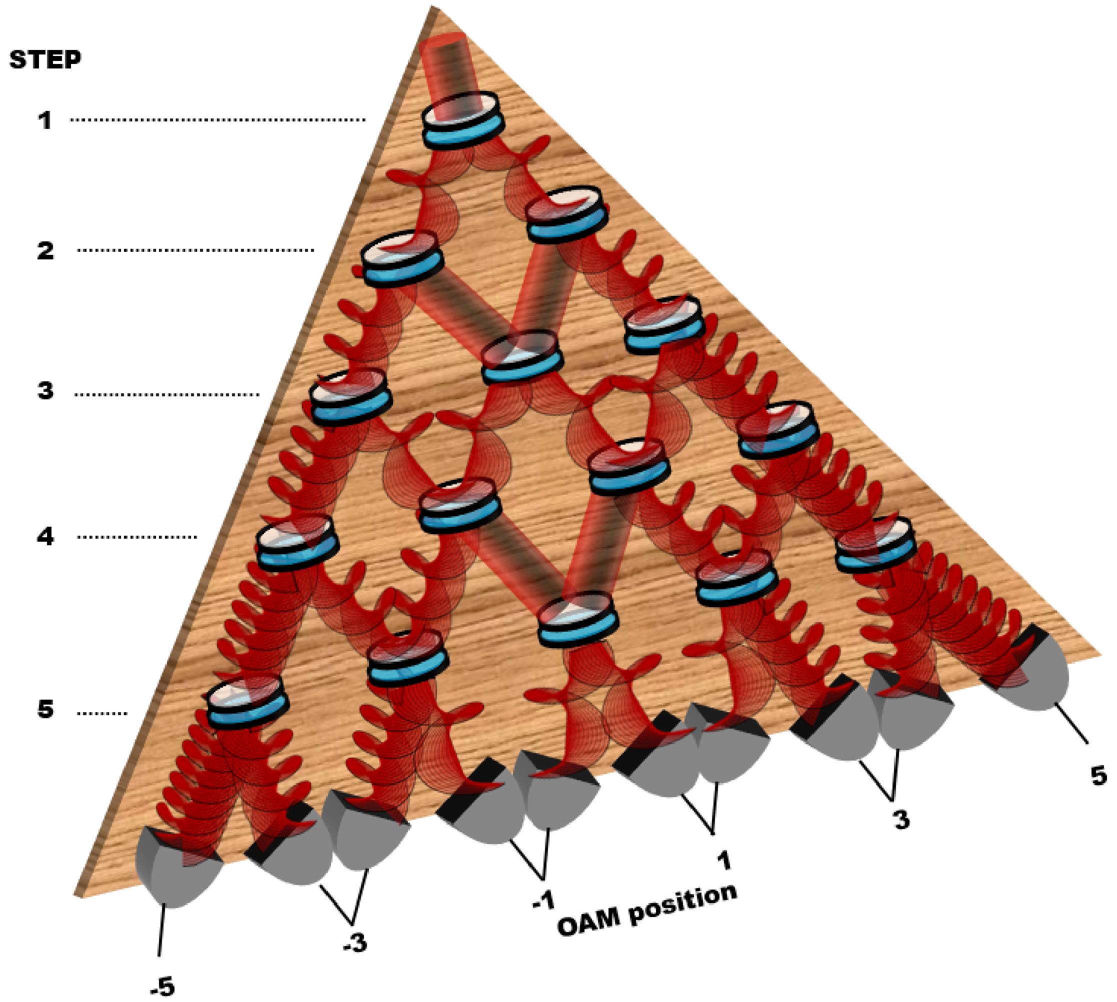

FIGURE 4.1: Diagram of an optical OAM Galton board illustrating a walk within the degrees of freedom of light.

Here, each beamsplitter is replaced with the QP(white)-QWP(blue) concatenation indicated in Eq. 3.47. Interacting with a $q = 0.5$ QP generates a twist with handedness related to the incident CP, resulting in the incident beam OAM being laddered in the positive and negative directions. The walker (light beam) then moves in the OAM 'position' space accordingly, forming non-separable superpositions with the polarization states. This is shown as moving to the left or right on the Galton board as related to the number of twists in the beam. After the OAM shift, the beam traverses a waveplate, such as the QWP set at 45 degrees. This consequently flips the polarization coin, forming a superposition of CP states before reaching the next QP. In accordance with the optical Galton board of Chapter 1, the beam 'meets itself' at the different OAM positions, resulting in interference of the amplitudes. Capturing the intensity of the beam associated with each OAM value is then equivalent to taking a measurement on the classical system where the characteristic QW distribution may be seen whereby a distinct increase in the variance over the RW should become prominent. One practical advantage of walking in OAM space that may be emphasized here is the physical size of the position space. For example, in the beam-splitter method, an array of beamsplitters are required which branches out as $O(n^2)$ with the number of steps, (n), required. For an OAM position space, all the twists and thus positions are superimposed in the same beam such that a theoretically infinite space for moving the walker exists in a single beam of light.

Working with the Jones matrices of these elements affords an ease and simplicity in simulating these walks, however, as the OAM QW then takes place in the polarization degree of freedom or, rather, the coin basis (as was described in Section 2.1.3). Furthermore, determination of the QW distribution of the nth step is simply the case of raising the concatenation to the nth power:

$$|\psi\rangle_n = [[\hat{C}(45)_{QWP}][\hat{QP'}]]^n$$

where $|\psi\rangle$ refers to the overall state of the light walker. Taking the Hadamard example further, the nth step of the QW is given by:

$$|\psi\rangle_n = (\frac{1}{\sqrt{2}}\begin{bmatrix}1 & 1\\ 1 & -1\end{bmatrix}\begin{bmatrix}ie^{i2q\phi} & 0\\ 0 & ie^{-i2q\phi}\end{bmatrix})^n = \begin{bmatrix}a\\ b\end{bmatrix}$$

where the $[a;b]$ matrix represents a general input mode polarization. Looking at the 5th step with a diagonal input polarization,

$$|\psi\rangle_5 = \frac{(1-i)}{2\sqrt{2}}(\frac{1}{\sqrt{2}}\begin{bmatrix}1 & 1\\ 1 & -1\end{bmatrix}\begin{bmatrix}ie^{i2q\phi} & 0\\ 0 & ie^{-i2q\phi}\end{bmatrix})^5 = \begin{bmatrix}1\\ i\end{bmatrix}$$

the following distribution is calculated in the HV basis (to exhibit a more complex case):

$$\Rightarrow \frac{1}{8}\begin{bmatrix}-e^{i3\phi}+4e^{i3\phi}+e^{i5\phi} & -2ie^{-i\phi}+2ie^{i\phi}-ie^{-i3\phi}-2ie^{i3\phi}-ie^{i5\phi}\\ -2ie^{-i\phi}+2ie^{i\phi}+2ie^{-i3\phi}+ie^{i3\phi}+ie^{i5\phi} & -4e^{-i3\phi}+e^{i3\phi}-e^{-i5\phi}\end{bmatrix}\begin{bmatrix}1\\ 1\end{bmatrix}$$
$$= \frac{1}{8}\begin{bmatrix}-e^{i3\phi}+4e^{i3\phi}+e^{i5\phi}-2ie^{-i\phi}+2ie^{i\phi}-ie^{-i3\phi}-2ie^{i3\phi}-ie^{i5\phi}\\ -2ie^{-i\phi}+2ie^{i\phi}+2ie^{-i3\phi}+ie^{i3\phi}+ie^{i5\phi}-4e^{-i3\phi}+e^{i3\phi}-e^{-i5\phi}\end{bmatrix}$$

Here each exponential term represents the OAM state with the $i\phi$ coefficient expressing which OAM position, as was described for Eq. 2.34 in Chapter 2. The weightings for each of the phase or exponential terms (i.e. OAM positions) are then the amplitude terms for each associated mode of that step in the quantum walk. Taking the modulus squared of the amplitudes then represent the intensities to be measured and thus the associated QW distribution.

$$\Rightarrow \frac{1}{64}[|-1+i|^2e^{-i5\phi}+(|-1-i|^2+|-4+2i|^2)e^{-i3\phi}+(|-2i|^2+|-2i|^2)e^{-i\phi}$$
$$+(|2i|^2+|2i|^2)e^{i\phi}+(|4-2i|^2+|i+1|^2)e^{i3\phi}+|1-i|^2e^{i5\phi}]$$

It should be noted that the moduli for the amplitudes of the same OAM are taken separately for each basis (i.e. the top and bottom matrix indices) as they are orthogonal and thus should be determined independently from the other. Their summation then yields the results as shown in the table inset of Fig. 4.2. Here the simulated values of the experimental design are compared to the general simulation method, following the mathematics described in Chapter 2 for this step of the walk. The corresponding experimental and theoretical simulation MATLAB scripts are attached in the Appendices. The correlation of these outputs further illustrates the validity of this scheme in implementing the QW. The walker is expected to interfere over the OAM values according to the polarization states, yielding a QW with classical light where the QP acts as a classical entanglement generator between these degrees of freedom.

4.1.2 Configuration

In the brief QW implementation review (Section 3.1), the practicality and different methods available for physically realizing this QW was discussed, however, there are several criteria that was not looked at in terms of creating a QW system that is maximally beneficial to exploiting this phenomenon. More specifically, when one considers the implications of using this as either a

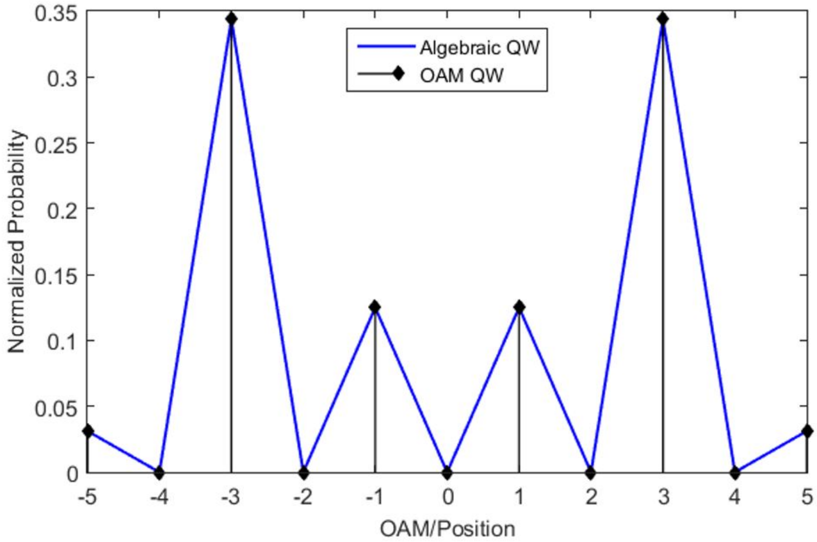

OAM	Probability
-5	$^{1}/_{32}$
-3	$^{11}/_{32}$
-1	$^{4}/_{32}$
1	$^{4}/_{32}$
3	$^{11}/_{32}$
5	$^{1}/_{32}$

FIGURE 4.2: Distribution of a symmetrical Hadamard QW for step 5 where the experimental simulation of the spatial mode quantum walk is observed in comparison to the simulation of an equivalent generic QW determined by Eq. 2.21 and 2.22. Table inset: Corresponding summary of the in-text calculated probabilities.

computational tool or an avenue for simulating quantum systems, simply generating a QW distribution falls substantially short of what is needed. Generating a physical QW setup to achieve this, in fact, requires a robust, sustainable scheme with flexibility, a high degree of coherence and large position space [23]

For instance, real world QWs often have complex propagation characteristics that occur over large position spaces. Here, excitons traversing a light harvesting complex in photosynthesis or particle transport in disordered media are two such examples. Both these properties also apply computationally speaking. Universal quantum computation with 1D QWs requires a substantially large position space [44; 174]. Experimentally, as was seen in Section 3.1, this equates to all positions requiring distinct states in which the walker can exist. This can necessitate a considerable number of physical resources, which may be seen with the number of beamsplitters in the optical Galton board or the number of QP-QWP concatenations in the OAM equivalent. Consequently, scalability of the resources is imperative.

While several computational implementations and simulations are possible with 1D QWs, such as with universal computation and looking at movement on single molecule chains, significant advantages also hold for extending the dimensionality. Faster speedup is generally possible in 2D with algorithms as well as simulations where more convoluted walks can take place. The search algorithm designed by Shenvi *et. al.* [38] is one such case where implementation in 1D possesses no benefit over the classical alternatives [175], but in higher dimensions, the characteristic speedup is afforded. In fact, computation is much faster in higher dimensions as the number of steps scale down substantially to cover the desired number of positions [176]. It may be noted that a multi-dimensional QW is also possible with classical light according to the scheme outlined in Ref. [135].

Control over the position space characteristics and coin operations for the walker at different positions corresponds to effective control of the underlying position space as well as the characteristics of how the walker traverses the position space. In terms of implementing the algorithms, effective alteration of the position space and conditional translations at each of these nodes corresponds to different operations on the walker such that certain algorithmic steps may be exacted through engineering the overall operations of these controls. In other words, by adjusting the coin operations at different time steps and positional nodes, it is possible to enact quantum logic on the walker state so as to achieve the desired computation for the output state [23]. This specified level of control corresponds to flexibility in the QW implementation system.

Accordingly, a QW system should have a high degree of flexibility in order to accommodate both the algorithms required for the desired computation as well as changing between different algorithms to achieve a complete system for universal computation. This criterion also extends into the simulation aspect of QWs. As may be intuitively construed, different positions in the walking space demands specific conditions. This is consequently determined by the conditional operations on the walker that correlates to alter both how the walker behaves as well as the properties of the underlying position space. Experimentally, this corresponds to control of the initial state of the walker and the coin operations for each position. Alteration of the coin operations at each step also affords dynamical control which offers temporal influence on the algorithmic and simulation applications.

Scalability, flexibility and a large position space are not the only properties necessary for a useful QW scheme, however. The QW evolution also needs to remain coherent, both in the positional spread as well as over the number of required steps. Due to the basic evolution of the walker relying on interference mechanics, any variation in the phase, not due to the operations imposed, alters the interference and the outcome and produces erroneous results. Therefore, implementation of the QW should be robust such that the coherence of the walker and repeatability of the outcome is preserved over the positional states and temporal steps.

A last consideration in a successful physical implementation is the detection scheme and the extent thereof. Preforming measurements for each position is another non-trivial undertaking. Moreover, doing so for different steps within the propagation is beneficial for monitoring the dynamics and mechanisms of the walk; this is particularly essential when considering the phenomenon in terms of simulations. It follows that tracking and reconstruction of both the spatial (position) and temporal (steps) evolution of the walk is fundamental to completely harnessing QWs as a resource.

The scheme proposed by Goyal *et. al.* [126] in 2013 incorporates much of these criteria with the QP and QWP, as was described in the previous section. Here the walker is formed by a single pulse of classical light which is directed into a loop configuration, as illustrated in Fig. 4.3. The pulse is admitted into this external resonator by a beamsplitter (BS) and reflected with 3 mirrors such that the pulse is returned to the beamsplitter. A percentage of the pulse is then transmitted out of the loop while the rest is reflected for another round trip (RT). By placing a QP and QWP inside the resonator, each RT corresponds to a step in a Hadamard QW according to Eq. 4.5. Each partial pulse transmission out of the resonator may then be directed through a mode sorter and sorting lens. Placing a CCD in the focal plane of the sorting lens then captures the OAM mode distribution and weightings contained within the pulse. The use of a $4-f$ imaging system within the resonator mitigates the divergence of the modes propagating inside.

It follows that the QW evolves temporally with each step occurring at multiples of the RT time. Consequently, as each RT pulse is partially transmitted by the BS, the whole probability distribution for each position may be simply retrieved; also, by restricting the CCD exposure time, the OAM distribution of the pulse (walker) for a single step may be isolated. The setup thus allows each step to be easily monitored. Moreover, the setup is maximally scalable where the physical resources do not change with the number of steps, but everything rather remains constant where only one QP-QWP set is required for an entire walk. As the WP acts as the coin operator, changing the coin state is easily achievable, making the system simple to modify so as to impose different operations on the pulse. Here, control of initial state is additionally afforded by a WP before the resonator, as indicated by the HWP. This provides a fair degree of flexibility for extended applications of the QW. Additionally, by utilizing a QP with $q = 0.5$, a shift of 1 OAM

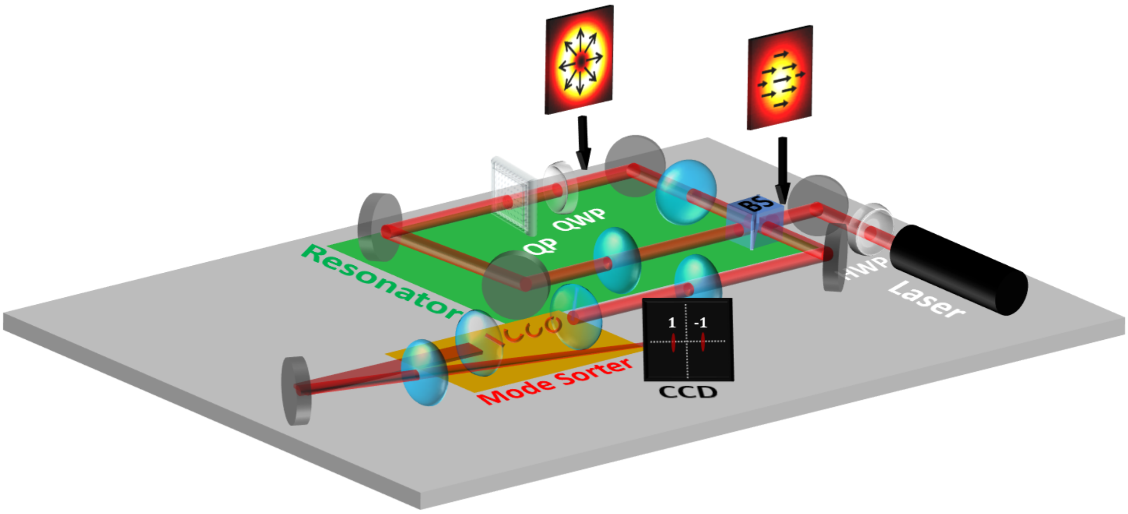

FIGURE 4.3: Conceptual design (as follows from [126]) of a physical system that will result in the implementation of a QW in the spatial modes of light.

in either direction is generated, allowing the range of the mode sorter detection scheme to be fully exploited.

4.2 Walking twisted light

The objective of this work is to implement a QW, in the classical regime, with spatial modes of light for the first time. Furthermore, experimentally achieving such a walk in a scalable and robust manner, forms a vital component for realistic impact in the future. As indicated in the configuration detailed in the previous section, the method proposed [126] forms a promising candidate. Actualization of the setup is explored in the following section, showing that such a walk is indeed possible, giving rise to promising implications. We additionally extend the experimental implementation of the scheme to include additional coins, showing the initial flexibility of the system without any significant modification. In the following chapter we conceptually expand this scheme to include more of the criteria discussed where the dimensionality and sustainability may be extended, furthering the applicability and practicality of this method for future implementation.

4.2.1 Experimental considerations and alignment

Physical implementation of QWs is a decidedly challenging task as evidenced by the extensive number of schemes mentioned in the beginning of the chapter. Accordingly, realization of the QW suggested requires several experimental considerations to the conceptual scheme introduced. Here the actual experimental setup used to implement the walks is examined along with the accompanying variables associated with the equipment utilized. Subsequently, the pulse width and spatial properties of the laser beam are considered along with synchronization of the generation and detection systems with reference to the boundaries of the constructed setup. Furthermore, the task of aligning such a resonator is detailed such that the walker maintains the same path around the loop with each iteration.

Experimental configuration

The experimental setup designed to realize the classical QW is shown in Fig. 4.4. Here a pulsed Spectraphysics Quanta-Ray DCR-11 q-switched laser generated a single input light pulse with 0

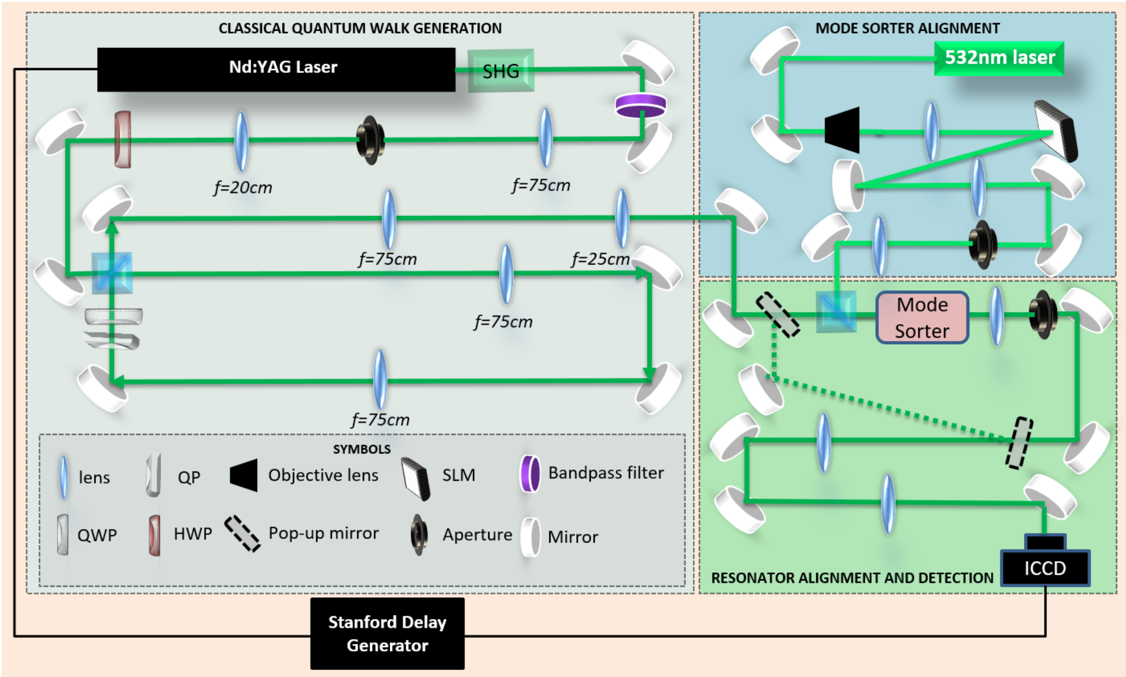

FIGURE 4.4: Schematic of the actual setup constricted for physical implementation of the QW.

OAM (initial position of the walker) at 1064 nm. A second harmonic generator (SHG) converted the wavelength to 532 nm through frequency doubling to remain within the ICCD detection range. Structuring a Gaussian intensity distribution of appropriate beam size was accomplished through a spatial filter as detailed further on. Following from Fig 4.3, propagation of the pulse through a HWP served to prepare the input polarization state symmetry (e.g. diagonal polarization for a symmetrical Hadamard QW), after which, it was injected into a rectangular loop resonator (3m perimeter) by a $50 : 50$ non-polarizing BS. Placement of the $q = 0.5$ QP and WP concatenation initialized the QW and advanced it by one step with each consecutive round trip. Scalability of the walk is thus realized where the total possible number of steps is only intensity dependent. The output pulse from the BS was subsequently imaged from the QP plane to the mode sorter.

Alignment of the mode sorter was attained by constructing an adjoining OAM mode generation setup as emphasized in the dark blue section of Fig. 4.4. Here a 532 nm diode laser was expanded with a $10x$ objective lens and collimated through an f=300 mm lens onto an SLM where phase and amplitude modulation was utilized to generate superpositions of LG beams. A $4-f$ system was built to isolate and image the 1st order onto the mode sorter. The SLM generated mode was then combined and aligned with the output mode from the resonator with a $50 : 50$ BS. By passing test OAM superpositions from the SLM through the MS, optimal alignment of the elements was then achieved. It is evident that the QW modes from the resonator were consequently aligned to the MS by proxy of the alignment to the SLM generated modes. Due to space constraints, the sorting or Fourier plane of the MS configuration was directed and imaged onto the ICCD plane with another $4-f$ system. Choice placement of a popup mirror before the MS and within the FP imaging system allowed the QP plane image to be re-imaged onto the ICCD with a lens placed between the pop-up mirrors. The second lens in the MS imaging system then served a dual purpose as the second imaging lens in the $4-f$ re-imaging system of the QP plane. This allowed the output beam structure for each pulse to be individually captured for each RT, simplifying the alignment process.

Subsequent capture of each RT pulse was achieved through utilization of an iStar AndOR

ICCD camera with a temporal resolution on the 10 nano-second scale. Synchronization between the initial laser pulse and recording window of the camera was attained with a Stanford delay generation working in combination with the iStar on-board digital delay generator which is covered in greater detail further on.

Pulse overlap and adjusting the prediction

As implementation of this resonator-type setup results in each round trip advancing the QW, it follows that each successive output pulse corresponds to a step in the walk with a constant time gap between each pulse that is related to the time taken for the pulse to circulate back to the output BS. The time gap (t) is consequently related to the length of the resonator (L) through the relation, $t = L/c$ where c refers to the speed of light in air and t the time. Here, the resonator must be longer or equal to the temporal pulse width to avoid overlap of the circulating pulse and thus an overlap in the QW steps. As a result, for the temporal pulse width of 10ns as estimated for the Spectra-physics laser, a resonator length of 3 m or larger is required where a 3 m resonator would output a QW step every 10 ns with an equivalent pulse width. With consideration of stability and alignment of the resonator, the resonator was designed in a 0.3 m $\times$ $1.7m$ rectangular configuration, yielding a 3 m path length for the pulse to traverse.

The temporal pulse width was consequently measured experimentally so as to allow for adjustments to the theoretical prediction and thus account for any OAM mode overlap in the results due to a larger pulse size. This was carried out by placing a Thorlabs DET210-a photodiode before the ICCD and measuring the average of 10 intensity pulses on a Tektronix TDS2024B 1GHz oscilloscope. The corresponding temporal parameters were then estimated by fitting the pulse to a Gaussian function of the form:

$$G(x) = ae^{-(x-b)^2/(2c^2)} + k \tag{4.8}$$

Where a determines the height of the pulse function, x refers to the x-axis position which is then adjusted by b. c indicates the width of the pulse and k adjusts the position along the y-axis. The corresponding parameters extracted from fitting Eq. 4.8 are summarized in Table 4.1 A SSE (sum

TABLE 4.1: Parameters for Gaussian fit to average pulse length measured from the Spectraphysics laser.

Parameter	Fitted value
a	0.06045
b	0.106 x 10^{-9}
c	6.107 x 10^{-9}
k	0.0040

of the squares of the error) of 0.002573 and R-squared value of 0.974 determined from the fitting both indicate that the function as well as the parameters are adequate reflections of the measured pulse for the walker.

Here the parameters may subsequently be used to yield both the mathematical description of the pulse as well as indicate the full-width half maximum (FWHM) and the full-width at one-tenth maximum (FWTM) values for the pulse length.

The FWHM is then given by

$$FWHM = 2\sqrt{2\ln{(2)}} \times c = 14.3ns$$

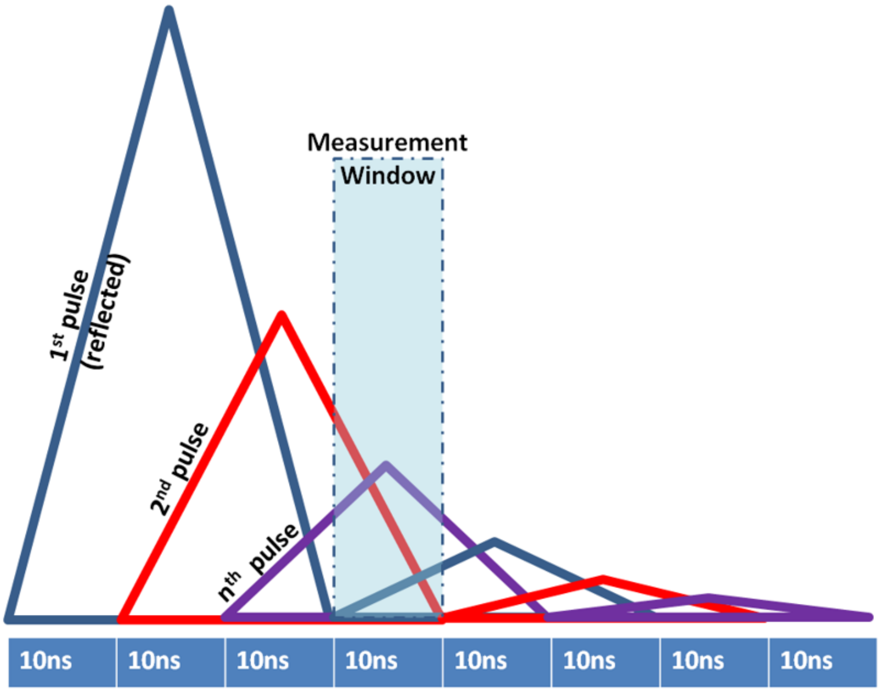

FIGURE 4.5: Illustration of pulse overlap and intensity effects for each pulse emitted from the resonator or step in the quantum walk.

with the FWTM also determined by

$$FWTM = 2\sqrt{2\ln(10)} \times c = 26.6ns$$

As the parameter b, indicates the position of the peak relative to a position, $b = 0$ allows the function to be centred at the origin, making it easier to work with. Additionally, k indicates the y-position which is also irrelevant, hence $k = 0$. It follows that the intensity distribution of the pulse may be characterized by the Gaussian function, $G(t)$:

$$G(t) = 0.0605e^{-t^2/(2(6.107ns)^2)} \tag{4.9}$$

It follows that the FWHM is close to the estimated value of 10 ns with 14.3 ns. Comprehensive prediction of the mode spectrum may be determined by considering the FWTM value, however, which is almost 3 times larger than the 10 ns expected for the resonator design, indicating a significant overlap. Modelling of the OAM mode spectrum overlap is therefore important for analysis of the measured distribution.

Two factors should be considered for experimental simulation of the distribution expected at each time step. These factors are (1) how the pulses overlap and (2) the intensity decrease occurring each RT due to the partial transmission through the BS. More specifically, with a FWTM of 30 ns and a resonator length corresponding to 10 ns, it follows that the pulse maximum for each RT output will have a contribution from the previous pulse as well as the next pulse as indicated in Fig. 4.5.

This is due to the $1st$ pulse being still initially reflected while the 1st resonator output occurs after the first 10 ns. It follows that at 10 ns, the $2nd$ section of the initial input is still being outwardly reflected, but is then combined by the 1st resonator 10 ns partial transmission. The 0th and 1st steps are then overlapping. The 10 ns output is also then partially reflected back into the resonator to then join the last 10 ns of the initial pulse entering the resonator. It follows that an

n =	Output pulse intensity
1	T^2
2	T^2R
3	T^2R^2
4	T^2R^3

TABLE 4.2: Illustration of the intensity scaling with each RT for a given beam-splitter.

overlap occurs between the initial pulse state (0 OAM) and the present step (± 1 OAM) such that when the $3rd$ 10 ns output occurs, the 0 OAM converts to ± 1 OAM (which is the present step) while the reflected bit becomes the future step (± 2 and 0 OAM) that overlaps for the last 10 ns. The resulting overlaps may be simplified into the diagram above.

Now as the measurements will be taken every 10 ns for the respective step, the overlap may be minimized to influences from the previous and future steps only as indicated by the blue dotted box. As mentioned, an additional factor needing consideration is the decrease in the internal resonator intensity which leads to a difference in the intensities of the overlapping components. Again, this is illustrated in Fig 4.5. Subsequently, the correction factor for the 'previous' pulse overlap contribution is larger than that of the 'future pulse'. Derivation of a general formula for a transmission percentage of the pulse T and subsequent reflection, $R = (1 - T)$:

(1) For a $R : T$ BS, $T\%$ is initially transmitted into the resonator, while $R\%$ is reflected, forming the first pulse and the $0th$ step of the QW. $\Rightarrow$ Relative intensity for $n = 0$ is R with T intensity inside the resonator.

(2) The next pulse output ($1st$ step of the QW) of the resonator is $T\%$ of the initial $T\%$ transmitted into the resonator. $\Rightarrow$ The relative intensity for $n = 1$ is $T(T) = T^2$ with $T \times (1-T)$ or TR intensity left within the resonator.

(3) The third pulse output/transmitted ($2nd$ step of the QW) is $T\%$ of the intensity left in the resonator, i.e. for $n = 2$, the output pulse intensity is given by T^2R while T^2R^2 is left.

It follows that the change in output pulse intensity follows the mathematical trend illustrated in Table 4.2,which implies that the general expression for the output pulse intensity and thus the relative weighting with regards to each step is then

$$w(n) = \begin{matrix} R & if\ n = 0 \\ T^2R^{n-1} & if\ n \neq 0 \end{matrix} \tag{4.10}$$

The temporal shape of the pulse also plays a role as it dictates the intensity distribution and thus the overlap between the pulses. This may be approximated by the best fit curve for the average temporal pulse as determined in Eq. 4.9. These intensity and temporal width factors may thus be used to augment the expectations such that the measured distribution may indicate both if a QW is indeed happening and what kind of QW is being achieved.

An adjusted diagram of the pulse overlap is presented as Fig. 4.6 (a) and (b) below. Figure 4.6 (a) indicates the extent of the pulse overlap while (b) illustrates the effects of the different weightings for a $50 : 50$ BS.

The dotted lines indicate the section of the pulse to be gated by the AndOR camera for the nth pulse in the QW series. The 'middle' section of the pulse may be determined by the formula:

$$a = \frac{PW - GW}{2} \tag{4.11}$$

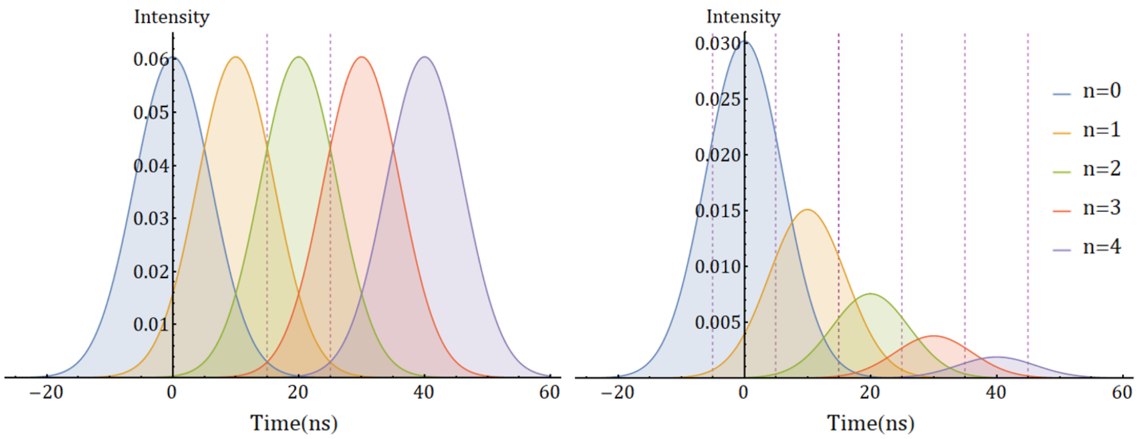

FIGURE 4.6: Adjusted diagram illustrating the pulse overlap for a 3 m = 10 ns resonator configuration where (a) the overlap is emphasized and (b) the weighting effects associated with loss in intensity incorporated.

where PW is the complete pulse width (which is assumed to be 40 ns based off the modelled pulse) and GW is the gate width (i.e. the time section of pulse to be captured). Here a is then an arbitrary parameter used to relate the overlapping sections to the middle of the pulse. It follows that the section of the nth step pulse will then be captured from

$$\frac{-PW}{2} + a = -20 + (\frac{40-10}{2}) = -5$$

to

$$\frac{PW}{2} - a = 20 - (\frac{40-10}{2}) = 5$$

It follows that the expected QW probability distribution for the 1st pulse $(n = 0)$ where the central distribution is captured will be given by:

n = 0:

$$[[QW_P(0)]w(0) \int_{\frac{-PW}{2}+a}^{\frac{PW}{2}-a} G(t)dt] + [[QW_P(1)]w(1) \int_{\frac{-PW}{2}+a-10}^{\frac{-PW}{2}+a} G(t)dt]$$

$$[[QW_P(2)]w(2) \int_{\frac{-PW}{2}+a-20}^{\frac{-PW}{2}+a-10} G(t)dt]$$

Similarly, for n = 1 and 2:

n = 1:

$$[[QW_P(0)]w(0) \int_{\frac{PW}{2}-a}^{\frac{PW}{2}-a+10} G(t)dt] + [[QW_P(1)]w(1) \int_{\frac{-PW}{2}+a}^{\frac{PW}{2}-a} G(t)dt]$$

$$[[QW_P(2)]w(2) \int_{\frac{-PW}{2}+a-10}^{\frac{-PW}{2}+a} G(t)dt] + [[QW_P(3)]w(3) \int_{\frac{-PW}{2}+a-20}^{\frac{-PW}{2}+a-10} G(t)dt]$$

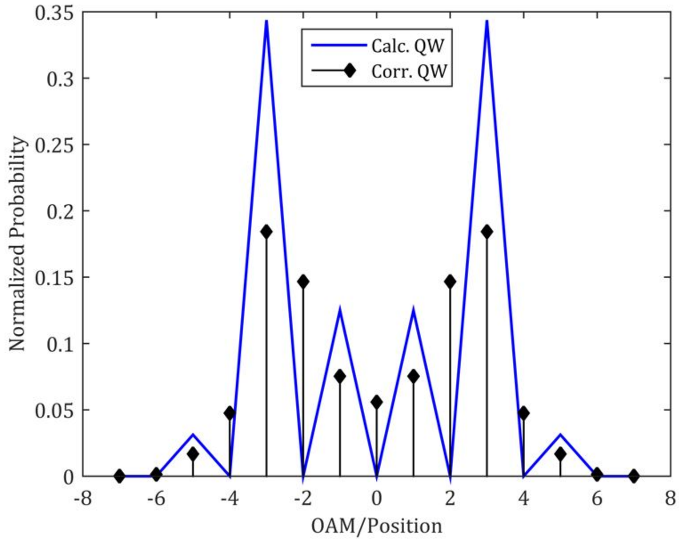

OAM	Calculated QW	Corrected QW
-7	0	1.23 x 10^-5
-6	0	0.00140
-5	0.03125	0.01678
-4	0	0.04750
-3	0.34375	0.18434
-2	0	0.14667
-1	0.125	0.07536
0	0	0.05588
1	0.125	0.07536
2	0	0.14667
3	0.34375	0.18434
4	0	0.04750
5	0.03125	0.01678
6	0	0.00140
7	0	1.23 x 10^-5

FIGURE 4.7: Step 5 of the OAM QW with (Corr. QW) and without (Calc. QW) the experimental corrections. Inset table: Comparison between the corrected and uncorrected experimental quantum walk distribution for step, $n = 5$ and detected pulse 6.

n = 2:

$$[[QW_P(0)]w(0)\int_{\frac{PW}{2}-a+10}^{\frac{PW}{2}-a+20} G(t)dt] + [[QW_P(1)]w(1)\int_{\frac{PW}{2}-a}^{\frac{PW}{2}-a+10} G(t)dt]$$
$$[[QW_P(2)]w(2)\int_{\frac{-PW}{2}+a}^{\frac{PW}{2}-a} G(t)dt] + [[QW_P(3)]w(3)\int_{\frac{-PW}{2}+a-10}^{\frac{-PW}{2}+a} G(t)dt]$$
$$+ [[QW_P(4)]w(4)\int_{\frac{-PW}{2}+a-20}^{\frac{-PW}{2}+a-10} G(t)dt]$$

It follows that with the exception of pulses 1 and 2, the following generalization applies:

n:

$$[[QW_P(n-2)]w(n-2)\int_{\frac{PW}{2}-a+10}^{\frac{PW}{2}-a+20} G(t)dt]$$
$$+ [[QW_P(n-1)]w(n-1)\int_{\frac{PW}{2}-a}^{\frac{PW}{2}-a+10} G(t)dt]$$
$$[[QW_P(n)]w(n)\int_{\frac{-PW}{2}+a}^{\frac{PW}{2}-a} G(t)dt] + [[QW_P(n+1)]w(n+1)\int_{\frac{-PW}{2}+a-10}^{\frac{-PW}{2}+a} G(t)dt]$$
$$+ [[QW_P(n+2)]w(n+2)\int_{\frac{-PW}{2}+a-20}^{\frac{-PW}{2}+a-10} G(t)dt]$$

Where $QW_P(n)$ is the QW probability distribution of the nth step. For comparison, Fig. 4.7 below shows the normalized expected Hadamard probability distribution for the associated $6th$ pulse ($n = 5$) to be detected by the AndOR camera with an inset table yielding the specific values. The corrected distribution displayed is for the case of a $50 : 50$ beam-splitter acting as the resonator output window.

Comparing the calculated distribution to that of the corrected one, the same diverging trend is still apparent. The maxima here still appear near the edges of the distribution with the highest weightings occurring at the same positions. It follows that the expected difference occurring from the overlapping modes within the cavity is a broadening of the peaks as well as the presence of probabilities in the adjacent positions. Consequently, the generated QW should still retain the characteristic qualities associated with the pure QWs.

Beam profile and spatial filtering

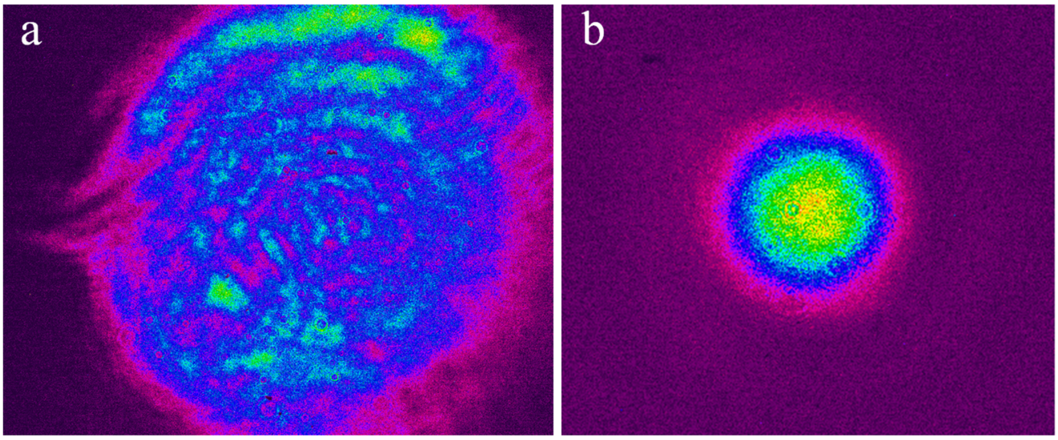

FIGURE 4.8: False color map images of the nearfield pulsed laser output beam (a) before spatial filtering and (b) after spatial filtering. The spatially filtered beam is smaller than the original as it was de-magnified in the spatial filtering process.

Preparation of the input beam for the appropriate evolution of the beam modes is necessary by elimination of any aberrations and unwanted modes contained in the initial laser generated beam. Figure 4.8 (a) yields the transverse output profile generated by the Spectraphysics DCR-11 laser necessary for pulses on the nanosecond timescale. From the transverse distribution, the presence of aberrations and additional modes are evident in addition to a large beam width of 3 mm which is averse to maintaining an appropriate beam size at larger steps due to high OAM values. To prepare the necessary Gaussian mode, a spatial filter as illustrated in Fig. 4.8 was applied to the beam where a 50 νm pinhole was placed in the Fourier plane of the $4-f$ system with lenses of focal lengths, $f1 = 750$ mm and $f2 = 200$ mm respectively functioning as a demagnification telescope. Here the pinhole was three times larger than the calculated Gaussian beam width in the FP, resulting in the extraneous modes being filtered out spatially. The focal length ratio $(f2/f1)$ between the lenses additionally formed a demagnification telescope to reduce the beam size to 2 mm.

The spatial filter output beam is given in Fig. 4.8 (b) where a Gaussian intensity distribution can be seen along with the appropriate demagnification. It follows that this beam may then be successfully propagated through the setup such that any modes generated are due to the QW. In addition, the feasible beam size with regards to optical component dimensions at higher OAM modes or greater steps allows for a more sustainable walk.

Pulse synchronization and gating

Attaining the OAM spectrum of a specific QW step requires a camera capture time (gating time) equal to or smaller than the output pulse temporal width. This is possible on the nanosecond (ns) scale with an AndOR iStar ICCD camera (734 series) through a photocathode optical shutter that

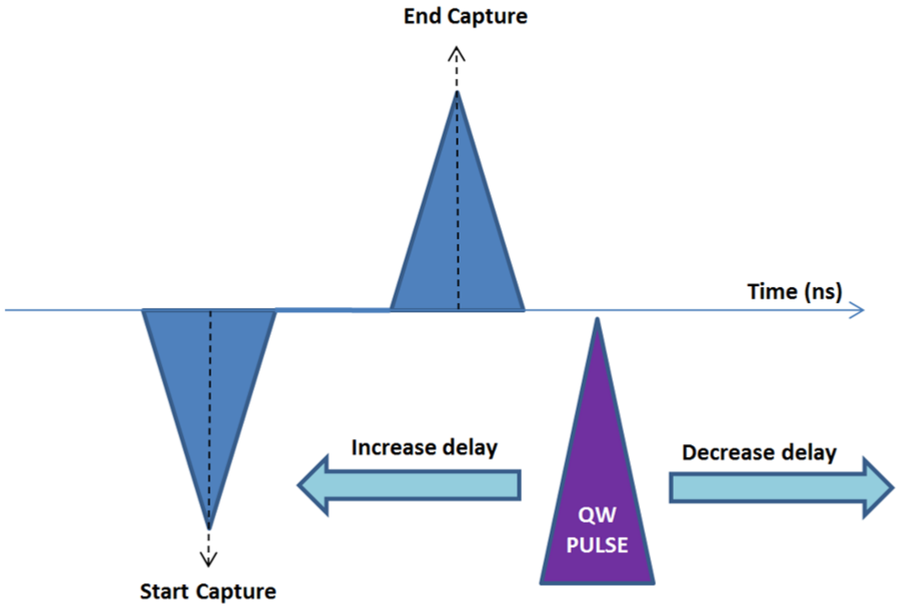

FIGURE 4.9: Schematic illustrating the procedure necessary to correctly capture an output pulse for a single step or round trip in the quantum walk.

allows the intensity to reach the ICCD and thus be captured for a specified gate width. It is possible to determine the opening and closing of the photocathode by monitoring the electronic signals sent to enact the operation with an oscilloscope. As indicated in Fig. 4.9, the opening is determined with a negative pulse and closing with a positive pulse.

As mentioned, location of the desired output pulse (step) additionally requires synchronization between the camera and laser pulse emission through a digital delay generator. It follows that a specific time delay must be placed between the pulse emission and opening of the photocathode which is equivalent to the time taken for the electronic signals to travel to the respective components as well as the time for the pulse to reach the resonator, circulate the resonator a desired number of times, travel through the sorter and reach the camera. This delay may be experimentally achieved by placing a photodiode at the same distance from the output as the camera and triggering oscilloscope. The AndOR trigger may then be monitored in conjunction with the time it takes for the pulse to reach the photodiode. Adjustment of the calculated time delay adjusts the first detected pulse (step 0) temporal position as depicted in Fig. 4.10. After determination of the initial pulse delay, isolation of the desired step or pulse output is achieved by adding an additional delay of Nt that is related to the resonator circulation time, t and number of steps, N.

Determination of the appropriate delay required for synchronization of the camera and laser pulse is demonstrated in Fig. 4.10. The graphs along the lower row of the figure are signals recorded by a oscilloscope monitoring the photocathode triggering signals as well as the arrival of the emitted laser pulse due to a trigger pulse from the digital delay generator for the same nanosecond time scale (x-axis). The y-axis then represents the associated voltages. It follows that the blue profile is the laser pulse detected by the photodiode, placed the same distance as the camera from the output pulse and the red profile is the trigger signals operating the opening (first large dip) and closing (first large spike) of the photocathode. Transparent green overlays on the respective graphs emphasize the period for which the camera is recording the pulse intensity and thus the section of the pulse captured. As indicated, the gate width (capturing time) was set to 10 ns.

Images above each of the oscilloscope graphs are the transverse intensity distributions captured

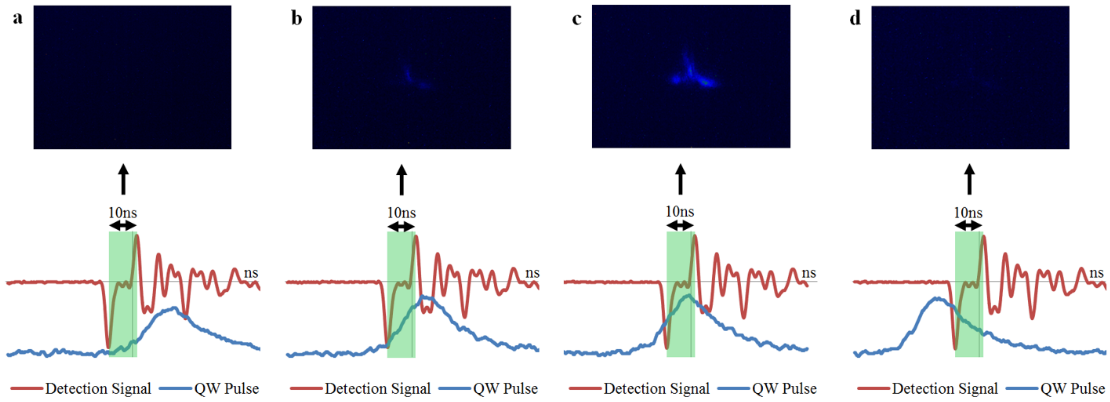

FIGURE 4.10: Experimental illustration of synchronization required between the AndOR camera and pulsed laser for accurate output pulse capture from the QW resonator. Delay time settings were decreased from (a-d).

in the respective 10 ns gated windows where the delay between the photocathode and laser triggers from the digital delay generator was systematically decreased from (a) through to (b) for a three-lobe spatial profile. It can thus be seen from (a)-(b) how the pulse moves into the capturing window of the camera before the maximum pulse intensity is captured in (c) and then moving past the range again in (d). The variation in intensity of the captured modes clearly show the synchronization effects of the time delay parameter and the desired position for ideal analysis of an output pulse with (c).

Application of the appropriate synchronization time delay was determined with the method illustrated in Fig. 4.10. The first pulse in the resonator setup is crucial in capturing the desired QW step or output pulse. Subsequent addition of a step-related time delay constant, Nt, to the initial delay allows for the capture of the intensity distribution related to that step (N) or output pulse (as explained in the methods). This is illustrated in Fig. 4.11 for the experimental setup. Here successive output pulse intensity distributions from $N = [0, 4]$ were captured with a 10 ns gate width in the mode sorter Fourier plane. A clear evolution in the distribution may be seen across the steps, indicating a spread in the intensity distribution and thus the successful capture of additional output pulses according to the associated delay settings. It follows that this method would be effective in attaining the OAM spectra of each QW step, allowing real-time observation of the walk.

Aligning the loop

Precise alignment of the resonator is of significant importance such that the beam (walker) is both retained within the walk and is correctly modulated by the QP. Subsequently, the pulse must be reflected back onto exactly the same path as was initially traversed at every interaction with the beam-splitter (BS). Several steps were construed in order to obtain such an alignment. Initially, the laser was set to run in continuous mode where the pulses were emitted at a frequency of 10 Hz, forming a semi-continuous beam and thus allowing the path to be easily recognized. The BS, transmitting light into the resonator, was then aligned such that both the reflected and transmitted components followed marked straight paths at 90 degrees from the other. Afterwards, a rectangular path was mapped out with the use of two apertures placed after one another to form the subsequent perimeters. The beam was then made to reflect off the centre of each of the resonator mirrors and traverse the path marked out until reaching the BS again. This resulted in an initial crude alignment of the system. Further iterative steps were then taken to refine the alignment by adjusting the tip

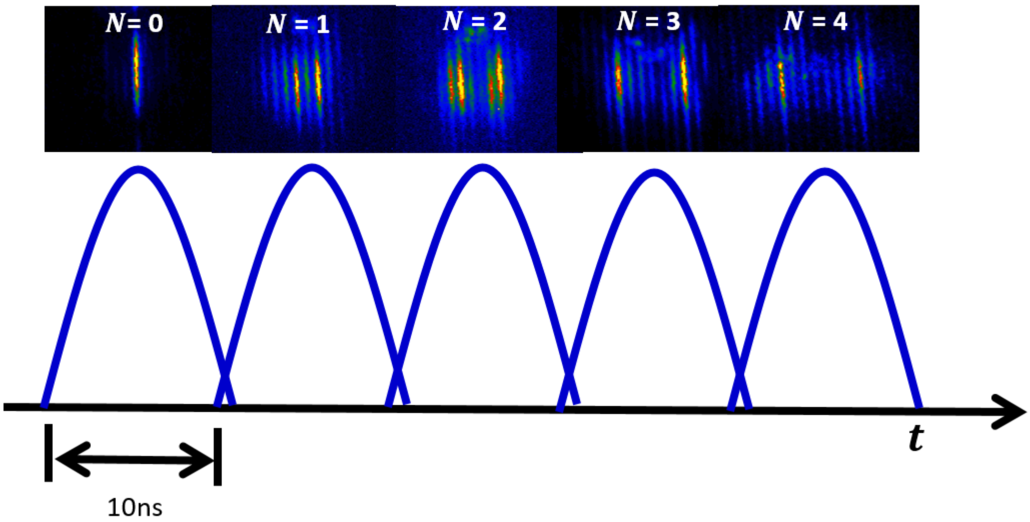

FIGURE 4.11: Example evolution of output intensity distributions as captured every consecutive 10ns from the first output pulse, marking each round trip made by the circulating light beam for the QW resonator.

and tilt degrees of freedom for the resonator mirrors such that the pulse transmitted out of the resonator followed the path of the initial beam reflected from the BS.

From the initial alignment, the reflected beam was aligned on a straight path marked out by two apertures placed 1m away from the other after reflection off the mirror shown in Fig. 4.12. Through adjustment of mirrors M2 and M3, the resonator output beam was then iteratively 'walked' through the nearest (A1) and furtherest (A2) apertures respectively. It follows that by aligning the resonator outputs to the initial beam, the component reflected back into the resonator retains the same path within the resonator.

Placement of a Spiricon camera (CCD) near the furtherest aperture allowed the positions of the respective beams to be better identified. By observing the beams here, alignment to the reflected beam could be further improved. Here, iterative adjustments of M1 and M3 allowed the momentum and spatial position of the output beam to correspond that of the reflected one. This is illustrated in Fig 4.12 where the 1st and 2nd RT outputs may be easily identified alongside the reflected beam. It should be noted that the beams were separated substantially for better illustration of the method in Fig 4.13 (a).

Following Fig. 4.13 indices, M1 was adjusted to place the 1st output beam in the centre of the reflected beam. M3 was then adjusted to combine the 1st and 2nd output beams which is initially off-centre. M1 was then readjusted to move the 1st output back to the centre of the reflected beam. Readjustment of M3 to recombine the output beams result should have them positioned slightly closer to the centre of the reflected beam. Iteration of these adjustments then yield the 1st and 2nd output beams combined at the centre of the reflected beam as seen in Fig. 4.13 (h).

Verifying the alignment and any further adjustments were achieved by temporally observing the beams on the AndOR camera. For this, the laser was set to single pulse mode such that synchronization with the camera allowed different RT output pulses to be examined. Here the imaging system outlined in Fig 4.4 was employed with the pop-up mirrors flipped upright such that the position of the reflected beam was marked on the camera and compared to the beam positions in the subsequent time steps (other RT pulse outputs). If further adjustments were required, M1 and M2 were then iteratively adjusted along the temporal time scale. Here M1 was used to adjust the position of the 2nd output pulse and M3 the position of the 7th output pulse. Iterative adjustments

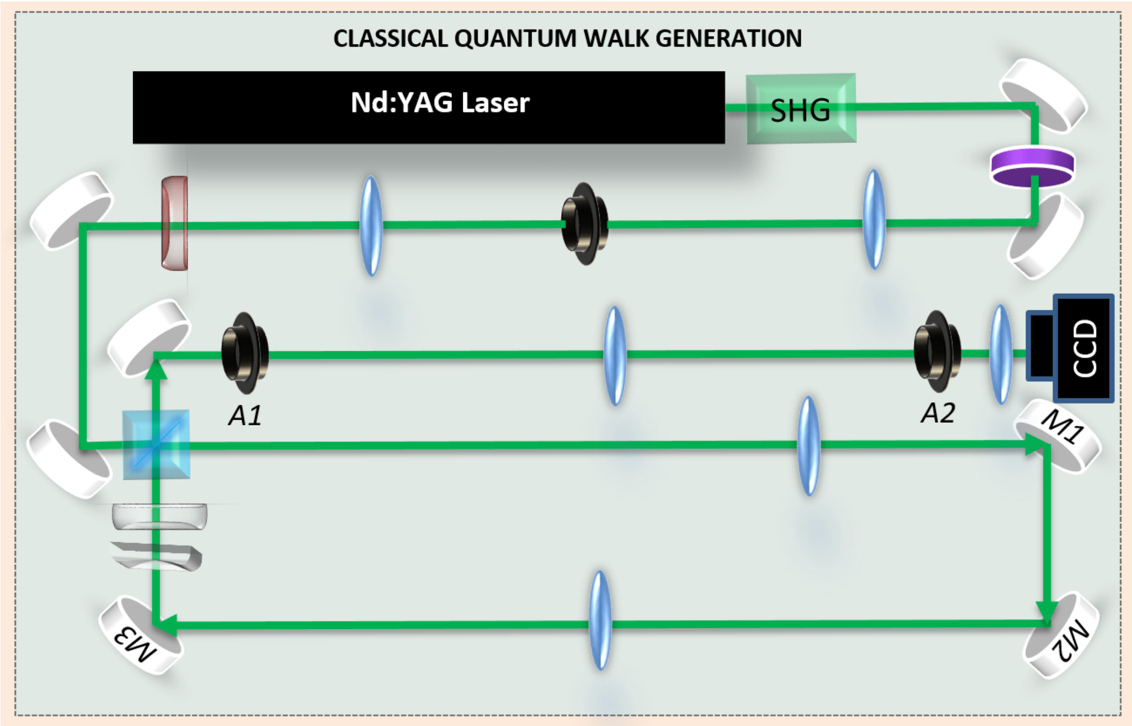

FIGURE 4.12: Selective schematic of Fig. 4.4 indicating the mirrors used for the alignment as well as aperture and camera positions.

then further aligned the resonator to an acceptable standard for reasonable results to be expected from the MS.

4.2.2 Experimental demonstration

Demonstration of the QW was attempted with implementation of both the refractive and 3-copy diffractive sorters for the reasons outlined in the mode sorter analysis section. Subsequently, initial implementation of the conventional Hadamard QW was carried out with the refractive sorter in view of achieving the largest number of steps. This was achieved by placing the QWP with the fast axis at 45^o after the QP, as outlined in Fig. 4.4 and Eq. 4.7. By adjusting the fast axis angle of the HWP before the resonator, the coin state for the walker was initialized as desired. The results obtained are shown in Fig. 4.14 alongside the distributions expected from the simulation outlined in Section 3.3.1.

For a diagonal input, the HWP was rotated to 67.5^o, resulting in a symmetrical initial coin state as shown in Chapter 2. The results are given as Fig 4.14 (a-c) for steps 1, 2 and 8 respectively. A Gaussian-like distribution may be seen in the first two steps with Fig. 4.14 (a) and (b), as expected for the classical case and the initial QW. Good correlation with the first step in (a) is shown where a similarity of 87.1% is seen. A small divergence in Fig. 4.14 (b) may be observed where the intensity near the center of the distribution dips, giving a reduction in the similarity where S = 84.3%. This deviation may be attributed to a distortion from the overlapping of the 1-copy sorter, as was seen in Fig 3.29, coupled with slight misalignment of the mode sorter elements. However, as the walker is taken through further steps, a clear divergence in the OAM weightings from the center position is evident from the distribution shown in Fig 3.4.14 (c). In step 8, a fair correlation between the simulated and measured distribution is seen with a similarity of 87.3% alongside a distinct divergence of the OAM weightings detected away from the central position (OAM = 0) and towards the outer edges, yielding the characteristic QW distribution.

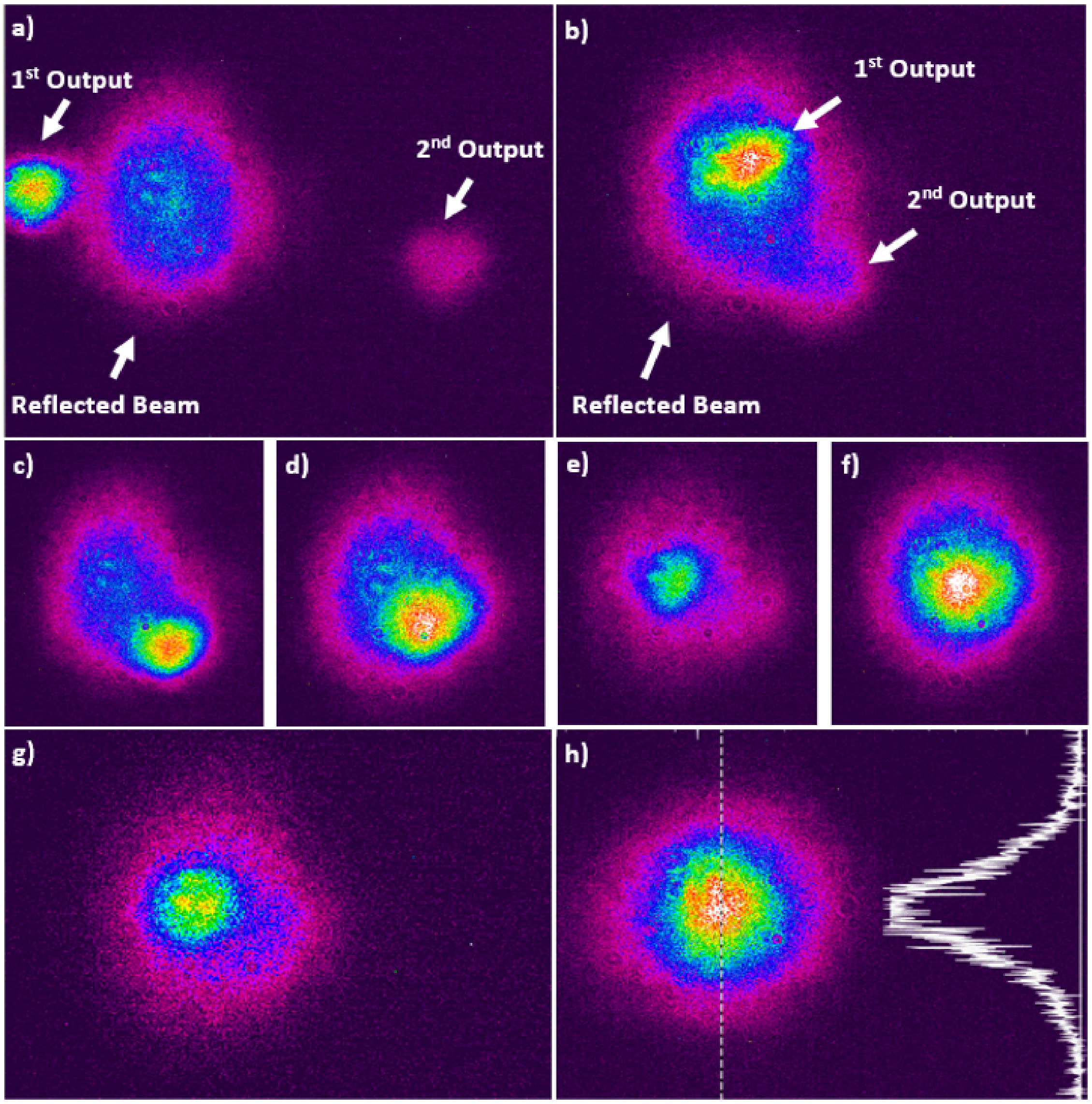

FIGURE 4.13: Images illustrating the resonator alignment procedure where (a) indicates the beams visible in an appropriate plane of choice outside the resonator. The reflected beam is larger than the output beams as the lens system inside the resonator operates as a demagnification telescope to counteract the increase in beam size caused by higher OAM modes. Iterative alignment with M1 and then M2 is shown for the successive images (b)-(g) before achieving the aligned output indicating alignment of the resonator and subsequent modes (h).

By placing the HWP at 45^o, the coin state of the pulse was changed to horizontal polarization, reflecting an asymmetrical input state with respect to the Hadamard coin operator. Accordingly, from Chapter 2, the QW distribution expected should exhibit asymmetry where the OAM weighting towards one of the outer edges is significantly stronger than the other. Figure 4.14 (d)-(f) show the measured results for steps 1, 2 and 5 for these initialized conditions. Here, again, fair agreement between the detected and simulated modes may be seen with the detected modes following the characteristic trend expected for a QW. More specifically, the initial OAM distribution begins centered around the origin with step 1 and exhibiting a similarity of S = 0.843. After step 2, the weightings already form a slight divergence to the left with a high degree of correlation seen with respect to the simulated values as evidenced by a similarity of over 90%. Continuing the QW to step 5, this asymmetrical divergence may be clearly seen in Fig 4.14(f) where the experimental measurements show a similarity of 89.9%. Here the asymmetrical nature of the walk is evident with the weightings detected for the OAM values towards the left being 3 times greater than that of the right, alongside a distinct reduction in weightings at the central OAM value.

Here the largest number of steps that were achieved with the refractive sorter and 50:50 beam-splitter, used to couple light out of the resonator, is shown in Fig 4.14 (c) with 8 steps. Additionally, the similarity values observed are well within the bounds expected for the 1-copy mode sorter for all the distributions measured. This is evidenced as lowest value of 84% for the QW compares favourably to the 79.1% seen in the mode sorter analysis.

As was mentioned in the framework outlined for this spatial mode QW, the waveplates form coins based on their polarization flipping attributes. Accordingly, the QWP set to 45^o is a specific case, resulting in the customary Hadamard coin. In fact, a plethora of different coins may be constructed by adjusting and construing different waveplate combinations and angles. Consequently, a large degree of flexibility is afforded to adjust the environment experienced by the walker by proxy of the coin operator. This is subsequently demonstrated through a few different variations as shown further on. For this case, the focus was towards the change in distribution rather than the sorting range. Consequently, the 3-copy diffractive mode sorter was utilized in place of the refractive sorter. A 90:10 (reflection: transmission) beam-splitter was then also implemented as a result of experimental constraints as well as to preserve the light circulating within the resonator and thus compensate for the additional energy lost to the 0th order of the diffractive optic. It follows that the simulated distributions were then also altered accordingly.

More specifically, rotation of the QWP fast axis to 90^o results in another well-known coin that was also analyzed in Chapter 2. This forms the balanced coin as may be seen by substituting the angle into Eq. 4.4, as shown by

$$\hat{C}(90)_{QWP} = i\begin{bmatrix} ie^{-i\pi} & 1 \\ 1 & ie^{i\pi} \end{bmatrix} = i\begin{bmatrix} -i & 1 \\ 1 & -i \end{bmatrix} = \begin{bmatrix} 1 & i \\ i & 1 \end{bmatrix} \tag{4.12}$$

From Chapter 2, a distinct effect of this coin is seen as a result of the symmetry given by the imaginary numbers in the operator. Subsequently, the asymmetrical distribution formed by the asymmetrical initialized coin state, such as the horizontal polarization state from Fig 4.14 (d)-(f), results in a symmetric or balanced distribution with this coin. This effect may be seen in Fig. 4.15 for step 4 of the QW with a horizontal initial coin state. Here the QWP set at 45^o yielded the distribution seen in Fig. 4.15 (a). Rotating the QWP to form the balanced coin then resulted in the distribution measured in Fig. 4.15 (b). It follows that the symmetry of the distribution is restored despite the asymmetrical input state where equal weighting may be observed for the intensity peaks at OAM = ± 2.

A stronger similarity may be observed between the simulated and measured distributions than was seen for the refractive sorter with 95.4% in both cases. This correlates well with the expectations formed from the mode-sorter analysis where a 96.8% similarity was achieved.

The built-in coin resulting from the polarization flipping action of the QP also forms one of the extreme variations of the QW spectrum. The subsequent operator is thus,

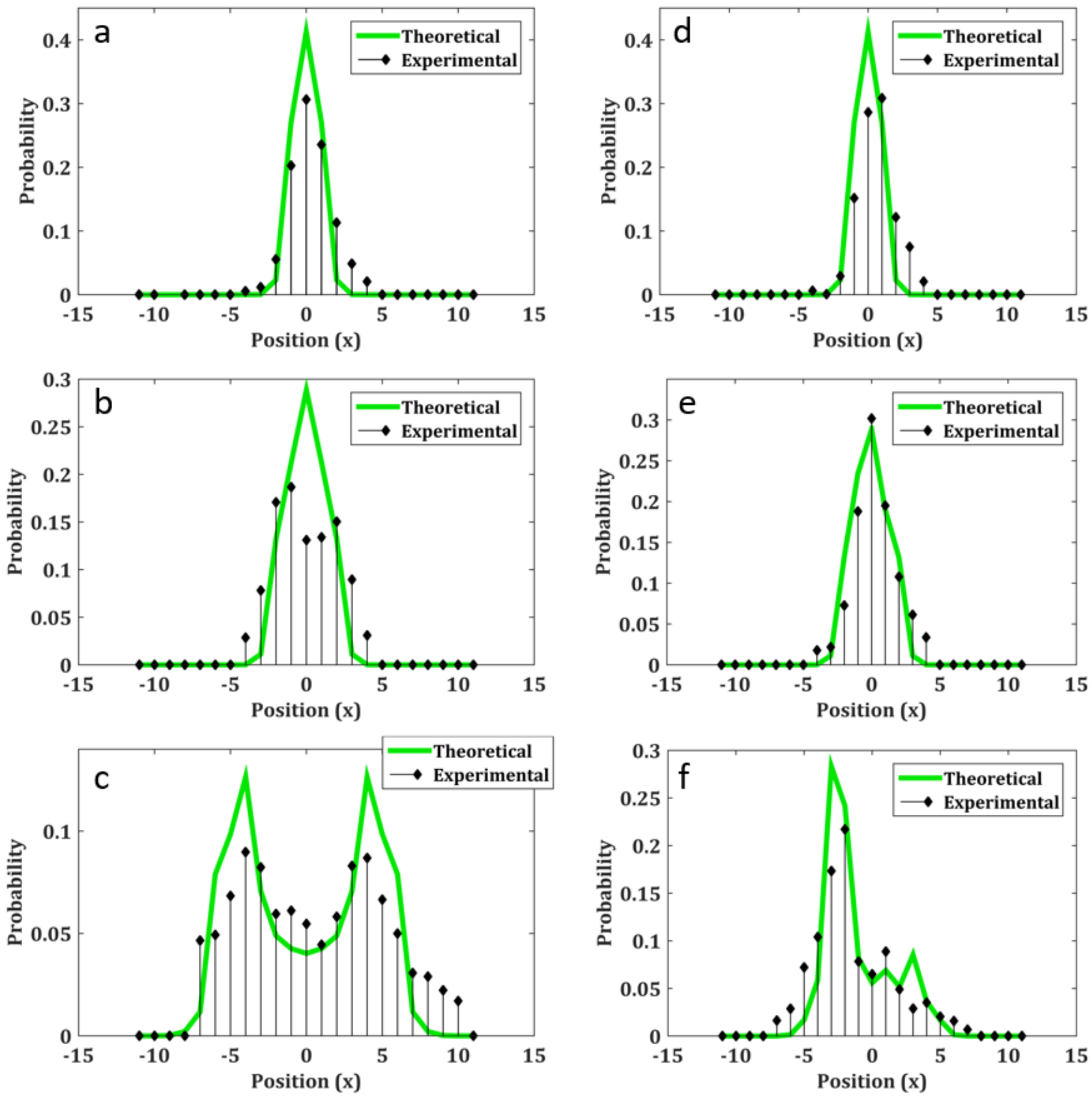

FIGURE 4.14: Experimental results for a Hadamard QW for a (a-c) symmetrical input polarization state and (d-f) asymmetrical input polarization state. (a,d) Step 1 with S = 0.871 and S = 0.843, (b,e) Step 2 with S = 0.843 and S = 0.921, (c) Step 8 with S = 0.873, (f) Step 5 with S = 0.899.

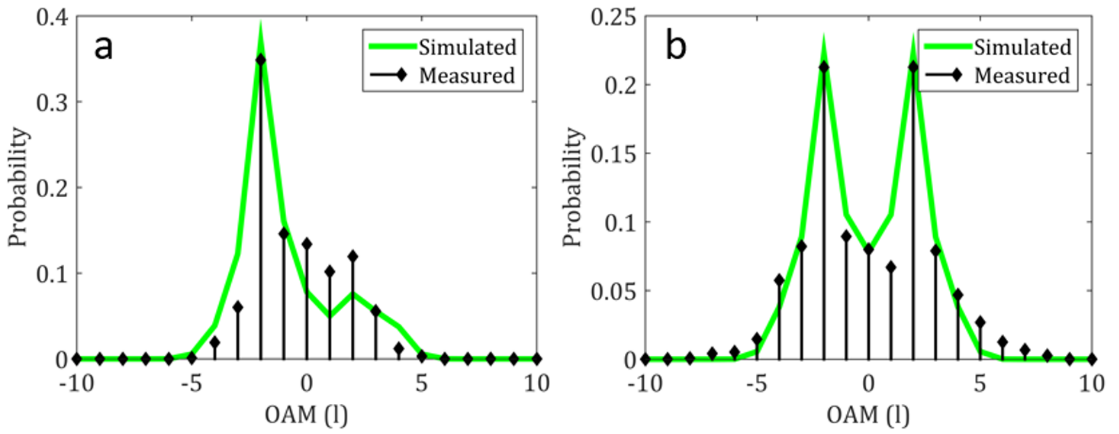

FIGURE 4.15: Experimental results illustrating the transition from the (a) Hadamard coin with S = 0.945 to (a) balanced coin with S = 0.954 for step 4 in the QW for an initialized horizontal coin state.

$$\hat{C}(90)_{QWP} = i \begin{bmatrix} 0 & 1 \\ 1 & 0 \end{bmatrix} \tag{4.13}$$

This coin actually forms the equivalent of a NOT-operation [23], causing the walker to completely exchange polarization states and as such alternate directionalities of the steps. The walker then oscillates about the origin, perpetually propagating from OAM = 0 to ± 1 depending on the step. With the overlapping pulses from the experimental implementation, this corresponds to a distribution about the origin whereby the weightings between these OAM values fluctuate with the step number.

Results from this coin are shown in Fig. 4.16 (a)-(c) for steps 1, 4 and 5 respectively. Here the distinct confinement of the distribution to the origin or initial position of the walker is evident throughout the steps. Step 4, in particular, bares significant contrast to the same step distributions shown for Fig 4.15 where the maximum weighted OAM state is 0 as opposed to the ± 2 states with a characteristic dip at the 0 state.

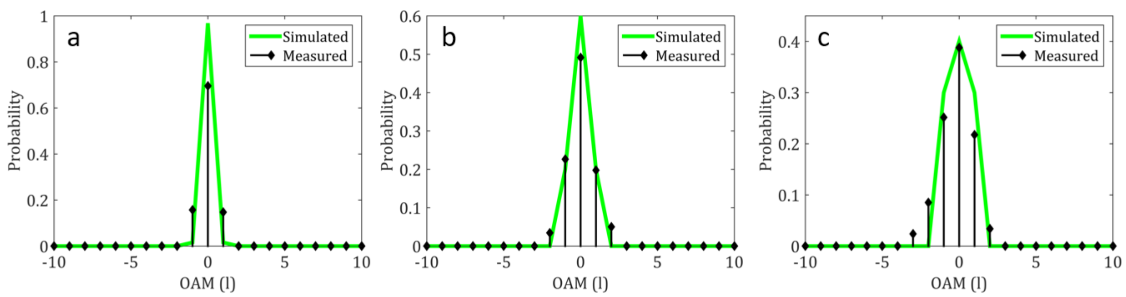

FIGURE 4.16: Experimental results for (a) Step 1 with S = 0.844, (b) Step 4 with S = 0.911 and (c) Step 5 with S = 0.854 of a NOT-coin QW for an initial diagonal coin state.

The similarities associated with the modes detected in this case has a notable decrease in correlation compared to the high values expected from the mode sorter analysis. This may be explained due to the increased sensitivity of the sorter to the changes in both the beam size and alignment as opposed to the refractive sorter. In the previous case, the mode sorter was aligned to a specific step, demonstrating the change in distribution for a specific output pulse. In this case, however, the mode sorter was aligned to accept a range of modes which decreased the accuracy associated with the detected modes. Consequently, an increase in cross-talk may be observed in the higher-step distributions with small detections of outlying modes are seen, such as at ± 2, where such modes are not expected. These similarities, however, still show fair agreement between the simulated and measured values, illustrating the action of the NOT-coin generating an extreme QW where the walker is confined about the origin and oscillating between the fundamental first positions.

Another extreme QW may be generated by considering the effect of an additional HWP at 0^o. The corresponding coin operator is determined by,

$$\hat{C}(0)_{HWP} = [HWP(0)][HWP_{QP}] = \begin{bmatrix} 0 & i \\ i & 0 \end{bmatrix} \begin{bmatrix} 0 & i \\ i & 0 \end{bmatrix} = - \begin{bmatrix} 1 & 0 \\ 0 & 1 \end{bmatrix} \tag{4.14}$$

Equation 4.14 is in fact the identity coin with the extraneous global phase factor of -1 being disregarded. It follows that the operation of this coin is to continually ladder each state in the same direction, causing no interference between the states in comparison to the NOT-coin which yielded maximal interference within the walker. As a result, this coin generates states at the extremes of the distribution for each step, such that maximal variance is seen for the QW. Due to the experimental overlap, this extreme laddering is still evident, however, with a slight broadening of OAM states about that extreme value.

Measurement of the QW is shown in Fig 4.17 (a)-(c) where step 0, 3 and 4 are shown. Here a clear profile of walker evolution can be observed with the walker beginning at the origin in Fig 4.17 (a) and centring at the most extreme positions for each step. This is seen as positions ± 3 at step 3 in Fig. 4.17 (b) and ± 4 at step 4 in Fig. 4.17 (c). The increase in positional spread is substantially noticeable in comparison of step 4 here with that of the NOT-coin (Fig. 4.13 (b)) as well as the Hadamard and balanced coins (Fig. 4.15). Here with the NOT-coin, the two distributions appear the inverse of the each other. In between these extremes, the Hadamard and balanced coins centre about ± 2.

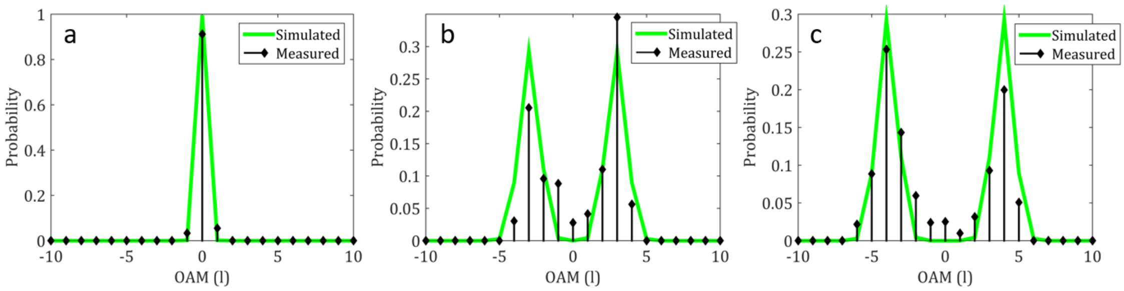

FIGURE 4.17: Experimental results for (a) Step 0 with S = 0.943, (b) Step 3 with S = 0.869 and (c) Step 4 with S = 0.871 of the extreme QW with an identity coin for an initial diagonal coin state.

The similarities seen for these distributions again show a fair correspondence with expectations and are within similar bounds that was seen in the NOT-coin case for identical reasons. The asymmetry in steps 3 and 5 may be attributed to slight misalignment of the output pulses to the mode sorter system which was exacerbated by the increased sensitivity of the diffractive sorters.

4.2.3 Challenges and limitations

In the previous section, we demonstrated a scalable, robust system with a high degree of flexibility from the significant degree of control that was afforded with both the initial walker state and the coin the walker may experience. Although these factors show great promise for furthering the development of a successful system based on this phenomenon, the questions still arise as why the maximum number of steps was limited to 8 as well as how feasible the accuracy and precision of the results can be for further steps in the QW. Accordingly, we review the practical challenges and limitations experienced with this implementation for a spatial mode QW.

Walker generation, step synchronization and intensity retention

The initial challenges encountered with the system may be conferred with the laser system implemented. As was shown in section 4.2.1, the spatial profile of the beam was neither single mode nor of a symmetrical profile. This was corrected with the implementation of a spatial filter where a pinhole placed in the FP of a $4-f$ system filtered out the additional radial modes and generated a Gaussian spatial profile. Two distinct disadvantages were intrinsic to this technique. Firstly, as the pinhole was filtering out the extraneous modes, it was also decreasing the amount of initial intensity that could be coupled into the resonator. One approach that may be considered would be to increase the intensity of the beam being spatially filtered and thus increase the percentage of the light being passed through the filter. Secondly, this is limited to the damage threshold of the pinhole, setting an upper boundary on this value; now as the beam is focused into a diffraction-limited spot in the FP, the energy density experienced by the pinhole is high which severely decreases this upper-bound. As a result, the maximum amount of energy which could be passed though the pinhole was 1 mW.

Phase matching drift over time from the SHG employed was also seen. This caused the shape of the spatial distribution in the filtering plane to alter which then caused the pinhole position to be slightly off-center. As a result, a further reduction in the percentage of light let through was seen. This would then have to be corrected through small adjustments of the phase matching alignment.

Another issue discussed in detail previously was the temporal width of the pulse in comparison to a realistic and stable resonator length. Here the pulse was estimated to be 30ns long. We solved this issue by incorporating the overlapping pulses into the simulation and evaluating the results in terms of the modified distribution. This, however, is not an ideal solution which comes with further issues. Specifically, the simulation depends on capturing a specific portion of the pulse from each round trip where the weightings from each pulse could be quantified. However, as the step is determined by the temporal gating time based off the initial pulse, the jitter in the synchronization system of about 2-3 ns resulted in this weighted influence being more of an approximation. As a result, several measurements of the same step would be required to mitigate the effect and the average taken to be a good resemblance of the approximation.

Further challenges encountered resulted from the synchronization limitations between the camera and laser system. Here the AndOR camera formed the limiting factor in terms of how many pulses could be evaluated and thus was utilized as the triggering mechanism. For alignment, time and stability purposes the AndOR camera could be run in a continuous mode which captured frames at a steady rate. Here a fire signal was sent to the laser at a constant frequency, allowing measurements and checks to be carried out with a small delay between frames. Due to the operation mechanisms of the camera, this frequency had a maximum value of 2 Hz which was far less than the recommended 10 Hz operating frequency of the laser. Consequently, several problems resulted in terms of the long-term operation of the system. Namely, a slow drift occurred in terms of the pulse synchronization where the RT pulse selected by setting the delay would drift out of the time frame such that the next pulse was actually being captured after a 30 min running window. Resetting the system would then return the system to a reliable state for another 30 min. This additionally had an effect on the accuracy of the RT measured against the simulated distributions. Furthermore, a slow decrease in the intensity of the pulse being generated by the laser accompanied the pulse drift observed, resulting in a restriction on the maximal number of steps which could be comfortably captured.

Another hindering factor with regards to the efficient capture of different time steps from the resonator was the amount of light being coupled out of the resonator as a result of losses in each round trip. Subsequently, the pulse intensity decreased for every additional step captured, as such, in addition to altering the gain of the camera, an adjustment of neutral density filters placed before the camera was required for transitions between the different steps.

Detecting the walk: expected accuracy and precision

As this mode sorter was already extensively evaluated, this will only briefly be covered here in view of furthering the QW steps. As was observed previously, two choices of mode sorters were available with a traditional refractive sorter in comparison to a diffractive 3-copy sorter. Here, a trade-off between using these sorters was seen for the range of sorted OAM modes, the range of allowed input beam sizes, and the accuracy of the detected mode weightings along with the associated cross-talk. Evaluation of the results seen in the previous section showed that only a fair accuracy may be expected for the refractive sorter due to the overlapping modes. This allowed the distribution to be comparable to that which was simulated, but could also be notably improved. Precise alignment of the diffractive sorter for the QWP symmetrical coin case showed that this is indeed possible. On the other hand, due the number of round trips required by the QW, a change in beam size as well as any variation in the alignment resulted in a significant decrease in the accuracy such that the similarity range became comparable to that of the refractive sorter for the QWs with the HWP coins.

It follows that the refractive sorter holds the most promise for detecting a large number of steps with more practicality as both the beam size and OAM increases with the number of steps. Accordingly, only small adjustments to the alignment of the elements would be required for acceptable detection of the distributions. Implementation of the diffractive sorter in this case would require a significant number of attempts to demagnify the beam as the QW steps increase, in addition, the re-alignment would also require adjustment of the sorter every 20 modes for the accuracy to hold.

Coin preservation

Another impact on the QW was the effect of dielectric mirrors on the polarization state of the pulse. Thorlabs E03 dielectric mirrors were used in the cavity were the expected percentage of horizontal and vertical light reflected was over 98%. While the dielectric mirrors preserve these states of polarization, they also induce a variable phase difference between the components that is wavelength and angle of incidence dependent. As the QW depends on the phase difference between these components being constant due to the circular polarization dependence of the QP, these mirrors act as additional QWP coins with each reflection. This effect may then be mitigated by placing another WP in the cavity for the correction of the un-wanted phase alteration by the elements. For the QW implemented here, the totality of the mirror phase adjustments was that of the HWP of Eq. 4.13. Therefore, by incorporation of this effect, the QWs were measured in Section 3.4.2.

Improvement

A significant amount of improvements may be expected for the implementation of a laser source which generates an initial Gaussian beam with a FWTM pulse width of 1 ns at wavelength not requiring an SHG. With the same 10 ns cavity, the reflected pulses would not overlap inside the cavity, resulting in a distinct separation between the pulses coupled out of the resonator. This would allow for easier selection of the correct step in the QW with the synchronization system. Additionally, the QW distribution would result in the OAM modes for each round trip being alternatively even and odd, causing the overlap issue with the refractive sorter to be mitigated as there would be no adjacent OAM modes. Without the spatial filter, the energy of the initial pulse put into the resonator could also be increased, allowing the number of detectable RTs to be significantly increased. Here the upper bound on the intensity would be that of the WP or QP inside the resonator. The lack of an SHG would also result in the beam profile remaining constant, removing much of the uncertainty associated with the walk.

With regards to adjustments to the intensities incident on the ICCD, a motorized filter wheel could be implemented in place of the manual system. Accordingly, a set change in the filters before the ICCD could be automated with the synchronization such that an optimal amount of light is detected. The practicality of capturing a large number of steps is then improved significantly with the time between captured steps being set by the adjustment time for the filter wheel which could be a matter of 1-2 seconds.

4.2.4 Conclusion

In conclusion, we have established the framework set out by Goyal *et. al.* [126] for a classical QW in the spatial modes of light and extended the flexibility of the system for variations in the coin and initialization steps of the walk. The various experimental considerations were explained and discussed in detail as well as the technique developed for alignment of a 4-mirror resonator. The expected QW distribution was also adjusted to include the experimental limitations of the resonator length and pulse width.

Altogether, several QWs were successfully demonstrated with classical light in the OAM and spatial DoF despite the challenges and limitations discussed. Moreover, the QW was also demonstrated utilizing two different detection systems with varying degrees of accuracy. While the correlation between the simulated and measured distributions was not optimal, fair agreement was seen with the similarity of the experimental data not falling below 84%. Additionally, some distribution similarities were found to be higher than 90% with implementation diffractive sorter and as high as 95% with the most optimal alignment.

Here the scalability of the system is evident with 8 steps achieved from only 1 set of coin and conditional step operators (QP and WP). The high degree of control available for the initialization is clearly demonstrated through alteration of the Hadamard QW symmetries through adjustment of the initial polarization state of the walker. Furthermore, a high degree of flexibility was also shown for choice cases of coins, yielding QWs of differing symmetry as well as the extreme cases where maximal and minimal interference was seen within the walker.

It follows that with improvements to the system, successful demonstration of practical QWs for a large number of steps is within reach. Consequently, the concept and implementation of this scheme has been explored in detail, laying the foundation for further implementation and uses. In the following chapter, the impact of this is explored along with additional adjustments which could further the practicality of this scheme for effective implementation in the future.

Chapter 5

Outlook and future work

5.1 Summary and outlook

Over the course of this dissertation, the quantum walk phenomenon was examined in detail with an in-depth look at the principles and properties associated with QWs. Chapter 1 gave a broad, intuitive overview of the QW concept. In here, the versatility of this phenomenon was discussed with promising applications ranging anywhere from quantum computing to simulating systems such as energy transport in photosynthesis and Anderson localization in Bose-Einstein condensates. Here the mathematical framework was reviewed in Chapter 2, using Dirac and matrix notation. From this we looked at the dynamics associated with the walk as well as the implications of the types of coins employed, laying the foundation for physical and intuitive understanding. It was seen that due to the particle-wave nature of the quantum properties of particles undergoing this mechanism, the walker interfered with itself and spread over the space in which it was walking. Accordingly, the wave nature of this phenomenon could be seen to relate to the mechanics associated with classical waves. Exploiting this, light as a wave was then discussed as a possible classical alternative for the QW.

In view of implementing light as a walker, the basic physics was briefly reviewed, highlighting two distinct properties associated with coherent, paraxial light. More specifically, natural solutions to the wave equation for transverse electric field distributions were considered. Here, emphasis was placed on the solution in cylindrical coordinates with Laguerre-Gaussian spatial modes due to their popularity in the optics field and subsequent role in this work. From here the two properties explored in detail were OAM and different polarization states of light. These properties were seen to form two degrees of freedom for classical light which could be manipulated to generate beams with both spatially varying phase and polarization, yielding vector vortex beams. Such modes were then shown to have an interesting analogue in terms of the well-known quantum principle of entanglement. Utilizing the orthogonality of these spatial and polarization degrees of freedom, it was shown that a non-separable relation could be generated in the same entity, resulting in classical entanglement. Here, particular importance could then be drawn for the QW as these modes of light contain an additional well-researched analogue for the classical implementation of this quantum phenomenon which was not seen as clearly for other such classical implementations that were carried out. It followed that with these degrees of freedom, a closer walk along the quantum-classical divide could be made.

Accordingly, the question was then raised as to how this classical version differed, with so many similarities, to the quantum case. Subsequently, the implications and differences associated with attaining these different QWs was discussed, highlighting the ‘quantum’ of the QW. Here it was seen that the main differences separating the classical and quantum forms of the QW was the non-locality property unique to quantum mechanics as well as the measurement process where quantum particle probability functions were collapsed to a single state with each measurement. Meanwhile, in the classical case, the intensity of the wave for all the positions could be measured in a single snap-shot. Subsequently, the quantum case both contained an essence of randomness and required several rounds of measurements to build up the probability distribution.

The different properties and difficulties associated with making a QW ‘come to life’ was then discussed in detail with Chapter 3. Here reference was made to some of the numerous systems where such walks were attempted, both quantum mechanically and classically. From these implementations, an upper limit to the number of steps were seen, with all walks being limited to below 100 steps in both the quantum and classical case, which indicated the requirement for significant further development to this field for a more sustainable QW. Here the advantages of utilizing classical light was made evident with its robust properties as well as the improved degree of control afforded to manipulate the properties of light. The scheme utilizing the polarization and orbital angular momentum degrees of freedom, proposed by Goyal *et. al.* [126] in their physics review paper, was then highlighted as a particularly promising option in terms of these properties as well as the additional analogue associated with the ability to classically entangle them. Here OAM was suggested as a position space with a theoretically limitless number of states and polarization as the coin space, forming intrinsic sub-states for every OAM position state.

Such a realization, however, required the use of particular elements to form a QW ‘toolbox’. It followed that this toolbox was assembled with the various elements being characterized such that a good understanding was established for their performance, the physics behind their operation and the practical aspects of their experimental implementation. The toolbox was subsequently comprised waveplates, QPs, and mode sorters. Here waveplates were shown to manipulate the polarization states, converting between different basis states as well as forming assorted superpositions. Accordingly, this formed the coin operator, flipping polarization as desired. The QP was shown to ladder OAM states according to the polarization of the incident light with spin-to-orbital angular momentum conversion ruling the laddering process. Overall observation of the QP generation process showed the element to be a classical entanglement generator in specific cases, pairing the polarization states with OAM in a non-separable manner to form vector vortex beams and entangle the walker along its journey. The QP then formed the conditional step operator in the quantum toolbox. Consequently, concatenation of the QP and waveplate resulted in the QW evolution operator, causing the propagation of a classical quantum walk in the spatial modes of light.

Further evaluation of the modes being generated by the q-plate yielded interesting results. Here the modulation of light, by considering only the phase, was seen to result in OAM. Here the amplitude was disregarded, however, with consequence. Playing with only one aspect of the spatial profile was consequently seen to generate beams which were not solutions to the wave-equation and thus not preserved naturally. As a result, it was shown that nature then alters the disregarded amplitude factor itself upon propagation with the formation of radial modes. Power was shifted from the desired 0th order of the spatial distribution to diverge outwards. Moreover, this was seen to drastically increase in severity with the OAM magnitude. Care and experimental consideration was then noted for this vortex beam generation method where for higher OAM beams, additional considerations would be required. In terms of the QW, this required a smaller initial beam size, an imaging system between steps to mitigate divergence of the beams and the use of larger optical elements so as to contain the spatial spread of the modes.

The effectiveness of realizing a QW lies as much in the walking as detecting the walker. Consequently, the last elements in the toolbox involved unravelling the twisted light, or OAM, to uncover where the walker was and ‘how much’ of the walker was at each position. Performance and accuracy of the mode sorter, in lieu of this, was of particular importance where any inaccuracies would directly affect the precision and reliability of the generated walk. Subsequently, two types of sorters (refractive and diffractive) were evaluated for appropriate application. The sorting action of the mode sorter was first illustrated experimentally with each OAM mode transformed into spatially separated elongated spots, comparatively yielding ‘how much’ of the walker was in each mode. Accordingly, the OAM-dependent spot position, spot resolution, viable range of adequately sorted OAM modes, cross-talk, resolution of adjacent spots and detection of multiplexed OAM mode weightings were evaluated for the sorters. Here, an overall trade-off was seen between the refractive (1-copy) and 3-copy diffractive sorter performance. The refractive sorter was found to be more suited for larger OAM detection ranges and variable incident beam sizes at the cost of accuracy and a notable degree of cross-talk into adjacent modes. On the other hand, the 3-copy diffractive sorter was seen to yield more accurate and precise results with significantly less cross-talk at the cost of OAM mode range, increased sensitivity and large restrictions on the incident beam size variability. It followed that for quantum walks aimed at achieving as many steps as possible, the refractive sorter was more suitable. Likewise, for quantum walks where the distribution at a few, select steps was of interest, the 3-copy diffractive sorter was the optimal choice.

With the toolbox completed for a QW in the spatial modes of light, we addressed how one could implement such a walk in further detail. Here, in Chapter 4, the walk was developed in the convenient coin space by implementing Jones matrices. Experimental implementation of a largely practical QW was then considered so as to realize a system that could be largely effective. Such a system was seen to require high degrees of coherence, control, flexibility and scalability such that many steps, finite resources and arbitrary operations could be easily carried out. Following this, the experimental scheme proposed by Ref. [126] was seen to be highly optimal where an external resonator could continuously circulate a pulse of light (the walker) through the QW elements. This liberated the amount of QW optics from the number of steps taken.

Details on actualizing the experimental scheme were then discussed where the consequential restrictions and limitations imposed for a robust system were explored. Here the experimental setup constructed was examined along with the subsequent considerations. More specifically, the walker was shown to overlap in the resonator, resulting in a convolution of the round-trip modes. Simulation of this effect lead to an adjustment of the traditional QW distribution where it was shown to broaden out the distribution into adjacent OAM modes, but maintained the same diverging trend. Here, the laser mode was also seen to require demagnification and spatial filtering. As the steps evolved over time, the isolation of each step was explored through synchronization of the laser and camera. A procedure for fine alignment of the resonator was then developed for optimal results.

Utilizing this setup, we demonstrated, for the first time, a QW with classical spatial modes of light. Here OAM and polarization were consequently shown to be an interesting base for a QW which was significantly more robust and easier to manipulate than on the quantum mechanical level, with a twist.

By employing the refractive sorter, the customary Hadamard walk was obtained where the system was pushed to yield a maximum number of steps within the practical limitations of the equipment available. Accordingly, the largest number of steps achieved for this configuration was 8, forming a proof of principal in terms of the viability of this scheme where only a single set of propagation and coin elements were used. This doubled the number of steps that were acquired in the quantum counterpart of this experiment [117] where only 4 steps were achieved with a linear scaling of the QWP-QP elements. Additionally, observation of successive steps in the quantum walk distribution required the addition and removal of QWP-QP sets, in the quantum case, resulting in the system requiring new alignment for each step. Conversely, imaging the different steps only required alteration of the delay set in the synchronization system in this implementation.

A significant degree of flexibility and control was shown where the symmetry of the Hadamard QW was altered by changing the initial state of the walker by simply rotating a half-wave plate before the resonator. Three additional types of QWs were also achieved through alteration of the coin by employing different waveplates and rotation of the fast axis. Here the different coins changed the dynamics of the quantum walk, highlighting the interference property of the QW. Subsequently, a range of different degrees of interference was achieved, resulting in adjustments in the variance of the walk. By employing a NOT-coin, maximal interference lead to oscillation of the walker about the initial position, without either a spreading of the walker along the positions, as would be expected with the classical random walk, or a divergence of the walker from the initial position as traditionally expected for a quantum walk. The Hadamard coin, previously, showed intermediary interference with equally weighted superpositions yielding maximal classical entanglement of the coin states with each position. Here, by simply altering the phase between the coin basis states with a balanced coin, the symmetry of the QW distribution was also shown to change. Pursuing the other extreme of the QW, an identity coin lead to the greatest variance possible with the walker occupying only the outer positions of the distribution with no interference occurring as it propagated. Achieving these different variations in the same system showed the flexibility and repeatability desired for practical implementations of a QW system.

Here, an additional advantage was obtained where classical entanglement afforded an additional analogue to the quantum of the quantum walk. With this property of non-separability already being well studied [71; 74–76; 177], and used in similar analogous capacities [77; 111; 128; 132; 178], possibility for further insight is evident. Here one could employ some of the analysis tools such as the Bell inequality [179] and entropy measures [180], already being exploited from the quantum regime, to study additional aspects of the quantum simulations that was not obvious in the other classical implementation methods. Here the main limit experienced is the non-locality properties found for the quantum case. However, there are additional convenient restrictions that do not apply here which may also work towards favoring this method, such as the non-cloning theorem [180–182] which implies that you cannot copy the quantum state or information. Classically, this is not an issue which may lead to amplification advantages which are discussed in the next section as a possible improvement to the implementation exhibited here.

The question of how this implementation and method compares to the ideal characteristics of an optimal quantum walk may now be addressed. Here a significant degree of flexibility was shown possible with control over the initial walker state and coins easily demonstrated. However, what about using the quantum walk for dynamical environments or operations that require the coin operation change for every step? While this was not demonstrated here, it is possible through simple modifications with an electro-optical phase modulator as discussed in the next section. Ultimate flexibility where environmental or coin control at the positional level is consequently the next step. For this scheme, this remains an open question as this would require an element that was biased to every OAM value, which would cause polarization adjustments based on the twist or phase of the beam while leaving this property relatively changed. Perhaps a solution for consideration is to implement a coin that also altered the underlying architecture of the position space i.e. altered and marked the OAM based on the polarization in a variable and controllable manner.

Considering the dimensionality criteria, the quantum walk here was confined to 1D and as such the computational and simulation limitations associated with it. This may, nonetheless, also be further explored with simple adjustments to the scheme and forms an additional avenue for future work as detailed in future work. As this work formed a proof of principal experimental realization of this quantum walk, the scalability of the system was shown where the resource that scaled with the number of steps was simply time. Accordingly, the physical resources could remain constant, allowing the limitation to the number of steps to be confined to the loss of intensity in each round trip as well as the initial intensity of the walker. Here the scheme was consequently limited to only 8 steps due to the available equipment. Subsequently, with an adjustment in the quality of the initial state from the walker, greater intensity as well as a much larger number of viable steps could be reasonably expected. Here, another amplification technique discussed later also opens the possibility for hundreds of steps. Detection of the quantum walk in this implementation falls within the ideal criteria which is an important aspect when both evaluating an algorithm and understanding a quantum process by using the QW as a simulation. This was achieved with real-time measurement and step selection where the only consideration here was the mode sorter alignment. Here, the QW distribution at each step was achieved with a single snap-shot in time.

Altogether, a first-time implementation of a quantum walk with classical spatial modes of light was demonstrated. We discussed and showed the viability of the scheme used to become a versatile platform for practical, easy computations and simulations. The experiments afforded insight into the operations of the elements used to exact the required transformations in the polarization and spatial degrees of freedom. Furthermore, we walked the quantum-classical divide to obtain the robust scalability desired. The door to another analogue was consequently opened in this gray area which may be exploited to further the understanding of quantum mechanical phenomenon based on classical entanglement properties in this regime. It follows that the great potential associated with quantum walks in spatial modes, a plethora of benefits and versatile uses are possible.

5.2 Future work

The scheme proposed by Goyal *et. al.* [126] and explored in this work offers a diverse platform to carry out many different implementations of the QW. Where previously we showed the feasibility of obtaining such a QW with classical light and demonstrated the flexibility of the system, here we extend the system to show how it may be diversified. It may consequently be used to carry out interesting forms of the QW which allow it to be a substantial basis for which different computations and simulations can be easily achieved for future work in this area.

5.2.1 Two-coin steps and dynamical walks

One particularly simple augmentation to the QW is the addition of another QP-WP set where the WPs form different coins. This concept is illustrated in Fig. 5.1 (a). It follows that for every odd and even step, the walker will experience the equivalent of a different environment or operation. Subsequently, the walker undergoes a periodic alteration with the number of steps, such as a particle in a periodic potential. This may then also be further extended to include more intricate periodic operations as required.

Another simple augmentation may result from the addition of an electro-optic phase modulator (EOM) to the resonator after a QWP. Here the EOM works on a temporal scale where a variable phase difference may be induced between the horizontal and vertical components of light based on the voltage placed over the crystal. The EOM subsequently has a coin operation similar to [23],

$$|\psi\rangle\, EOM(v) = \begin{bmatrix} e^{i\varphi_H(v)} & 0 \\ 0 & -e^{i\varphi_V(v)} \end{bmatrix} \tag{5.1}$$

where v is the voltage placed over the crystal, $\varphi_H(v)$ is the voltage-dependent phase imparted to the horizontal polarization component and , $\varphi_V(v)$ is the voltage-dependant phase imparted to the vertical polarization component. It follows that the voltage over the EOM may be switched

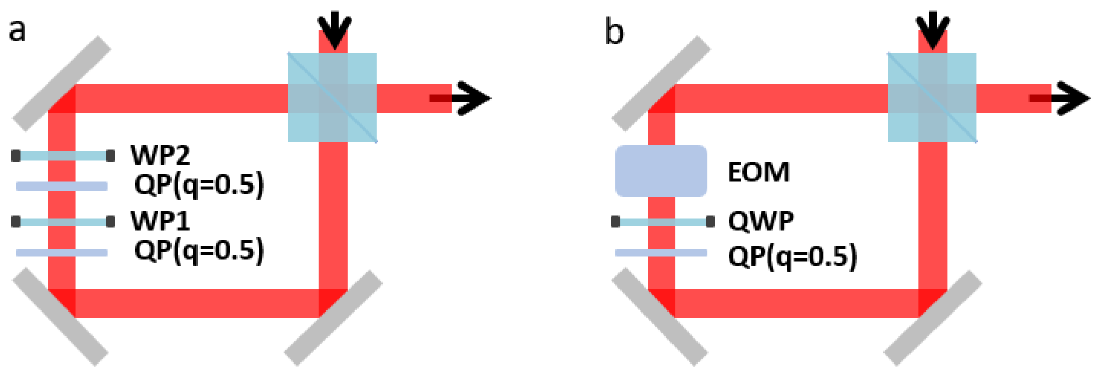

FIGURE 5.1: Schematics for (a) a two-coin and (b) a dynamical QW for the scheme explored in this work.

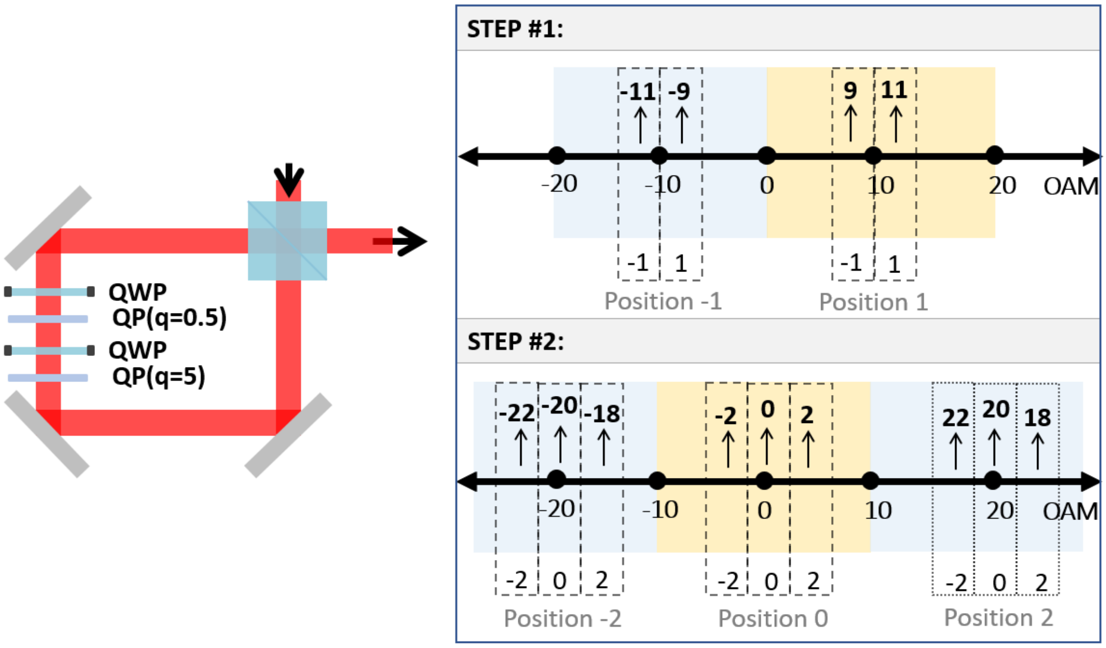

FIGURE 5.2: Illustration the schematic for a QW within a QW and a demonstration of the walker movement in a pseudo-2D space for 2 steps of the walk.

temporally such that at every RT the pulse experiences a different coin configuration. This opens the possibility to achieving a dynamical QW where full control of the environment for every step can be achieved, resulting in a greater degree of flexibility in the system. Accordingly, the walker may experience a plethora of dynamical environments or operations as needed for simulation or for different algorithms by simply programming a desired time-dependent voltage which is synchronised with the QW system.

5.2.2 A quantum walk within a quantum walk

The dimension of the QW may also be extended into 2D by implementing a quantum walk within a first, initial one. This type of 2D walk follows a similar idea which was implemented in a time QW by Schreiber *et. al.* [183]. In this context, it works by considering a pseudo-OAM subspace in a larger OAM subspace by choosing a QP with a larger charge, such as the $q = 5$ in Fig.5.2. Multiples of this OAM value (i.e. $nx10$) forms the larger OAM space and represents the walker in one dimension. A WP following this QP is then the coin for this dimension. By placing a secondary QP-WP concatenation after this with a smaller charge (e.g. $q = 0.5$), the secondary pseudo-subspace is formed. It follows that the walker takes one large step, such as the ± 10 in Fig. 5.2 and smaller steps about each of these nodes to ± 9 and ± 11 respectively. The intensity of the light (probability of the walker) is then measured in a large bin between the multiples of the large charge (the colored squares in Fig. 5.2 and for each of the specific OAM values (dotted squares). The larger bins yield the probability of the walker for the equivalent positions in the one dimension ($x - direction$) while the smaller (dotted) bins yield the probability of the walk in the other dimension ($y - direction$). Further steps then propagate both the large and small QW such that a 2D QW takes place for every RT.

The number of positions here then scales much larger than in the 1D walk for each step such that a much larger walk may be implemented in a far shorter number of RTs. For instance, taking 10 RTs results in 21 x 21 = 441 possible positions as opposed to only 21 taken in the equivalent 1D case. It follows that far less complications are required here to implement a simulation or computation than for the 1D case. The question here then becomes, how far can we push the dimensions of the pseudo spaces with appropriate q-plate charges?

Different WPs may also be used such that the walker experiences different environments in each direction that it spreads. Implementation of the two EOMs for each dimension may also yield a significant degree of flexibility and numerous options for different environments to be simulated or possible algorithms to be implemented. Moreover, this nested quantum walk does not necessarily need to be confined to 2D. Accordingly, with sufficiently large spaces, how many quantum walks within quantum walks can be made?

5.2.3 Amplifying away losses

As indicated previously, there is no restriction on copying states in the classical realm. Subsequently, it is possible to amplify the spatial modes of the walker, where it is not so in the quantum case. Based on the results by Sroor *et. al.* [184], by utilizing an Nd:Yag crystal in the system, the spatial modes may be amplified for a QW implemented with a 1064 nm wavelength such that the weightings and modes are preserved. Consequently, a lossless classical QW may be generated where a theoretically limitless number of steps may be achieved. Accordingly, a maximally sustainable QW is possible with this scheme. The question here then becomes: "where is limitless in the laboratory?"

5.2.4 Conclusion

The concepts suggested here are only a few examples of the possibilities based on the principals of a QW with spatial modes and classical light in conjunction with the resonator scheme as a platform. Here, a significant contribution to the usefulness of a classical QW may be seen with these implementations. One last degree of freedom, that is yet to be considered, is a method for obtaining dynamical control of the coin state at each OAM position in every step. The closest scheme for adapting this setup was proposed by Ref. [185] where a Dove prism is incorporated, generating an 'electric' QW. Here, an OAM-dependent phase is imparted to each OAM mode, allowing an OAM-related phase to be 'seen' by the walker. However, full independent control for the environment at each position is still elusive. An additional avenue, where merging quantum and classical computing may also be explored. Here, by combining machine learning with the QW system may also serve to further and enhance the performance of QWs in future executions. As such, the development and implementation of a maximally optimal system still requires notable development. This scheme, however, in light of the requirements for an ideal QW system, holds substantial promise.

Appendix A

MATLAB simulation codes for the QW

A.1 QW theoretical simulation

```
n=60;%number of steps

%% Defining the conditional translation operator

S_plus = diag(ones(1,(2*n+1)-1),-1);
S_plus(1,(2*n+1))=1; %shift operator - shifts position up by one
S_minus = S_plus.';%shift operator - shifts position down by one
C_plus = [1 0;0 0]; %coin projection operator - isolates the heads
state (positive direction)
C_minus = [0 0;0 1]; %coin projection operator - isolates the tails
state (negative direction)
T_plus = kron(S_plus,C_plus); %heads conditional translation operator
T_minus = kron(S_minus,C_minus); %tails conditional translation operator
T = T_plus + T_minus; %total conditional translation operator

%% Defining the coin operator

theta = 1.*pi()/4;
phi = 0.*pi()/4;
fi = 0; %Hadmard coin values

%coin = [cos(theta), exp(i.*phi).*sin(theta);  exp(i.*fi).*sin(theta),
-exp(i.*(phi+fi)).*cos(theta)]; %local coin operator
% coin = (1/sqrt(2)).*[1 1; 1 -1]; %Hadmard Coin
 coin = (1/sqrt(2)).*[1 1i; 1i 1]; %Balanced Coin
C = kron(eye(2*n+1),coin); %complete coin operator

%% Defining initial state

Head = [1;0]; %heads - positive direction indicator
Tail = [0;1]; %tails - negative direction indicator

symm_coin_ini = (1/sqrt(2)).*(Head+(1i.*Tail));
asymm_coin_ini = (1/sqrt(2)).*(Head-Tail);
Horiz_OAM_ini = (1/sqrt(2)).*(Head+Tail);
begin = zeros(2*n+1,1);
begin((2*n)/2+1,1)=1;
```

```
Phi = kron(begin,Horiz_OAM_ini); %this is always even e.g. n=1 imples
size 2, n=2 implies size 4, n=3 implies size 6

%% Taking n steps

n_step = (T*C)^n; %operator yielding the nth step probability once
acting upon initial state
Phi_n = n_step*Phi;
Probs = abs(Phi_n).^2;
Prob_H = Probs(1:2:end); %All the probabilities associated with Heads
internal state - over all spanned positions
Prob_T = Probs(2:2:end); %All the probabilities associated with Tails
internal state - over all spanned positions
Prob = Prob_H + Prob_T;
P = [(-n:1:n).', Prob];

%% Plotting the QW

Y = P(1:2:end,2); %choose all the positions occupied with probabilities
X = P(1:2:end,1); %Positions occupied with probabilities
QW = area(X,Y);
xlabel('Position (x)')
ylabel('Probability')
QW.EdgeColor = [0,0.7,0];
QW.FaceColor = [0,0.90,0];

% QW2 = area(P(:,1),P(:,2)); %Plotting all points
% xlabel('Position (x)')
% ylabel('Probability')
% QW2.EdgeColor = [0,0.7,0];
% QW2.FaceColor = [0,0.90,0];

%% variance of the QW

va = P(:,2).*(P(:,1)-zeros(2*n+1,1)).^2; %variance for the individual
positions
var = sum(va) % total varaince for a walk of n steps
```

A.2 OAM QW simulation

```
Appendix A
%%% Optical Elements (Jones Matricies) %%%
clear, clc;
syms phi
q = 0.5;
QP = [cos(2*q*phi) sin(2*q*phi); sin(2*q*phi) -cos(2*q*phi)];
%QP = [0 exp(-1i*2*q*phi); exp(1i*2*q*phi) 0];
QWP_fwd = [1 1i; 1i 1];
QWP = (1/sqrt(2)).*[1 1i; 1i 1];
QWP_bkwd = (1/sqrt(2)).*[1 -1i; -1i 1];
Mirror = [1 0; 0 -1]; %modify later for setup when looking at curved
mirrors
H = [1;1]; V = [0;1];
R = (1/sqrt(2)).*[1;1i]; L = (1/sqrt(2)).*[1;-1i];

   %1% Initial Step
    Operators_1 = simplify(rewrite(QWP_fwd*QP,'exp'));

   %3% nth Measurement
  for n = 5
   % n = input('How many round trips? ') ; %n+1 steps are taken...

    Step_n = (simplify(rewrite(QWP_fwd*QP,'exp')))^n;
    Full_trip = Step_n*Operators_1;
    Meas_n = simplify(expand(simplify(rewrite(Full_trip*H,'exp'))))
    %pretty(Meas_n)
    [Prob1, Term1] = coeffs(Meas_n(1,1)); %Horizontal pol = Probs_H
    [Prob2, Term2] = coeffs(Meas_n(2,1)); %Vertical pol = Probs_V
    Prob1 = abs(Prob1).^2;
    Prob2 = abs(Prob2).^2;

    if mod(n,2) == 0
       P = [Prob1(1:n) + Prob2(1:n),Prob2(1,n+1),Prob1(1,n+1)]; %EVEN
       Pos1 = ones(1,(0.5*n+1)).*(n+1)-[n:-2:0]; %EVEN n %creates
positive positions in   the patterns coeffs catagroizes them
       Pos2 = Pos1.*-1; %same, but for the negative positions
       res = reshape([Pos2(:)',Pos1(:)'], size(Pos2,2),2)'; %uses
'flattening' of the   matrix to reorder the positions and combine
favorably
       Position = res(:)'; %EVEN
    else
       P = [Prob1(1:n-1) + Prob2(1:n-1),Prob2(1,n),Prob1(1,n),Prob2(1,n+1)+
      Prob1(1,n+1)]; %ODD
       Pos1 = ones(1,(n+1)/2).*(n+1)-[n-1:-2:0]; %ODD n %creates positive
positions in  the patterns coeffs catagroizes them
       Pos2 = Pos1.*-1; %same, but for the negative positions
       res = reshape([Pos2(:)',Pos1(:)'], size(Pos2,2),2)'; %uses
'flattening' of the  matrix to reorder the positions and combine favorably
```

```
       Position = [res(:)',0]; %ODD %adds the 0 position and reflattens
to complete the  interlace between the positions
    end

    Proba = P./sum(P); %normalize values
    Probability = double(Proba); %Converts symbolic numbers into real,
workable ones
    Prob_Dis = [Position;Probability]'; %Combines position and probability
of       distribution
    Dist = sortrows(Prob_Dis,1) %sorts the matrix in ascending order
based on the 2nd  argument (so its sorting the positions while maintaining
the associated  probabilities)

    %plot(Dist(:,1),Dist(:,2))

     xlswrite('C:\Users\Bereneice\Desktop\QW_Prediction.xlsx',Dist,(n+1))%
    % writes each step onto the associated excel page number

     end
```

A.3 Experimental OAM QW correction

```
T = 0.50; %transmission fraction of beamsplitter output
R = 0.50; %reflection fraction value of beamsplitter output
PW = 30; %pulse width in ns
GW = 10; %gate width in ns (the time period for which the pulse is
captured with the AndOR camera
a = (PW-GW)/2; %the time sections for pulse overlap within the capture
window

for n=0:100 %note sheetn = step #n in the xlsread (step #0 is not
there as it is trivial)

    step_0_dist = [[-(n+2):(n+2)]',[zeros(n+2,1);1;zeros(n+2,1)]];

     n_1 = xlsread('C:\Users\Bereneice\Desktop\QW_Prediction.xlsx',...
     sprintf('Sheet%d',(n+1)),sprintf('A1:B%d',(2*(n+2))));
     ne_1 = [[kron(n_1(1:end-1,:), [1;0])];n_1(end,:)];
     A4 = [ne_1(1,1)+1:2:ne_1(end,1)]';
     nex_1 = [kron([A4,zeros(size(A4))],[0;1]);[0,0]];
     next_1 = [zeros(1,2);[ne_1 + nex_1];zeros(1,2)];

     n_2 = xlsread('C:\Users\Bereneice\Desktop\QW_Prediction.xlsx',...
     sprintf('Sheet%d',(n+2)),sprintf('A1:B%d',(2*(n+2))));
     ne_2 = [[kron(n_2(1:end-1,:), [1;0])];n_2(end,:)];
     A4 = [ne_2(1,1)+1:2:ne_2(end,1)]';
     nex_2 = [kron([A4,zeros(size(A4))],[0;1]);[0,0]];
     next_2 = [ne_2 + nex_2];

    if n == 0
       Corr_Dist = (step_0_dist(:,2).*w(0,T,R).*...
       integral(@G,-(PW/2)+a,(PW/2)-a))+(next_1(:,2).*w(1,T,R).*...
       integral(@G,-(PW/2)+a-10,-(PW/2)+a))+ (next_2(:,2).*w(2,T,R).*...
       integral(@G,-(PW/2)+a-20,-(PW/2)+a-10))
       QWC_distribution = [next_2(:,1) Corr_Dist]

    elseif n == 1
         n_d = xlsread('C:\Users\Bereneice\Desktop\QW_Prediction.xlsx',...
         sprintf('Sheet%d',(n)),sprintf('A1:B%d',(2*(n+2))));
         n_di = [[kron(n_d(1:end-1,:), [1;0])];n_d(end,:)];
         A3 = [n_di(1,1)+1:2:n_di(end,1)]';
         n_dis = [kron([A3,zeros(size(A3))],[0;1]);[0,0]];
         n_dist = [zeros(2,2);[n_di + n_dis];zeros(2,2)];

 Corr_Dist = (step_0_dist(:,2).*w(0,T,R).*...
 integral(@G,(PW/2)-a,(PW/2)- a+10))+ (n_dist(:,2).*w(1,T,R).*...
 integral(@G,-(PW/2)+a,(PW/2)-a))+(next_1(:,2).*w(2,T,R).*...
 integral(@G,-(PW/2)+a-10,-(PW/2)+a))+(next_2(:,2).*w(3,T,R).*...
 integral(@G,-(PW/2)+a-20,-(PW/2)+a-10))
       QWC_distribution = [next_2(:,1) Corr_Dist]
```

```
    elseif n == 2
        n_d = xlsread('C:\Users\Bereneice\Desktop\QW_Prediction.xlsx',...
        sprintf('Sheet%d',(n)),sprintf('A1:B%d',(2*(n+2))));
         n_di = [[kron(n_d(1:end-1,:), [1;0])];n_d(end,:)];
         A3 = [n_di(1,1)+1:2:n_di(end,1)]';
         n_dis = [kron([A3,zeros(size(A3))],[0;1]);[0,0]];
         n_dist = [zeros(2,2);[n_di + n_dis];zeros(2,2)];

         p_1 =  xlsread('C:\Users\Bereneice\Desktop\QW_Prediction.xlsx',...
         sprintf('Sheet%d',(n-1)),sprintf('A1:B%d',(2*(n+2))));
         pr_1 = [[kron(p_1(1:end-1,:), [1;0])];p_1(end,:)];
         A2 = [pr_1(1,1)+1:2:pr_1(end,1)]';
         pre_1 = [kron([A2,zeros(size(A2))],[0;1]);[0,0]];
         prev_1 = [zeros(3,2);[pr_1 + pre_1];zeros(3,2)];

         Corr_Dist = (step_0_dist(:,2).*w((0),T,R).*...
         integral(@G,(PW/2)-a+10,(PW/2)- prev_1(:,2).*w((n-1),T,R).*...
         integral(@G,(PW/2)-a,(PW/2)-a+10))+(n_dist(:,2).*w(n,T,R).*...
         integral(@G,-(PW/2)+a,(PW/2)-a))+(next_1(:,2).*w((n+1),T,R).*...
         integral(@G,-(PW/2)+a-10,- PW/2)+a))+(next_2(:,2).*w((n+2),T,R).*...
         integral(@G,-(PW/2)+a-20,-(PW/2)+a-10))
         QWC_distribution = [next_2(:,1) Corr_Dist]

    else
         n_d = xlsread('C:\Users\Bereneice\Desktop\QW_Prediction.xlsx',...
         sprintf('Sheet%d',(n)),sprintf('A1:B%d',(2*(n+2))));
         n_di = [[kron(n_d(1:end-1,:), [1;0])];n_d(end,:)];
         A3 = [n_di(1,1)+1:2:n_di(end,1)]';
         n_dis = [kron([A3,zeros(size(A3))],[0;1]);[0,0]];
         n_dist = [zeros(2,2);[n_di + n_dis];zeros(2,2)];

         p_1 =  xlsread('C:\Users\Bereneice\Desktop\QW_Prediction.xlsx',...
         sprintf('Sheet%d',(n-1)),sprintf('A1:B%d',(2*(n+2))));
         pr_1 = [[kron(p_1(1:end-1,:), [1;0])];p_1(end,:)];
         A2 = [pr_1(1,1)+1:2:pr_1(end,1)]';
         pre_1 = [kron([A2,zeros(size(A2))],[0;1]);[0,0]];
         prev_1 = [zeros(3,2);[pr_1 + pre_1];zeros(3,2)];

         p_2 =  xlsread('C:\Users\Bereneice\Desktop\QW_Prediction.xlsx',...
         sprintf('Sheet%d',(n-2)),sprintf('A1:B%d',(2*(n+2))));
         pr_2 = [[kron(p_2(1:end-1,:), [1;0])];p_2(end,:)];
         A1 = [pr_2(1,1)+1:2:pr_2(end,1)]';
         pre_2 = [kron([A1,zeros(size(A1))],[0;1]);[0,0]];
         prev_2 = [zeros(4,2);[pr_2 + pre_2];zeros(4,2)]; %matrix
with all...
         %positions and associated prob (added the missing 0 ones)
and of...
         % the same dimension of  the largest input

       Corr_Dist = (prev_2(:,2).*w((n-2),T,R).*...
```

```
        integral(@G,(PW/2)-a+10,(PW/2)- a+20))+(prev_1(:,2).*w((n-1),T,R).*...
        integral(@G,(PW/2)-a,(PW/2)-a+10))+(n_dist(:,2).*w(n,T,R).*...
        integral(@G,-(PW/2)+a,(PW/2)-a))+(next_1(:,2).*w((n+1),T,R).*...
        integral(@G,-(PW/2)+a-10,-(PW/2)+a))+(next_2(:,2).*w((n+2),T,R).*...
        integral(@G,-(PW/2)+a-20,-(PW/2)+a-10))
        QWC_distribution = [next_2(:,1) Corr_Dist]
    end
    xlswrite('C:\Users\Bereneice\Desktop\QW_correction_code\...
    QW_Correction.xlsx',QWC_distribution,(n+1))%
    % writes each pulse onto the associated excel page number such
that e.g.
    % sheet 1 = step 0; output pulse 1
    % sheet 2 = step 1; output pulse 2
end
```

Appendix B

Publications

Published:

Sephton, B., Dudley, A. and Forbes, A. (2016). Revealing the radial modes in vortex beams. Applied Optics, 55(28), p.7830.

In preparation:

Ruffato, G., Girardi, M., Massari, M., Mafakheri, E., Sephton, B., Capaldo, P., Forbes, A. and Romanato, F. (2018). A compact diffractive sorter for high-resolution demultiplexing of orbital angular momentum beams. Prep.

Sephton, B. et. al.(2018). Quantum walks with classically entangled light. Prep.

Revealing the radial modes in vortex beams

BERENEICE SEPHTON,[1,2] ANGELA DUDLEY,[1,2] ANDREW FORBES[1,2*]

[1]CSIR National Laser Centre, P.O. Box 395, Pretoria 0001, South Africa
[2]School of Physics, University of Witwatersrand, Private Bag 3, Wits 2050, South Africa
*Corresponding author: andrew.forbes@wits.ac.za

Light beams that carry orbital angular momentum are often approximated by modulating an initial beam, usually Gaussian, with an azimuthal phase variation to create a vortex beam. Such vortex beams are well defined azimuthally, but the radial profile is neglected in this generation approach. Here we show that a consequence of this is that vortex beams carry very little energy in the desired zeroth radial order, as little as only a few percent of the incident power. We demonstrate this experimentally and illustrate how to overcome the problem by complex amplitude modulation of the incident field.

OCIS codes: *(080.0080) Geometric optics; (080.4865) Optical vortices (230.0230); Optical devices; (230.3720) Liquid-crystal devices*

1. Introduction

For beams of the form $E_0(r)e^{-il\phi}$, Allen *et. al.* associated the index, *l*, with orbital angular momentum (OAM) carried by light where ϕ is the azimuthal angle and *r* the radial coordinate [1]. Beams with the azimuthal mode ($e^{-il\phi}$) that adhere to the paraxial approximation are consequently known to contain a well-defined OAM of $l\hbar$ per photon [1,2]. These azimuthal modes are also known as vortex beams in light of the associated helical twisting of the wave front along the propagation axis [1,3,4]. Vortex beams have since found many important applications (most of which are highlighted in Refs 4 and 2) such as optical tweezing [5], laser material surface processing [6,7], quantum entanglement [8,9], optical communication [10–12], image processing [13]and quantum metrology [14]. Subsequent creation of these beams is of great interest and a surfeit of techniques have been developed for their creation, including spiral phase plates [15], holograms [16], spatial light modulators [17], spiral Fresnel lenses [18], cylindrical lenses [16, 17], q-plates [19–21]and directly inside the source [22]. In the utilization of these vortex beams, the radial structure is often disregarded as the fundamental radial mode (*p* = 0) is a ubiquitous choice in OAM experiments with few exceptions seen in the implementation and characterization of optical fibers [23] and recently a quantum random walk [24].

Here the effect of the missing radial component is investigated and shown to have a deleterious effect on the spatial power distribution of the desired OAM modes. Standard approaches to creating such beams are revealed to manifest unwanted radial modes that can contain the majority of the energy. Furthermore, we show how to rectify this problem through complex amplitude modulation.

2. Vortex Beams

A vortex beam may be written as an azimuthal phase variation with a Gaussian envelope in the generation (waist) plane:

$$\boldsymbol{\psi^l(r,\phi) = G(r)e^{-il\phi}} \qquad \textbf{(1)}$$

where $G(r) = e^{-(r/w_0)^2}$ is the Gaussian envelope, *r* is the radial coordinate, w_0 the Gaussian beam waist, $e^{-il\phi}$ the azimuthal phase variation with associated OAM of $l\hbar$ per photon [1, 2], where *l* is a non-zero integer. It has been noted that vortex beams may also be expressed as a special case of Hypergeometric-Gaussian modes [25].

This vortex field, however is not a solution to the free-space wave equation and as such vortex beams are not eigenmodes of free-space, resulting in the excitation of supplementary fields [26] and spatial polarization variance with propagation [27].

OAM-carrying beam structures fulfilling the conditions of the free-space paraxial wave equation include Bessel [28,29] and Laguerre-Gaussian (LG) modes [1,4,26] with which these general vortex beams may subsequently be compared. Analysis could be generalized to either of the mode types, but this paper will focus on the LG modes whereby the amplitude at the beam waist is given by [30]:

$$\boldsymbol{LG_{p,l}} = \sqrt{\frac{2p!}{\pi w_0^2(p+|l|)!}}\underbrace{\left(\frac{r\sqrt{2}}{w_0}\right)^{|l|} L_p^{|l|}\left(\frac{2r^2}{w_0^2}\right)e^{-\left(\frac{r}{w_0}\right)^2}}_{\textbf{amplitude term}} e^{-il\phi} \qquad \textbf{(2)}$$

Here $L_p^{|l|}(x)$ is the Laguerre polynomial of orders p, l where the radial index, indicating the number radial nodes, is $p \geq 0$

It can be seen that for pure LG vortex modes (p = 0), there is an additional amplitude term, $\left(r\sqrt{2}/w_0\right)^{|l|}$, that ensures the invariance associated with the eigenmodes as they propagate. Similar terms with the same effect are also present in Bessel-Gaussian and other beams that are eigenmodes of free- space. It is often unappreciated that it is this radial amplitude term, which is dependent on the azimuthal index ($|l|$), and not the azimuthal phase term itself ($|l|\phi$), which is responsible for the characteristic beam core intensity null associated with vortex beams. The observation of a null in vortex beams without this amplitude term is instead due to high spatial frequencies induced by the helicity of the phase together with their attenuation due to the finite apertures in the optical system [31].

It is well-known that an optical field may be expressed as a linear combination of basis modes [32–34]:

$$\boldsymbol{U(r)} = \sum_j \boldsymbol{c_j \psi_j(r)} \quad (4)$$

where $r = (x, y)$ is the spatial coordinate in the transverse plane and $\psi_j(r)$ represents the basis mode. The complex correlation coefficient, $c_j = \rho_j e^{i\Delta\varphi_j}$ weights the contribution of each of the basis modes where ρ_j is the corresponding mode amplitude and $\Delta\varphi_j$ the intermodal phase difference between the jth mode and a selected reference mode. It thus follows that the vortex beam (of a particular azimuthal index, l) may easily be expressed in terms of LG modes of the same azimuthal index

$$\boldsymbol{U^l(r,\phi)} = \sum_p \boldsymbol{c_p LG_{p,l}(r)} \quad (5)$$

Here $|c_p|^2$ yields the power weighting of the vortex beam among the LG modes and can be expressed as [25]:

$$\boldsymbol{c_p} = \sqrt{\frac{(p+|l|)!}{p!}} \frac{\Gamma(p+\frac{|l|}{2})\Gamma(\frac{|l|}{2}+1)}{\Gamma(\frac{|l|}{2})\Gamma(p+|l|+1)} \quad (6)$$

where $\Gamma(x)$ is the gamma function. It is clear that the vortex beam is the sum of many radial modes in the LG basis, i.e., the same azimuthal index as the vortex beam but with several radial indices. The implication is that the power in the desired p = 0 mode can be very small, approaching zero as the azimuthal index increases.

Ensuing evaluation of the modes indicate a significant spread of the power distribution to the outer spatial distributions, increasing concomitantly with the input OAM content. In other words, rings around the central beam appear due to additional radial indices when analyzed in terms of LG modes. This is illustrated in Fig. 1 where the power content of each mode, radial and azimuthal, in the LG basis is shown for a given input azimuthal mode.

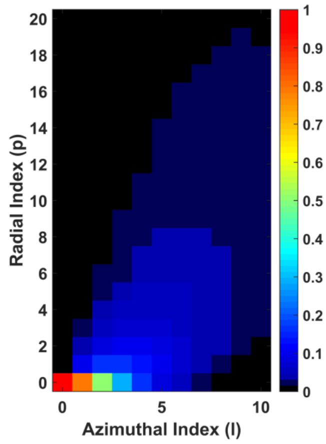

Fig 1. Theoretical density plot, determined from Eq. 6, illustrating the spread of power into radial modes for vortex beams generated through phase-only transformations and thus lacking the amplitude term highlighted in Eq. 2.

For example, an input vortex mode of l = 1 has only 78% of its energy in the $LG_{0,1}$ mode, with the rest spread across higher radial modes. It can be seen from Fig. 1 that there is a clear increase in the modal spreading as the input OAM of the vortex beam is increased: an input vortex mode of l = 10 has only 0.4% of its energy in the $LG_{0,10}$ mode. Consequently, a direct result of the missing amplitude term is an increase in the power distribution as the OAM content of the vortex beam increases. This is seen by the increased spread of blue over the p-values at higher OAM values. Observation of the low intensity also indicates a low power content in any one of the radial modes with higher OAM. Furthermore, there is a movement of power concentration to higher radial modes with OAM as evidenced by the lower intensity (black) for p = [0, 2] of l = [7, 10]. In fact, beyond l = 4 the power content of the zeroth radial mode, the desired mode, is close to zero.

3. Experimental Methodology and Results

A. Methodology

Figure 2 displays the experimental set-up for generation and analysis of a vortex beam in terms of LG radial modes. Two steps were required for the experiment: generation of the vortex beams and subsequent decomposition into LG radial modes with the same azimuthal index.

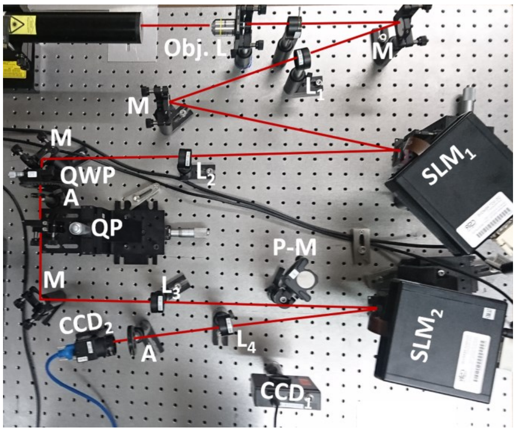

Fig. 2. Image of the experimental setup used to decompose the vortex beams into LG basis modes and measure the power distribution between radial modes. Obj. Lens, objective lens (10X); M, mirror; P-M, pop-up mirror; L, lens; SLM, spatial light modulator; A, aperture; QWP, quarter-wave plate; QP, q-plate (q = 0.5); CCD, camera.

1. Beam Generation

To generate vortex beams, a horizontally polarized HeNe laser of wavelength ~633 nm was expanded through a 10X objective lens and collimated by L_1 (f_1 = 400mm), before being directed onto a reflective PLUTO-VIS HoloEye spatial light modulator (8 μm, 1920 x 1080 pixels, calibrated at a 2π phase shift for ~633 nm) marked as SLM_1. SLM_1 was programmed with an azimuthally varying phase profile, resulting in the 1st diffraction order possessing the required structure as given by Eq. 1. Addition of the quarter-wave plate (QWP) and q-plate (QP) seen in Fig. 2 allowed for the creation of vector vortex beams, which will be discussed later.

2. Modal Decomposition

An important technique, essential for analyzing the generated beams in terms of LG modes is modal decomposition. This technique is often used for characterizing beams, whereby any optical field may be expressed as a linear combination of basis modes as described in Eq. 4. Here we let the basis set be the chosen LG modes (Eq. 2) allowing an arbitrary input field, $U(r)$, to be described by a weighted superposition of these modes. Orthonormality of the LG elements can be exploited to ascertain the weighting coefficients ($c_{p,l}$) by taking an inner product between the input field and desired LG mode [33,34]:

$$\boldsymbol{c_{p,l} = \langle U(r) | LG_{p,l}(r) \rangle = \iint_{\mathbb{R}^2} U(r) LG_{p,l}(r)^* \, d^2r} \quad \textbf{(7)}$$

where integration is over all space and $LG_{p,l}(r)^*$ is the complex conjugate of Eq. 2. The complex conjugate of a basis mode is often referred to as a match filter [35,36]. Determination of the coefficient in terms of the field reflected off of SLM_1 ($U(r)LG_{p,l}(r)^*$) is possible by taking the Fourier transform of Eq. 7 to yield:

$$\boldsymbol{U_{p,l}(k_x, k_y) = \iint U(x,y) LG_{p,l}(x,y)^* \, e^{-i(k_x x + k_y y)} dxdy} \quad \textbf{(8)}$$

where k_x, k_y are wave vectors. The on-axis intensity at the Fourier plane (i.e. at the plane of CCD_2) provides a physical measurement of the inner-product given in Eq. (7). The on-axis point $(k_x, k_y) = (0,0)$, produces an expression equivalent to Eq. 7:

$$\boldsymbol{U_{p,l}(0,0) = \iint_{\mathbb{R}^2} U(r) LG_{p,l}(r)^* \, d^2r = c_{p,l}} \quad \textbf{(9)}$$

It follows that the intensity at the field center, $I(0,0)$, will then yield the power weighting (i.e. square of the weighting coefficient)

$$\boldsymbol{I_j^{\rho}(0,0) = |U_{p,l}(0,0)|^2 = |c_{p,l}|^2} \quad \textbf{(10)}$$

Characterization of the vortex beam only extends to intensity correlations and not intermodal phase decomposition. Therefore, for the scope of this paper, decomposition was restricted to determining only the amplitude terms as described above.

Experimentally the amplitude decomposition was obtained through an optical inner product measurement (Eq. 7) between the experimental field, $U(r)$, generated by SLM_1 and the match filter, $LG_{p,l}(r)^*$ on SLM_2 with a thin lens performing the Fourier transformation. First, isolation and imaging of the 1st diffraction order onto the match filter (SLM_2) was achieved through a 4f imaging system (lenses L_2 (f_2 = 300 mm) and L_3 (f_3 = 300 mm) with an aperture placed in the Fourier plane. The Fourier transform of the resultant field after SLM_2 ($U(r)LG_{p,l}(r)^*$) was achieved with lens L_4 (f_4 = 200 mm). An aperture placed before CCD_2 (PointGrey) isolated the 1st diffraction order allowing the optical inner-product to be recorded where an on-axis signal dictated a correlation between the generated mode and match-filter, while an on-axis null indicated a mismatch. A pop-up mirror (P-M), placed equidistant between SLM_2 and CCD_1 (Spiricon, LBA-FW-SCOR-7350115), was used to image the generated nearfield to facilitate alignment of the optical elements.

B. System Verification

Testing of the system alignment and subsequent confirmation of the associated technique was achieved by performing a modal decomposition on $LG_{p,0}$ and $LG_{0,l}$ beams where p = [0, 7] and l = [-4, 4]. Intensities were detected at the origin of the Fourier plane by CCD_2 positioned in this plane, after the Fourier transformation was carried out by L_4. The intensity detected by a single pixel at the origin yielded the power measurement. It follows that direct correlation is expected whereby maximal intensity is detected at the origin of the Fourier plane for conjugate modes generated by SLM_1 and SLM_2, while null intensity is detected at the origin for all other modal combinations.

Figure 3 displays the system test results in the form of density plots. Here the main red diagonals illustrate strong detection of the corresponding modes as expected with negligible detected intensities for the non-correlating LG modes.

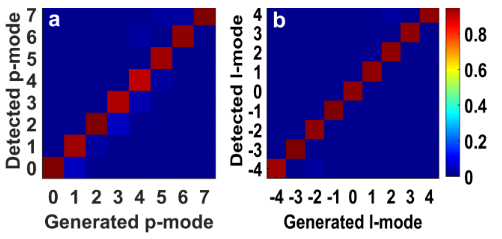

Fig. 3. Modal decomposition density plots for decomposition of radial (a) and OAM (b) LG modes of $p = [0, 7]$ and $l = [-4, 4]$ respectively into the LG basis for determination of experimental system accuracy and reliability. The false colors indicate the fractional detected power with summation of intensities in each row yielding unity.

Cross-talk evidenced by off-axis intensities greater than 0 (light blue) seen in Fig. 3 is due to system misalignment and aberrations in the optical elements. This, however, is minimal indicating good system alignment as well as minimal adverse aberrational effects. Consequently, a good degree of accuracy and reliability can be expected for modes detected by the system.

C. Vortex Radial Fields

An $l = 1$ vortex structure (without the amplitude term) was generated by encoding SLM_1 as described earlier. Decomposition of the beam was performed for radial modes, $p = [0, 7]$ which yielded values for the power coefficients described by Eq. 6. Figure 4 displays these experimental values in terms of percentages together with the theoretical values (blue curve) calculated from Eq. 6 for comparison.

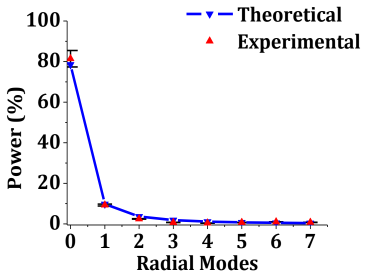

Fig. 4. Experimental and theoretical comparison of power weighting across radial modes $p = [0, 7]$ for a vortex mode of $l = 1$. The blue line (theoretical) is included to guide the eye. Error bars for $p > 0$ are too small to be observed.

Majority of the power (78.5%) is still retained within the fundamental radial order, with maximal distribution of the remaining power between immediate adjacent radial modes. Summation over the theoretical power coefficients indicates that 95% of the total power falls within the $p \leq 4$ radial range.

The experimental values are in excellent agreement with the expected theoretical values as seen by close positioning of the respective data points and the maximum deviation of ~2% occurring within the system error at $p = 0$.

Similarly, encoding SLM_1 with a vortex structure of $l = 10$ (Eq. 1) generated a vortex mode of high OAM for radial decomposition and analysis. Decomposition of the field was performed for LG radial modes, $p = [0, 18]$. A plot of results similar to that of Fig. 4 is presented in Fig. 5 with theoretical (blue curve) and experimental comparison (red data points).

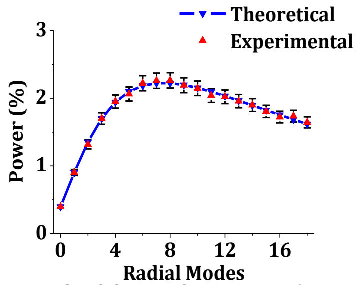

Fig. 5. Experimental and theoretical comparison of power weighting across radial modes = [0, 18] for a vortex mode of $l = 10$. The blue line (theoretical) is included to guide the eye.

Good agreement between theoretical and experimental values are again evident with all experimental values (red) falling within acceptable range of theoretical predictions (blue) as indicated by the error bars.

A significant shift and redistribution of power can be seen across the radial modes in comparison to $l = 1$ (Fig. 4) as a result of the higher OAM content. The power maximum being centered at $p = [7, 8]$ and a drop of ~78.1% power in the fundamental mode (as only 0.4% remains in this mode for Fig. 5) clearly illustrates this. Additionally, the maximum power carried in a single radial mode decreased by ~76.3% as seen in the power difference between $p = 0$ (Fig. 4) and $p = 7$ (Fig. 5), indicating that ~76.3% more of the power is distributed amongst other modes than for a mode with OAM of an order of magnitude less. Furthermore, summation over the first 50 theoretical power coefficients only yields 64% of the total beam power and 95% can be seen to be spread over the first 500 radial modes.

Further experimentation including the addition of a QWP and QP as depicted in Fig. 2, allowed for a special case of vector vortex modes to be tested. Such q-plates are now routinely used in laboratories to create scalar and vector vortex beams by imparting an azimuthal–only phase to the input beam, as was done with the SLM, but by geometric phase control [21] rather than dynamic phase control. We find identical results for the q-plate as reported here for the SLM. This is illustrated in Fig. 6 where the detected radial modes were removed for an $l = 1$ beam generated by the QP by passing a beam with the amplitude term pre-encoded such that the azimuthal term supplied by the QP creates an eigenmode of free space. It follows that 100% power is expected in the fundamental mode.

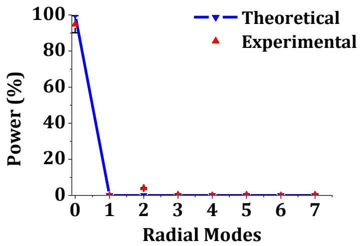

Fig. 6. Experimental and theoretical comparison of power weighting across radial modes p = [0, 7] for a QP-generated vortex mode of l = 1 with the radial modes removed. The blue line (theoretical) is included to guide the eye. Error bars for p > 0 are too small to be observed.

It can be seen that maximal intensity exists in the fundamental radial mode, confirming that it is the phase variation itself (the vortex) and not the manner in which it is implemented that matters. Aberrations present in the QP are detected as an additional radial mode (p = 2), causing the slight mismatch. It may thus be concluded that minimal aberrations were present in the QP and as such, poor beam quality would be due to the unmodulated azimuthal induced phase and not the quality of the QP itself.

Clear dissipation of vortex beam power over an increasing number of radial modes can subsequently be seen with beams of higher OAM content which should inspire caution in their utilization and generation for high OAM experiments.

Images of the beams with (LG) and without (azimuthal-only vortex) the amplitude term of different OAM values (l = 5, 10) were taken in the far field for visual illustration of the amplitude term effect. This is presented in Fig. 7. The values shown on the bottom-right corners give the corresponding theoretical and experimental percentage power contained in the desired p = 0 mode.

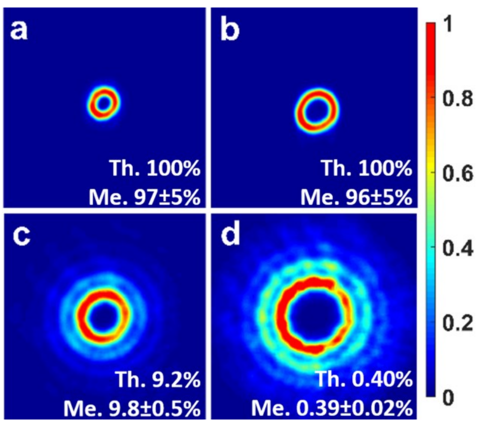

Fig. 7. Experimental far-field images of vortex beams (a) l = 5, (b) l = 10 containing the amplitude term and (c) l = 5, (b) l = 10 without the amplitude term, illustrating its effect on the retention of beam power within the lower order radial modes as well as encoded beam structure. Measured (Me.) and theoretical (Th.) values for the percentage power occurring in the p = 0 mode of the beam are displayed in the bottom-right corner. Intensities are normalized to the highest value for the individual images and thus are not indications of relative power differences between the beams.

Figure 7(a) and (b) display $LG_{0,5}$ and $LG_{0,10}$ beams in the far-field where the power is seen to be confined to the fundamental radial mode as expected. Comparison with the respective beams with missing amplitude terms (c) and (d) clearly show further radial power distribution by the supplementary rings. An increase in the shift of power to farther rings with an increase in OAM is also evident. Additionally, modes (c) and (d) are larger than that of the modes containing the amplitude term, demonstrating the distribution of maximal power to further radial modes as the diameter of the radial mode with the peak power is then larger than the fundamental mode.

This is supported by the power values given in the bottom corners, where a very high percentage of the beam power is seen to be contained in the fundamental radial mode for beams (a) and (b) that contain the amplitude term and much poorer percentages for beams (c) and (d) without the term. Furthermore, the percentage power in the p = 0 mode may be appraised as beam purity where the amplitude-containing beams can be seen to have a high beam purity as opposed to the deteriorating purity apparent in the beams without this vital term.

Reconsidering the LG equation (Eq. 2) it follows that one could expect the Laguerre term to be solely responsible for the radial power distribution as it controls the radial degree of freedom (p). In the case where p = 0, however, this polynomial term reduces to 1 and subsequently has no effect on the radial distribution. Examining the OAM modulated amplitude term, it could also be naively expected that it does not contribute to radial distribution, but on comparison of Eq. 1 and 2, it is clear that for p = 0, this is the only non-constant term missing and thus is responsible for the difference observed between these azimuthal-only vortex beams and the LG beams which are eigenmodes of free-space. It follows that exclusion of this term removes the OAM dependent amplitude modulation and forces nature to correct for it by introducing radial distributed fields that may be interpreted as additional radial modes in the LG basis. Outspreading of the beam power is subsequently a direct consequence of forcing nature to exact OAM modulation of the amplitude whereby this unintended effect is rapidly enhanced with increased OAM content in the vortex beam.

Implications of this phenomenon can be deleterious for experimental work where beam power and mode purity is a concern, particularly when beams of higher OAM are required. Generation of these missing-amplitude beams in such experiments could result in many issues such as detection thresholds, increased measurement uncertainties as well as the number of optical components it will be possible to use in the experimental design. Due to this drastic power loss with OAM, utilization of these beams could additionally cause beam power to become an issue in experiments where it would ordinarily not be a consideration.

In establishing amplitude modulation to prevent this, however, there will be initial overall transmissive and/or diffractive power losses induced by the methods currently available including spatial light modulators where there is perceptible loss in beam power. Subsequently, consideration of experimental parameters is an important factor. Beams that are not of small OAM result in radial power distributions to such a degree that the nature-inspired power loss far outweighs the loss induced by the technique required for introducing OAM amplitude modulation.

6. Conclusion

In conclusion, we have analyzed the radial distribution of azimuthal-only vortex beams through decomposition into radial LG basis modes and compared them to the mathematical structure of these eigenmodes. Results demonstrated a rapid increase in radial power divergence with OAM content along with a shift in the power maximum to farther radial positions. Corresponding deterioration of mode purity was subsequently inferred. Further inspection between the modes led to the deduction that this phenomenon was the natural response to the absence of amplitude modulation by OAM. Subsequently, presence of this amplitude term correlates to a counter-intuitive control of radial power distribution. Awareness of this dissipation of beam power from the zeroth order is important for many experiments that require high levels of beam power in these radial modes as well as the solution to this problem by amplitude modulation.

References

1. L. Allen, M. W. Beijersbergen, R. J. C. Speeruw, and J. P. Woerdman, "OAM Transformation Laguerre-Gaussian Laser Modes," Am. Phys. Soc. **45**, 8185–8188 (1992).
2. A. M. Yao and M. J. Padgett, "Orbital angular momentum: origins, behavior and applications," Adv. Opt. Photonics **3**, 161–204 (2011).
3. E. J. Galvez, B. L. Rojec, and K. R. McCullough, "Imaging optical singularities: Understanding the duality of C-points and optical vortices," in *Proc. of SPIE* (2013), Vol. 8637, p. 863706.
4. M. W. Beijersbergen, L. Allen, H. E. L. O. van der Veen, and J. P. Woerdman, "Astigmatic laser mode converters and transfer of orbital angular momentum," Opt. Commun. **96**, 123–132 (1993).
5. H. He, M. E. J. Friese, N. R. Heckenberg, and H. Rubinsztein-Dunlop, "Direct Observation of Transfer of Angular Momentum to Absorptive Particles from a Laser Beam with a Phase Singularity," Phys. Rev. Lett. **75**, 826–829 (1995).
6. J. J. J. Nivas, S. He, A. Rubano, A. Vecchione, D. Paparo, L. Marrucci, R. Bruzzese, and S. Amoruso, "Direct Femtosecond Laser Surface Structuring with Optical Vortex Beams Generated by a q-plate.," Sci. Rep. **5**, 17929 (2015).
7. O. J. Allegre, W. Perrie, S. P. Edwardson, G. Dearden, and K. G. Watkins, "Laser microprocessing of steel with radially and azimuthally polarized femtosecond vortex pulses," J. Opt. **14**, 085601 (2012).
8. A. Mair, A. Vaziri, G. Weihs, and A. Zeilinger, "Entanglement of the orbital angular momentum states of photons," Nature **412**, 313–316 (2001).
9. A. Vaziri, G. Weihs, and A. Zeilinger, "Superpositions of the Orbital Angular Momentum for Applications in Quantum Experiments," J. Opt. B Quantum Semiclass. Opt. **4**, S47–S51 (2002).
10. J. Wang, J.-Y. Yang, I. M. Fazal, N. Ahmed, Y. Yan, H. Huang, Y. Ren, Y. Yue, S. Dolinar, M. Tur, and A. E. Willner, "Terabit free-space data transmission employing orbital angular momentum multiplexing," Nat. Photonics **6**, 488–496 (2012).
11. B. Guan, R. P. Scott, C. Qin, N. K. Fontaine, T. Su, C. Ferrari, M. Cappuzzo, F. Klemens, B. Keller, M. Earnshaw, and S. J. B. Yoo, "Free-space coherent optical communication with orbital angular, momentum multiplexing/demultiplexing using a hybrid 3D photonic integrated circuit.," Opt. Express **22**, 145–56 (2014).
12. G. Gibson, J. Courtial, M. Padgett, M. Vasnetsov, V. Pas'ko, S. Barnett, and S. Franke-Arnold, "Free-space information transfer using light beams carrying orbital angular momentum.," Opt. Express **12**, 5448–5456 (2004).
13. J. a Davis, D. E. McNamara, D. M. Cottrell, and J. Campos, "Image processing with the radial Hilbert transform: theory and experiments.," Opt. Lett. **25**, 99–101 (2000).
14. V. D'Ambrosio, N. Spagnolo, L. Del Re, S. Slussarenko, Y. Li, L. C. Kwek, L. Marrucci, S. P. Walborn, L. Aolita, and F. Sciarrino, "Photonic polarization gears for ultra-sensitive angular measurements," Nat. Commun. **4**, 2432 (2013).
15. M. W. Beijersbergen, R. P. C. Coerwinkel, M. Kristensen, and J. P. Woerdman, "Helical-Wave-Front Laser-Beams Produced With a Spiral Phaseplate," Opt. Commun. **112**, 321–327 (1994).
16. V. Y. Bazhenov, M. V Vasnetsov, and M. S. Soskin, "Laser beams with screw dislocations in their wavefronts," JETP Lett. **52**, 429–431 (1990).
17. M. Reicherter, T. Haist, E. U. Wagemann, and H. J. Tiziani, "Optical particle trapping with computer-generated holograms written on a liquid-crystal display," Opt. Lett. **24**, 608–610 (1999).
18. M. Harris, C. A. Hill, P. R. Tapster, and J. M. Vaughan, "Laser modes with helical wave fronts," Phys. Rev. A **49**, 3119–3122 (1994).
19. B. Piccirillo, S. Slussarenko, and L. Marrucci, "The orbital angular momentum of light: genesis and evolution of the concept and of the associated photonic technology," Riv. Nuovo (2013).
20. S. Slussarenko, A. Murauski, T. Du, V. Chigrinov, L. Marrucci, and E. Santamato, "Tunable liquid crystal q-plates with arbitrary topological charge," Opt. Express **19**, 4085–4090 (2011).
21. L. Marrucci, C. Manzo, and D. Paparo, "Optical spin-to-orbital angular momentum conversion in inhomogeneous anisotropic media," Phys. Rev. Lett. **96**, 163905 (2006).
22. D. Naidoo, F. Roux, A. Dudley, I. Litvin, B. Piccirillo, L. Marucci, and A. Forbes, "Controlled generation of higher-order Poincare sphere beams from a laser," Nat. Photonics **10**, 327–332 (2016).
23. O. Shapira, A. F. Abouraddy, J. D. Joannopoulos, and Y. Fink, "Complete Modal Decomposition for Optical Waveguides," CThB2 (2005).
24. F. Cardano, F. Massa, E. Karimi, S. Slussarenko, D. Paparo, C. de Lisio, F. Sciarrino, E. Santamato, and L. Marrucci, "Photonic quantum walk in a single beam with twisted light," Sci. Adv. **1**, E150087 (2015).
25. E. Karimi, G. Zito, B. Piccirillo, L. Marrucci, and E. Santamato, "Hypergeometric-Gaussian modes," Opt. Lett. **32**, 3053–3055 (2007).
26. A. Forbes, *Laser Beam Propagation: Generation and Propagation of Customized Light* (2014).
27. D. Yang and S. Wu, *Fundamentals of Liquid Crystal Devices* (2006).
28. J. Durnin, J. Miceli, and J. H. Eberly, "Diffraction-free beams," Phys. Rev. Lett. **58**, 1499–1501 (1987).
29. J. Arlt and K. Dholakia, "Generation of high-order Bessel beams by use of an axicon," Opt. Commun. **177**, 297–301 (2000).
30. B. E. Saleh and M. . Teich, *Fundamentals of Photonics*, 2nd Editio (John Wiley & Sons, 2007).
31. F. S. Roux, "Optical vortex density limitation," Opt. Commun. **223**, 31–37 (2003).

32. T. Kaiser, D. Flamm, S. Schröter, and M. Duparré, "Complete modal decomposition for optical fibers using CGH-based correlation filters," Opt. Express **17**, 9347 (2009).
33. I. A. Litvin, A. Dudley, F. S. Roux, and A. Forbes, "Azimuthal decomposition with digital holograms.," Opt. Express **20**, 10996–1004 (2012).
34. C. Schulze, S. Ngcobo, M. Duparré, and A. Forbes, "Modal decomposition without a priori scale information.," Opt. Express **20**, 27866–73 (2012).
35. D. Flamm, C. Schulze, D. Naidoo, S. Schroter, A. Forbes, and M. Duparre, "All-digital holographic tool for mode excitation and analysis in optical fibers," J. Light. Technol. **31**, 1023–1032 (2013).
36. A. Forbes, A. Dudley, and M. McLaren, "Creation and detection of optical modes with spatial light modulators," Adv. Opt. Photonics **8**, 200 (2016).

Bibliography

1. Pal, R. *Electromagnetic, mechanical, and transport properties of composite materials* (CRC Press, 2014).
2. Mukhopadhyay, S. N. & Das, D. K. *Oxygen Responses, Reactivities, and Measurements in Biosystems* (CRC Press, 1994).
3. Smouse, P. E. *et al.* Stochastic modelling of animal movement. *Philosophical Transactions of the Royal Society of London B: Biological Sciences* **365,** 2201–2211 (2010).
4. Bachelier, L. *Louis Bachelier's theory of speculation: the origins of modern finance* (Princeton University Press, 2011).
5. Marder, M. P. *Condensed matter physics* (John Wiley & Sons, 2010).
6. Einstein, A. On the movement of small particles suspended in stationary liquids required by the molecular kinetic theory of heat. *Ann. d. Phys* **17,** 322 (1905).
7. Perrin, M. J. *Brownian Movement and Molecular Reality: Translated from the Annales de Chimie Et de Physique, 8 Series, September 1909, by F. Soddy* (Taylor & Francis, 1910).
8. Pearson, K. The problem of the random walk. *Nature* **72,** 342 (1905).
9. Wang, J. & Manouchehri, K. *Physical implementation of quantum walks* (Springer, 2013).
10. Dembo, A., Peres, Y., Rosen, J. & Zeitouni, O. Thick points for planar Brownian motion and the Erdős-Taylor conjecture on random walk. *Acta Mathematica* **186,** 239–270 (2001).
11. Stewart, I. Mathematics: Where drunkards hang out. *Nature* **413,** 686 (2001).
12. Sessions, R. B., Oram, M., Szczelkun, M. D. & Halford, S. E. Random walk models for DNA synapsis by resolvase. *Journal of Molecular Biology* **3,** 413–425 (1997).
13. Trautt, Z. T., Upmanyu, M. & Karma, A. Interface mobility from interface random walk. *Science* **314,** 632–635 (2006).
14. Hoshino, S. & Ichida, K. Solution of partial differential equations by a modified random walk. *Numerische Mathematik* **18,** 61–72 (1971).
15. Anteneodo, C & Morgado, W. Critical scaling in standard biased random walks. *Physical Review Letters* **99,** 180602 (2007).
16. Adamic, L. A., Lukose, R. M., Puniyani, A. R. & Huberman, B. A. Search in power-law networks. *Physical Review E* **64,** 046135 (2001).
17. Venegas-Andraca, S. E. Quantum walks: a comprehensive review. *Quantum Information Processing* **11,** 1015–1106 (2012).
18. Ambainis, A. Quantum walk algorithm for element distinctness. *SIAM Journal on Computing* **37,** 210–239 (2007).
19. Blanchard, P. & Hongler, M.-O. Quantum random walks and piecewise deterministic evolutions. *Physical review letters* **92,** 120601 (2004).
20. Sellke, T. Reinforced random walk on the d-dimensional integer lattice. *preprint* (1994).
21. Aldous, D. Minimization algorithms and random walk on the d-cube. *The Annals of Probability,* 403–413 (1983).

22. Kunert, J., Montag, A. & Pöhlmann, S. The quincunx: history and mathematics. *Statistical Papers* **42,** 143–169 (2001).

23. Schreiber, A. *Quantum Walks in Time* PhD thesis ().

24. Aharonov, Y., Davidovich, L. & Zagury, N. Quantum random walks. *Physical Review A* **48,** 1687 (1993).

25. Meyer, D. A. From quantum cellular automata to quantum lattice gases. *Journal of Statistical Physics* **85,** 551–574 (1996).

26. Kempe, J. Quantum random walks: an introductory overview. *Contemporary Physics* **44,** 307–327 (2003).

27. Farhi, E. & Gutmann, S. Quantum computation and decision trees. *Physical Review A* **58,** 915 (1998).

28. Orsucci, F. F. & Sala, N. *Reflexing Interfaces: The Complex Coevolution of Information Technology Ecosystems: The Complex Coevolution of Information Technology Ecosystems* (IGI Global, 2008).

29. Chandrashekar, C., Srikanth, R & Laflamme, R. Optimizing the discrete time quantum walk using a SU (2) coin. *Physical Review A* **77,** 032326 (2008).

30. Ambainis, A., Kempe, J. & Rivosh, A. *Coins make quantum walks faster* in *Proceedings of the sixteenth annual ACM-SIAM symposium on Discrete algorithms* (2005), 1099–1108.

31. Ambainis, A., Bach, E., Nayak, A., Vishwanath, A. & Watrous, J. *One-dimensional quantum walks* in *Proceedings of the thirty-third annual ACM symposium on Theory of computing* (2001), 37–49.

32. Knight, P. L., Roldán, E. & Sipe, J. Quantum walk on the line as an interference phenomenon. *Physical Review A* **68,** 020301 (2003).

33. Gerry, C. & Knight, P. L. *Introductory quantum optics* (Cambridge university press, 2005).

34. Gard, B. T., Cross, R. M., Anisimov, P. M., Lee, H. & Dowling, J. P. Quantum random walks with multiphoton interference and high-order correlation functions. *JOSA B* **30,** 1538–1545 (2013).

35. Bouwmeester, D., Marzoli, I., Karman, G. P., Schleich, W. & Woerdman, J. Optical galton board. *Physical Review A* **61,** 013410 (1999).

36. Kempe, J. in *Approximation, Randomization, and Combinatorial Optimization.. Algorithms and Techniques* 354–369 (Springer, 2003).

37. Childs, A. M. *et al. Exponential algorithmic speedup by a quantum walk* in *Proceedings of the thirty-fifth annual ACM symposium on Theory of computing* (2003), 59–68.

38. Shenvi, N., Kempe, J. & Whaley, K. B. Quantum random-walk search algorithm. *Physical Review A* **67,** 052307 (2003).

39. Kendon, V. M. A random walk approach to quantum algorithms. *Philosophical Transactions of the Royal Society of London A: Mathematical, Physical and Engineering Sciences* **364,** 3407–3422 (2006).

40. Potoček, V, Gábris, A., Kiss, T. & Jex, I. Optimized quantum random-walk search algorithms on the hypercube. *Physical Review A* **79,** 012325 (2009).

41. Childs, A. M. & Goldstone, J. Spatial search by quantum walk. *Physical Review A* **70,** 022314 (2004).

42. Tani, S. Claw finding algorithms using quantum walk. *Theoretical Computer Science* **410,** 5285–5297 (2009).

43. Rudinger, K. *et al.* Comparing algorithms for graph isomorphism using discrete-and continuous-time quantum random walks. *Journal of Computational and Theoretical Nanoscience* **10,** 1653–1661 (2013).

44. Lovett, N. B., Cooper, S., Everitt, M., Trevers, M. & Kendon, V. Universal quantum computation using the discrete-time quantum walk. *Physical Review A* **81,** 042330 (2010).

45. Yang, Y.-G., Pan, Q.-X., Sun, S.-J. & Xu, P. Novel image encryption based on quantum walks. *Scientific Reports* **5,** 7784 (2015).

46. Vlachou, C., Krawec, W., Mateus, P., Paunkovic, N. & Souto, A. Quantum key distribution with quantum walks. *arXiv preprint arXiv:1710.07979* (2017).

47. Blankenship, R. E. *Molecular mechanisms of photosynthesis* (John Wiley & Sons, 2014).

48. Mohseni, M., Rebentrost, P., Lloyd, S. & Aspuru-Guzik, A. Environment-assisted quantum walks in photosynthetic energy transfer. *The Journal of Chemical physics* **129,** 11B603 (2008).

49. Crespi, A. *et al.* Anderson localization of entangled photons in an integrated quantum walk. *Nature Photonics* **7,** 322 (2013).

50. Roati, G. *et al.* Anderson localization of a non-interacting bose–einstein condensate. *Nature* **453,** 895 (2008).

51. Wiersma, D. S., Bartolini, P., Lagendijk, A. & Righini, R. Localization of light in a disordered medium. *Nature* **390,** 671 (1997).

52. Hu, H., Strybulevych, A, Page, J., Skipetrov, S. E. & van Tiggelen, B. A. Localization of ultrasound in a three-dimensional elastic network. *Nature Physics* **4,** 945 (2008).

53. Kitagawa, T. *et al.* Observation of topologically protected bound states in photonic quantum walks. *Nature Communications* **3,** 882 (2012).

54. Schrödinger, E. An undulatory theory of the mechanics of atoms and molecules. *Physical review* **28,** 1049 (1926).

55. Born, M. Quantenmechanik der stoßvorgänge. *Zeitschrift für Physik* **38,** 803–827 (1926).

56. Griffiths, D. J. *Introduction to Quantum Mechanics* (Pearson Education India, 2005).

57. Dirac, P. A. M. *The principles of quantum mechanics* **1st edition** (Oxford university press, 1930).

58. Fox, M. *Quantum optics: an introduction* (OUP Oxford, 2006).

59. McMahon, D. *Quantum mechanics demystified* (McGraw-Hill, 2013).

60. Benenti, G, Casati, G & Strini, G. Principles of quantum computation and information. Vol. 1: Basic concepts (2004).

61. Vaughan, S. *Scientific Inference: Learning from Data* doi:10.1017/CBO9781139176071 (Cambridge University Press, 2013).

62. Nayak, A. & Vishwanath, A. Quantum walk on the line. *arXiv preprint quant-ph/0010117* (2000).

63. Reitzner, D., Nagaj, D. & Bužek, V. Quantum walks. *Acta Physica Slovaca. Reviews and Tutorials* **61,** 603–725 (2011).

64. Endrejat, J. & Buettner, H. Entanglement measurement with discrete multiple-coin quantum walks. *Journal of Physics A: Mathematical and General* **38,** 9289 (2005).

65. Abal, G, Siri, R, Romanelli, A & Donangelo, R. Quantum walk on the line: Entanglement and nonlocal initial conditions. *Physical Review A* **73,** 042302 (2006).

66. Hartmann, W. M. *Signals, sound, and sensation* (Springer Science & Business Media, 2004).

67. De Valcárcel, G. J., Roldán, E. & Romanelli, A. Tailoring discrete quantum walk dynamics via extended initial conditions. *New Journal of Physics* **12,** 123022 (2010).

68. Davisson, C. J. Are electrons waves? *Journal of the Franklin Institute* **205,** 597–623 (1928).

69. Thomson, J. J. XL. Cathode rays. *The London, Edinburgh, and Dublin Philosophical Magazine and Journal of Science* **44,** 293–316 (1897).

70. Doyle, B. *Metaphysics: Problems, Paradoxes, and Puzzles, Solved?* (I-Phi Press, 2016).

71. Aczel, A. D. *Entanglement: the greatest mystery in physics* (Raincoast Books, 2002).

72. Tonomura, A., Endo, J, Matsuda, T, Kawasaki, T & Ezawa, H. Demonstration of single-electron buildup of an interference pattern. *American Journal of Physics* **57,** 117–120 (1989).

73. Schrödinger, E. *Discussion of probability relations between separated systems* in *Mathematical Proceedings of the Cambridge Philosophical Society* **31** (1935), 555–563.

74. Spreeuw, R. J. A classical analogy of entanglement. *Foundations of Physics* **28,** 361–374 (1998).

75. Aiello, A., Töppel, F., Marquardt, C., Giacobino, E. & Leuchs, G. Classical entanglement: oxymoron or resource? *arXiv preprint arXiv:1409.0213* (2014).

76. Luis, A. Coherence, polarization, and entanglement for classical light fields. *Optics Communications* **282,** 3665–3670 (2009).

77. McLaren, M., Konrad, T. & Forbes, A. Measuring the nonseparability of vector vortex beams. *Physical Review A* **92,** 023833 (2015).

78. Karimi, E. & Boyd, R. W. Classical entanglement? *Science* **350,** 1172–1173 (2015).

79. Huygens, C. & Thompson, S. P. *Treatise on Light.(Translated by Silvanus P. Thompson.).* (1952).

80. Newton, I. A letter of Mr. Isaac Newton, professor of the mathematicks in the University of Cambridge; containing his new theory about light and colors: Sent by the Author to the Publisher from Cambridge, Febr. 6. 1671/72; In Order to be Communicated to the R. Society. *Philosophical Transactions* **6,** 3075–3087 (1972).

81. Newton, I. *1730* (1952).

82. Jackson, J. D. *Classical Electrodynamics* (John Wiley & Sons, 2012).

83. Griffiths, D. J. *Introduction to electrodynamics* ().

84. Saleh, B. E., Teich, M. C. & Saleh, B. E. *Fundamentals of photonics* (Wiley New York, 1991).

85. Forbes, A. *Laser beam propagation: generation and propagation of customized light* (CRC Press, 2014).

86. Bouchet, O., Sizun, H., Boisrobert, C. & De Fornel, F. *Free-space optics: propagation and communication* (John Wiley & Sons, 2010).

87. Dudley, A. L. *Superpositions of light fields carrying orbital angular momentum* PhD thesis (2012).

88. Svelto, O. & Hanna, D. C. *Principles of lasers* (Springer, 1998).

89. Siegman, A. E. *Lasers* (University Science Books, 1986).

90. Davis, L. Theory of electromagnetic beams. *Physical Review A* **19,** 1177 (1979).

91. Quimby, R. S. *Photonics and lasers: an introduction* (John Wiley & Sons, 2006).

92. Andrews, D. L. & Babiker, M. *The angular momentum of light* (Cambridge University Press, 2012).

93. Andrews, D. L. *Photonics, Volume 1: Fundamentals of Photonics and Physics* (John Wiley & Sons, 2015).

94. Phillips, R. L. & Andrews, L. C. Spot size and divergence for Laguerre Gaussian beams of any order. *Applied Optics* **22,** 643–644 (1983).

95. Allen, L., Beijersbergen, M. W., Spreeuw, R. & Woerdman, J. Orbital angular momentum of light and the transformation of Laguerre-Gaussian laser modes. *Physical Review A* **45,** 8185 (1992).

96. Allen, L & Padgett, M. The Poynting vector in Laguerre–Gaussian beams and the interpretation of their angular momentum density. *Optics Communications* **184,** 67–71 (2000).

97. Allen, L, Padgett, M. & Babiker, M. in *Progress in Optics* 291–372 (Elsevier, 1999).

98. Poynting, J. H. *et al.* The wave motion of a revolving shaft, and a suggestion as to the angular momentum in a beam of circularly polarised light. *Proc. R. Soc. Lond. A* **82,** 560–567 (1909).

99. Beth, R. A. Mechanical detection and measurement of the angular momentum of light. *Physical Review* **50,** 115 (1936).

100. Roxworthy, B. J. & Toussaint Jr, K. C. Optical trapping with π-phase cylindrical vector beams. *New Journal of Physics* **12,** 073012 (2010).

101. Kimura, W. *et al.* Laser acceleration of relativistic electrons using the inverse Cherenkov effect. *Physical Review Letters* **74,** 546 (1995).

102. Abouraddy, A. F. & Toussaint Jr, K. C. Three-dimensional polarization control in microscopy. *Physical Review Letters* **96,** 153901 (2006).

103. Mair, A., Vaziri, A., Weihs, G. & Zeilinger, A. Entanglement of the orbital angular momentum states of photons. *Nature* **412,** 313 (2001).

104. JONES, R. A new calculus for the treatment of optical systems: I Description and discussion of the calculcs. *J. Opt. Soc. Am.* **31,** 488 (1941).

105. Poincaré, H. *Théorie mathématique de la lumiere* (Gauthier Villars, 1892).

106. Sharma, K. K. *Optics: principles and applications* (Elsevier, 2006).

107. Hall, D. G. Vector-beam solutions of Maxwell's wave equation. *Optics letters* **21,** 9–11 (1996).

108. Zhan, Q. Cylindrical vector beams: from mathematical concepts to applications. *Advances in Optics and Photonics* **1,** 1–57 (2009).

109. Maurer, C., Jesacher, A., Fürhapter, S., Bernet, S. & Ritsch-Marte, M. Tailoring of arbitrary optical vector beams. *New Journal of Physics* **9,** 78 (2007).

110. Milione, G., Sztul, H., Nolan, D. & Alfano, R. Higher-order Poincaré sphere, Stokes parameters, and the angular momentum of light. *Physical review letters* **107,** 053601 (2011).

111. Ndagano, B., Sroor, H., McLaren, M., Rosales-Guzmán, C. & Forbes, A. Beam quality measure for vector beams. *Optics letters* **41,** 3407–3410 (2016).

112. Ryan, C. A., Laforest, M., Boileau, J.-C. & Laflamme, R. Experimental implementation of a discrete-time quantum random walk on an NMR quantum-information processor. *Physical Review A* **72,** 062317 (2005).

113. Feist, A. *et al.* Quantum coherent optical phase modulation in an ultrafast transmission electron microscope. *Nature* **521,** 200 (2015).

114. Karski, M. *et al.* Quantum walk in position space with single optically trapped atoms. *Science* **325,** 174–177 (2009).

115. Zähringer, F *et al.* Realization of a quantum walk with one and two trapped ions. *Physical Review Letters* **104,** 100503 (2010).

116. Schmitz, H. *et al.* Quantum walk of a trapped ion in phase space. *Physical Review Letters* **103,** 090504 (2009).

117. Cardano, F. *et al.* Quantum walks and wavepacket dynamics on a lattice with twisted photons. *Science Advances* **1,** e1500087 (2015).

118. Cardano, F. *et al.* Statistical moments of quantum-walk dynamics reveal topological quantum transitions. *Nature communications* **7,** 11439 (2016).

119. Alberti, A. & Wimberger, S. Quantum walk of a Bose-Einstein condensate in the Brillouin zone. *Physical Review A* **96,** 023620 (2017).

120. Schreiber, A *et al.* Decoherence and disorder in quantum walks: from ballistic spread to localization. *Physical Review Letters* **106,** 180403 (2011).

121. Boutari, J *et al.* Large scale quantum walks by means of optical fiber cavities. *Journal of Optics* **18,** 094007 (2016).

122. Perets, H. B. *et al.* Realization of quantum walks with negligible decoherence in waveguide lattices. *Physical Review Letters* **100,** 170506 (2008).

123. Sansoni, L. *et al.* Two-particle bosonic-fermionic quantum walk via integrated photonics. *Physical Review Letters* **108,** 010502 (2012).

124. Qi, F, Wang, Y., Ma, Q. & Zheng, W. Experimentally simulating quantum walks with self-collimated light. *Scientific reports* **6,** 28610 (2016).

125. Regensburger, A. *et al.* Photon propagation in a discrete fiber network: an interplay of coherence and losses. *Physical Review Letters* **107,** 233902 (2011).

126. Goyal, S. K., Roux, F. S., Forbes, A. & Konrad, T. Implementing quantum walks using orbital angular momentum of classical light. *Physical review letters* **110,** 263602 (2013).

127. Venegas-Andraca, S. E. Quantum walks for computer scientists. *Synthesis Lectures on Quantum Computing* **1,** 1–119 (2008).

128. Ndagano, B. *et al.* Characterizing quantum channels with non-separable states of classical light. *Nature Physics* **13,** 397 (2017).

129. Li, P., Sun, Y., Yang, Z., Song, X. & Zhang, X. Classical hypercorrelation and wave-optics analogy of quantum superdense coding. *Scientific Reports* **5,** 18574 (2015).

130. Sun, Y. *et al.* Non-local classical optical correlation and implementing analogy of quantum teleportation. *Scientific Reports* **5,** 9175 (2015).

131. Pinheiro, A. *et al.* Vector vortex implementation of a quantum game. *JOSA B* **30,** 3210–3214 (2013).

132. Töppel, F., Aiello, A., Marquardt, C., Giacobino, E. & Leuchs, G. Classical entanglement in polarization metrology. *New Journal of Physics* **16,** 073019 (2014).

133. Song, X., Sun, Y., Li, P., Qin, H. & Zhang, X. Bell's measure and implementing quantum Fourier transform with orbital angular momentum of classical light. *Scientific Reports* **5,** 14113 (2015).

134. Cardano, F. *et al.* Detection of Zak phases and topological invariants in a chiral quantum walk of twisted photons. *Nature Communications* **8,** 15516 (2017).

135. Goyal, S. K., Roux, F. S., Forbes, A. & Konrad, T. Implementation of multidimensional quantum walks using linear optics and classical light. *Physical Review A* **92,** 040302 (2015).

136. Hecht, E. *Optics* 213–214 (Addison Wesley, 1998).

137. Naidoo, D. *et al.* Controlled generation of higher-order Poincaré sphere beams from a laser. *Nature Photonics* **10,** 327–332 (2016).

138. Marrucci, L., Manzo, C & Paparo, D. Optical spin-to-orbital angular momentum conversion in inhomogeneous anisotropic media. *Physical Review Letters* **96,** 163905 (2006).

139. He, H, Friese, M., Heckenberg, N. & Rubinsztein-Dunlop, H. Direct observation of transfer of angular momentum to absorptive particles from a laser beam with a phase singularity. *Physical Review Letters* **75,** 826 (1995).

140. Padgett, M. & Bowman, R. Tweezers with a twist. *Nature Photonics* **5,** 343 (2011).

141. Allegre, O., Perrie, W, Edwardson, S., Dearden, G & Watkins, K. Laser microprocessing of steel with radially and azimuthally polarized femtosecond vortex pulses. *Journal of Optics* **14,** 085601 (2012).

142. Batterman, R. W. Falling cats, parallel parking, and polarized light. *Studies in History and Philosophy of Science Part B: Studies in History and Philosophy of Modern Physics* **34,** 527–557 (2003).

143. Berry, M. V. Quantal phase factors accompanying adiabatic changes. *Proc. R. Soc. Lond. A* **392,** 45–57 (1984).

144. Pancharatnam, S. *Generalized theory of interference and its applications. Part 1: Coherent pencils* in *Proceedings of the Indian Academy of Sciences* (1956), 247–262.

145. Pancharatnam, S. *Generalized theory of interference and its applications. Part 2: Partially coherent pencils* in *Proceedings of the Indian Academy of Sciences* (1956), 398–417.

146. Bomzon, Z., Kleiner, V. & Hasman, E. Pancharatnam–Berry phase in space-variant polarization-state manipulations with subwavelength gratings. *Optics Letters* **26,** 1424–1426 (2001).

147. Marrucci, L *et al.* Spin-to-Orbital Optical Angular Momentum Conversion in Liquid Crystal "q-Plates": Classical and Quantum Applications. *Molecular Crystals and Liquid Crystals* **561,** 48–56 (2012).

148. Devlin, R. C. *et al.* Spin-to-orbital angular momentum conversion in dielectric metasurfaces. *Optics Express* **25,** 377–393 (2017).

149. Bomzon, Z., Biener, G., Kleiner, V. & Hasman, E. Space-variant Pancharatnam–Berry phase optical elements with computer-generated subwavelength gratings. *Optics Letters* **27,** 1141–1143 (2002).

150. Piccirillo, B, Slussarenko, S, Marrucci, L & Santamato, E. The orbital angular momentum of light: genesis and evolution of the concept and of the associated photonic technology. *Riv. Nuovo Cimento* **36,** 501–555 (2013).

151. Slussarenko, S. *et al.* Tunable liquid crystal q-plates with arbitrary topological charge. *Optics Express* **19,** 4085–4090 (2011).

152. Lin, D., Fan, P., Hasman, E. & Brongersma, M. L. Dielectric gradient metasurface optical elements. *Science* **345,** 298–302 (2014).

153. Kaiser, T., Flamm, D., Schröter, S. & Duparré, M. Complete modal decomposition for optical fibers using CGH-based correlation filters. *Optics Express* **17,** 9347–9356 (2009).

154. Litvin, I. A., Dudley, A., Roux, F. S. & Forbes, A. Azimuthal decomposition with digital holograms. *Optics Express* **20,** 10996–11004 (2012).

155. Schulze, C., Ngcobo, S., Duparré, M. & Forbes, A. Modal decomposition without a priori scale information. *Optics Express* **20,** 27866–27873 (2012).

156. Flamm, D. *et al.* All-digital holographic tool for mode excitation and analysis in optical fibers. *Journal of Lightwave Technology* **31,** 1023–1032 (2013).

157. Forbes, A., Dudley, A. & McLaren, M. Creation and detection of optical modes with spatial light modulators. *Advances in Optics and Photonics* **8,** 200–227 (2016).

158. Mok, F., Diep, J., Liu, H.-K. & Psaltis, D. Real-time computer-generated hologram by means of liquid-crystal television spatial light modulator. *Optics Letters* **11,** 748–750 (1986).

159. Rosales-Guzmán, C. & Forbes, A. *How to shape light with spatial light modulators* (SPIE Press, 2017).

160. Clark, T. W., Offer, R. F., Franke-Arnold, S., Arnold, A. S. & Radwell, N. Comparison of beam generation techniques using a phase only spatial light modulator. *Optics Express* **24,** 6249–6264 (2016).

161. Yang, D.-K. *Fundamentals of liquid crystal devices* (John Wiley & Sons, 2014).

162. Durnin, J., Miceli Jr, J. & Eberly, J. Diffraction-free beams. *Physical Review Letters* **58,** 1499 (1987).

163. Arlt, J & Dholakia, K. Generation of high-order Bessel beams by use of an axicon. *Optics Communications* **177,** 297–301 (2000).

164. Beijersbergen, M. W., Allen, L., Van der Veen, H. & Woerdman, J. Astigmatic laser mode converters and transfer of orbital angular momentum. *Optics Communications* **96,** 123–132 (1993).

165. Roux, F. S. Optical vortex density limitation. *Optics communications* **223,** 31–37 (2003).

166. Karimi, E., Zito, G., Piccirillo, B., Marrucci, L. & Santamato, E. Hypergeometric-gaussian modes. *Optics Letters* **32,** 3053–3055 (2007).

167. Bryngdahl, O. Geometrical transformations in optics. *JOSA* **64,** 1092–1099 (1974).

168. Berkhout, G. C., Lavery, M. P., Courtial, J., Beijersbergen, M. W. & Padgett, M. J. Efficient sorting of orbital angular momentum states of light. *Physical Review Letters* **105,** 153601 (2010).

169. Mirhosseini, M., Malik, M., Shi, Z. & Boyd, R. W. Efficient separation of the orbital angular momentum eigenstates of light. *Nature Communications* **4,** 2781 (2013).

170. Lavery, M. P. *et al.* Refractive elements for the measurement of the orbital angular momentum of a single photon. *Optics Express* **20,** 2110–2115 (2012).

171. O'Sullivan, M. N., Mirhosseini, M., Malik, M. & Boyd, R. W. Near-perfect sorting of orbital angular momentum and angular position states of light. *Optics express* **20,** 24444–24449 (2012).

172. Ruffato, G. *et al.* A compact diffractive sorter for high-resolution demultiplexing of orbital angular momentum beams. *Scientific Reports* **8,** 10248 (2018).

173. Lavery, M. P. *et al.* Efficient measurement of an optical orbital-angular-momentum spectrum comprising more than 50 states. *New Journal of Physics* **15,** 013024 (2013).

174. Childs, A. M. Universal computation by quantum walk. *Physical Review Letters* **102,** 180501 (2009).

175. Lovett, N. B. *et al.* Spatial search using the discrete time quantum walk. *Natural Computing* **11,** 23–35 (2012).

176. Kendon, V. Where to quantum walk. *arXiv preprint arXiv:1107.3795* (2011).

177. Lee, K. & Thomas, J. Entanglement with classical light fields. *Physical Review A* **69,** 052311 (2004).

178. Francisco, D. & Ledesma, S. Classical optics analogy of quantum teleportation. *JOSA B* **25,** 383–390 (2008).

179. Aspect, A., Grangier, P. & Roger, G. Experimental tests of realistic local theories via Bell's theorem. *Physical Review Letters* **47,** 460 (1981).

180. Wootters, W. K. Entanglement of formation and concurrence. *Quantum Information & Computation* **1,** 27–44 (2001).

181. Yuen, H. P. Amplification of quantum states and noiseless photon amplifiers. *Physics Letters A* **113,** 405–407 (1986).

182. Barnum, H., Caves, C. M., Fuchs, C. A., Jozsa, R. & Schumacher, B. Noncommuting mixed states cannot be broadcast. *Physical Review Letters* **76,** 2818 (1996).

183. Schreiber, A. *et al.* A 2D quantum walk simulation of two-particle dynamics. *Science,* 1218448 (2012).

184. Sroor, H., Lisa, N., Naidoo, D., Litvin, I. & Forbes, A. Purity of vector vortex beams through a birefringent amplifier. *Physical Review Applied* **9,** 044010 (2018).

185. Goyal, S. K., Roux, F., Forbes, A. & Konrad, T. *The scalable implementation of quantum walks using classical light* in *Complex Light and Optical Forces VIII* **8999** (2014), 89991A.